Structure-kinetics relationships in micellar solutions of nonionic surfactants

Daniel Colegate

Structure-kinetics relationships in micellar solutions of nonionic surfactants

A thesis submitted in partial fulfilment of the requirements for the degree of Doctor of Philosophy in the University of Durham, by

Daniel Colegate

Durham University

Department of Chemistry and Ustinov College

University of Durham

Summer 2009

Structure-kinetics relationships in micellar solutions of nonionic surfactants

A thesis submitted in partial fulfilment of the requirements for the degree of Doctor of Philosophy in the University of Durham, by

Daniel Colegate

Department of Chemistry and Ustinov College

Micellar surfactant solutions are highly complex systems containing aggregates of different shapes and sizes all in dynamic equilibrium. I have undertaken an investigation into the kinetic processes that occur in micellar surfactant solutions subjected to both bulk perturbations and close to expanding surfaces.

Supporting information regarding the equilibrium properties of surfactant micelles has been acquired using several experimental techniques including small-angle neutron scattering (SANS) and pulsed field gradient spin echo (PFGSE) nmr.

Bulk exchange kinetics between micelles and monomers in solution have been investigated using both numerical modelling and stopped-flow dilution experiments. My results show that conventional theories of monomer-micelle exchange kinetics apply only under very limited conditions. In order to understand how micelle solutions respond to large perturbations from equilibrium a different approach is required. I have hypothesised an alternative monomer-micelle exchange mechanism. This hypothesis has been tested using numerical modelling and comparison of theoretical predictions with the results of stopped-flow perturbation experiments. These experimental results are consistent with my hypothesis.

In addition to bulk exchange kinetics, I have also undertaken a detailed experimental investigation of adsorption kinetics from micellar systems on the millisecond timescale. Again my results indicate that conventional theoretical approaches are incomplete and I suggest an alternative adsorption pathway that should be included in future theories of adsorption from micellar surfactant solutions.

Acknowledgements

Throughout my doctoral studies I have always been able to rely on the advice and support of my supervisor, Professor Colin Bain. His expert guidance and quick thinking have helped to guide my steps these past three and a half years and I will always be grateful to him for guiding my development in academia. I have also bent the ear of uncountable academics during my time in the Bain group, but special mention should go to Julian Eastoe for letting me use up some of his neutron beam time when my own data was found lacking and to Lian Hutchings for letting a naive physical chemist into his synthetic lab'. I am also very grateful to Dr. Nicolas Peron who worked tirelessly to acquire the PFGSE NMR data that I have found so useful.

Throughout my time in Durham I have been privileged to work in an office full of well-meaning eccentrics and have never struggled to find a sympathetic ear or willing tea drinking partner throughout the difficult times and late nights.

Finally, there are no words that I can find to capture how much I attribute the happiness of my time in Durham to my being able to share it with Esther.

Glossary of abbreviations

Surfactants and chemicals

TX-100	Triton X-100
$C_{10}E_8$	octaethyleneglycol decyl ether
$C_{12}E_8$	octaethyleneglycol dodecyl ether
$C_{14}E_8$	octaethyleneglycol tetradecyl ether
$C_{16}E_8$	octaethyleneglycol hexadecyl ether
$C_{12}E_6$	hexaethyleneglycol dodecyl ether
$C_{14}E_6$	hexaethyleneglycol tetradecyl ether
C_{14}DAPS	tetradecyldimethylammonio-1-propanesulfonate
α-C_{12}malt	alpha-n-dodecyl D-maltoside
β-C_{12}malt	beta-n-dodecyl D-maltoside
β-C_{14}malt	beta-n-tetradecyl D-maltoside
Py	Pyrene
CTAB	hexadecyltrimethylammonium bromide

Acronyms

Cmc	Critical micelle concentration
DST	Dynamic surface tension
SANS	Small-angle neutron scattering
SAXS	Small-angle X-ray scattering
SALS	Small-angle light scattering
PFGSE-NMR	Pulsed field gradient spin echo nuclear magnetic resonance
NMR	Nuclear magnetic resonance
OFC	Overflowing cylinder
MBP	Maximum bubble pressure
LDV	Laser Doppler velocimetry
SWSE	Sum of weighted squared errors
MD	Molecular dynamics
MT	Molecular thermodynamics

Table of Contents

Chapter 1

Kinetic Processes in Micellar Surfactant Solutions

Surfactants are ubiquitous in aqueous systems. Phospholipids form the membranes that envelop biological cells and segregate them internally into functional compartments. Amphiphilic proteins act as nature's emulsifiers. Surfactants are used to stabilise pharmaceutical, cosmetic and agrochemical formulations, as cleaning and wetting agents, as dispersants and stabilisers, as lubricants, as foam stabilisers and as catalysts, to list but a selection of their applications. A characteristic of most surfactants is that, above some concentration (the critical micelle concentration, cmc), they aggregate into mesoscopic structures such as micelles of various shapes (spheres, disks, rods, worms), lamellar sheets or vesicles. Some surfactants, such as double-chained phospholipids, have such low monomer solubilities that essentially all the interesting physical properties of the surfactant are those of the aggregates. Other surfactants, including the majority of synthetic detergents, are present in practical applications both as monomers and as micelles; the physical behaviour of the system depends on the properties of both moieties and on the interconversion between them. Surfactants also aggregate at interfaces with structures that may be different from those in the bulk phase.

Over the past half-century a vast body of information has been amassed on the equilibrium structural properties of surfactants. A number of standard techniques exist for the characterisation of new surfactant systems. In surfactant chemistry, the dynamic properties of surfactant solutions are often as important as the equilibrium behaviour. Whether one is looking at the fusion of membranes, the release of an encapsulated drug, the coalescence of droplets, the conditioning of hair, the collapse of a foam, the break-up of a jet or the wetting of a fabric, it is the dynamical properties of surfactants that determine the macroscopic consequences. While reasonable progress has been made in modelling the adsorption kinetics of pure monomeric surfactants our understanding of adsorption processes in micellar systems is much less satisfactory.

Chapter 1 contains a review of the current state of knowledge on surfactant adsorption kinetics, beginning with a brief introduction to equilibrium systems before considering adsorption kinetics from monomeric systems and then finally micellar systems.

1.1. Understanding Equilibrium Adsorption

To interpret dynamic surface tension data a good understanding of equilibrium adsorption properties is essential. In this brief section I will outline the theoretical framework which underpins analysis of kinetic data later in this document.

1.1.1 Equilibrium Surface Coverage

The determination of the amount of surfactant adsorbed at an interface is usually calculated indirectly from interfacial tension measurements. For solutions below the cmc an increase in the bulk surfactant concentration (c_b) results in a decrease of equilibrium surface tension, γ_{eq}. Above the cmc γ_{eq} remains approximately constant with extra monomer forming micelles. An abrupt change in the γ_{eq} vs. ln c curve indicates the value of the cmc.

From data such as this the amount of surfactant adsorbed at the interface may be calculated using the Gibbs adsorption equation which is given below. The adsorbed amount is usually expressed in terms of the surface excess, Γ, which is the excess of solute per unit area of the surface over what would be present if the bulk concentration prevailed all the way to the surface. For dilute solutions the surface excess and surface concentration are approximately equivalent numerically, since the bulk concentration is so small that there would be almost zero coverage if the bulk concentration prevailed all the way to the interface.

1.1.2 The Gibbs Adsorption Equation

The Gibbs adsorption equation is fundamental to all adsorption processes. In its most general form; [1]

$$d\gamma|_{T,P} = -\sum_i \Gamma_i d\mu_i \qquad (1.1)$$

where $d\gamma$ is the change in surface tension of the solvent, Γ_i is the surface excess of the i^{th} component in the system and $d\mu_i$ is the change in chemical potential of the i^{th} component. At equilibrium between the bulk and interfacial phases, $d\mu_i = RTd\ln a_i$, where a_i is the activity of the i^{th} component, R is the ideal gas constant and T is the absolute temperature. For dilute solutions activity coefficients tend to one and $a = m/m^{\ominus}$ with bulk concentration. For solutions containing only one solute the Gibbs equation is often given in the form;

$$\Gamma = -\frac{1}{nRT}\left(\frac{\partial\gamma}{\partial\ln c}\right)_T \tag{1.2}$$

where the factor n is used here to represent a constant which depends on the number of species constituting the surfactant and adsorbing at the interface. For a nonionic surfactant, or a uni-univalent ionic surfactant in the presence of excess electrolyte of common counterion, n = 1. For a uni-univalent ionic surfactant in the absence of electrolyte n = 2. If one measures the surface tension at a range of different bulk concentrations, then equation (1.2) may be applied to obtain an equilibrium adsorption isotherm, Γ (c). There are many methods available for the determination of surface tension including force methods (Wilhelmy plates, du Nouy ring), shape methods (pendant drop) or pressure methods (maximum bubble pressure). [2]

1.1.3 Theoretical adsorption isotherms and surface equations of state

The purpose of an adsorption isotherm is to relate the surfactant concentration in the bulk and the amount of surfactant adsorbed at the interface. Using equation (1.2) and a proper adsorption isotherm, one may derive a corresponding surface equation of state $\gamma(\Gamma)$, and then find $\gamma(c)$. Chang *et* al [2] give an introduction into some of the most commonly used isotherms in their review of dynamic surface tension methods.

The simplest adsorption isotherm is the linear Henry isotherm,

$$\Gamma = K_H c \tag{1.3}$$

where K_H is the equilibrium adsorption constant, an empirical measure of surface activity. Henry's isotherm only applies for very low surface concentrations and

corresponds to gaseous monolayers of non-interacting molecules. Another drawback is that no maximum surface excess is defined. The surface equation of state, $\gamma(\Gamma)$ can be derived from the Gibbs equation (1.2);

$$\Pi = \gamma_0 - \gamma = -nRT\Gamma \tag{1.4}$$

where Π is the surface pressure. This expression is analogous to the 3-D perfect gas equation.

The most commonly used non-linear adsorption isotherm is the Langmuir isotherm.

$$\Gamma = \Gamma_\infty \frac{K_L c}{1 + K_L c} \tag{1.5}$$

where Γ_∞ is the maximum surface coverage and K_L is the Langmuir constant. Here the parameter Γ_∞ is a theoretical limit which cannot normally be reached because of the constraint of maximum concentration due to the cmc or limiting solubility. The Langmuir model assumes that every adsorption site is equivalent, that the probability of occupying a given site is independent of the occupancy of neighbouring sites and that there is no interaction between adsorbed monomers. The corresponding surface equation of state is the Szyszkowvski equation.

$$\Pi = nRT\Gamma_\infty \ln(1 + K_L c) \tag{1.6}$$

Deviations from the Langmuir isotherm are often attributable to the failure of the assumption of independent and equivalent adsorption sites.

The Frumkin isotherm builds on the Langmuir isotherm by accounting for solute-solute interactions at a non-ideal surface. Its usual stated form is;

$$c = \frac{1}{K_F} \frac{\Gamma}{\Gamma_\infty - \Gamma} \exp(-A(\Gamma/\Gamma_\infty)) \tag{1.7}$$

where K_F is the Frumkin equilibrium adsorption constant and A is a measure of the non-ideality of mixing in the surface layer. This isotherm is appropriate mostly for nonionic surfactants. The corresponding equation of state is;

$$\Pi = -nRT\Gamma_\infty \ln\left(1-\frac{\Gamma}{\Gamma_\infty}\right) - \frac{1}{2}nRTA\Gamma_\infty\left(\frac{\Gamma}{\Gamma_\infty}\right)^2 \quad (1.8)$$

1.1.4 Isotherms from neutron reflection

The use of neutron reflection (NR) to study the structure of monolayers adsorbed at interfaces began in the 1980's. The pioneering work of Thomas and Penfold *et al* [3-5] has built a wealth of information on the composition of surfactant layers at the air–water interface. A comprehensive review of neutron reflection data and its complementarity to other surface techniques was published in 2000.[6] Neutron reflection also provides an accurate measurement of surface excess, which allows precise isotherms to be constructed.

1.2. Kinetics of adsorption from monomeric surfactant solutions

Surfactant adsorption is not an instantaneous process. The kinetics of surfactant adsorption has been the subject of extensive theoretical and experimental study for more than half a century [7, 8].

An overview of the background theory of surfactant adsorption is given by Eastoe and Dalton [9]. The first step in studying the adsorption kinetics of surfactants at the air-water interface is to obtain reliable data on the surface excess as function of time, $\Gamma(t)$. This time dependence is notoriously hard to measure directly since techniques that measure the surface excess, such as neutron reflection, require long acquisition times. The classical method is to measure the dynamic surface tension and use an equilibrium surface equation of state to relate the measured surface tension data to surface excess. The assumption that the equilibrium relationship still applies during the dynamic process was first stated by Hansen and Wallace [10]. This assumption implies that the surface tension is dependent only on the surface coverage and is not affected by any rearrangement/reorientation the molecules may undergo. Posner *et al* [11] carried out surface potential studies and concluded that the slow orientation process results in negligible, if any, surface tension changes.

A freshly formed surface has a surface tension γ close to that of the pure solvent γ_0. Over time this surface tension value decays to an equilibrium value γ_{eq} as surfactant molecules

diffuse to the surface and adsorb. The behaviour of γ vs. time is known as the dynamic surface tension, $\gamma(t)$ or DST. There are a wide variety of techniques available for studying the DST appropriate for different adsorption timescales, as shown in Figure 1.

Equilibrium adsorption remains a dynamic state, where the adsorbing flux of surfactant monomers j_{ads} is equal to the desorbing flux j_{des}. If a surface at equilibrium were expanded then immediately after the expansion the surface excess Γ would be less than the equilibrium value ($\Gamma < \Gamma_{eq}$), so to re-establish equilibrium the adsorbing flux would now be greater than the desorbing flux ($j_{ads} > j_{des}$). The opposite would be true if the surface were contracted. A simple kinetic relationship is $d\Gamma / dt = j_{ads} - j_{des}$. This physical picture is summarised in Figure 2.

A more rigorous description of dynamic surface tension is to say that a freshly created interface has $\Gamma < \Gamma_{eq}$ so that the adsorbing flux of monomers exceeds the desorbing flux and the surface excess increases, causing the surface tension to decay.

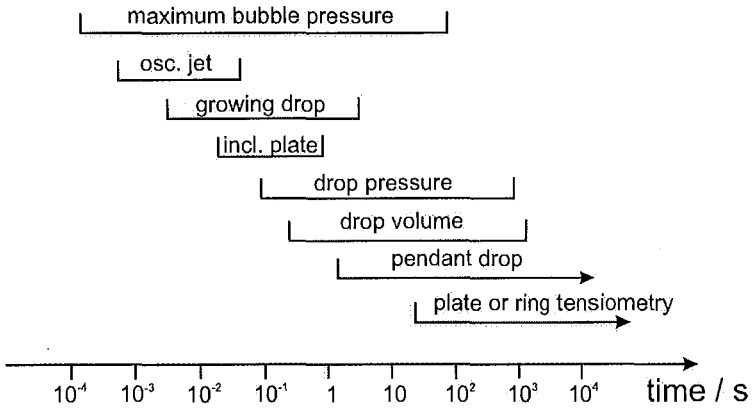

Figure 1: Applicable timescales for different surface tension techniques

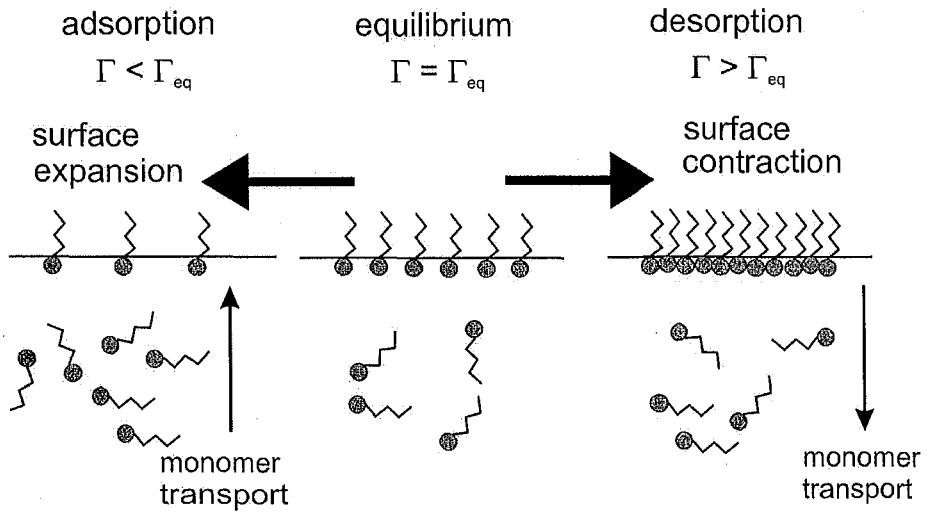

Figure 2: Surface deformation driving monomer flux to the interface

In order to model adsorption to the air-water interface one may consider the adsorption process as two discrete components. The first component is the diffusion of surfactant molecules from the bulk to the subsurface; the second component is the transfer of molecules from the subsurface to the surface. The subsurface is an imaginary plane just below the surface. There are two main kinetic models that describe this process: (1) diffusion controlled and (2) mixed kinetic-diffusion control.

1.2.1 Diffusion to the subsurface

The subsurface is a boundary between the domain in which diffusion occurs and the domain in which adsorption occurs. As molecules adsorb to the surface the subsurface concentration is decreased so diffusion occurs in the bulk to replenish the subsurface. The domain in which diffusion takes place is much larger than the adsorption layer. The Ward-Tordai equation [12] accounts for diffusion of monomers from the bulk to the subsurface and for back diffusion. The equation's usual form is

$$\Gamma(t) = 2c_b\sqrt{\frac{D_{mon}t}{\pi}} - 2\sqrt{\frac{D_{mon}}{\pi}}\int_0^{\sqrt{t}} c_s d(t-\tau) \qquad (1.9)$$

where c_b is the bulk surfactant concentration, c_s is the subsurface concentration, D_{mon} is the monomer diffusion coefficient and τ is a dummy variable of integration. If $c_s(t)$ were known then $\Gamma(t)$ could be calculated. Johannsen *et al* [13] proposed an empirical form of

$c_s(t)$ but since c_s can never be measured directly such work is of primarily theoretical interest. Another approach is to postulate a relationship between $\Gamma(t)$ and $c_s(t)$ and substitute the expression into equation(1.9). However, because of the back diffusion integral the resulting expression cannot usually be solved analytically. The relationship between $\Gamma(t)$ and $c_s(t)$ depends upon the adsorption model being used, diffusion or mixed kinetic-diffusion controlled.

1.2.2 Diffusion-only controlled adsorption

In the diffusion-only case there is no activation energy barrier for the transfer of molecules between the subsurface and the surface. The surface and subsurface are therefore at local equilibrium and one may use an equilibrium adsorption isotherm such as equations (1.3), (1.5) and (1.7) to relate the subsurface concentration to the surface excess. Sutherland [14] substituted the linear Henry isotherm (equation (1.3)) into the Ward-Tordai equation. In this very dilute limit the analytical solution for the relationship between $\Gamma(t)$ and $c_s(t)$ is

$$\frac{c_s(t)}{c_0} = \frac{\Gamma}{K_H c_0} = 1 - \exp\left(\frac{D_{mon} t}{K_H^2}\right) \operatorname{erfc}\left[\frac{(D_{mon} t)^{1/2}}{K_H}\right] \tag{1.10}$$

By considering the limiting behaviour of the exponentials and complementary error functions, Sutherland also gave asymptotic solutions for the time-dependence of surface excess at long and short times. For the more complex, non-linear isotherms numerical methods must be used to solve the Ward-Tordai equation, which are reviewed by Chang and Franses. [2]

Hansen [15] also developed a model for diffusion-controlled adsorption at the air/liquid interface with simultaneous evaporation, producing an equation that was very similar to the Ward-Tordai equation. Like Sutherland [14], Hansen considered the short and long time limiting cases. Using a Maclaurin's series expansion of his adsorption equation for short times and deriving an asymptotic solution at long times, Hansen predicted the same time dependence as Sutherland; for short times $\Gamma \propto t^{1/2}$ and for long times $\Gamma \propto t^{-1/2}$.

Other approximate solutions to the Ward-Tordai equation have been derived such as that by Joos and Van den Bogaert [16] who used diffusion penetration theory to avoid the

requirement to integrate the diffusion equation. However asymptotic solutions are more easily applied to surface tension decays. Fainerman, Miller and Makievski [17] analysed existing and newly derived asymptotic solutions of the adsorption kinetic equations in the regions of infinitely small and infinitely long surface lifetimes for single and multi-component systems, on non-deforming and deforming surfaces and under stationary and non-stationary conditions. The asymptotic behaviour for the rate of diffusion controlled adsorption at both long and short times for a non-deforming surface are given below.

i) Short-time approximation, $t \rightarrow 0$

At the beginning of adsorption back diffusion may be neglected in (1.9) so only the first term in the Ward-Tordai equation is considered.

$$\Gamma(t) = 2c_0\sqrt{\frac{D_{mon}t}{\pi}} \tag{1.11}$$

Since we are in the limit of low surface coverage we can use the linear Henry equation of state (equation(1.4)) to give the short-time solution for surface tension decay:

$$\gamma_{t\rightarrow 0} = \gamma_0 - 2nRTc_o\sqrt{\frac{D_{mon}t}{\pi}} \tag{1.12}$$

ii) Long-time approximation, $t \rightarrow \infty$

At long times the subsurface concentration approaches the bulk concentration so can be factored outside the integral in equation (1.9). Rearrangement of the resulting expression gives

$$\Delta c_{t\rightarrow\infty} = c_0 - c_s = \Gamma\sqrt{\frac{\pi}{4D_{mon}t}} \tag{1.13}$$

Using the Gibbs equation (1.2) and rearranging gives the solution for long-time surface tension decays;

$$\gamma_{t\rightarrow\infty} = \gamma_{eq} + \frac{nRT\Gamma_{eq}^2}{c}\sqrt{\frac{\pi}{4D_{mon}t}} \tag{1.14}$$

Equations (1.12) and (1.14) describe adsorption as a purely diffusion controlled process. One may fit measured dynamic surface tension data using these equations to test whether adsorption is behaving in a diffusion controlled way.

1.2.3. Mixed kinetic-diffusion controlled adsorption

Baret [18] described the adsorption process with the statement: "The number of solute molecules which adsorb at the interface is equal to the number of solute molecules which, having diffused from the bulk to the subsurface, cross the adsorption energy barrier". The term 'adsorption barrier' incorporates all factors that may affect adsorption such as steric, electronic or kinetic requirements. Baret concluded that the diffusion process dominates initially but switches to mixed kinetics as equilibrium is approached.

In the limit that adsorption were entirely controlled by kinetic considerations then one could neglect the diffusion problem entirely, since there would be no concentration gradient in the bulk. It is far more likely, however, that neither the diffusion process nor adsorption process can be entirely neglected. This is the case of mixed kinetic-diffusion control. Monomers diffuse from the bulk to the subsurface obeying the same equations as the purely diffusion controlled case. To adsorb, however, they must also satisfy a number of conditions. Unlike in the diffusion-only case, the subsurface is not necessarily at local equilibrium with the surface. Instead of using equilibrium adsorption isotherms to relate $\Gamma(t)$ and $c_s(t)$, one must account for the adsorption/desorption step using a kinetic expression,

$$\frac{d\Gamma(t)}{dt} = r_1 - r_{-1} \tag{1.15}$$

where r_1 and r_{-1} are the rates of adsorption and desorption respectively. It is reasonable to assume that the rate of adsorption depends on both $\Gamma(t)$ and $c_s(t)$ while the rate of desorption depends only on $\Gamma(t)$. Then, following Borwankar and Wasan [19], equation (1.15) may be rewritten as

$$\frac{d\Gamma(t)}{dt} = k^a G[\Gamma(t)]c_s(t) - k^d F[\Gamma(t)] \tag{1.16}$$

where k_a is the adsorption rate, k_d is the desorption rate and G and F are functions of Γ. In the limit $t \to \infty$, $d\Gamma(t)/dt = 0$ and equation (1.16) reduces to an equilibrium adsorption isotherm. Therefore, if the equilibrium adsorption isotherm is known for a particular system, one should apply a consistent kinetic model. Work done by Hsu *et al* [20] indicates that it is possible to find an isotherm that predicts well the equilibrium adsorption data but gives a poor fit to the dynamic surface tension data if only a limited range of $\gamma(c)$ data are used. The incorrect choice of equilibrium model may lead to the application of an incorrect kinetic model and can cause mistakes in the calculation of diffusion coefficients. Chang and Franses review a variety of kinetic models [2]. As in the diffusion-only case, an analytical solution is only possible for a kinetic expression consistent with a Henry isotherm.

Rather than making the approximation that either the diffusion process or an adsorption barrier are rate limiting, Liggieri and co-workers [21, 22] attempt to combine both factors in a renormalised diffusion treatment. They begin their analysis using expressions for the adsorption and desorption rates that account for an interfacial energy barrier. Only molecules striking the surface with energy larger than ε_a are adsorbed and among the adsorbed molecules only those with energy larger than ε_d are desorbed. Since an entropic contribution to adsorption/desorption is usually present, ε_a and ε_d must be considered to be free energies. The adsorption flux is

$$r_1 = \frac{1}{4} \nu C_d \exp(-\varepsilon_a / kT) \tag{1.17}$$

where ν is mean velocity of molecules in the bulk, C_d is the volume concentration and k is the Boltzmann constant. The term $(1/4)\nu C_d$ is the number of molecules striking unit surface in unit time. The desorption flux is given by

$$r_{-1} = \Gamma \frac{kT}{h} \exp(-\varepsilon_d / kT) \tag{1.18}$$

with h being Planck's constant. Using a substitution for ν from the kinetic theory of gases, $\nu = 4(kT/2\pi m)^{1/2}$ where m is the molecular mass, equation (1.15) now reads

$$\frac{d\Gamma}{dt} = \frac{1}{4}\nu\left(C_d - \frac{\Gamma}{L\exp(-\varepsilon_a / kT)}\right)\exp(-\varepsilon_a / kT) \tag{1.19}$$

where

$$L = \frac{h}{(2\pi mkT)^{1/2}}\exp(\varepsilon_d / kT) \tag{1.20}$$

and L is a constant with the dimensions of length. Equation (1.19) is a linear sorption kinetic equation, which may be rewritten in the form

$$\frac{d\Gamma}{dt} = k^a C_d - k^d \Gamma \tag{1.21}$$

with

$$k^a = (kT / 2\pi m)^{1/2}\exp(-\varepsilon_a / kT) \tag{1.22}$$

and

$$k^d = (kT / h)\exp(-\varepsilon_d / kT) \tag{1.23}$$

When deriving the Ward-Tordai equation (1.9) for diffusion only adsorption, one must include a boundary condition that states that the diffusional flux is equal to the increase in Γ,

$$\frac{d\Gamma}{dt} = D_{mon}\left(\frac{\partial C}{\partial x}\right)_{x=0} \tag{1.24}$$

where x is the coordinate normal to the surface. When an adsorption barrier exists, Liggieri insists that the problem may still be treated in this way by defining a renormalized diffusion coefficient, D_{eff}

$$\begin{aligned} D_{eff} &= \frac{1}{4}\nu\lambda\exp(-\varepsilon_a / kT) \\ &= D_{mon}\exp(-\varepsilon_a / kT) \end{aligned} \tag{1.25}$$

where λ is the mean free path, and $D_{mon} = \nu\lambda / 2$ as shown by statistical mechanics. The problem is now reduced to a diffusion-only treatment with a modified Ward-Tordai equation

$$\Gamma(t) = 2c_0\sqrt{\frac{D_a t}{\pi}} - 2\sqrt{\frac{D_a}{\pi}}\int_0^{\sqrt{t}} c_s d(t-\tau) \tag{1.26}$$

where $$D_a \equiv \frac{D_{eff}^2}{D} = D\exp\left(\frac{-2\varepsilon_a}{RT}\right) \quad (1.27)$$

This approach greatly simplifies analysis of dynamic surface tension data since equation (1.26) applies regardless of the value of ε_a. Furthermore, the assumptions of local equilibrium at the surface and the absence of an adsorption barrier are independent in this framework. It is therefore possible to treat equation (1.26) using a local equilibrium treatment even in the presence of an important adsorption barrier. The asymptotic solutions to the Ward-Tordai equation ((1.12) and (1.14)) can be used to deduce the diffusion coefficient for a particular system. Any variation in the value of D with a change in experimental conditions, such as temperature or concentration, may indicate the presence of an adsorption barrier. This approach is useful in providing a simple theoretical framework to quantify deviations from pure diffusion control. However, the level of simplification prohibits more detailed analysis of the origin of any adsorption barriers.

1.2.4 Empirical studies on the adsorption kinetics of nonionic surfactants

Lin and co-workers have carried out extensive studies on the adsorption kinetics of nonionic surfactants at the air-water interface, primarily using pendant bubble tensiometry, which are summarised below. The basic theoretical framework is to test a variety of kinetic mechanisms, including the Langmuir and Frumkin models, which may be summarised by equation (1.28). The rate of adsorption is proportional to the subsurface concentration and the proportion of available sites at the surface $(1-\Gamma/\Gamma_{max})$, whilst the rate of desorption is dependent on the surface excess. Equation (1.16) takes the form

$$\frac{d\Gamma}{dt} = \beta\exp(-\varepsilon_a/RT)c_s(\Gamma_{max}-\Gamma) - \alpha\exp(-\varepsilon_d/RT)\Gamma \quad (1.28)$$

where α and β are pre-exponential factors and ε_a and ε_d are the activation energies for adsorption and desorption, respectively. To account for the change of the activation energies with surface coverage Lin *et al* use the functional form

$$\varepsilon_a = \varepsilon_a^0 + \nu_a \Gamma^n$$
$$\varepsilon_d = \varepsilon_d^0 + \nu_d \Gamma^n \quad (1.29)$$

where ε_a^0, ε_d^0, ν_a and ν_d are constants. As stated in section B.3, as $t \to \infty$, equation (1.28) reduces to an equilibrium adsorption isotherm. Substituting the expressions for the change in activation energy with surface coverage (equation (1.29)) and setting $d\Gamma / dt = 0$ gives

$$\frac{\Gamma}{\Gamma_{max}} = x = \frac{c}{c + a\exp(kx^n)} \quad (1.30)$$

where $k = (\nu_a - \nu_d)\Gamma_{max}^n / RT$ and $a = \alpha / \beta \exp[(\varepsilon_a - \varepsilon_d)/RT]$.

If one allows *n*, *a* and *k* to vary then one is using generalised Frumkin kinetics and the corresponding isotherm in equations (1.28) and (1.30) respectively. When $n = 1$ one is using Frumkin kinetics/isotherm and when $\nu_a = \nu_d = k = 0$, the Langmuir kinetic model and corresponding isotherm.

Lin *et al* have demonstrated that cohesive forces between adsorbed molecules could significantly affect the activation energy for the adsorption/desorption process. [23-25] In decanol solutions for instance, the initially slow induction period followed by accelerating surface tension decay is due to attractive van der Waal's forces between the hydrocarbon chains in the monolayer, which increase with surface coverage. This is a case of cooperative adsorption where interactions in the monolayer promote further adsorption. These cohesive forces are typical of surfactants with small polar head groups and long, slender hydrocarbon tails and act to decrease the rate of desorption whilst having little affect on the adsorption rate. As a result, the surface tension decay to a non-deforming surface is diffusion controlled but if a near-saturated surface is contracted the resulting desorption obeys mixed kinetic-diffusion control.

Lin *et al* also proposed that for some surfactants, the kinetics may switch from diffusion controlled to mixed kinetic-diffusion controlled as the bulk surfactant concentration is increased. [26] Lin *et al* have studied the DST behaviour of octaoxyethylene glycol dodecyl ether ($C_{12}E_8$) as a function of bulk concentration during adsorption to a clean, non-deforming surface and during deformation of a saturated surface. [27, 28] The Frumkin and

generalised Frumkin isotherms fit the equilibrium surface tension values better than the Langmuir isotherm indicating significant intermolecular interactions between the adsorbed molecules. The fitting parameters also indicate that adsorption is anti-cooperative so adsorption becomes more difficult as surface coverage increases. This anti-cooperative behaviour may be related to steric hindrance of the hydrated ethylene oxide headgroups clustered near the interface. By numerically fitting the dynamic data using the Ward-Tordai and the generalised Frumkin kinetic model, Lin calculated the effective diffusion coefficient as a function of bulk concentration. His results indicate that adsorption to a clean non-deforming surface is purely diffusion controlled in dilute solutions but switches to mixed kinetic-diffusion control for more concentrated solutions. For a saturated surface which is rapidly compressed, desorption obeyed mixed kinetic-diffusion control.

Lin and co-workers have repeated this work using other homologues in the C_mE_8 series. [29] Adsorption was anti-cooperative for $C_{10}E_8$, $C_{12}E_8$ and $C_{14}E_8$ and all three obeyed mixed kinetic-diffusion control upon compression of an equilibrated interface. Both $C_{10}E_8$ and $C_{12}E_8$ switched from diffusion only to mixed kinetics as a function of bulk concentration, although it is interesting to note that for $C_{14}E_8$ no switch to mixed kinetics was observed.

It is important to remember that an adsorption barrier is always present. The concepts of diffusion-only and mixed kinetics are purely theoretical and only indicate which process is rate limiting for certain conditions.

Eastoe *et al* [9] have observed similar behaviour for other nonionic surfactants. Using a maximum bubble pressure tensiometer, Eastoe compared the dynamic surface tension decays of $C_{10}E_4$ and $C_{10}E_5$ to the asymptotic equations of Miller *et al.* [17] The monomer diffusion coefficients had been determined independently using Pulsed Field Gradient Spin Echo NMR (PFGSE-NMR) measurements. The short-time asymptote fitted the surface tension decay well, but the long time asymptote predicted a lower surface tension than was measured, indicating an adsorption barrier at higher surface coverage.

By measuring the DST as a function of temperature Eastoe [9] attempted to evaluate the magnitude of the adsorption barrier. To simplify analysis, Eastoe used a nonionic di-chained glucamide surfactant (di-(C6-Glu)) which shows little variation of cmc or Γ_{cmc} as a function of temperature and which has a high cloud point. The value D_{eff} at

temperatures between 20°C and 50°C was calculated from measured surface tension decays. This value was then compared to a predicted diffusion coefficient based upon PFGSE-NMR measurements at 25°C, adjusted for viscosity effects using the Stokes-Einstein relation. The ratio D_{eff} / D revealed an adsorption barrier, the magnitude of which was calculated using an approach similar to Liggieri *et al.* [21,22]

1.3. Adsorption kinetics from micellar solutions

The adsorption behaviour discussed above does not account for the additional kinetic processes that occur in solutions above the cmc when micelles are present. It is generally accepted that micelles have negligible equilibrium adsorption at the air-water interface, since the surface tension remains almost independent of concentration above the cmc. As an extension of this equilibrium observation standard models of adsorption from micellar solutions assume that the rate constant for the adsorption of micelles is zero under non-equilibrium conditions. [30-41] Micelles may still influence adsorption kinetics, but they must first break down into monomers which then adsorb to the interface. This physical picture is summarised in Figure 3. This no-flux boundary condition is justifiable for ionic surfactants with no added electrolyte, since charged micelles will be repelled from a charged interface. However, it is less obvious why micelles of non-ionic surfactants should not adsorb directly to the air-water interface. Data from my early experiments, published in 2005, indicate that direct micelle adsorption can occur at a diffusion controlled rate in solutions of the nonionic surfactant, $C_{14}E_8$. [42] This pathway was also suggested in a transport theory by Maldarelli and co-workers for micellar solutions of the similar nonionic surfactant $C_{14}E_6$. [43]

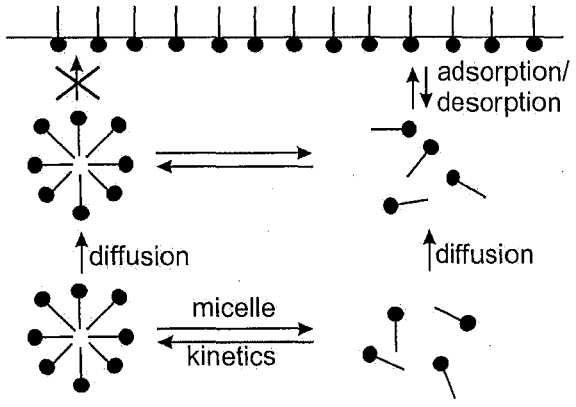

Figure 3: Standard adsorption model from micellar solutions, neglecting direct micelle adsorption.

As in the case of a surfactant monolayer, there is a dynamic equilibrium between monomers in the bulk of the solution and those in micelles. For a proper understanding of the kinetics of adsorption from micellar solutions it is important to have a detailed insight into the kinetics of the system at equilibrium. Existing knowledge of monomer-micelle exchange kinetics in equilibrium systems is outlined briefly below. I will also return to this topic in significantly more detail in Chapters 4 and 5.

1.3.1 Monomer-micelle exchange kinetics at equilibrium

The kinetics of micelle formation and breakdown at equilibrium has been studied using similar techniques to those used for studying fast reactions in liquids. In the case of micellar solutions these techniques are used to perturb an equilibrium system slightly and to monitor the subsequent relaxation to the new equilibrium. In stopped flow experiments [44-46] changes in micelle concentration are induced by rapidly diluting micellar solutions, whilst for temperature or pressure jump techniques [46-50] the position of equilibrium is rapidly changed. A shift in equilibrium may also be induced using the propagation of ultrasound [45, 51]. The ultrasonic method, which has decreased in popularity as the experiments are time consuming, measures the ultrasonic adsorption α/ω^2 (α = adsorption coefficient, ω= angular frequency) at as many frequencies as possible. Since the propagation of ultrasound induces local changes in pressure that are frequency dependent, this propagation also affects the monomer-micelle exchange process. This interaction is detected in the adsorption spectrum.

Despite intense experimental effort, a satisfactory theory of micelle association was not immediately forthcoming. Different experimental techniques found relaxation times that differed by more than three order of magnitude. Some authors, such as Muller [52], began to hypothesise that there may be two distinct physical processes occurring simultaneously. It was not until 1974 and the theory of Aniansson and Wall that these observations were finally explained. Their theory has since become universally adopted as a basis for the interpretation of relaxation results. [53-55]

Aniansson and Wall assumed that changes in aggregation number take place only by individual monomer uptake and loss and that the micelle size distribution consists of three distinct regions. They used the following kinetic model;

$$A_1 + A_{n-1} \underset{k_n^-}{\overset{k_{n-1}^+}{\rightleftarrows}} A_n \tag{1.31}$$

where A_n denotes an aggregate containing n monomers. In their micelle size distribution almost all surfactant material is contained within a region of pre-micellar aggregates (monomer, dimers, trimers etc.) or a region of proper micelles (represented by a Gaussian distribution). These two regions are connected by an intermediate region containing a very low concentration of aggregates.

Aniannson and Wall's treatment predicts the existence of two relaxation times corresponding to two separate processes, in agreement with experimental evidence. The first is a rapid attainment of quasi-equilibria in the two end regions followed by a slower pseudo-stationary flow from one end to the other. To explain this in physical terms, consider a perturbation from equilibrium which results in an excess micelle concentration relative to the new equilibrium value. The micelles initially shed monomers by the fast process, changing the mean aggregation number at a constant number of total micelles in the system. There is, however, a limit on the number of monomers a spherical micelle may lose by this fast process before the increasing chemical potential of the aggregate remaining becomes prohibitive[1]. At this point the system enters a quasi-equilibrium state. Subsequent evolution of the system consists of a slow change in the number of micelles and the average aggregation number, which proceeds via the low concentration region and maintains local equilibrium in the two thick ends. These two processes are depicted in Figure 4.

[1] The variation of chemical potential with aggregation number is considered in detail in Chapter 4. For non-spherical micelles the form of the chemical potential vs. aggregation number curve is much shallower than for a spherical micelle. It may be the case that non-spherical micelles can shed many more monomers via this rapid micelle breakdown process before entering quasi-equilibrium. However, since Aniansson and Wall use a spherical micelle as their paradigm and most of the systems I will study later form spherical micelles, I will restrict this discussion to the spherical case.

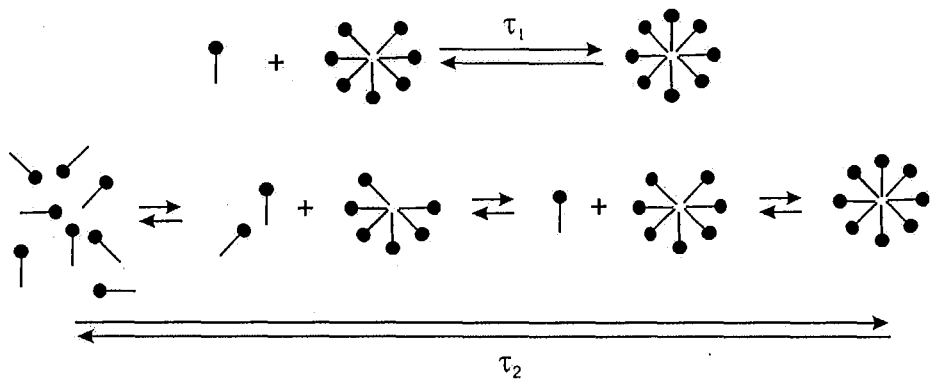

Figure 4: Physical interpretation of two separate relaxation processes

The assumptions made by Aniansson and Wall make it possible to consider the time intervals corresponding to the fast and slow micellisation processes separately in a mathematical treatment, producing two simple equations for the two discrete relaxation times. The derivation for these two equations is given in much greater detail in Chapter 4. For the fast process of monomer exchange

$$\frac{1}{\tau_1} = \frac{k^-}{\sigma^2} + \frac{k^-}{N} a(1+c_0) \tag{1.32}$$

where σ is the width of the Gaussian micelle distribution and N is the average aggregation number. The c_0 term is the average relative deviation from equilibrium and tends to one for the conditions under which the Aniansson and Wall theory may be applied. Finally the term $a = (c_b - \text{cmc})/\text{cmc}$ and is a measure of bulk concentration. In order to derive equation (1.32) Aniansson and Wall assumed that the dissociation rate constant for an individual monomer from a micelle is concentration independent and is given by k^-. Equation (1.32) provides a useful linear relationship between the relaxation time and surfactant concentration.

The relaxation time of the slow process for concentrations close to the cmc is

$$\frac{1}{\tau_2} = \frac{N^2}{\text{cmc}} \frac{1}{R} \frac{1}{1+\frac{\sigma^2}{N} a} \tag{1.33}$$

where R may be interpreted as a resistance to flow through the intermediate region, $R = \sum (\bar{c}_n k_n^-)^{-1}$. The concentration dependence of the slow process is more complicated

than the rapid process. Wennerström and Lindman [56] review a range of values for the parameters in equations (1.32) - (1.33) based upon relaxation studies. The rapid monomer exchange of the τ_1 process is primarily diffusion controlled, whilst the complete dissolution/formation of micelles in the τ_2 process is several orders of magnitude slower and highly dependent upon surfactant structure.

One very important and often overlooked restriction of the Aniansson and Wall model is that the expressions derived above are only valid for small perturbations from equilibrium where linerarisation of the underlying differential equations is valid. Aniansson and Wall did consider the effect of larger perturbations from equilibrium on the relaxation time τ_2. The resulting expression, however, is much more complex than equation (1.33) and not practically applicable.

There has been a limited amount of work examining the effect of perturbation amplitude on the measured relaxation time. Tondre and Zana [46] examined the effect of the size of the perturbation on the experimentally determined slow relaxation time τ_2. Their work was motivated by the observation that stopped-flow methods tended to give τ_2 values which were much larger than those measured by T-jump methods for identical systems. They found that as the perturbation amplitude in stopped-flow decreased, the values of τ_2 from the two methods converged. Even today, however, measurements of τ_2 by different techniques are sometimes in serious disagreement: for example, values of τ_2 for NaPFO micelles obtained by Eastoe (using SAXS [57]) and Furo (using NMR [58]) differ by more than two orders of magnitude.

These discrepancies are important to note for two reasons. (1) One must take great care when using literature values for micelle lifetimes. Some researchers overlook the restrictions on perturbation amplitude and apply the Aniansson and Wall solutions in a haphazard manner. (2) Many authors modelling adsorption kinetics from micellar solutions tend to treat τ_1 and τ_2 as colligative properties of a particular system which may not be the case. For rapidly expanding, non-equilibrium surfaces the perturbation experienced by micelles close to the interface will be equivalent to a large dilution and the Aniansson and Wall restrictions will be violated.

In Chapters 4 and 5 I undertake a detailed analysis of the Aniansson and Wall model for monomer-micelle exchange using a variety of numerical simulation approaches to

develop an understanding of micelle relaxation as a function of perturbation amplitude. I will also show that the Aniansson and Wall approach may not be appropriate at all for many nonionic micellar systems and that a completely different exchange pathway may be operative.

1.3.2 Mass transport and adsorption in micellar surfactant systems.

As the bulk concentration is increased above the cmc, the time taken for a surface to reach equilibrium continues to shorten, reflecting acceleration in transport of surfactant molecules to the interface. Since the monomer concentration remains approximately constant above the cmc, this observation indicates that micelles may accelerate the mass transport of surfactant to the surface. There are two ways that micelles may influence the rate of adsorption.

1) As monomer adsorbs to the surface the subsurface monomer concentration is depleted. As in sub-cmc systems monomer diffuses from the bulk to replace the adsorbed molecules. The depletion of monomer near the surface perturbs the monomer/micelle equilibrium causing micelle disassembly. This micelle disassembly creates a corresponding micelle concentration gradient in the bulk which drives diffusion of micelles to the surface.

2) Micelles may adsorb directly to the surface.

Standard models of adsorption kinetics from micellar systems have neglected the second route and focused solely on the way micelles influence mass transport. Modelling the mass transport in micellar systems involves replacing the single monomer diffusion equation with a system of two equations for monomers and micelles respectively, including a term to account for interconversion between the species. This problem was considered for the first time by Lucassen [59] for the case of small perturbations of an equilibrium surface, using Kresheck's [49] simplified model of micellisation kinetics. Later, Miller [38] used numerical methods to solve a model of adsorption from micellar solutions to nascent water surfaces using the same assumptions. Fainerman [60] was the first to take into account Aniansson and Wall's two-step theory of micellisation. Fainerman considered two time regimes, one where the timescales for monomer and micelle diffusion are of the same order as the slow kinetic process, τ_2, and one in which the

diffusion timescales are of the order of the fast kinetic process, τ_1. This same approach has been refined by subsequent authors including Danov [31], and Noskov [40].

Noskov [40] considers diffusion in micellar systems when the surface is close to equilibrium, using the Aniansson and Wall micellisation kinetic model. Noskov's treatment is limited to the case of small deviations from equilibrium $\delta c_n = \bar{c}_n$ where c_n is concentration of the n^{th} aggregate (barred symbols denote equilibrium values). Under these conditions the diffusion equations for aggregates may be written as

$$\frac{\partial \delta c_n}{dt} = D_n \nabla^2 \delta c_n + k_{n-1}^{+}(\bar{c}_1 \delta c_{n-1} + \bar{c}_{n-1} c_1) - k_n^{-} \delta c_n + k_{n+1}^{-} \delta c_{n+1} - k_n^{+}(\bar{c}_n \delta c_1 + \bar{c}_1 \delta c_n), \quad n = 2...n_{\max} \tag{1.34}$$

where D_n is the diffusion coefficient of the n^{th} aggregate and is assumed to be concentration independent. Equation (1.34) differs only slightly from the kinetic equations which describe monomer-micelle exchange within the Aniansson and Wall framework. The addition of the term $D_n \Delta \delta c_n$ accounts for the transfer of aggregates in solution, whilst the Laplace operator, ∇^2, indicates another essential difference; all variable c_n are now functions not only of time, but also of space co-ordinates. The monomer diffusion equation is constructed from the monomer-micelle exchange equation in a similar way.

$$\frac{d\delta c_1}{dt} = D_1 \delta c_1 - 2k_2^{-} \delta c_2 + 2k_1^{+} \bar{c}_1 \delta c_1 + \sum_{n>2} k_n^{-} \delta c_n - \sum_{n>1} k_n^{+}(\bar{c}_1 \delta c_n + \bar{c}_n \delta c_1) \tag{1.35}$$

If one assumes that the characteristic diffusion timescale τ_D, that is proportional to the ratio of the square of the diffusion length and the diffusion coefficient ($\tau_D \propto L_D^2 / D$), is longer than τ_2 then one may assume local equilibrium between micelles and monomers. However, if the diffusion timescale is less than τ_2 then one must account for the existence of a 'quasi-equilibrium' state amongst the diffusing species. Once the diffusion equations have been linearised for either of these two cases the solutions may be used to formulate a mathematical description of adsorption from micellar solutions, after applying appropriate boundary conditions. Numerous authors have used mathematical models such as this, applied to a variety of experimental platforms, to elucidate micelle kinetic parameters from dynamic surface tension data. [32-35, 37, 41] However, such work is

inherently flawed since the theoretical treatment of mass transport in micellar solutions has been limited to small perturbations from equilibrium, [40] whilst dynamic surface tension methods, which create fresh interfaces, lead to significant deviations from equilibrium.

As with bulk relaxation methods, it has been observed that different experimental platforms lead to varying relaxation times. Dushkin *et al* [61] attempted to reconcile the different techniques. It should be remembered, however, that micelle relaxation times τ_1 and τ_2 were originally defined for equilibrium. That the experimental relaxation time varies with the experimental platform, which each corresponds to a different perturbation from equilibrium, should come as no surprise. A general model of adsorption kinetics should not treat the relaxation time as a colligative property but account for the observation of a variable relaxation time.

The models described above assume that direct micelle adsorption cannot occur and incorporate corresponding boundary conditions. In 2005 I undertook a series of experiments that provided conclusive evidence for the direct adsorption of micelles of non-ionic surfactants to a nascent air-water interface at a diffusion controlled rate, without first breaking down into monomers. [42] The experimental details and results are given in Chapter 7. These results demonstrate the need for the incorporation of an additional pathway into standard models for surfactant adsorption in micellar solutions, with the relaxation of the no-flux boundary condition on the micellar distribution.

Other research has also found evidence for this direct adsorption mechanism. In a 2006 edition of Colloids and Surfaces, published to commemorate Professor Ivanov, Maldarelli and co-workers [43] published a transport model for the limit of fast micelle break-up compared to the diffusion timescale, but for large perturbations from equilibrium. This study uses $C_{14}E_6$, which has a very low cmc ($< 10^{-6}$ M) so timescales for the diffusion of free monomer, τ_D^{mon} may be longer than the timescale for micelle breakdown τ_2. The authors assume that in this rapid micelle breakdown limit the micelles disassemble along a reaction boundary and are able to maintain the monomer concentration, c_{mon} = cmc provided that at least some micelles remain present in solution. The precise mechanism of breakdown is unimportant.

Two possible regimes emerge. For concentrations just above the cmc the diffusion timescale for micelles, τ_D^{mic} is long compared to both the breakdown rate and the kinetic adsorption rate at the surface, τ_K. Initially micelles are able to diffuse to the subsurface, break-up and surfactant monomer adsorbs to the surface. However, since $\tau_D^{mic} < \tau_K$ micelles become depleted in the subsurface and a micelle free zone emerges. The reaction boundary gradually moves into the bulk. Within the reaction boundary c_{mon} = cmc. Within the micelle-free zone, c_{mon} < cmc. Monomer diffuses to the subsurface and adsorbs to the surface obeying the kinetic relationships described above for sub-micellar solutions. As equilibrium is reached the flux of monomer to the surface decreases and the reaction front gradually moves back to the subsurface. The formation of a micelle-free zone during adsorption from micellar solutions had already been postulated by Bain *et al* [62].

In the second regime, at higher bulk concentrations, $\tau_D^{mic} < \tau_K$ so the bulk diffusion of micelles to the subsurface 'keeps up' with the kinetic adsorption of monomer to the surface. The reaction boundary remains at the sublayer. These two regimes are shown in Figure 5 and Figure 6.

Maldarelli *et al* [43] developed corresponding mass transport equations for the case of adsorption to a spherical interface which were tested using pendant bubble tensiometry for the $C_{14}E_6$ systems. Model simulations predicted that a micelle free zone does not emerge for bulk concentrations $c_0 \geq 4.25$ cmc. For concentrations less than this value a micelle free zone does emerge. The experimental surface tension decays for $c_0 < 4.25$ cmc agreed well with the model predictions. For higher concentrations, where the micelle-free zone does not emerge, the model predicts that a single, kinetically determined relaxation time representing the fastest possible rate of adsorption should be observed. This was not the case: instead the relaxation times continue to shorten with increasing bulk concentration. This observation indicates, in contrast to the standard picture and in agreement with my earlier work [42], that micelles present in the subsurface may adsorb directly to the surface.

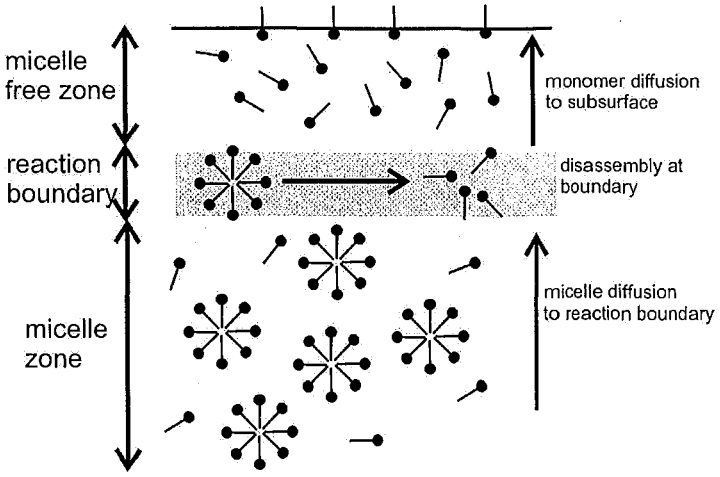

Figure 5: The distribution of surfactant for concentrations just exceeding the cmc

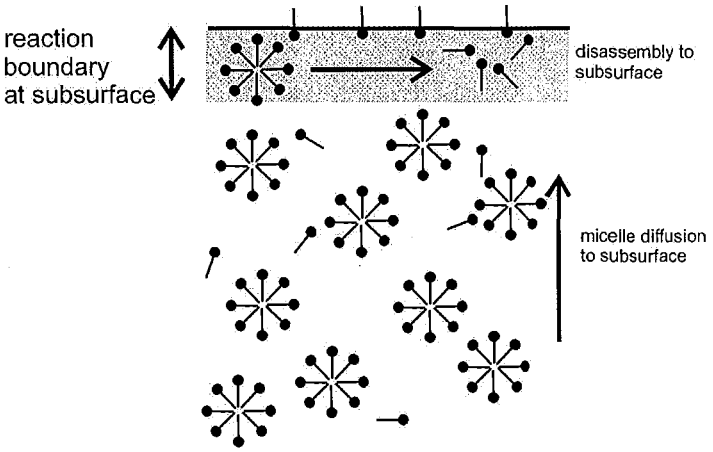

Figure 6: The distribution of surfactant for concentrations much larger than the cmc.

However, in many cases the evidence for a direct adsorption mechanism is not so explicit but rather contained within discrepancies between experimental data and conventional theories. For example, also published in the special edition of Colloids and Surfaces was an article by Fainerman and co-workers [34] detailing dynamic surface tension of micellar solutions in the sub-millisecond time range using the maximum bubble pressure method. As in previous work [33, 35, 36] the authors use linearised solutions of the mass transport problem to calculate micelle breakdown times from the surface tension decays by imposing the zero-flux boundary condition on micelles. It is interesting that one of the surfactants included in this paper is $C_{14}E_8$ which I have shown may adsorb directly to a nascent air-water interface from concentrated solutions. Figure 7 is taken directly from that paper. Note how for concentrated solutions the surface pressure is significantly

greater than the model predictions at short times. This discrepancy could be explained by allowing direct micelle adsorption.

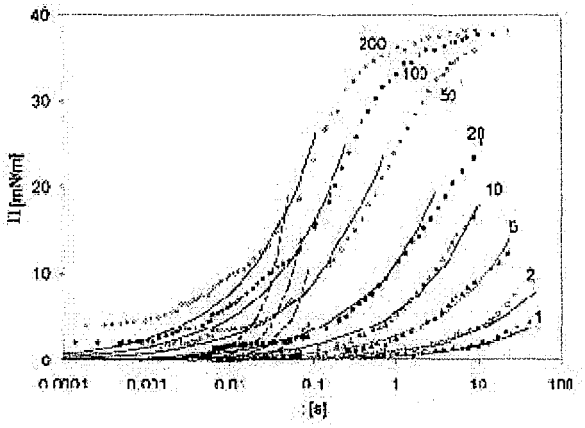

Figure 7: Dynamic Surface tension for $C_{14}E_8$ solutions as a function of the effective surface lifetime. The solid lines are model predictions assuming zero-flux of micelles to the surface. Concentrations are given in cmc multiples.

1.4. Summary

The theory outlined in this chapter represents the conventional thinking regarding kinetic processes in micellar solutions. The diffusion and adsorption of monomers is theoretically described by a two-step process: diffusion to a subsurface followed by adsorption from the subsurface to the surface. A range of equilibrium isotherms and corresponding kinetic schemes are available to describe the adsorption step with the most applicable scheme depending on the surfactant and the surface coverage. For surfactant solutions above the cmc the situation is significantly more complicated. The dynamic equilibrium between micelles and monomers has typically been explained using the kinetic model put forward by Aniansson and Wall. Their elegant solutions are appealing and easy to apply but care should be taken due to the restrictive assumptions made during their derivation. Their model fails to account for systems subjected to large perturbations from equilibrium, which is the case for many experimental and industrial applications.

Finally, the adsorption of surfactant from micellar solutions is dependent on the mass transport of monomers and micelles and on the inter-conversion between them. There are two primary failings with most of the existing literature on this topic: (1) failure to account for the variability of micelle relaxation time with perturbation amplitude and (2) the assumption that micelles cannot adsorb directly to an air-water interface is not

generally valid. In the rest of this work I will attempt to develop more detailed structure-kinetics relationships which overcome these theoretical problems.

Chapter 2

Overview of Experimental Approach

There are numerous exchange processes occurring simultaneously in a micellar solution. In many experiments designed to probe one particular exchange process, analysis of experimental data is complicated by the requirement to account for other exchange processes occurring at a comparable rate. Traditionally, the rate of these additional processes will be assumed or calculated based upon existing theory and literature values, allowing the process of interest to be investigated. Rather than relying on such complicated analyses I have tried to adopt an approach where I have measured as many relevant parameters as possible in order to minimise assumption. In this chapter I will give an overview of the techniques that I have used to explore structure-kinetics relationships in micellar solutions. The purpose of this chapter is to emphasise how the different methods employed complement each other, allowing a more complete picture of structure-kinetics relationships to emerge.

2.1. Surfactant Systems

The micellar systems investigated in this work all carry zero net charge. I have used a range of polyoxyethylene, sugar-based and zwitterionic surfactants. As the aims of this work are to understand micellar properties, the chain lengths were sufficiently long to keep the critical micelle concentration (cmc) low for the more polar head-groups, but also sufficiently short to confer solubility for the less polar headgroups (see Table 1 and Figure 8).

To study the effect of head group variation I have used a range of C_{14} surfactants; hexaethyleneglycol tetradecyl ether ($C_{14}E_6$), octaethyleneglycol tetradecyl ether ($C_{14}E_8$), β-1-n-tetradecyl D-maltoside (β-C_{14}malt) and tetradecyldimethylammonio-1-propanesulfonate (C_{14}DAPS). Also included in the head group variation category are the α - and β- anomers of n-dodecyl D-maltoside (α / β-C_{12}malt). All these surfactants are commercially available as single homologues/isomers.

The effect of the structure of the hydrocarbon tail has been studied with a range of octaethyleneglycol alkyl ethers (C_nE_8, n = 12, 14, 16) and Triton X-100, a decaoxyethylene surfactant with an alkyl-substituted aromatic ring. Triton X-100 is the only 'commercial' surfactant in this series. The structure of Triton X-100 varies in the number of oxyethylene groups and in the branching of the alkyl chain. Previous work on mixtures of non-ionic surfactants with different EO chain lengths has shown nearly ideal mixing; [63] the polydispersity of the head group is unlikely to have a major influence on the micellar kinetics.

Micelles of pure ionic surfactants carry a large, variable and somewhat uncertain charge due to the degree of dissociation of the counterions. To study the effect of charge on micelle kinetics in a controlled way, I doped a small amount of a charged surfactant into non-ionic micelles. This technique proved highly informative in my previous study of $C_{14}E_8/C_{16}TAB$ (hexadecyltrimethylammonium bromide) mixtures with low mole fractions, χ, of the cationic moiety ($\chi < 0.1$). Under these dilute conditions, the ionic surfactant is fully ionised. The partition coefficients of the ionic surfactants between the micelle and bulk solution can be calculated. [64]Varying the mole fraction of $C_{16}TAB$ allows the charge on the micelle to be varied continuously in a controlled manner. Adding charge to the micelles increases the diffusion coefficient, because of the presence of migration fields [65], and decreases the adsorption rate constant due to electrostatic barriers. These charge effects need to be decoupled from changes in micelle structure. In order to verify that the micelle structure is unchanged by the low levels of charge doping a small part of my small angle neutron scattering (SANS) time was used to investigate $C_{14}E_8/C_{16}TAB$ and β-C_{14}malt /$C_{16}TAB$ mixtures containing up to 10% mole fraction of $C_{16}TAB$. No change in micelle structure was detected in either system. It is reasonable to assume that there is no appreciable change in micelle structure for all of the charge doped systems I have used in this work since 10% is the maximum mole fraction I have added.

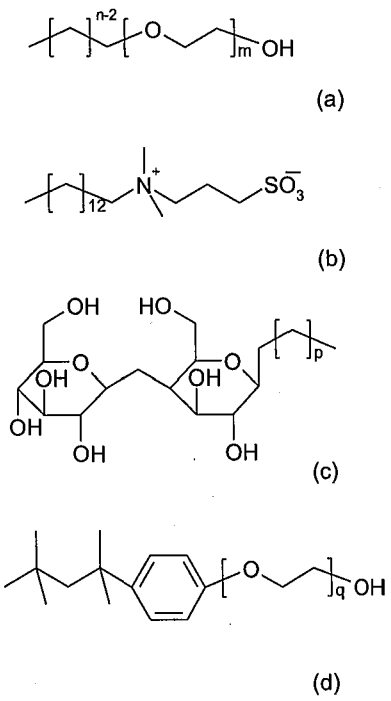

Figure 8: Structure of proposed surfactants. (a) Polyoxyethylene glycol ethers, CnEm. (b) Tetradecyl dimethylammoniopropanesulfonate, C14DAPS. (c) alkyl-D-maltosides. (d) Triton-X-100, q = 9-10

	c_{cmc} / mM
$C_{10}E_8$	1.0 [66]
TX-100	0.35 [67]
C_{14}DAPS	0.275 [68]
α-C_{12}malt	0.15 [69]
β-C_{12}malt	0.18 [70]
$C_{12}E_8$	0.071 [66]
$C_{14}E_8$	0.009 [66]
$C_{16}E_8$	0.001 [66]
$C_{12}E_6$	0.073 [71]
$C_{14}E_6$	0.006 [72]
β-C_{14}malt	0.0175 [73]

Table 1: Literature values of the cmc for the non-ionic surfactants used in this work

2.2 Experimental techniques

2.2.1. Platforms for studying adsorption kinetics

In order to study adsorption kinetics from micellar solutions one must use concentrations well above the cmc to ensure that micelles rather than monomers dominate the adsorption process. For surfactants with cmc > 0.1 mM, such solutions equilibrate with a freshly-created interface on the millisecond timescale. Historically the two principle techniques for studying surfactant adsorption on the millisecond timescale have been the oscillating jet and maximum bubble pressure (MBP) method. [2] These techniques measure surface tension and use an equilibrium equation of state to calculate the surface excess, making the assumption of local equilibrium. For surface ages of just a few milliseconds, far from equilibrium, this is not necessarily a good assumption. Furthermore, the complex hydrodynamics of these two systems require assumptions to be made in order to calculate the surface age. (For examples see the work of Fainerman et al using MBP [33-35]). It is preferable to use systems with well-characterised hydrodynamics.

One well-established technique for the study of non-equilibrium surface's under steady-state conditions is the overflowing cylinder (OFC) [62, 74-77]. Liquid is pumped vertically upwards though a cylinder and flows out over the rim. The surface is static at the centre of the cylinder and accelerates radially out towards the rim with surface expansion rates of the order 10 s^{-1}. This expansion rate corresponds to surface ages in the range 0.1–1 seconds. The surface is flat near the centre of the cylinder so this technique lends itself to numerous surface techniques including Fourier transform infra-red (FTIR), ellipsometry and neutron reflection.

To access even greater rates of surface expansion a gravity driven water jet with diameter of the order 1 mm and flow velocities in the range 1 ms^{-1} was constructed by Battal and Bain [78], giving expansion rates up to 300 s^{-1}, equivalent to surface ages less than 40 ms. Two non-invasive laser techniques, laser Doppler velocimetry and ellipsometry, were used to characterise the hydrodynamics and surface excess respectively. Bain *et al* studied the adsorption of the cationic surfactant hexadecyltrimethylammonium bromide (C_{16}TAB). They observed that the surface tension gradient in the jet, created by surfactant adsorption, reduced the surface velocity of the jet by up to 30%. Such surface tension driven flow effects are termed Marangoni effects [79]. In a collaborative effort, Weiss and Darton [80] developed an analytical model of the jet flow. I have since used this

system to study surfactant adsorption from concentrated micellar solutions of non-ionic surfactants and reveal similar Marangoni effects along with a previously unexplored pathway for micelle adsorption. [42, 81]

Surfactant effects in liquid jets have been studied before. In 1964, Hansen [82] presented a method for treating the Marangoni effects in liquid jets mathematically. In 1978 Davies and Makepiece [83] used high speed photography to track the movement of talc particles in a jet at high Reynolds numbers, observing reductions in surface velocity up to 24%. In 1979 Jobert and Leblond [84] used LDV to observe Marangoni effects in solutions of sodium dodecyl sulphate up to the critical micelle concentration. However, the apparatus designed by Battal and Bain [78] is the first that I am aware of which measures both hydrodynamics and surface excess simultaneously.

The gravity-driven laminar water jet was my primary experimental platform for the study of surfactant adsorption kinetics on the millisecond timescale. As in the work of Battal and Bain [78] I have applied the non-invasive laser techniques of LDV and ellipsometry to measure both the hydrodynamics and surface excess simultaneously. Laser Doppler velocimetry is an interference technique, whereby two tightly focused laser beams are crossed within a flowing liquid, creating interference fringes in the crossing volume. If the beam path is constructed such that these interference fringes are orientated perpendicular to the liquid flow, then light scattered by particles or air bubbles in the liquid will be modulated at a frequency that is proportional to the flow velocity. Ellipsometry is a laser technique that measures a change in the polarisation of light upon reflection from an interface. The change in polarisation is related to surface anisotropy due, for instance, to the adsorption of surfactant molecules at the interface. It was adsorption kinetic data from the liquid jet platform that first indicated that existing models of adsorption kinetics from micellar solutions were unsatisfactory and prompted the further exploration of structure-kinetics relationships in micellar solutions. These data will be presented in Chapter 7.

2.2.2. Small-angle neutron scattering (SANS)

In order to begin understanding the rate of surfactant adsorption at the air-water interface it is important to understand the influence of mass-transport in the bulk solution. Mass transport is affected by several factors including the hydrodynamic flow in the jet, the rate at which monomers enter and exit micelles in the bulk solution and the dimension of

the micelles, which determines their diffusion coefficient. There are many possible techniques that may be used to explore the size and shape of colloidal particles, particularly those techniques which make use of small-angle scattering effects. In this work I have used small-angle neutron scattering (SANS) to explore the dimensions of micelles formed by the surfactants outlined in section 2.1.

SANS has been widely used to measure the size and shape of micelles, but rarely at the low concentrations (~1 – 4 mM) that are needed to study kinetics of adsorption on the millisecond timescale. SANS has advantages over small-angle X-ray scattering (SAXS) and light scattering in that D_2O can be used to enhance the contrast between the micelle and solvent, which is of particular benefit at low concentrations.

The determination of micelle dimensions is a useful tool in order to predict diffusion coefficients and compare those values to the results of measurements made using other techniques. There are, however, more important reasons to determine micelle dimensions than simply validating other measurements. Micelle dimensions may influence the rate of exchange of monomers between the bulk solution and micelles. As explained in Chapter 1, for an equilibrium solution this process was described mathematically by Aniansson and Wall more than three decades ago. By assuming stepwise monomer uptake and loss they were able to predict two distinct system relaxation times, a prediction which agreed with existing experimental results. In their theory Aniansson and Wall took a small, spherical micelle as their paradigm which determined the distribution of aggregation number and variation in free energy across 'aggregation space'. In reality many surfactants do not form such simple aggregates and for micelles of other shapes (e.g. rods) the thermodynamics are quite different. One has to envisage other mechanisms in which the micelle may go through a series of shape changes before finally disaggregating. Non-spherical micelles are of greater practical value due to their interesting rheological properties, bicontinuous and coacervate phases are of increasing interest and polymer-surfactant mixtures with complex hierarchical structures are widely used. The breakdown and exchange kinetics of such structures is poorly studied.

The results of my SANS experiments are presented in Chapter 3.

2.2.3. Pulsed field gradient spin echo NMR

Rather than rely entirely on diffusion coefficients calculated from micelle dimensions, I will also use data derived using Pulsed Field Gradient Spin Echo NMR (PFGSE-NMR) experiments performed as part of this project by Nicolas Peron, a postdoctoral researcher in the Bain Group. The measurement of diffusion coefficients by PFGSE-NMR is well-established, if time-consuming. Previous work with P. Griffiths has established that 0.1 mM is around the practical lower limit for hydrocarbon surfactants. Where the cmc is significantly lower than 0.1 mM, the monomer diffusion coefficient may be extrapolated from shorter homologues. This data is used as supporting information in Chapter 7.

2.2.4. Numerical modelling methods

Along with extensive experimental effort dedicated to understanding monomer-micelle exchange kinetics in systems subjected to large perturbations from equilibrium I have also undertaken a detailed theoretical analysis of this process. This theoretical analysis has been performed using the Matlab computational package. Starting from fundamental thermodynamic considerations I have calculated the distribution of aggregate sizes in a real micelle solution. Using these micelle size distributions I have then considered the feasibility of the Aniansson and Wall kinetic model when applied to nonionic micellar solutions subjected to large perturbations from equilibrium. This work is reported in Chapter 4.

Following on from a series of apparent failings in the Aniansson and Wall model which are revealed in Chapter 4, I then present an alternative theoretical model which overcomes many of the problems associated with this conventional approach. My new model and its predictions are given in Chapter 5.

2.2.5. Stopped-flow dilution

Another important parameter in the interpretation of adsorption kinetic data in micellar solutions is the rate at which monomers may enter and leave micelles. As with micelle dimensions, the rate of monomer-micelle exchange kinetics is also of significant interest as a stand-alone topic and will be given particular attention in this work – both experimentally and theoretically. In order to probe the rate at which monomers enter and leave micelles experimentally it is necessary to perturb a micellar system and monitor the relaxation back to equilibrium. Only a limited number of authors have considered the

effect of the perturbation amplitude on the measured relaxation data and concluded that the calculate micellar lifetimes are highly dependent on the corresponding perturbation [46].

Since a micelle in the region of a rapidly expanding surface experiences a perturbation similar to a rapid dilution and corresponding to a large perturbation, I have concentrated my efforts on understanding monomer-micelle exchange kinetics for systems subjected to large perturbations. Of the numerous available techniques only stopped-flow rapid mixing allows for the possibility of large perturbations from equilibrium on the millisecond timescale. My relaxation data for solutions of non-ionic surfactants subjected to rapid dilutions is presented in Chapter 6.

2.3. Summary

In attempting to measure as many of the relevant parameters as possible I have endeavoured to minimise the number of assumptions required in the analysis of experimental data. The experiments at the centre of this research are adsorption kinetics measurements made using the gravity-driven laminar jet. As was outlined in Chapter 1, adsorption data of this kind can only be analysed with a detailed knowledge of micelle and monomer mass-transport, monomer-micelle exchange kinetics and system hydrodynamics. Whilst the hydrodynamics can be measured directly on the liquid jet platform, the mass transport and exchange kinetics must be determined using other methods. The mass-transport of micelles and monomers can be measured directly using PFGSE-NMR and verified based on micelle dimensions determined from SANS measurements. Micelle dimensions are also important for the thermodynamic considerations involved in the understanding of monomer-micelle exchange kinetics which is explored both theoretically and experimentally using stopped-flow methods.

Chapter 3

Characterisation of micelle dimensions with small-angle neutron scattering

Small angle scattering is a collective name given to the techniques of small angle neutron (SANS), X-ray (SAXS) and light (SALS) scattering. In each technique radiation is scattered by a sample and the resulting scattering pattern provides information about the size, shape and orientation of some component of the sample. To a large extent the techniques are complementary. For example, light scattering cannot be applied to an optically opaque sample and SAXS cannot easily be applied to very thick samples whilst SANS (and SAXS) probe different length scales to SALS. There is also a great deal of similarity between the different scattering methods. Perhaps the most important is the fact that, with minor adjustments, the same basic equations and laws can be used to analyse data from each of the techniques. However, since the techniques were developed in different time periods by different groups of scientists the terminologies which have evolved are often very different.

In this chapter I will detail work done at the ISIS facility, using SANS as a technique to study colloidal systems. This work was carried out in order to probe micelle sizes in the low concentration regimes corresponding to my surfactant adsorption studies, since most previous experiments had used relatively high concentrations to make data acquisition more straightforward. Whilst the ultimate aim of my work was to relate micelle characteristics to adsorption behaviour, the determination of micelle size and shape remains interesting in itself.

The chapter begins with an overview of the theory of neutron scattering summarised from the excellent introduction by Ryong-Joon Roe [85].

3.1. Theory

3.1.1. Basic properties of the neutron.

A neutron is an uncharged elementary particle of mass m equal to 1.675×10^{-27}kg and spin ½. Its kinetic energy E and momentum p are given by

$$E = \frac{1}{2}mv^2 \tag{3.1}$$

and

$$p = mv \tag{3.2}$$

where v is velocity. Neutrons also exhibit wave-like behaviour with the wavelength λ given by the de Broglie relation

$$\lambda = \frac{h}{p} = \frac{h}{mv} \tag{3.3}$$

where h is Planck's constant. For the purpose of scattering experiments there are two techniques used to generate neutrons, nuclear fission in a nuclear reactor or by bombardment of a heavy metal target with high energy protons (spallation). In both cases the neutrons which emerge are of high velocities and must be slowed down to be useful in SANS experiments. This moderation can be achieved by repeated collisions of neutrons with atoms in a moderating material such that neutrons achieve an approximate equilibrium as a 'gas' at the temperature of the moderator. The velocity spectrum of the neutrons is given by the Maxwell-Boltzmann distribution in a gas at equilibrium

$$f(v) = 4\pi\left(\frac{m}{2\pi kT}\right)^{3/2} v^2 \exp\left(\frac{mv^2}{2kT}\right) \tag{3.4}$$

where k is the Boltzmann constant. The maximum of the function occurs at

$$v = \left(\frac{2kT}{m}\right)^{1/2} \tag{3.5}$$

Some typical values for energy and wavelength of neutrons moderated at different temperatures is given in Table 2. It is significant that the wavelengths of these neutrons are of the order of 1 Å making neutrons a useful tool for investigating the structure of matter. This wavelength range is comparable to that which may be obtained using X-rays and in many ways the scattering behaviour of neutrons and X-rays are similar, but there are some very important differences which must be considered.

	Cold	Thermal	Hot
T (K)	25	330	2000
v (ms^{-1})	642	2333	5743
E (meV)	2.16	28.4	172
λ (Å)	6.16	1.696	0.689

Table 2 – Comparison of typical neutron parameters at different moderator temperatures.

A fundamental difference between neutrons and X-ray photons is the energies of the particles. As shown in Table 2 the energy of thermal neutrons is of the order of 10 meV. In comparison the energy of an X-ray photon of similar wavelength, given by $E = hc/\lambda$ is of the order 10 keV. The average energy associated with the motion of atoms arising from vibrational, rotational and translational motions, is of the order of $kT \approx 20$ meV at ambient conditions. Thus X-ray scattering has the potential to seriously degrade sensitive samples. Also, when X-rays are scattered by matter any exchange of energy is difficult to resolve. If neutrons are scattered inelastically their energies are modified to an appreciable extent, which can be determined experimentally. The use of incoherent neutron scattering to study the motion of atoms in a sample is very useful and is one area where neutron scattering clearly distinguishes itself from SAXS.

Perhaps the most important fundamental difference is the mechanism by which neutrons and electromagnetic radiation interact with matter. X-rays (and light) are scattered by electrons surrounding atomic nuclei but neutrons are scattered by the nucleus itself. This single fact has some important consequences.

In the case of light and X-rays the scattering cross-section of an atom is directly proportional to polarisability or the number of electrons present, respectively, and increases with atomic number Z. For neutrons the strength of interaction with a particular nucleus does not vary in a systematic way with atomic number. Even isotopes of the same element may have different neutron scattering cross sections. The most significant isotopic variation occurs for $Z = 1$. Because the scattering cross sections of hydrogen and deuterium are so different neutron scattering is not only able to see hydrogen isotopes but also differentiate between them.

Since atomic nuclei are 10^4-10^6 times smaller than typical neutron wavelengths they may be treated as point scatterers. As a result, nuclear scattering length is constant over the entire range of scattering angles. This is very different in the case of X-rays where atomic diameters are only 0.1-1 times typical wavelengths and scattering length varies with scattering angle.

The interaction of neutrons with matter is very weak and the adsorption of neutrons by most materials is small, making neutrons a very penetrating sample probe in comparison to X-rays and light. This is particularly useful not only for very thick samples, but also samples which are contained inside complex pieces of apparatus such as Couette cells.

Finally, since neutrons have a magnetic moment an additional scattering mechanism exists whereby neutrons may interact with the spin and orbital magnetic moments of atoms with unpaired electrons. Such scattering behaviour can provide important information about the magnetic structure of materials.

There are also disadvantages to using neutron radiation. Obviously neutron scattering requires specialised neutron beam facilities which are costly to construct and run. According to the ISIS website there are currently 37 neutron sources in 21 countries. Five of these sources use spallation to generate neutrons, the rest use nuclear reactors. The total number of SANS instruments is 32, of which 18 are based in Europe. The demand for beam time typically outstrips the available time by a factor of 2 or 3.

Another drawback of neutrons is the relatively low flux of neutrons in comparison to light and X-ray sources. It is also difficult to focus neutrons and collimation of a neutron beam is done at the expense of the already limited flux.

3.1.2. Scattering and Interference

The term *flux* describes the *strength* of a beam of radiation. When the radiation is regarded as a stream of particles, such as neutrons or photons, the flux J is given as the number of particles passing through unit area per second. When radiation is regarded as a wave the flux is related to the square of the amplitude of the oscillating wave field, $J \propto |A|^2 = AA^*$ where A^* is the complex conjugate of A. For radiation emitted or scattered from a point source, it is more convenient to express the flux as the number of particles transmitted per second through a unit solid angle rather than unit area. In this way the measure of flux becomes independent of the distance from the source.

When a collimated beam of neutrons, flux J_0, is incident on a sample the scattered spherical wave emanates in all directions. By measuring the ratio of scattered flux J to incident flux as a function of scattering angle we may learn about the structure of the sample. Since J_0 refers to a plane wave and J refers to a spherical wave the ratio J/J_0 has

the dimension of area per solid angle. In neutron scattering this ratio is referred to as the differential scattering cross section.

$$\frac{d\sigma}{d\Omega} = \frac{J}{J_0} \tag{3.6}$$

This expression gives the probability that a neutron is scattered into a unit solid angle in a given direction. Below we will see how theoretical expressions have been derived which relate the differential scattering cross section to sample structure.

The resultant scattering intensity when a beam of neutrons is incident on matter results from a combination of two phenomena: (1) scattering of neutrons by individual atomic nuclei and (2) interference among the waves scattered by these primary events. We first consider scattering by a single nucleus. The efficacy of neutron scattering by a nucleus is expressed by the scattering length b of the nucleus. The differential scattering cross section of an individual nucleus is

$$\frac{d\sigma}{d\Omega} = b^2 \tag{3.7}$$

The value of scattering length is independent of neutron wavelength, is invariant to scattering angle and is not related in any systematic way to atomic number as explained above.

The interference of scattered waves from two scattering nuclei may now be considered. The amplitude of a wave of frequency ν and wavelength λ travelling in the x-direction may be expressed as

$$A(x,t) = A\cos[2\pi(\nu t - x/\lambda)] \tag{3.8}$$

where A is the modulus of $A(x,t)$. Rewriting this in complex notation is more convenient for scattering manipulations, thus

$$A(x,t) = Ae^{i2\pi(\nu t - x/\lambda)} \tag{3.9}$$

Consider a wave scattered by two nuclei located at points O and P (Figure 9). A detector is placed in the direction specified by the unit vector **S** at a distance far from the scattering nuclei. Provided scattering is coherent and there is no phase change on

scattering the phase difference $\Delta\phi$ of the two waves arriving at the detector depends only on the path length difference δ

$$\Delta\phi = \frac{2\pi\delta}{\lambda} \tag{3.10}$$

Designating the position of P relative to O by $\mathbf{r}$ we have QP = $\mathbf{S}_0 - \mathbf{r}$ and OR = $\mathbf{S} - \mathbf{r}$ and therefore the phase difference is

$$\Delta\phi = \frac{2\pi}{\lambda}(\mathbf{S}_0 \cdot \mathbf{r} - \mathbf{S} \cdot \mathbf{r}) = -2\pi\mathbf{s} \cdot \mathbf{r} \tag{3.11}$$

Where

$$\mathbf{s} = \frac{\mathbf{S} - \mathbf{S}_0}{\lambda} \tag{3.12}$$

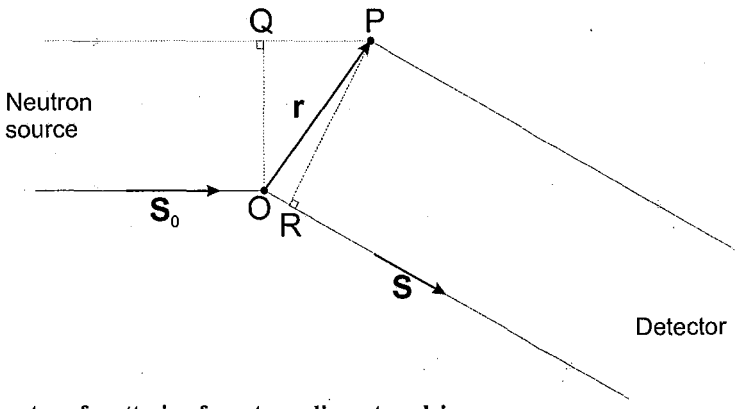

Figure 9- Geometry of scattering from two adjacent nuclei

In the neutron scattering community the quantity $\mathbf{q}$ is used instead of $\mathbf{s}$ where $\mathbf{q} = 2\pi\mathbf{s}$ and this notation will be used for the rest of this document. The vector $\mathbf{q}$ is referred to as the scattering vector and completely characterizes the scattering geometry. The magnitude of $\mathbf{q}$ is related to the scattering angle by

$$|\mathbf{q}| = q = \frac{4\pi \sin\theta}{\lambda} \tag{3.13}$$

Writing the spherical waves scattered by the nuclei at O and P respectively as

$$\begin{aligned} A_O(x,t) &= A_0 b e^{i2\pi(\nu t - x/\lambda)} \\ A_P(x,t) &= A_0 b e^{i2\pi(\nu t - x/\lambda)} e^{i\mathbf{q}\cdot\mathbf{r}} \end{aligned} \tag{3.14}$$

Then the amplitude of the resultant wave arriving at the detector is the sum of these components

$$A_{\text{det}}(x,t) = A_0 b e^{i2\pi(\nu t - x/\lambda)}(1+e^{i\mathbf{q}\cdot\mathbf{r}}) \tag{3.15}$$

The flux arriving at the detector is AA^*

$$J(\mathbf{q}) = A_0^2 b^2 (1+e^{-i\mathbf{q}\cdot\mathbf{r}})(1+e^{i\mathbf{q}\cdot\mathbf{r}}) \tag{3.16}$$

where the t and x dependent terms have cancelled out. It is therefore sufficient to express the time-averaged amplitude of the scattered wave as

$$A(\mathbf{q}) = A_0 b\ (1+e^{-i\mathbf{q}\cdot\mathbf{r}}) \tag{3.17}$$

The flux $J(\mathbf{q})$ and amplitude $A(\mathbf{q})$ are written explicitly as functions of $\mathbf{q}$ to emphasise their dependence on scattering geometry. Equation (3.17) may be easily generalised to describe scattering from N identical scatterers

$$A(\mathbf{q}) = A_0 b \sum_{j=1}^{N} e^{-i\mathbf{q}\cdot\mathbf{r}_j} \tag{3.18}$$

Where $\mathbf{r}_j$ denotes the position of the jth scatterer relative to an arbitrary origin. When the scatterers are numerous and continuously dispersed the summation may be replaced with an integral. Taking $n(\mathbf{r})d\mathbf{r}$ to represent the number of scatterers within volume element $d\mathbf{r} = dx\,dy\,dz$ then we may write

$$A(\mathbf{q}) = A_0 b \int_V n(\mathbf{r}) e^{-i\mathbf{q}\cdot\mathbf{r}} d\mathbf{r} \tag{3.19}$$

where $\rho(\mathbf{r}) = b\,n(\mathbf{r})$ is the scattering length density distribution and the V in the integration sign indicates the integration is to be performed over the entire illuminated sample volume. The Fourier transform of a function $f(x)$ is defined as

$$F(q) = \int_{-\infty}^{\infty} f(x) e^{-iqx} dx \tag{3.20}$$

Therefore equation (3.19) demonstrates that the amplitude of the scattered wave is proportional to the three-dimensional Fourier transform of the local number density of scattering centres in a sample.

3.1.3. Relating scattered intensity to structure

The term intensity is used to denote the differential scattering cross-section $d\sigma/d\Omega$, i.e. the ratio $J(\mathbf{q})/J_0$. The scattering amplitude, given by equation (3.19) is therefore related to the scattering intensity by

$$I(\mathbf{q}) = \frac{|A(\mathbf{q})|^2}{A_0^2} = \left| \int_V \rho(\mathbf{r}) e^{-i\mathbf{q}\cdot\mathbf{r}} d\mathbf{r} \right|^2 \tag{3.21}$$

Stated in words, the scattered intensity is the absolute square of the Fourier transform of the scattering length density distribution. In this work we are assuming that scattering is weak and that any one neutron is only scattered once within the sample. This approach is called Kinematic Theory. Expansion of equation (3.21) gives

$$I(\mathbf{q}) = \frac{A(\mathbf{q})A^*(\mathbf{q})}{A_0^2} = \left[\int \rho(\mathbf{u}') e^{-i\mathbf{q}\cdot\mathbf{u}'} d\mathbf{u}' \right] \left[\int \rho^*(\mathbf{u}) e^{i\mathbf{q}\cdot\mathbf{u}} d\mathbf{u} \right] \tag{3.22}$$

By defining a new variable $\mathbf{r} = \mathbf{u}' - \mathbf{u}$ we then have

$$\begin{aligned} I(\mathbf{q}) &= \int \left[\int \rho(\mathbf{u}) \rho^*(\mathbf{u}+\mathbf{r}) d\mathbf{u} \right] e^{-i\mathbf{q}\cdot\mathbf{r}} d\mathbf{r} \\ &= \int \Gamma_\rho(\mathbf{r}) e^{-i\mathbf{q}\cdot\mathbf{r}} d\mathbf{r} \end{aligned} \tag{3.23}$$

where $\Gamma_\rho(\mathbf{r})$ is defined as

$$\Gamma_\rho(\mathbf{r}) = \int \rho(\mathbf{u}) \rho(\mathbf{u}+\mathbf{r}) d\mathbf{u} \tag{3.24}$$

and is called the autocorrelation function of $\rho(\mathbf{r})$. The autocorrelation function describes the relationship between neighbouring sample regions $\mathbf{u}$ and $\mathbf{u}'$ separated by a distance $\mathbf{r}$. Since the average value of $\rho(\mathbf{u})\rho(\mathbf{u}')$ is given by

$$\langle \rho(\mathbf{u}) \rho(\mathbf{u}') \rangle = \frac{\int \rho(\mathbf{u}) \rho(\mathbf{u}+\mathbf{r}) d\mathbf{u}}{\int d\mathbf{u}} = \frac{\Gamma_\rho}{V} \tag{3.25}$$

the autocorrelation function thus describes how the scattering length densities in neighbouring regions, separated by $\mathbf{r}$ are *correlated* to each other. Equation (3.23) may

be regarded as a starting point for the discussion of scattering phenomena in relation to sample structure.

In a scattering experiment $I(\mathbf{q})$ is measured. The scattering vector $\mathbf{q}$ has dimensions of length^{-1} and spans a three dimensional reciprocal space. The information about the structure of the sample is contained within the function $\rho(\mathbf{r})$ which exists in real space and its Fourier transform gives the amplitude $A(\mathbf{q})$, a function in reciprocal space. If $A(\mathbf{q})$ could be determined over all $\mathbf{q}$ the real space function $\rho(\mathbf{r})$ and hence information about the structure of the sample could be recovered by the inverse Fourier transform

$$\rho(\mathbf{r}) = \int A(\mathbf{q}) e^{i\mathbf{q}\cdot\mathbf{r}} d\mathbf{r} \tag{3.26}$$

The information contained in $A(\mathbf{q})$ and $\rho(\mathbf{r})$ is equivalent. The information in $I(\mathbf{q})$ and $\Gamma_\rho(\mathbf{r})$ is also equivalent since $\Gamma_\rho(\mathbf{r})$ in real space may be recovered by inverse Fourier transform of $I(\mathbf{q})$

$$\Gamma_\rho(\mathbf{r}) = \int I(\mathbf{q}) e^{i\mathbf{q}\cdot\mathbf{r}} d\mathbf{r} \tag{3.27}$$

The relationship between $A(\mathbf{q}), \rho(\mathbf{r})$, $I(\mathbf{q})$ and $\Gamma_\rho(\mathbf{r})$ is summarised in Figure 10. The reason for the difficulty of recovering sample structure from scattered intensity is now apparent. The autocorrelation conversion (equation (3.23)) or the squaring of amplitude to give intensity (equation (3.21)) results in the loss of some information contained in $\rho(\mathbf{r})$ and $A(\mathbf{q})$ respectively. The amplitude is a complex quantity and in converting amplitude into intensity, which is a real quantity, all information on phase angle is lost along with the means of directly determining structure.

The usual solution to this problem is to assume a model structure and see how well it fits the experimental intensity data.

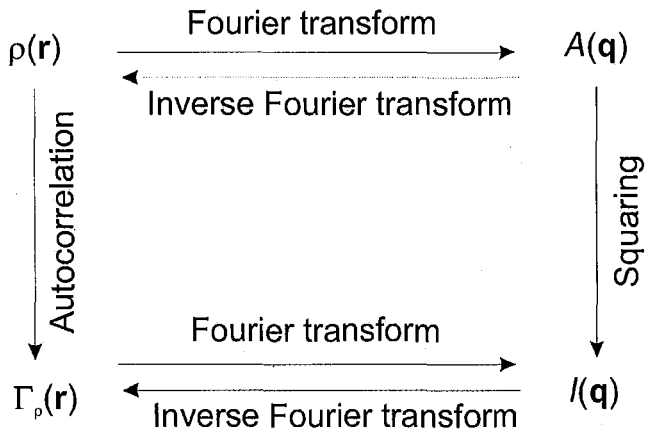

Figure 10 – Mathematical relationship between $A(\mathbf{q})$, $\rho(\mathbf{r})$, $I(\mathbf{q})$ and $\Gamma_\rho(\mathbf{r})$

Finally we derive a very important result which describes why scattered intensity depends only on the contrast between different sample regions rather than the absolute values of scattering length.

If we denote the average value of $\rho(\mathbf{r})$ in a sample as $\langle\rho\rangle$, then the deviation at any one point may be expressed as

$$\eta(\mathbf{r}) = \rho(\mathbf{r}) - \langle\rho\rangle \tag{3.28}$$

The autocorrelation function of $\eta(\mathbf{r})$ is

$$\Gamma_\eta(\mathbf{r}) = \int \eta(\mathbf{u})\eta(\mathbf{u}+\mathbf{r})d\mathbf{u} \tag{3.29}$$

The autocorrelation function $\Gamma_\rho(\mathbf{r})$ of $\rho(\mathbf{r})$ can then be written as

$$\begin{aligned}\Gamma_\rho(\mathbf{r}) &= \int\left[\eta(\mathbf{u})+\langle\rho\rangle\right]\left[\eta(\mathbf{u}+\mathbf{r})+\langle\rho\rangle\right]d\mathbf{u} \\ &= \int\eta(\mathbf{u})\eta(\mathbf{u}+\mathbf{r})du + \langle\rho\rangle^2\int d\mathbf{u} + \langle\rho\rangle\int\eta(\mathbf{u})d\mathbf{u} + \langle\rho\rangle\int\eta(\mathbf{u}+\mathbf{r})du\end{aligned} \tag{3.30}$$

The third term in equation (3.30) is zero by the definition of $\eta(\mathbf{r})$ and the fourth term also goes to zero except when $\mathbf{r}$ is of the same order of magnitude as the sample dimension. Therefore equation (3.30) reduces to

$$\Gamma_\rho(\mathbf{r}) = \Gamma_\eta(\mathbf{r}) + \langle\rho\rangle^2 V \tag{3.31}$$

Substitution of equation (3.31) into equation (3.23) then gives scattered intensity as

$$I(\mathbf{q}) = \int \Gamma_\eta(\mathbf{r}) e^{-i\mathbf{q}\cdot\mathbf{r}} d\mathbf{r} + \langle \rho \rangle^2 V \delta(\mathbf{q})$$

where the second term results from the Fourier transform of unity which is equal to the delta function. The scattered intensity is therefore made up of two terms with the second term representing scattering from the sample as a whole, as if it were uniform scattering length density. This contribution is sometimes termed null scattering and is experimentally unobservable since it swamped by the much more intense transmitted beam. The outcome of this analysis is that scattered intensity is not determined by the absolute value of scattering length density but rather the fluctuations within the sample. To increase scattering the contrast between regions in the sample must be increased. This is a very important result which allows experimentalists to take advantage of the large difference in scattering length of hydrogen and deuterium.

3.1.4. Small angle scattering of dilute micellar systems

For dilute colloidal systems the spacing between different scattering particles is greater than 10 Å, so for typical neutron wavelengths the relevant scattering occurs at scattering angles 2θ less than 2°. The reciprocity between $\mathbf{r}$ and $\mathbf{q}$ means that information on large scale structures is contained in $I(\mathbf{q})$ at relatively small $\mathbf{q}$. Although all of the results derived above apply to scattering in general there are certain theoretical results specifically derived for the analysis of small angle scattering data. These results incorporate some additional assumptions only applicable in the small angle regime such as $\sin\theta \approx \theta$ and the assumption that any structure on scales less than 10 Å does not exist. This means one may ignore the individual atomic scattering since the atomic inhomogeneity is on a scale much smaller than the experiment can determine.

Provided a micelle solution is sufficiently dilute one may assume that individual micelle positions are not correlated to each other. It follows that waves scattered by different micelles lack coherence. The overall intensity is then simply the sum of the intensity of rays scattered from individual micelles.

For micelles with a well-defined, simple geometric shape it is possible to calculate the intensity curve for the whole q-range without making any assumptions. The amplitude of scattering from a single particle is calculated according to

$$A(\mathbf{q}) = \int_V \eta(\mathbf{r}) e^{-i\mathbf{q}\cdot\mathbf{r}} d\mathbf{r} \qquad (3.32)$$

Where $\rho(\mathbf{r})$ has been replaced by $\eta(\mathbf{r})$, the contrast of scattering length density, following the discussion above. Intensity is then obtained by taking the absolute square of scattered intensity followed by averaging over all micelle orientations since the sample contains a large number of scatterers taking random orientations.

I begin by considering scattering from a sphere, which is particularly simple as it does not require orientational averaging. A solid sphere of radius R and uniform contrast η_0 is defined by

$$\eta(\mathbf{r}) = \begin{cases} \eta_0 & \text{for } r \le R \\ 0 & \text{for } r \ge R \end{cases} \tag{3.33}$$

where the choice of r is arbitrary and has been taken to be at the centre of the micelle. The three dimensional Fourier transform of a function, expressed in spherical polar coordinates is

$$F(\mathbf{q}) = \int_{\Phi=0}^{2\pi} \int_{\Theta=0}^{\pi} \int_{r=0}^{\infty} f(r,\Theta,\Phi) e^{-i\mathbf{q}\cdot\mathbf{r}} r^2 \sin\Theta dr\, d\Theta\, d\Phi \tag{3.34}$$

If $f(\mathbf{r})$ is real and depends only on the length of the vector $\mathbf{r}$, then the function $F(\mathbf{q})$ is also real and integration with respect to Θ and Φ can be performed without knowledge of $f(\mathbf{r})$. The polar axis is chosen to coincide with the direction of the vector $\mathbf{q}$, thereby letting $\mathbf{q}\cdot\mathbf{r} = qr\cos\Theta$. With this change of variable $\cos\Theta \to u$ and equation (3.34) becomes

$$\begin{aligned} F(q) &= \int_{\Phi=0}^{2\pi} \int_{u=-1}^{1} \int_{r=0}^{\infty} f(r) e^{-iqru} r^2 dr\, du\, d\Phi \\ &= 2\pi \int_{r=0}^{\infty} f(r) r^2 \frac{e^{iqr} - e^{-iqr}}{qr} dr \\ &= 4\pi \int_{0}^{\infty} f(r) r^2 \frac{\sin(qr)}{qr} dr \end{aligned} \tag{3.35}$$

This derivation and the definition of contrast given in equation (3.33) may be inserted into equation (3.32) and giving, for a system of spherical scatterers

$$\begin{aligned} A(\mathbf{q}) &= \int_0^\infty \eta(r) 4\pi r^2 \frac{\sin qr}{qr} dr \\ &= \frac{\eta_0}{q} \int_0^R 4\pi r \sin(qr) dr \\ &= \eta_0 v \frac{3(\sin qR - qR\cos qR)}{(qR)^3} \end{aligned} \tag{3.36}$$

where v is the volume of the spheres, $(4/3)\pi R^3$. The intensity of scattering from a sphere is therefore

$$I(q) = \eta_0^2 v^2 \frac{9(\sin qR - qR\cos qR)^2}{(qR)^6} \tag{3.37}$$

Similar expressions exist for other simple geometric shapes exist although the derivations are more involved and require orientational averaging of the intensity expression. For a thin rod of length L and negligible cross sectional area the average scattering over all orientations is given by [85]

$$I(q) = \eta_0^2 v^2 \frac{2}{qL}\left[\mathrm{Si}(qL) - \frac{1-\cos qL}{qL}\right] \tag{3.38}$$

where

$$\mathrm{Si}(x) = \int_0^x \frac{\sin u}{u} du \tag{3.39}$$

For a thin circular disc of radius R and negligible thickness [85]

$$I(q) = \eta_0^2 v^2 \frac{2}{q^2R^2}\left[1 - \frac{J_1(2qR)}{qR}\right] \tag{3.40}$$

where $J_1(x)$ is the first order Bessel function. It is interesting to note that since the sine, cosine, sine integral and Bessel functions all remain finite as $q \to \infty$ the asymptotic form of the intensity curves for each shape at large q has the form $I(q) \propto q^{-\alpha}$ where the exponent α is 4 for spheres, 2 for thin discs and 1 for thin rods, reflecting the dimensionality of the shape.

So far I have only considered what happens when micelles are scattering independently. If the concentration of micelles continued to increase then interference among the

scattered waves would have to be considered. In the simplest case of a sample containing N spherical particles of radius R of uniform contrast η_0 the amplitude of scattered radiation is given by

$$\sum_{j=1}^{N} A_1(q)e^{-i\mathbf{q}\mathbf{r}_j} \tag{3.41}$$

where $\mathbf{r}_j$ is the position of the centre of the jth micelle relative to an arbitrary origin. The intensity is obtained by taking the absolute square averaged over an ensemble of similar systems (or time) giving

$$I(\mathbf{q}) = I_1(q)\left[N + \left\langle \sum_{j=1}^{N}\sum_{k\neq j} e^{-i\mathbf{q}\mathbf{r}_{jk}} \right\rangle\right] \tag{3.42}$$

where $\mathbf{r}_{jk} = \mathbf{r}_j - \mathbf{r}_k$ and I_1(q) is the independent scattering given by equation (3.37). In order to evaluate the second term the pair distribution function $g(\mathbf{r})$ may be introduced by saying that $\langle n\rangle g(\mathbf{r})d\mathbf{r}$ is the probability of finding another particle in the volume element $d\mathbf{r}$ at a distance $\mathbf{r}$ from a given particle with $\langle n\rangle$ the average number density of particles in the system. Rewriting equation (3.42) in terms of $g(\mathbf{r})$ leads to

$$I(q) = NI_1(q)\left[1 + \langle n\rangle \int_0^{\infty} 4\pi r^2 \{g(r)-1\}\frac{\sin qr}{qr}dr\right] \tag{3.43}$$

where $\langle n\rangle$ is the average number density of particles in the system. The term in parenthesis is often termed the structure factor. Since my work has been carried out in very dilute solutions there has been no need to introduce a structure factor to model my scattering data.

Examination of the form of the shape specific scattering equations (3.37), (3.38) and (3.40) along with the appropriate corrections for inter-micelle interference such as the example in equation (3.43) allows one to write a general form for the experimental scattering intensity and explain the source of each component term.

$$I(q) \equiv \frac{d\sigma}{d\Omega} = N_p V_p^2 (\Delta b)^2 P(q)S(q) + B_{inc} \tag{3.44}$$

where N_pV_p gives the volume fraction of scattering particles, $(\Delta b)^2$ is the square of the contrast between the scatterers and the solvent, $P(q)$ is a shape dependent form factor such as those in equations (3.37), (3.38) and (3.40), $S(q)$ is the interparticle structure factor and B_{inc} is the incoherent background signal. Equation (3.44) highlights all of the key system parameters that affect scattering intensity.

3.2. Experimental

3.2.1. ISIS neutron source

Neutrons are produced at ISIS by a spallation process. A heavy metal target is bombarded with pulses of highly energetic protons from a powerful accelerator, driving neutrons from the nuclei of the target atoms. The acceleration chain begins with a Penning H^- ion source at a potential of -665 kV. The extracted H^- beam is accelerated to ground and injected into the linac with an energy of 665 keV. The four tank Alvarez type linear accelerator accelerates the beam to 70 MeV providing a 200 μs long, 22 mA H^- pulse.

On entry to the synchrotron, the H^- ion beam is passed through a 0.3 μm thick aluminium oxide stripping foil that removes both electrons from the H^- ions in the beam converting them to protons. The proton beam is injected over approximately 130 turns of the synchrotron to minimise space charge effects and allow accumulation of 2.8×10^{13} protons.

Once injection is complete, a harmonic RF system traps the injected beam into two bunches and accelerates them to 800 MeV on the 10 ms rising edge of the sinusoidal main magnet field. There are six double-gap ferrite-tuned RF cavities which provide a peak accelerating voltage of 140 kV per beam revolution. Immediately prior to extraction the pulses are 100 ns long and are separated by 230 ns.

The proton beam will make approximately 10 000 revolutions of the synchrotron as it is accelerated before being deflected in a single turn into the extracted proton beam line (EPB). This is accomplished using three fast kicker magnets in which the current rises from 0 to 5 kA in 100 ns. The entire acceleration process is repeated 50 times a second.

The spallation target is made from the heavy metal tantalum. Protons hitting nuclei in the target material trigger an intranuclear cascade, placing individual nuclei into a highly excited state. The nuclei then release energy by evaporating nucleons (mainly neutrons),

some of which will leave the target, while others go on to trigger further reactions. Each high energy proton delivered to the target results in the production of approximately 15 neutrons.

The neutrons produced in this way generally have high energies and velocities and must be slowed down to be useful for condensed matter studies as explained in the introduction above. The moderators at ISIS are ambient temperature water (43°C), liquid methane (100 K) and liquid hydrogen (20 K). The moderators are small, about 0.5 l, and are surrounded by a water-cooled beryllium reflector which scatters neutrons back into the moderators and doubles the useful flux of neutrons.

The characteristics of the neutrons produced by the ISIS pulsed source are significantly different from those produced at continuous nuclear reactor sources. In particular, time-of-flight techniques may be applied to such polychromatic neutron beams, giving a direct determination of the energy and wavelength of each neutron, and allowing fixed scattering geometries to be used. Measurements can cover a wide spectral range in both energy and momentum transfer with good signal-to-noise levels, and the sharpness of the initial 0.4 μs neutron pulse is preserved by the small moderators, giving a rich, high energy component to the under-moderated spectrum, or allowing high instrument resolution to be achieved.

3.2.2. SANS at ISIS

SANS experiments are carried out on the LOQ beamline schematically depicted in Figure 11 using liquid hydrogen moderated neutrons. It is the q-range which defines the sizes of structures which may be probed, therefore it is necessary to work with a neutron beam with a well-defined q-range to avoid confusion during data analysis. The primary flight path consists of a Soller supermirror bender to remove neutrons with wavelengths less than 2 Å, a variable opening chopper to select the desired q-range and frame overlap mirrors to remove neutrons with wavelengths greater than 12 Å. Table 3 shows how the resultant q-range varies with chopper settings. Two scintillator detectors sit at either end of the primary flight path each preceding a variable aperture. The sample environment sits roughly 11 m from the moderator. The long primary flight path assists the collimation of the incident neutrons. The second cadmium aperture defines the diameter of the incident neutron beam in the range 2 – 20 mm. The incident flux depends on the beam diameter, collimation and performance of the ISIS target. A typical time averaged flux is

2×10^5 cm^{-2} s^{-1}. After scattering the secondary flight path is an evacuated chamber to the detector which sits roughly 15 m from the moderator. As neutrons are essentially nonionising when passing through matter their detection is accomplished by first inducing nuclear reactions which produce ionising particles. The detector at LOQ is a ^3He-CF_4 filled ORDELA "area" detector with a 64 cm x 64 cm active area and 5 mm resolution. Neutrons arriving at the detector produce protons in the following reaction

$$^3He + n \rightarrow {}^3He + p + 0.77\ MeV \qquad (3.45)$$

The standard sample environment on LOQ consists of an automated, thermostatted, laser positioned sample changer.

Chopper Frequency / Hz	Chopper Phase / us	λ / Å	q / Å
25	5020	2.2 – 10.0	0.008 – 0.25
50	5020	2.6 – 6.7	0.012 – 0.23
50	10800	6.3 – 10.0	0.008 – 0.07

Table 3 – Chopper settings and resultant wavelength and q-range on LOQ, 126 ° opening

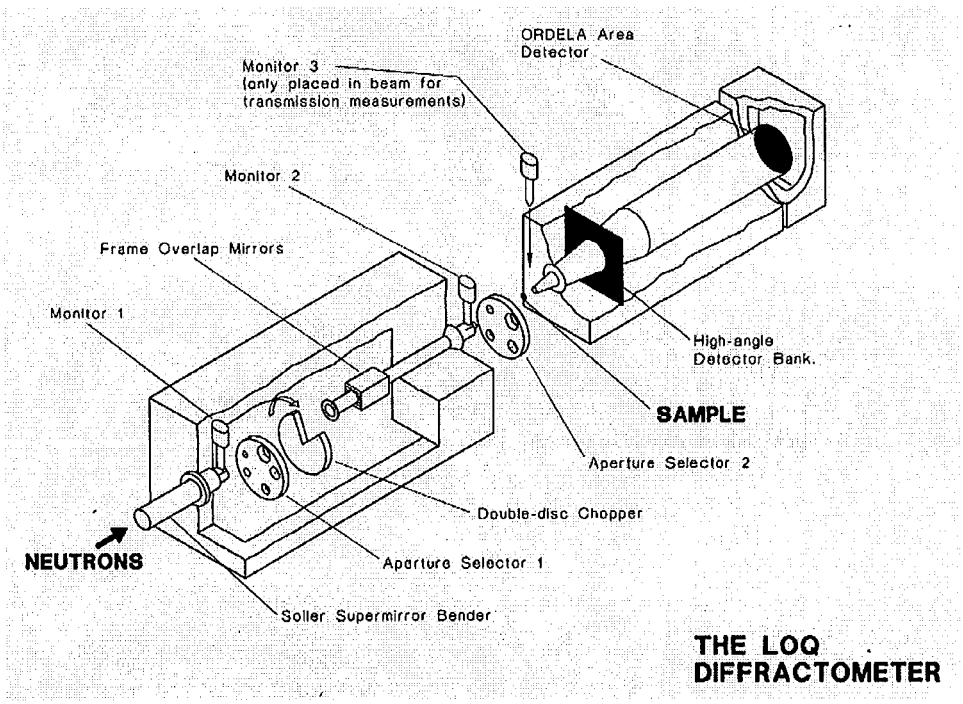

Figure 11 – schematic of the LOQ diffractometer at ISIS

The experimental intensity determined on LOQ takes the general form

$$I(\lambda,\theta) = I_0(\lambda)\Delta\Omega h(\lambda)TV\frac{d\sigma}{d\Omega} \tag{3.46}$$

where I_0 is the incident flux, h is the detector efficiency, T is the sample transmission and the differential scattering cross-section is described in detail above and contains all the structural information about the sample. The first three terms are clearly instrument-specific while the last three terms are sample dependent.

Data are collected for a specified total flux of neutrons with acquisition times determined by the beam current. To determine instrument parameters an initial empty 'CAN' run is performed. Sample transmission may be calibrated by running two experiments on each sample, a longer scattering experiment and a shorter transmission experiment. These two data sets may be combined later, along with the CAN run using the COLLETTE software to output absolute scattered intensity.

Data fitting of the final scattering spectra is carried out in the FISH program written by R. K. Heenan. This program is best suited to fitting of curves with a relatively large number of data points by a model of few parameters. Fitting is by a standard iterative least squares method involving computation of first derivatives of each calculated data point with respect to each parameter in the model.

3.2.3. Sample Environment

Since neutron flux is a limiting factor in SANS experiments it is desirable to work with concentrated samples to maximise scattering within reasonable acquisition times. My sample concentrations were selected to be of the same order as the concentrations of interest in liquid jet adsorption studies, i.e. of the order 1 mM. Micellar surfactant solutions were prepared on the day of the SANS experiment at 1, 2 and 4 mM for each surfactant. All samples were made up in D_2O to maximise contrast with the hydrogenated surfactants. Scattering lengths are given in Table 4 below.

As my sample concentrations are low, exogenously determined by the corresponding adsorption dynamics, other instrumental factors were adjusted to maximise scattering. Although ISIS operates at 50 Hz LOQ tends to operate at 25 Hz utilising only half of the neutrons produced but probing a large q-range per measurement. Since the micelles I

aimed to probe were expected to lie within a given size range it was possible to tune the chopper to operate at 50 Hz with q-range 0.01 – 0.2 $Å^{-1}$ which was suitable for my measurements. Samples were run with the largest possible path length (5 mm) and beam diameter 12 mm (rather than the standard 8 mm). Increasing the illuminated volume introduces slight errors within the point source approximation. Scattering was carried out for 80, 120 and 160 mA for bulk concentrations 4, 2 and 1 mM respectively, where the current refers to the current in the synchroton rather than the integrated flux scattered by the sample. Transmission runs were each collected over 15 mA.

3.3. Previous studies of the size of nonionic micelles

Before outlining the results of my work it is useful to consider a handful of the numerous other studies performed on similar nonionic micellar systems at higher concentrations.

Triton X-100 (TX-100) has been extensively studied for decades. In the late 1970s Robson and Dennis [86] reviewed the then current state of knowledge regarding the size, shape and hydration of TX-100 micelles. Previous work, using light scattering and centrifugation and assuming spherical micelles gave micelle molecular weights ranging from 60,000 to 150,000 corresponding to aggregation numbers from 100 to 250. Using geometrical considerations Robson and Dennis showed that a spherical micelle is unlikely unless part of the ethylene oxide chain is embedded in the core. By taking the micelle molecular weight to be 90,000, corresponding to an aggregation number of 143, the excess micelle volume and hence water content was calculated for both a prolate and oblate ellipsoid. By comparing this geometric value to a value derived from intrinsic viscosity measurements, Robson and Dennis concluded that an oblate ellipsoid is the most likely structure, with approximately 3.5 water molecules per ethylene oxide unit. However the choice of micelle molecular weight is arbitrary and the length of the ethylene oxide chain and density of the hydrophilic region is unknown .

In 1989 La Mesa *et al* [87] studied water self-diffusion in TX-100 solutions using PFGSE-NMR. The diffusion of water in micellar solutions is related to both micelle hydration and to a lesser extent micelle size and shape. It was found that water self-diffusion data are largely lower than expected assuming only obstruction effects. This large discrepancy was entirely assigned to micelle hydration since the authors ruled out the possibility of non-spherical aggregates based on viscosity measurements. The uncertainty in their hydration value is quite large, but La Mesa *et al* reported values in the range 3-4 water

molecules per EO unit. Again, one can question the validity of this numerical answer due to the assumption of spherical micelles only.

Goyal *et al* [88] used SANS to study TX-100 solutions over a wide range of concentrations from 1% to 15% by weight. However, they based their data fits only on the oblate ellipsoidal model discussed by Robson and Dennis. The data fits presented in their publications fall some way beneath the experimental scattering data at low q indicating that perhaps other shapes should have been considered.

The polyoxyethyleneglycol monoalkyl ether family of surfactants (C_nE_m) has also been extensively studied for some time using a diverse range of techniques.

Using PFGSE-NMR in isotropic solutions of $C_{12}E_8$ Lindmann and co-workers [89] estimated a spherical micelle radius of 3.1 nm at 25°C which varied very little with temperature. The hydration of the micelle was estimated at 6 water molecules per ethylene oxide group, although this was based upon an aggregation number of 55 which is much lower than other estimates. Obviously an increase in aggregation number would reduce the hydration since the volume in the shell not taken up by ethylene oxide chains would be reduced. This value of the hydration number may be regarded as an upper limit.

Kato *et al* also used pulsed-field gradient n.m.r and dynamic light scattering to measure the self-diffusion and mutual diffusion coefficient of $C_{12}E_8$ respectively. [90]} The limiting value for the hydrodynamic radius is in good agreement with Lindmann's value of 3.1 nm.

The emergence of SANS in the1980s as a tool for measuring micelle sizes resulted in a period of great interest in the C_nE_m surfactant micelles. In 1984 Zulauf *et al* [91] published the micelle size of $C_{12}E_8$ over the whole isotropic phase region, concluding that there was very little change in micelle structure. However, a recent study by Furo [92] at 5% wt. concentration using PFGSE NMR on $C_{12}E_8$ solutions suggests a decrease in diffusion coefficient with temperature, which would be consistent with micellar growth.

Subsequent work by Zulauf et al [93] used SANS measurements on several C_nE_m surfactants including $C_{12}E_8$ and $C_{16}E_8$. Micelles were modelled as spherical two shell particles over a range of concentrations and temperatures up to the lower consolute boundaries. The corresponding micelle radii are 3.1 nm for $C_{12}E_8$ and 3.8 nm for $C_{16}E_8$ with aggregation numbers of 95 and 150 respectively. The reported hydration numbers

decrease with increasing concentration in the case of $C_{12}E_8$ but are quite scattered for other surfactants in the study with values in the range 1 – 2.5 water molecules per ethylene oxide unit. The authors considered the possibility of nonspherical micelles but were limited by the unavailability of theoretical expressions for fitting anisotropic micelles.

Penfold and co-workers [94] have used SANS to study the alignment under shear flow of the apparently rod like micelles of $C_{16}E_6$ and $C_{16}E_8$ in the presence of salting in and salting out electrolyte. This work is particularly interesting since the shear rates close to the surface of the liquid jet are large. Their work had two aims: (1) to establish whether the evolution of micelle rod length is associated with a change in rod cross-section and whether there is any evidence for the coexistence of rods and disk micelles close to the lower consolute boundary and (2) to find information on micelle polydispersity and flexibility. Although the data published are not directly comparable to my systems some interesting trends are revealed. For $C_{16}E_6$ systems studied the fitted scale factor decreases as temperature is increased. These variations in scale factor cannot, within the model used, be attributed to changes in rod cross section, flexibility or polydispersity and perhaps reflect some inadequacy in the short dimension used in the model. It is possible that a reduction in hydration of EO chains allows greater micelle flexibility which would affect the scattered intensity. For both systems studies the authors observe an initial increase in micelle rod length and eventually a decrease with increasing temperature as the cloud point is approached. The increase in rod length is attributable to the dehydration-driven reduction in area per molecule whereas the subsequent reduction in length is attributable to changes in the intramicelle EO-EO interaction.

A more recent study by Penfold and co-workers [95] looked at the micelles structure of $C_{12}E_8$, $C_{12}E_6$ and $C_{16}E_8$ at 5% wt. concentration in mixtures of water – ethylene glycol. Both $C_{12}E_8$ and $C_{12}E_6$ were modelled as two-shell spherical micelles.

Sato and co-workers [96] used light scattering to characterise the micelles of several C_nE_8 surfactants with n = 10, 12 and 14. The authors conclude the micelles are spherical in each case and that micelle hydration decreases with increasing alkyl chain length. The total micelle radii were 3.0, 3.2 and 3.4 nm for n = 10, 12 and 14 respectively with corresponding aggregation number 45, 62 and 81.

Einaga and co-workers [97, 98] have carried out extensive studies on micelles of C_nE_m type surfactants using both static (SLS) and dynamic light scattering (DLS) measurements over a range of temperatures. The SLS results are analysed to give the weight-average molecular mass and dimensions of micelles using a thermodynamic theory for wormlike spherocylinder micelles formulated by Sato. DLS is used to determine the micelle translational diffusion coefficients.

The C_nE_6 surfactants studied, $C_{12}E_6$ and $C_{14}E_6$, are reported to form rodlike micelles at all temperatures and concentrations. Concentrations corresponding to roughly 4, 20 and 80 mM were used with temperatures in the range 25 – 50 °C for $C_{12}E_6$ and 15 – 40 °C for $C_{14}E_6$. They deduced that the cross-sectional diameter, *d*, of the micelles was similar for each surfactant at ~ 6nm in each case. Rod length, *L*, varied only slightly with concentration, but increased rapidly with increasing temperature. For instance, at 4mM bulk concentration the length of the $C_{12}E_6$ increased from 25 nm at 25 °C to 200 nm at 50 °C. Micelles of $C_{14}E_6$ were significantly longer than their shorter chain analogue at all concentrations. At 4 mM bulk concentration the rod length of $C_{14}E_6$ micelles increased from 80 nm at 15 °C to 1600 nm at 40 °C. The increase in rod length with an increase in alkyl chain lengths was rationalised on the basis of increasing attractive interactions between hydrocarbon chains.

Measurements for C_nE_8 surfactants were carried out at higher temperatures than in my study but the trends are very interesting. For $C_{14}E_8$, $C_{16}E_8$ and $C_{18}E_8$ the micelle cross-section *d* was ~ 4 nm in each case, which seems unrealistically small since the length of a fully extended C_{12} chain is of the order 2 nm (equation (3.52)). Solutions of $C_{14}E_8$ were studied at temperatures ranging from 40 °C to 65 °C where the micelles were found to be rodlike. At 4 mM they found that rod length decreased rapidly with temperature, from 600 nm at 65 °C to 20 nm at 40 °C suggesting that micelles may well be spherical under the conditions in my study. Micelles of $C_{16}E_8$ were also found to be rodlike in the temperature range 25 °C to 50 °C. At 4 mM the rod length stayed roughly constant at 30 nm between 25 – 35 °C before rising rapidly with increasing temperature. Micelles of $C_{18}E_8$ were found to be rodlike and longer than both the $C_{16}E_8$ and $C_{16}E_8$ case. The increase in rod length with alkyl chain length was explained by the increase in attractive interactions between surfactant molecules.

Burchard et al [99] have used light scattering to study aqueous solutions of $C_{14}E_8$ in a wide temperature and concentration range. In the dilute regime (concentrations < 30% wt.)

micelles are found to be spherical up to 35 °C with radius of 3.7nm (double the value used by Einaga) and aggregation number of 119. Above this temperature micelle radius was found to increase rapidly, although this is unlikely when one considers the geometry of a surfactant monomer. This increase probably reflects a transition to a rodlike micelle consistent with the findings of Einaga.

Alkyl maltoside surfactant micelles have not been so widely investigated as these polyoxyethylene alkyl ethers but there has still been significant interest. Auvray et al [69] have investigated the micelle structure of the α- and β- anomers of n-dodecyl-D-maltosides in water using SANS and SAXS. Surfactants were investigated at concentrations of 20 and 40 mM and results analysed using a spherical or ellipsoidal micelle model. The alpha anomer is reported to form spherical micelles with an aggregation number of 75 whilst the beta maltoside is fitted with an oblate ellipsoidal model with aggregation number of 132. The solvation of the head groups is estimated at around 8 water molecules per surfactant molecule which seems rather low. The authors rationalised the different structures based upon greater steric hindrance in the packing of alpha anomer head groups.

Ericsson et al [100] used light scattering and SANS to study the micelles of n-tetradecyl-β-D-maltoside with varying temperature at 50 mM. The authors concluded that the surfactant forms rodlike micelles with an elliptical cross-section which increases in length with increasing temperature.

The final family of surfactants in my work is the sulfobetaine surfactants. Del Mar Graciani *et al* [101] conducted a detailed study of sulfobetaine surfactant micelles in ethylene glycol – water mixtures. Aggregation number was obtained by studying the fluorescence quenching of pyrene by hexadecylpyridinium chloride. In pure water aggregation number was found to increase from 56 for C_{12}DAPS, 67 for C_{14}DAPS to 71 for C_{16}DAPS. Di Profio [102] and co-workers had carried out a very similar study, deriving an aggregation number for C_{14}DAPS of 60.

The effect of adding electrolyte to micellar solutions has also attracted great interest since electrolytes are often present in many practical applications concerning nonionic surfactants. The presence of such substances may affect both the intramicellar and intermicellar interactions. Although these interactions will be much weaker than in the corresponding ionic systems, they do have the potential to alter the structure and

dynamics properties of the micelles. It is well understood that electrolyte addition modifies the cloud point of nonionic surfactants. This effect is explained by a reduction in solubility usually referred to a 'salting out', or an increase in solubility commonly termed 'salting in' depending on the specific electrolyte/surfactant system.

Much of the work done with TX-100 is limited to the effects of added electrolyte on cloud point. Molina-Bolivar et al [103] examine the effect of added electrolyte concentration on micelle formation and structure in Triton X-100 solutions using combined static and dynamic light scattering along with a fluorescence probe technique. Addition of KCl to Triton X-100 solutions causes a reduction in the cmc due to the salting out effect referred to above. Added salt acts enhance the water structure such that a surfactant molecule must do additional work to dissolve in solution. The results of light scattering measurements also demonstrate the growth in micelle size and aggregation number with increasing electrolyte concentration. Microviscosity measurements also indicate an increase in micelle hydration with increasing salt concentration.

3.4. Results

Experimental SANS data are plotted for each surfactant in Appendix 1. Each plot also shows the best model fit to the scattering data. For the surfactant where structural ambiguity remains ($C_{12}E_6$ and β-C_{14}m) both prolate ellipsoid and rodlike fits are shown.

3.4.1. Model structures and data fitting

The nonionic surfactants included in this study have relatively large headgroups in comparison to their ionic analogues so their micelles are composed of two distinct regions. The most appropriate models allow for a hydrophobic core of tailgroups resembling a liquid hydrocarbon surrounded by a hydrophilic shell containing hydrated headgroups. Two such core/shell models were used to fit my scattering data. The first model allows micelles to be spheres or ellipsoids whilst the second incorporates rods and discs. These structures are shown in Figure 12.

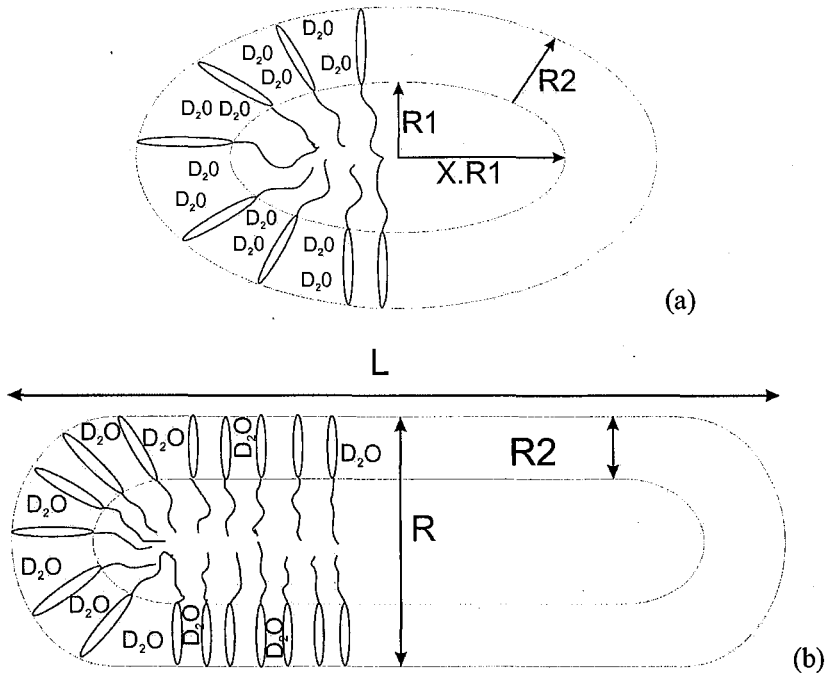

Figure 12 – Schematic model structures for SANS fitting. (a) ellipsoidal (b) rodlike

In general for small angle neutron scattering the scattering per unit solid angle per unit thickness of sample, in cm^{-1}, is

$$\frac{d\sigma(q)}{d\Omega} = N_D(\Delta\rho)^2 V^2 P(q) \tag{3.47}$$

where there are N_D particles cm^{-3} of volume V and the particle form factor $P(q)$ is normalised such that $P(q=0)=1.0$. The scattering length density difference between two phases $(\Delta\rho)$ may be easily calculated based upon the constituent atoms in each phase by the relation,

$$\rho = \sum n_i b_i \frac{\rho_{bulk} N_A}{MW} \tag{3.48}$$

which has units cm^{-2}.

The two-shell ellipsoid structure depicted in Figure 12 is incorporated within Model 24 of the FISH program. Fitting parameters include the radius of core, R1 and the aspect ratio X. Hence the core radii of the micelle are R1 : R1 : X.R1. Therefore X=1 corresponds to a sphere, X < 1 corresponds to an oblate ellipsoid and X > 1 corresponds to a prolate ellipsoid. Another possible fitting parameter is the volume fraction of water in the

hydrophilic shell, although allowing this value to vary is somewhat problematic and will be discussed further below. The final important fitting parameter is the 'scale' which is related to the first three terms in equation (3.47) although the exact relationship depends on the model chosen. For the two-shell ellipsoid model the scale parameter output from the FISH fitting procedure is [104]

$$\text{Scale} = 10^{-24}\phi_{Wet}V_{mic}(\rho_2 - \rho_3)^2 \tag{3.49}$$

where the subscripts 2 and 3 denote the hydrophilic shell and solvent respectively and the 'wet' volume fraction of scattering particles $\phi_{wet} = N_D V_{mic}$. Since the volume fraction of solvent within the micelle is a model parameter, the 'dry' volume fraction of scatterers for a particular fit can be calculated from the solvent volume fraction and the corresponding fitted scale parameter. Comparing this 'dry' volume fraction to the value expected based upon bulk concentration can give another useful insight into whether the fit is realistic. Each of these fitting parameters may be allowed to vary freely, constrained within a range or set at a specific value.

There are also two constrained model parameters which appear in the expression for the particle form factor but may not be assumed independent. The first of these is the thickness of the hydrophilic shell, R2. Since it is possible to estimate the ratio of the tail and dry head group volumes of the surfactant monomer based on the structure of the molecule, it follows that the ratio of core volume to shell volume must be related to the dry monomer ratio and the volume fraction of solvent in the shell. Therefore R2 is a constrained function of R1, the volume fraction of solvent in the shell and the dry head group to tail group ratio which are inputs to the model.

The second constrained parameter is the 'contrast' term which is dependent on the scattering length densities for each of the three phases along with the volume fraction of solvent in the shell. Therefore other inputs to the program include the scattering length densities for each of the separate phases, the core, shell and solvent.

From the fitted parameters it is simple to calculate the total micelle radii and aggregation number from the volume of the micelle core.

The two-shell, end-capped rod structure shown in Figure 12 is available as Model 18 of the FISH program and allows for both rods and discs. Fitting parameters are the outer

radius of the micelle R and the full length of the micelle L which includes the end-caps. In this case the scale parameter is related to the scattering length densities by the relationship, [104]

$$\text{scale} = 10^{-24} N V_{mic} (\rho_2 - \rho_3)^2 \tag{3.50}$$

where the subscripts 2 and 3 again refer to the hydrophilic shell and solvent respectively. As with the ellipsoidal model the volume fraction of solvent in the shell may also be used as a fitting parameter but I have adopted an alternative approach which is explained below.

As in the ellipsoidal model the contrast term and shell thickness are constrained functions of the volume fraction of solvent in the shell, the head and tail group volume ratio and scattering length densities of the three separate phases, which are inputs to the model.

For each of the data sets produced at LOQ, my approach to curve fitting was to begin with the simplest model structure (i.e. a sphere) and gradually increase the complexity to include ellipsoids, then rods and discs where it has been required.

It is possible that different model structures give identical quality fits to the experimental scattering data so it is useful to use some basic molecular geometry to rationalise which structures a particular surfactant may support. In a spherical micelle for instance, the radius of the hydrophobic core cannot exceed the fully extended length of the carbon tail whilst the thickness of the hydrophilic shell is unlikely to be larger than the fully extended length of the hydrophilic head group.

An excellent treatment of geometric packing considerations is given by Israelachvili [105] providing simple guidelines for which structure a particular amphiphile may favour. The packing properties depend on the optimal area per molecule at the core-shell interface, a_g, the volume V_t of the hydrocarbon tail, which will be assumed fluid and incompressible, and the maximum effective length the hydrocarbon chains can assume, L_t. This *critical length* is a semi-empirical parameter representing a somewhat vague cut-off length beyond which the hydrocarbon chain can no longer be considered fluid. I assume it is of the same order as the fully extended chain length l_{max}. According to Tanford

$$V_t \approx (27.4 + 26.9 n_c)\ \text{Å}^3 \tag{3.51}$$

and

$$L_t \leq l_{max} \approx (1.5 + 1.265 n_c)\ \text{Å} \tag{3.52}$$

per saturated hydrocarbon tail with n_c carbon atoms ($CH_3(CH_2)_{nc-1}$-X where X is some hydrophilic moiety). Once the values of a_g, V_t and L_t have been measured or estimated then it is possible to determine the shape and size into which these amphiphiles can pack. These parameters may be satisfied by a variety of structures. However, since the standard chemical potential will be roughly the same for all of these structures entropy will favour the structure with the smallest aggregation number. Israelachvili has shown that the value of a dimensionless packing parameter, $V_t / a_g L_t$, will determine whether surfactants form spherical micelles ($V_t / a_g L_t < 1/3$), cylindrical micelles ($1/3 < V_t / a_g L_t < 1/2$), vesicles or bilayers ($1/2 < V_t / a_g L_t < 1$) or inverted micelles ($V_t / a_g L_t > 1$).

Such simple considerations can give a valuable insight into whether or not the model fits to the experimental SANS data are rational and will be borne in mind throughout this results section.

3.4.2. Scattering length density calculations

The models in Figure 12 consist of three regions with different scattering length density, the core, shell and solvent. It is possible to calculate the scattering length densities for the different regions are obtained from a sum over the constituent atoms (equation (3.48)).

Table 4 shows the coherent scattering lengths for some common atoms. Table 5 uses these values to calculate the scattering length densities of the head group and tail group for each surfactant in this study. These calculations assume that the density of the hydrocarbon core is the same as the density of the appropriate liquid hydrocarbon whilst the head group density is taken from the partial molar volume of the corresponding group in water. The density of the C_{14}DAPS head group is assumed based upon similar groups in water. For surfactants with an ethylene oxide headgroup the first oxygen atom is included in the hydrocarbon tail by convention. [106] This convention makes only very minor differences to the scattering length density of each region. The scattering length density for the shell region is calculated during the fitting procedure by taking an average

of the scattering length density for water and the relevant headgroup, weighted by the volume fraction of solvent in the shell.

Atom	C	H	D	O	N	S
b / 10^{-12} cm	0.6646	-0.3739	0.6671	0.5803	0.936	0.2847

Table 4 – Scattering lengths for some common atoms

Surfactant	Head /tail	Mol. Form.	RMM / g	Density / gcm^{-3}	Volume / Å^3	Sum b / 10^{-12} cm	Sld/10^{10} cm^{-2}
Triton X100	H	$(CH_2CH_2O)_{10}H$	441.5	1.16[a]	633.2	3.765	0.595
	T	$C_{14}H_{11}O$	181.3	0.912[b]	330.1	0.704	0.200
$C_{12}E_8$	H	$(CH_2CH_2O)_8H$	353.4	1.16[a]	506.9	2.937	0.580
	T	$C_{12}H_{25}O$	185.3	0.833[c]	369.4	-0.792	-0.193
$C_{14}E_8$	H	$(CH_2CH_2O)_8H$	353.4	1.16[a]	506.9	2.937	0.580
	T	$C_{14}H_{29}O$	213.4	0.823[d]	430.5	-0.958	-0.206
$C_{16}E_8$	H	$(CH_2CH_2O)_8H$	353.4	1.16[a]	506.9	2.937	0.580
	T	$C_{16}H_{33}O$	241.4	0.813[e]	493.1	-1.125	-0.217
$C_{12}E_6$	H	$(CH_2CH_2O)_6H$	265.3	1.16[a]	380.5	2.110	0.554
	T	$C_{12}H_{25}O$	185.3	0.833[c]	369.4	-0.792	-0.193
$C_{14}E_6$	H	$(CH_2CH_2O)_6H$	265.3	1.16[a]	380.5	2.110	0.554
	T	$C_{14}H_{29}O$	213.4	0.823[d]	430.5	-0.958	-0.206
α–C_{12}malt	H	$C_{12}H_{16}O_{10}$	325.3	1.43[f]	377.9	5.926	1.568
	T	$C_{12}H_{25}O$	185.3	0.833[c]	410.3	-0.792	-0.193
β–C_{12}malt	H	$C_{12}H_{16}O_{10}$	325.3	1.43[f]	377.9	5.926	1.568
	T	$C_{12}H_{25}O$	185.3	0.833[c]	410.3	-0.792	-0.193
β–C_{14}malt	H	$C_{12}H_{16}O_{10}$	325.3	1.43[f]	377.9	5.926	1.568
	T	$C_{14}H_{29}O$	213.4	0.823[d]	464.4	-0.958	-0.206
C_{14}DAPS	H	$C_5H_{12}SO_3N$	166.2	1.2	230.0	0.577	0.251
	T	$C_{14}H_{29}O$	197.4	0.823[d]	429.6	-1.539	-0.358

a - For poly(ethylenexoxide) in water partial molar volume = 38 ml bmol^{-1} [107]
b - Density of 4-tert-octylphenol is 0.912 dcm-3 [108]
c - density dodecanol = 0.833 g/ml [108]
d - density tetradecanol = 0.823 g/ml [108]
e - density hexadecanol = 0.813 g/ml [108]
f – partial molar volume of maltose in water 228 cm^3 mol^{-1} [109]
Table 5 – Scattering length density calculations for surfactant regions

3.4.3. Spherical micelle systems

I first attempted to fit the data to a spherical core-shell micelle model. A number of systems fitted this model very well, in agreement with the literature results discussed above. For all of the surfactants discussed below, scattering data with best fit curves superimposed are plotted in Appendix 1.

3.4.3.1. $C_{12}E_8$

$C_{12}E_8$ is one of the most widely investigated nonionic surfactants and has been the subject of numerous SANS investigations at higher concentrations. The fits to my experimental scattering curves using a spherical micelle model are excellent. Based upon neutron reflection data by Thomas [6] the maximum area per molecule at a saturated planar interface is 62 Å^2 which I took to be the value of a_c. From equation (3.51) and (3.52), the volume and critical length of a 12 carbon chain are 350 Å^3 and 16.7 Å, respectively. Therefore the critical packing parameter defined by Israelachvili $v/a_0 l_c$ = 0.33 which lies on the boundary between spherical and rodlike micelles.

Experimental scattering data at 1, 2 and 4-mM are shown in Figure 13.

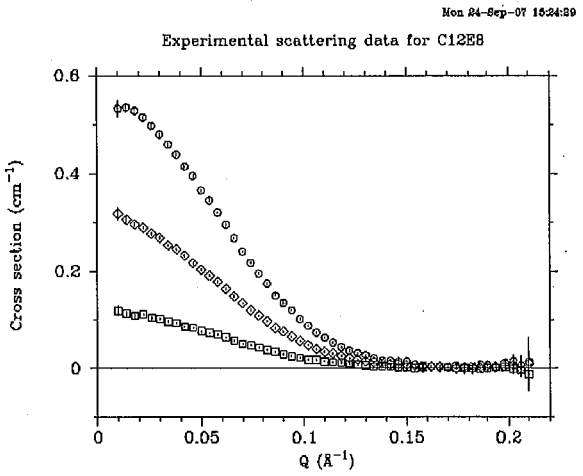

Figure 13- Experimental scattering data for $C_{12}E_8$ solutions at (○) 4-mM, (◊) 2-mM and (□) 1-mM. Error bars lie within the symbols except where shown.

In the spherical micelle model there are only two independent fitting parameters, the core radius R1 and the scale parameter. The volume fraction of solvent in the shell was treated as an input variable. Based upon the literature estimates discussed above I expect approximately 3 – 4 molecules of D_2O per ethylene oxide unit. These solvation values correspond to a volume fraction of 60 – 65% D_2O in the hydrophilic shell. I

systematically varied the water content in the range 40 – 75% corresponding to 1.5 – 6 water molecules per ethylene oxide unit at each concentration studied. The quality of the fit to the experimental data varied only marginally. The lowest sum of weighted square errors (SWSE) was found with 4 water molecules per ethylene oxide unit.

The reason the quality of the fit does not change is that the scale parameter, solvation and core radius are strongly correlated to each other. Figure 14 shows how fitted values for total micelle radius and aggregation number change with the hydration of the hydrophilic shell in 1-mM $C_{12}E_8$. In order to determine which fit provides the best physical description of the micelle, equation (3.49) may be applied to calculate the volume fraction of scattering particles for each fit. Only one of these values will be consistent with the known total amount of surfactant in solution. Figure 15 shows the calculate volume fraction of scattering particles for the fits in Figure 14. Based upon the bulk concentration and critical micelle concentration the actual volume fraction of surfactant within the micelle is 0.00047 which yields a value of 4 water molecules per ethylene oxide unit.

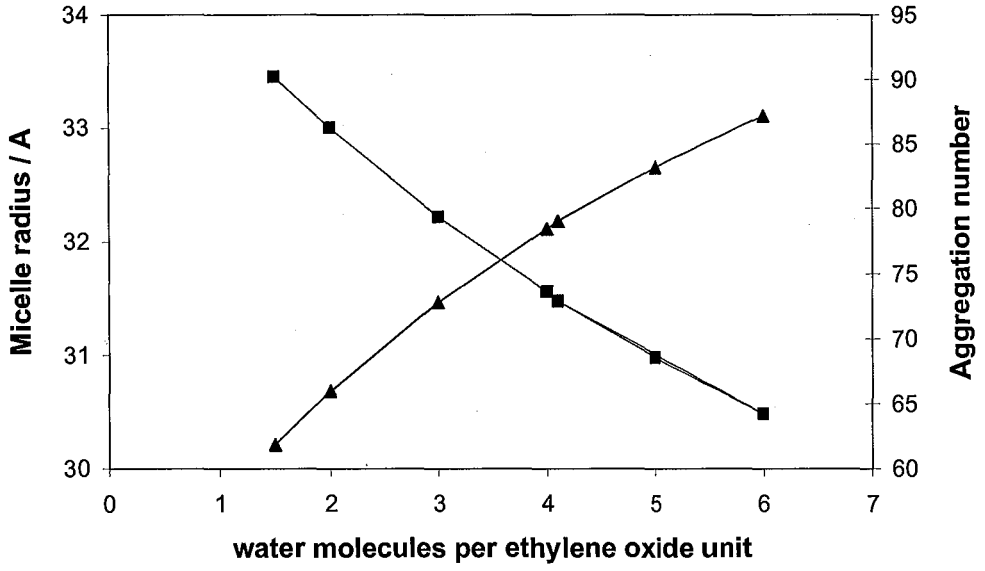

Figure 14 – Changes in micelle size parameters with changing solvation of the hydrophilic shell for spherical model fits to 1-mM $C_{12}E_8$ SANS data. (▲) micelle radius and (■) aggregation number. Lines are drawn to guide the eye only,

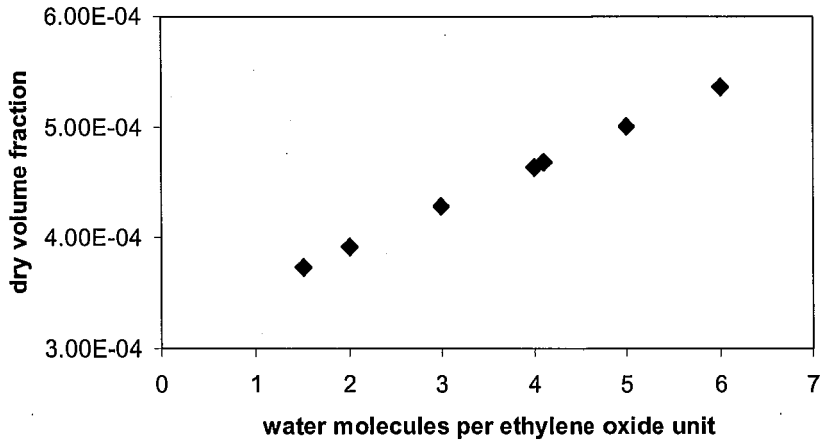

Figure 15 – changes in the fitted dry volume fraction with variation in solvation of hydrophilic shell for spherical model fits to 1-mM $C_{12}E_8$ SANS data.

Finally the best fit curves were analysed to see if the micelle size parameters are realistic. Table 6 gives the micelle core radii (R1), shell thickness (R2) and aggregation number at each bulk concentration.

c_b / mM	R1 / Å	R2 / Å	r_{mic} / Å	Nagg	Water per EO
1	18.7	13.3	32.0	75	4
2	19.6	12.4	31.9	85	3
4	19.0	13.5	31.8	84	3

Table 6 – Micelle size parameters for spherical $C_{12}E_8$ micelles when using best fit solvation values

First consider the core radius of ~ 19 Å. Based upon Tanford's equation (3.52) I estimated the fully extended length of a C_{12} chain as 16.7 Å. One must also consider that within this model I have incorporated an additional oxygen atom into the 'tailgroup'. The length of a C-O single bond is ~ 1.5 Å, which with a bond angle of 109.5° may add an additional 1.2 Å to the chain length. Therefore I expect the fully extended length of the entire tailgroup to be ~ 18 Å. I have performed data fitting with a constrained core radius, R1 < l_c, and there is no discernable affect on fit quality. It may be that the sphere distorts slightly, or that the ethylene oxide units mix into the core slightly to prevent any unfilled space in the core. However, the discrepancy between these calculated values and the model fit is very small and I conclude that the fitted value of ~19 Å is a reasonable one.

Secondly, consider the thickness of the shell. The ratio of core/shell volume must preserve the ratio of tailgroup to headgroup volume since this is a constraint in the model. The shell thickness is well within the extended length of an ethylene oxide octomer so I conclude that these fitting parameters are reasonable.

3.4.3.2. $C_{14}E_8$

My experimental scattering data for $C_{14}E_8$ fit a spherical micelle model. Again this structure can be assessed within the context of Israelachvili's geometrical model. The maximum surface area per molecule at a saturated planar air-water interface is 52 $Å^2$ [110] and the volume and critical length of the hydrocarbon chain from Tanfords equations are 404 $Å^3$ and 19.2 Å respectively. These values give a critical packing parameter of 0.4 which corresponds to a cylindrical micelle in the Israelachvili model, although one must bear in mind that these are only guidelines. For instance, ellipsoidal micelles are not accommodated in Israelachvili's model.

Comparison of the expected and fitted volume fractions from a spherical fit, as with $C_{12}E_8$, yields 3 water molecules per ethylene oxide unit in the shell. Table 7 gives the micelle size parameters for the $C_{14}E_8$ solutions using a spherical micelle model.

c_b / mM	R1 / Å	R2 / Å	r_{mic} / Å	Nagg	Water per EO
1	22.3	12.7	35.0	108	3
2	22.1	14.2	36.3	112	3
4	22.2	14.3	36.5	114	3

Table 7 – Micelle size parameters for spherical $C_{14}E_8$ micelles when using best fit solvation values.

Given that the fully extended length of a C_{14} chain is 19.2 Å, addition of an extra 1.2 Å to account for the C – O bond yields 21.4 Å which compares well with the core radius in these fits. The discrepancy of ~1 Å may be explained in the same way as for $C_{12}E_8$.

3.4.3.3. Dodecyl maltosides

The α and β geometric isomers provide an interesting model system to explore how subtle molecular differences can alter micelle structure. Again, the volume and fully extended length of a C_{12} chain are taken to be 350 $Å^3$ and 16.7 Å respectively. The surface excess at the cmc of the β - anomer is 3.3×10^{-6} mol m^{-2} corresponding to an area per molecule of just 50 $Å^2$ and giving a packing parameter of 0.42. [111] Therefore, although these micelle may be spherical (as with $C_{14}E_8$) one should not be surprised if an ellipsoidal fit is required. I have been unable to find a literature value for the equilibrium surface excess of the α – anomer. The conformation of the headgroup in the α – anomer may lead to steric hindrance and may increase the area per molecule and reduce the packing parameter further towards the spherical regime, although based upon ellipsometry measurements in Chapter 7 it is likely that the surface excess is similar to

that for the beta anomer. First consider the fits to both 1-mM data sets with a spherical micelle model. (see Figure 15 and Table 8).

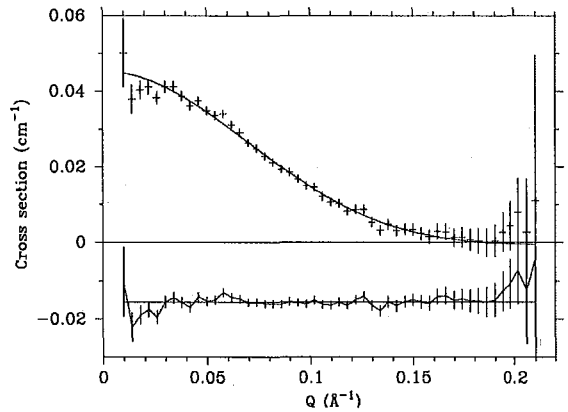

(a)

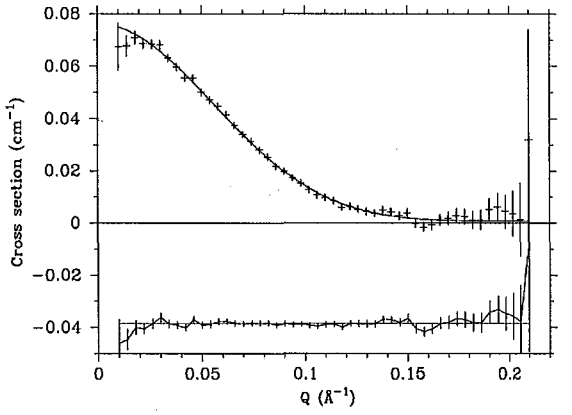

(b)

Figure 16: Spherical fits to 1-mM neutron scattering data for (a) α-C_{12}m and (b) β-C_{12}m.

anomer	R1 / Å	R2 / Å	r_{mic} / Å	Nagg	% water in shell
α	16.6	11.0	26.6	47	75
β	20.2	14.8	35	85	80

Table 8 – Size parameters for 1-mM solutions of α- and β-n-dodecyl maltoside using a spherical fit to the data in Figure 16.

The core radius of the α - anomer is well within the maximum length of the hydrocarbon chain, whilst the shell thickness is within the length of a maltose head group of 11 Å, calculated based upon standard bond lengths and angles. These data represent a physically realistic structure. Unfortunately due to an experimental error I am unable to analyse the data at 2 and 4 mM for this anomer. Early analysis of the experimental data from LOQ showed that the data for the two higher concentrations closely overlaid the 1 mM data, indicating an error in making up the solutions. Unfortunately there was no time to repeat these scattering runs.

For the β - anomer however, both the core radius and shell thickness are too large for the constituent groups. Fitting attempted with R1 constrained to a physically realistic value gave poor quality fits to the experimental data. I next attempted a series of ellipsoidal fits, with $X \neq 1$. Based upon the molecular structure I excluded any data fits which gave a shell thickness > 11 Å.

Elongating the micelle into either prolate or oblate structure has the effect of reducing the shell thickness for a given core volume. By manually adjusting X one may find the limits at which the shell thickness becomes reasonable. For 75% volume fraction of water in the hydrophilic shell (corresponding to ~ 40 water molecules per monomer), the shell thickness falls below 11 Å provided $X \leq 0.25$ or $X \geq 3.5$. Although both fits are reasonable the sum of weighted squared errors (SWSE) is smallest for the oblate model, as well as being a visibly closer fit. The key area when assessing the quality of these fits lies between $0.04 \leq Q \leq 0.11$ $Å^{-1}$ where the error bars are smallest. Both fits are shown in Figure 17. An oblate structure is also in agreement with the work of other authors. [69]

For each bulk concentration and volume fraction of water in the shell it is possible to determine the maximum aspect ratio that confines the shell thickness to a sensible value. The best fit structural and hydration parameters are given in Table 9.

c_b / mM	R1 / Å	X	R2 / Å	r_a / Å	r_c / Å	Nagg	% water in shell
1	25.4	0.48	11.0	36.4	23.2	80	65
2	24.9	0.5	11	35.9	23.4	79	65
4	25.8	0.45	10.9	36.7	22.5	79	65

Table 9 – Best fit structural parameters using an oblate ellipsoid model for beta-n-dodecyl maltoside.

In conclusion, the more sterically hindered α-anomer forms spherical aggregates containing roughly 50 monomers, whilst the more β-anomer forms oblate ellipsoidal micelles containing 80 monomers that appear to be independent of concentration.

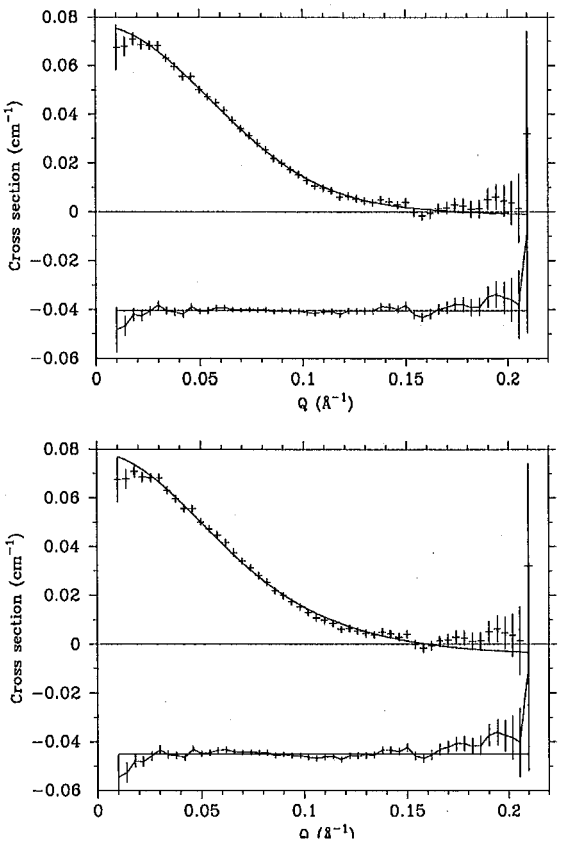

Figure 17: A comparison of (a) oblate and (b) prolate ellipsoidal fits to 1-mM β-C_{12}m micellar solution.

3.4.3.4. Tetradecyldimethylammoniopropanesulfonate

The surface excess at the cmc of C_{14}DAPS is 3.2 × 10^{-6} mol m^{-2} [112] corresponding to a surface area per molecule of 52 $Å^2$ and the volume and critical length of the hydrocarbon chain from Tanfords equations (3.51) and (3.52) are 404 $Å^3$ and 19.2 Å respectively. The critical packing parameter of 0.4 indicates that the micelles may be cylindrical although the literature indicates that micelles of C_{14}DAPS are spherical. The best fit parameters shown in Table 10.

c_b / mM	R1 / Å	R2 / Å	r_{mic} / Å	Nagg	% water in shell
1	20.0	8.1	28.1	78	70
2	20.0	10.8	30.8	78	80
4	20.0	10.9	31.0	79	80

Table 10 - Best fit size parameters for spherical C_{14}DAPS micelles

The radius of the core is reasonable based upon a C_{14} chain. An estimate of the length of the head group may be calculated from 2 C-N bonds, 2 C-C bonds, a C-S bond and S-O

bond giving approximately 10 Å. Therefore this spherical fit seems realistic based upon the molecular geometry.

3.4.4. Non-spherical micelle systems

Although one non-spherical system has already been found in the dodecyl maltosides, I now turn my attention to systems for which a spherical fit does not fit the data well at all. For all of the surfactants discussed below, scattering data with best fit curves superimposed are plotted in Appendix 1.

3.3.4.1. Triton X100

Robson and Dennis [86] used a critical length of the t-octylphenol group of 10 Å and a volume of 330 $Å^3$ based upon the density of t-octylphenol alcohol. The surface excess of a TX-100 saturated monolayer is 2.8×10^{-6} mol m^{-2} corresponding to an optimal surface area per molecule of 59 $Å^2$. [113] These values give a critical packing parameter of 0.56 which falls within the bilayer regime of Israelachvilis model. Again, one must remember that these regimes are only guidelines and we have already seen that some micelles still appear spherical even with a packing parameter > 1/3.

Comparisons of fits to a spherical, prolate and oblate ellipsoidal model (Figure 18) reveal that a spherical model fit is unsatisfactory. Of the two ellipsoidal models, the prolate micelle gives a much closer fit to the experimental scattering data. Also, the oblate fit requires an unrealistically small radial radius of 0.4 nm. The deviation from the fits to experimental data at very low q is most likely due to polydispersity in micelle sizes since TX-100 is known to contain a mixture of ethylene oxide chain lengths. Table 11 gives the best fit structural parameters using a prolate ellipsoidal model. The core radii are roughly 13.5 Å which is slightly longer than the expected value of 11.5 Å based on a 10 Å t-octylphenol group plus 1.5 Å C-O bond. However, it is not unreasonably large. Note also the reduction in shell hydration in comparison to other ethylene oxide based surfactants of the C_nE_m series, reflecting the shorter carbon tailgroup and hence tighter packing of ethylene oxide chains.

c_b / mM	R1 / Å	X	R2 / Å	r_a / Å	r_c / Å	Nagg	water per EO
1	13.7	3.15	11.0	24.7	54.1	103	1.5
2	14.0	3.0	12.2	26.2	54.1	104	2
4	13.6	3.16	12.5	26.1	55.5	101	2

Table 11 – Best fit structural parameters for prolate TX100 micelles.

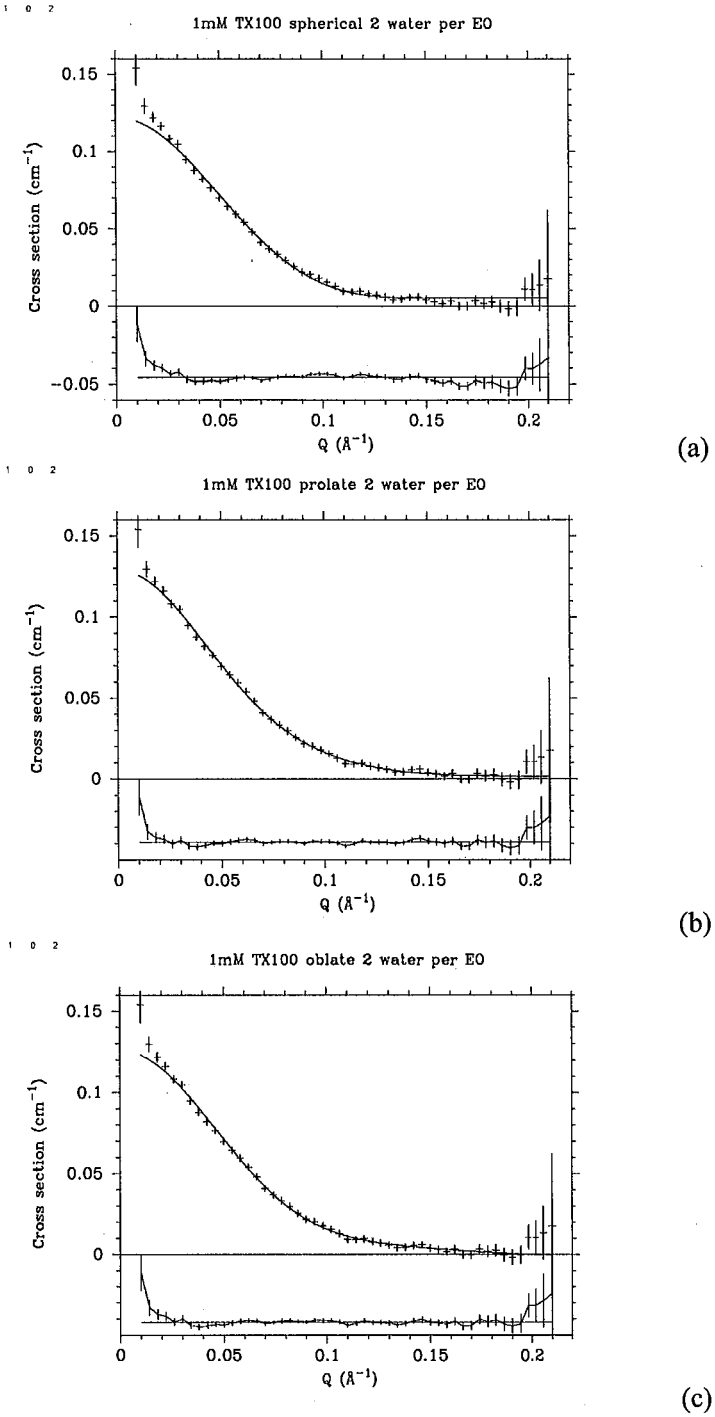

Figure 18: (a) Spherical, (b) prolate and (c) oblate model fits to TX-100 SANS data for a 1-mM solution

3.4.4.2. $C_{16}E_8$

The final surfactant in the C_nE_8 series presented a challenge with data fitting. Based upon Tanford's equations (3.51) and (3.52) the calculated volume and fully extended length of

a C_{16} chain is 458 Å^3 and 21.7 Å respectively. The surface excess at the cmc is 3.3×10^{-6} mol m^{-2} corresponding to an area per molecule of 50 Å^2 giving a packing parameter of 0.42. This surface excess has been calculate based upon ellipsometry measurements and explained in Chapter 7.3.1. This packing parameter value is slightly larger than the value for $C_{14}E_8$, although that surfactant fitted a spherical model very well.

For $C_{16}E_8$, spherical micelle models do not fit the data well. Of the ellipsoidal fits, a prolate model gives a closer fit to the data than an oblate model. However, as can be seen from the fits in Appendix 1, at very low q the scattered intensity exceeds the model value. This indicates some degree of larger scale structure and probably reflects polydispersity in the micelle sizes. It is unlikely that this data suggest larger scale rods since a log-log plot of the intensity data reveal the exponent in the intensity decay to be approximately 4 as is the case for spheres. Therefore I conclude that these small ellipsoidal models are satisfactory. Table 12 gives the best fit structural parameters from these models.

c_b / mM	R1 / Å	X	R2 / Å	r_a / Å	r_c / Å	Nagg	water per EO
1	20.1	2.2	14.7	34.8	58.7	144	4
2	19.9	2.3	14.8	34.7	61.0	149	4
4	20.2	2.4	15.0	35.1	62.4	156	4

Table 12 – Best fit structural parameters for prolate $C_{16}E_8$ micelles.

The core radius agrees very well with the expected value for the length of the C_{16} chain.

3.4.4.3. β-C_{14}malt

This maltoside surfactant, n-tetradecyl-β-maltoside presented similar difficulties to $C_{16}E_8$. The surface excess at the cmc of is 3.7×10^{-6} mol m^{-2} corresponding to a surface area per molecule of 45 Å^2. [100] The volume and critical length of the hydrocarbon chain from Tanfords equations (3.51) and (3.52) are 404 Å^3 and 19.2 Å, respectively giving a critical packing parameter of 0.47, making non-spherical micelles likely.

Experimental data were acquired at 40 °C to avoid problems with a Kraft temperature of 32 C. Model fitting to the experimental scattering data indicates that micelles are either prolate ellipsoids or rods. At bulk concentration of 4 mM a rodlike model clearly gives a better fit, whilst at 1 mM the prolate ellipsoid is marginally better. Unlike $C_{16}E_8$, these micelles appear to elongate as concentration in increased. The corresponding best fit parameters are shown in Table 13.

c_b / mM	R / Å	L / Å	R2 / Å	Nagg	% water in shell
1	23.6	92	10.6	347	40
2	23.0	134	10.2	536	50
4	23.8	210	11.2	873	60

c_b / mM	R1 / Å	X	R2 / Å	r_a / Å	r_c / Å	Nagg	% water in shell
1	17.0	3.0	13.1	30.1	65.0	147	70
2	15.8	5.0	9.0	24.9	87.4	191	60
4	15.5	7.5	9.3	24.8	125.5	272	60

Table 13 – Best fit parameters for β-C_{14}m micelles, (above) rod model, (below) prolate model.

It is clear that the choice of model has a large effect on the aggregation number and is therefore an important choice. The fully extended length of a C_{14} chain is 19.2 Å and neither model violates this limit. In Chapter 7 I will attempt to resolve this ambiguity through comparison of these data with PFGSE NMR data.

3.4.4.4. $C_{12}E_6$

The surface excess at the cmc of is 3.2×10^{-6} mol m^{-2} corresponding to a surface area per molecule of 52 $Å^2$. [6] The volume and critical length of the hydrocarbon chain from Tanfords equation's are 350 $Å^3$ and 16.7 Å, respectively giving a critical packing parameter of 0.4. As with n-tetradecyl-β-maltoside these micelles fit either prolate or rod like micelle models most closely. The micelles also elongate as concentration is increased. At 1 mM a prolate model gives a marginally better fit, whilst at 4 mM the rodlike model is clearly better. The best fit parameters for each model are shown in Table 14.

c_b / mM	R / Å	L / Å	R2 / Å	Nagg	water per EO
1	21.6	109	8.5	507	0.5
2	23.1	153	10.7	688	1.5
4	24.6	245	10.4	1512	1.5

c_b / mM	R1 / Å	X	R2 / Å	r_a / Å	r_c / Å	Nagg	water per EO
1	15.5	4.2	7.8	23.2	73.5	178	1
2	15.5	5.8	8.1	23.6	98.6	248	1
4	15.5	9.2	10.4	25.9	152.7	386	2

Table 14 – Best fit parameters for $C_{12}E_6$ micelles, (above) rod model, (below) prolate model.

As with n-tetradecyl-β-maltoside it is very difficult to choose between these two models and a resolution may only come through comparison with diffusion measurements in Chapter 7.

3.4.4.5. $C_{14}E_6$

This surfactant has been the most problematic to model accurately. In a SANS experiment it is the q-range that determines the range of sizes which can be probed. An advantage of spallation sources such as ISIS is the ability to probe a wide range in a single measurement. However, to minimise acquisition times I curtailed the q-range slightly to operate at 50 Hz rather than the usual 25 Hz, acquiring data with q = 0.01 – 0.21 $Å^{-1}$ corresponding to structures with sizes of the order 10 – 100 Å. For structures that extend outside of this size range (of the order of 1000 Å, for example) my experimental set-up becomes inappropriate. This appears to be the case with $C_{14}E_6$ micelles. Despite much effort, fits to my own data proved rather insensitive to size variations.

I am grateful to Professor Julian Eastoe and his research group for agreeing to run a sample on D22 at the ILL with a wider q-range. Experimental data from D22 were acquired for a 1-mM solution of $C_{14}E_6$ with q = 0.0028 – 0.3877. This data is very accurately fitted using a rod model. Best fit parameters give a long rod of outer radius 27.7 Å, length 4116 Å and shell thickness 10.2 Å. The best fit solvation value is equivalent to 2 water molecules per ethylene oxide unit.

3.5. Summary

Micelle dimensions for a range of nonionic surfactant systems have been probed using SANS. These micelle dimensions will be used in subsequent chapters in order to better understand both bulk micelle exchange kinetics and mass transport differences. Appendix 1 contains the scattering data with curve fits referred to in this chapter superimposed.

Chapter 4

Existing Theory of Micelle Breakdown Kinetics Evaluated using Numerical Modeling

The rate at which monomers enter and leave micelles and ultimately the lifetime of a micelle is of great importance for the adsorption kinetics from micellar solutions. Many researchers working in the field of adsorption kinetics deduce micellar lifetimes from perturbation experiments that have been analysed using some form of kinetic model. Since the mid-1970's the model of Aniansson and Wall [53-55] has been the generally accepted framework for the analysis of most systems. However, it is unclear why lifetimes deduced using a model derived for systems subjected to perturbations less than 1% away from equilibrium should still apply close to a non-equilibrium surface where up to 100% of the monomer has been depleted. In order to develop a deeper understanding of such processes I have used numerical modelling methods to simulate micelle breakdown under a range of conditions.

I will show that the rate at which monomers are released from micelles is strongly dependent on the local monomer concentration; the micellar lifetime should not be treated as a colligative property of a particular surfactant. Furthermore, my modelling will expose potential failings in the Aniansson and Wall model itself.

This chapter begins with a review of existing knowledge of exchange kinetics in micellar solutions. The remainder of the chapter outlines the use of those conventional theories to model micellar systems numerically, demonstrating that micelle breakdown kinetics are far more complicated than has previously been acknowledged.

4.1. Exchange Kinetics at Equilibrium

4.1.1 Conventional Monomer-Micelle Exchange Kinetics

Micellar solutions are highly complicated, containing aggregates of varying sizes, shapes, hydration and aggregation number in different amounts all in dynamic equilibrium. The 1960s and 1970s saw much experimental and theoretical work aimed at understanding the fundamental physical processes occurring in these dynamic systems of micelles.

Wennerström and Lindman captured the state of knowledge regarding monomer-micelle exchange kinetics at the end of this period in their 1979 review. [56]

Many experimental techniques had been used to examine the kinetic response of micellar systems to perturbation including stopped-flow [44-46], pressure-jump [47, 48], temperature jump [46, 49, 50] and ultrasonic adsorption [45, 51]. Despite this intense experimental effort a satisfactory theory which explained all of the available relaxation data was not immediately forthcoming. Ultrasonic adsorption measurements showed the existence of a fast relaxation process occurring on the microsecond timescale whilst stopped-flow, temperature-jump and pressure jump revealed a much slower process occurring on the millisecond timescale. In the early 1970s both relaxation times were attributed to some form of monomer exchange process, where the addition of the final monomer to the micelle was the rate determining step.

$$A_n \underset{k_{n-1,n}}{\overset{k_{n,n-1}}{\rightleftarrows}} A_{n-1} + A \tag{4.1}$$

Lang *et al* [50] point out that data which indicated a fast process occurring on the millisecond timescale did have some and common factors with the data which implied a slower process; (1) both were characterised by single relaxation times rather than distributions of relaxation times and (2) the reciprocals of both the long and short relaxation times increased linearly with bulk concentration.

Muller [52] was the first to emphasise the peculiarity of the situation where two relaxation times differing by several orders of magnitude were assigned to the same physical process. Muller pointed out that values of $k_{n,n-1} \approx 0.4-120\,\mathrm{sec}^{-1}$ (as reported by Kresheck[49]) "stand in flat contradiction to the repeated observation that process (4.1) is fast on the nmr timescale". Muller reasoned that if the interconversion of monomers and micelles was made up of $n-1$ steps similar to (4.1), then the slow relaxation time must reflect complete micelle dissolution via a random walk process with steps of unit size. If the system were close to equilibrium such that the probability of monomer uptake and loss was similar, then for large micelles one would expect roughly n^2 steps and the slow relaxation time could be approximated by

$$\tau \cong \frac{n^2}{2k_{n,n-1}} \tag{4.2}$$

Unfortunately this expression did not account for concentration effects and reasonable estimates of $k_{n,n-1}$ lead to τ values much longer than those measured in temperature-jump work.

Several other theories were proposed including that of Colen [114] who suggested that the slow relaxation process was due to reactions of aggregates of the form

$$A_i + A_j \rightleftarrows A_{i+j} \tag{4.3}$$

This proposal was later dismissed by other authors as being highly unlikely due to electrostatic repulsion in ionic micelles, the low concentrations of the intermediate aggregates involved and the reorganisation of surfactant monomers within aggregates that would have to occur (see Aniansson and Wall [55]).

It was the seminal work of Aniansson and Wall in 1974 [53] that finally produced a generally accepted theoretical description for the available kinetic data. By making a series of assumption regarding the perturbation amplitude and the micelle size distribution they were able to derive limiting solutions to the system of differential equations that describe changes in micelle concentration. Their model predicted that relaxation would occur in two stages on well-separated timescales and their simple expressions for the corresponding relaxation times were relatively easy to apply. Just one year later in 1975 Lang *et al* undertook a series of experiments which confirmed that micelle solutions were indeed characterised by two different relaxation times which differed by several orders of magnitude. In the following year Aniansson and Wall published a joint review in collaboration with Lang and co-workers which showed how their model could be used to fit Lang's experimental data and extract information about the micelle size distribution [55]. Since the mid-1970s and up to the present day Aniansson and Wall's model has become the cornerstone for the analysis of micellar kinetic data. In the words of Wennerström and Lindman, "...there seems to be no doubt that in essential points the theory of Aniansson and Wall provides a correct description of micellar kinetics...". Aniansson and Walls theory has since been applied by numerous experimentalists to fit their relaxation data and extract micelle lifetimes and information on the micelle size distribution [58, 115-120]. Their theory also forms the basis for all consideration of monomer-micelle exchange kinetics in models of adsorption from micellar solutions.

4.1.2. Further work on monomer-micelle exchange kinetics

In 1981 Kahlweit produced a review entitled "What do we know about micelles and which questions are still open"? [121] It is notable that throughout this 12 page review, in which Kahlweit outlines the theory of Aniansson and Wall and some minor modifications (see below) only one page covers the unanswered questions. These unanswered questions pertain to micelle structure, phase transitions at high concentrations and micellar catalysis. In fact the essential theory on monomer-micelle exchange kinetics has remained unchanged for more than 30 years although there have been several other theories put forward which can inform our thinking. In 1981 Hall [122]dealt theoretically with the influence of solution composition on the rate coefficients involved in the solutions of Aniansson and Wall in ionic surfactant solutions. His solutions include additional terms for ionic surfactants which account for non-ideality and micelle-counterion interactions.

Perhaps more significant was the work of Lessner, Kahlweit and Teubner [123] who were concerned with apparent discrepancies between the predictions of the Aniansson and Wall model and actual solution behaviour at high surfactant concentration. They proposed that as the bulk concentration increases the additional counterions compress the electrical double layer and micelles may begin to form by the merging of sub-micellar aggregates. This proposal is not dissimilar to the ideas of Colen, [114] which had been dismissed by Aniansson and Wall several years earlier. For non-ionic micelles they expected that such merging would occur for all bulk concentrations.

More recently Rusanov *et al* published a series of five papers, performing an in depth mathematical analysis of the micellisation process, starting from the essence of the Aniansson and Wall kinetic model. In the final paper [124] they summarise their work by outlining the characteristic kinetic times of micellisation in non-ionic surfactant solutions. Their theory finds no less than 9 characteristic kinetics times of micellisation which are ordered into a hierarchy. These times are the establishment of quasi-equilibrium concentrations of aggregates in (1) micellar, (2) sub-micellar (3) over-critical regions and (4) near-critical regions, (5) time between successive monomer emissions, (6) average micelle lifetime, (7) time to establish a quasi-stationary exchange of matter between solution and aggregates along with the (8) fast and (9) slow relaxation processes. As well as the complexity of their mathematical description the authors also propose no method

of probing their hierarchy experimentally making their work of entirely theoretical interest.

One finds some recent alternative approaches to the analysis of micellisation kinetics in the field of block copolymer micelles. For instance, In 2005 Nyrkova and Semenov [125] studied the formation and dissolution of micelles by considering the free energy of aggregates and using nucleation theory. Such a free energy approach avoids the assumptions involved in linearising the corresponding differential equations and permits the consideration of systems which are further from equilibrium. Their results showed that for sufficiently large aggregates the energy barrier to nucleation (and fission) became prohibitively high, due to the unfavourable intermediate aggregates. The size of this energy barrier was highly dependent upon the monomer concentration as were the corresponding micellisation kinetics. In fact for a typical copolymer micelle one might expect that micelles may never form on a realistic timescale (< 10 years!). These results appear to have attracted little attention in the field of copolymer micelles which are known to relax slowly due to their large molecular weights and the authors still support the essential premise of the Aniansson and Wall model and dismiss several alternative kinetic pathways, including the fusion of larger aggregates. As will be shown below, their results are far more general than has been acknowledged.

4.1.3. The Aniansson and Wall kinetic model

Aniansson and Wall's model [53-55] is based on the assumption that changes in micelle size occurs in unitary steps only. They further assume that aggregates occur in substantial amounts only in two regions of the aggregate size distribution, namely in the region of proper micelles and in the region of monomers. A distribution of this form is depicted by the solid line in Figure 19. If micelle system of this kind is perturbed such that there is an excess population in the region of proper micelles then material must move between these two regions, equivalent to a flow in 'aggregation space'. One may draw an analogy with heat conduction (or other general diffusion processes) by viewing a micellar solution as two metal blocks connected by a very thin wire, where one block represents pre-micellar aggregates and the other represents proper micelles with the thin wire corresponding to aggregation numbers in between. If the temperature in one block is altered rapidly then one would expect an initial rapid local adjustment followed by a much slower flow of heat from one block to the other.

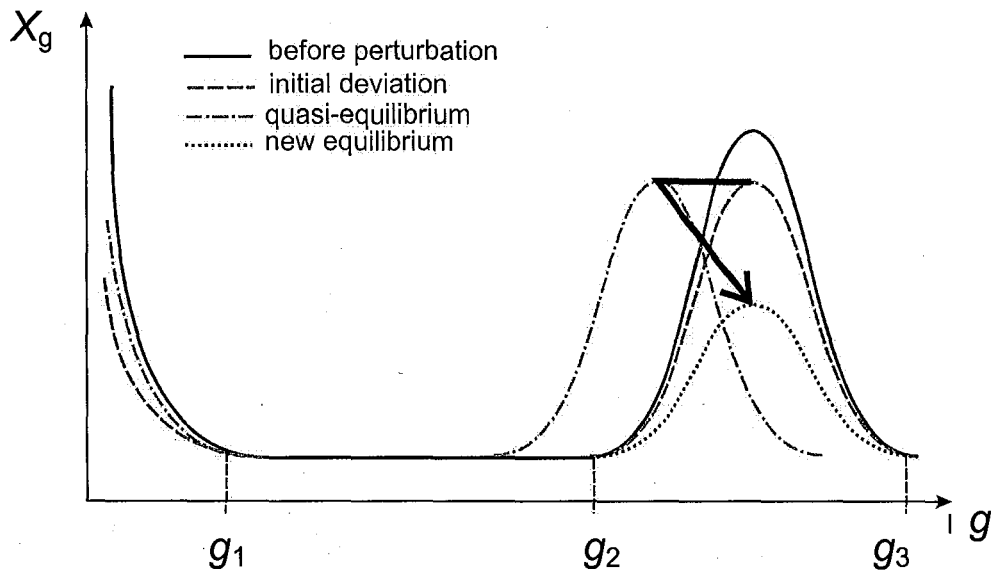

Figure 19: Aniansson and Wall schematic size distribution and expected response to a perturbation

Aniansson and Wall formalised their model in the following way:

1) The association and dissociation of micelles proceeds in unitary steps only.

Given that the concentration of dimers and trimers is generally much lower than that of the monomers, only a much greater rate of entrance and exit could make their contribution to the total rate of the same order of magnitude as the monomer contribution. Since the rate of monomer uptake is diffusion controlled and is an upper limit for the rate of fusion it is impossible for the rate of uptake of dimers and trimers to exceed this value.

2) For ionic surfactants the mobility of counterions is much greater than that of the surfactant molecular ions so that the counterions automatically readjust to the motion of the latter, i.e. counterions do not affect the rate.

The relevant kinetic processes can then represented by the following reactions:

$$X_1 + X_g \underset{k_g^d}{\overset{k_g^a}{\rightleftharpoons}} X_{g+1} \qquad g = 2,3,... \tag{4.4}$$

where X_g is the concentration of aggregates containing g monomers. The rate of change of concentration of each species is then governed by the following system of equations;

$$\frac{dX_g}{dt} = k_{g-1}^a X_{g-1} X_1 + k_g^d X_{g+1} - k_g^a X_g X_1 - k_{g-1}^d X_g \qquad g = 2,3... \tag{4.5}$$

and for monomers

$$\frac{dX_1}{dt} = \sum_{g=1}^{g_{max}-1} k_d^g X_{g+1} - k_a^g X_1 X_g \qquad (4.6)$$

This system of equations is of the same form as those introduced in 1935 by mathematicians Becker and Döring. [126]

Immediately following a perturbation they may be an excess of material in one region of the aggregate size distribution which must move to another region to re-establish equilibrium. The form of equation (4.4) indicates that this movement will occur in steps which are small compared to the total movement in aggregation space required and hence will have the character of flow.

By introducing an expression for the relative perturbation from equilibrium,

$$\xi_g = (X_g - \bar{X}_g)/\bar{X}_g \qquad (4.7)$$

(where $\bar{X}_g$ is the equilibrium concentration) and using the equilibrium relation,

$$k_a^g \bar{X}_g \bar{X}_1 = k_d^{g+1} \bar{X}_{g+1} \qquad (4.8)$$

Aniansson and Wall rewrote equations (4.5) and (4.6) in the form,

$$\bar{X}_g \frac{d\xi_g}{dt} = -(J_g - J_{g-1}) \qquad (4.9)$$

With

$$J_g = -k_d^g \bar{X}_g [\xi_g - \xi_{g-1} - \xi_1(1+\xi_{g-1})]. \qquad (4.10)$$

The term J_g represents the net number of aggregates passing from $g-1$ to g in unit time. Equation (4.10) closely resembles the equations for heat conduction in one dimension with g acting as the space coordinate, ξ_g the temperature, $\bar{X}_g$ the mass per unit length and k_d^g the conductivity per unit of mass per unit. The term $\xi_1(1+\xi_{g-1})$ provides an additional, space-independent driving force.

4.1.3.1 Understanding the separation of timescales

Consider a micelle system initially at equilibrium which is rapidly diluted, reducing the concentration of all species by a constant factor. The attainment of the new equilibrium state involves the replenishment of monomers and therefore the destruction of a proportion of the existing micelles. Aniansson and Wall's model, where only individual monomer uptake and loss are permitted, predicts that micelle destruction will occur in the following way. A reduction in monomer concentration will perturb all of the monomer/aggregate equilibria represented by equation (4.4) so as to favour monomer release over monomer uptake. It follows that a rapid dilution will result in a release of monomers with a corresponding reduction in the size of all aggregates. The entire aggregate size distribution will shift to lower aggregation numbers, with the number of aggregates remaining the same. The timescale for this process is the same as the timescale for individual monomer release.

Once the monomer concentration has recovered sufficiently the monomers and micelles reach pseudo-equilibrium, in which the rate of monomer uptake becomes equal to the rate of monomer loss once again; the monomer concentration is still less than the cmc and the average aggregation number of the micelles is less than the equilibrium value. In order to re-establish equilibrium some of the excess micelles must break down completely, with some of the monomers they release being taken up by those micelles that persist. In the Aniansson and Wall model, complete micelle breakdown may only occur by sequential monomer loss. Since the system is in a state of pseudo-equilibrium, where the probability of monomer loss is equal to the rate of uptake, the time required for a micelle of size 'N' to lose N-1 monomers may be evaluated using a random walk treatment. For a one-dimensional random walk with steps of ±1 of equal probability the number of steps required to move N steps away from the origin is approximately equal to N^2. For an average aggregation number of the order 100 the re-establishment of equilibrium amongst the excess micelles is expected to be at least several orders of magnitude slower than the rapid monomer loss process. This timescale may be extended or reduced if the rates of monomer uptake and loss rates are not exactly equal. A size distribution movement of this kind is shown on Figure 19.

In the next two sections I review the analytical solutions derived by Aniansson and Wall so that we may begin to understand their model solutions and why the applicability of those solutions is more limited than many authors have assumed.

4.1.3.2 The fast process – the attainment of pseudo-equilibria

The fast process described above occurs immediately following a perturbation which reduces the monomer concentration below the cmc. The imbalance of each and every monomer/aggregate equilibrium results in rapid release of monomers, changing the amount of material in the region of proper micelles but not the number of aggregates. This process happens on the timescale of individual monomer release and was treated theoretically by Aniansson and Wall.

Aniansson and Wall began by taking the distribution in the region of proper micelles ($s < g < j$) as Gaussian with

$$\bar{X}_g = X_0 e^{-(g-N)^2/2\sigma^2} \tag{4.11}$$

where N is the peak aggregation number and σ is the distribution width. A Gaussian distribution implies that

$$\frac{k_d^g}{k_a^g \bar{X}_1} = \frac{\bar{X}_{g-1}}{\bar{X}_g} = e^{-1/2\sigma^2} e^{(g-N)/\sigma^2} \tag{4.12}$$

The concentration ratio between adjacent aggregate sizes varies by a factor of $e^{2\sigma}$ in the range $n \pm \sigma$. Provided the distribution is not too narrow it is further assumed that k_a^g and k_d^g change very little and are assumed equal to k^+ and k^- in the region of proper micelles and that $\bar{X}_g$ and ξ_g change very slowly so that g may be taken as a continuous, differentiable variable.

Under these circumstances, Aniansson and Wall solved the Becker-Döring equations to yield a relaxation time τ_1 corresponding to the rapid monomer release process,

$$\frac{1}{\tau_1} = \frac{k^-}{\sigma^2} + \frac{k^-}{N} a(1+c_0) \tag{4.13}$$

where $a = (X_{tot} - \bar{X}_1)/\bar{X}_1$ is the ratio of surfactant in micelles and free monomers. The term $c_0 = \sum \xi_g \bar{X}_g / \sum \bar{X}_g$, is the average relative deviation from equilibrium which for the conditions of Aniansson and Walls derivation should be less than 1%. Under these conditions c_0 tends to unity. It is inherent in the assumptions made by Aniansson and

Wall that k^- and σ are concentration independent, since the Gaussian is a symmetric form of the micelle size distribution. Under these conditions equation (4.13) suggests that the τ_1 will be inversely proportional to bulk concentration. The average aggregation number N can be measured by light scattering methods or SANS and k^- can also be determined by calculation if one assumes diffusion controlled monomer uptake. It follows that equation (4.13) provides a method for determining the width of the micelle size distribution from measurements of τ_1 as a function of a_r.

4.1.3.3 The Slow Process: Pseudo-stationary flow for small perturbations

The slow process occurs when the monomer concentration is close enough to the cmc that pseudo-equilibrium exists between monomers and abundant micelles. In order to proceed analytically, Aniansson and Wall made a critical assumption, often overlooked in subsequent literature. The cross term in the inner bracket of equation (4.10) $\xi_1\xi_{g-1}$ is negligible if the deviation from equilibrium is sufficiently small. Aniansson and Wall placed a limit on the magnitude of $|\xi_g| < 10^{-2}$, equivalent to adding just 1 ml of pure water to 100 ml of micelle solution. Whilst some temperature jump and pressure jump experiments approach this small perturbation limit, many of the dynamic processes to which the Aniansson and Wall solutions have been applied are much further away from equilibrium.

Equation (4.10) indicates that the rate limiting quantities in the redistribution of material amongst aggregates will be the products $k_d^g \bar{X}_g$ and not just k_d^g as one may expect. After the system reaches pseudo-equilibrium material must be transmitted from the region of proper micelles to the region of monomers via the low concentration intermediate aggregate region. The rate of this process is governed by the resistance to flow through that region.

Consider the aggregation space as consisting of three parts, $1 \le g \le g_1$, $g_1+1 \le g \le g_2$ and $g_2+1 \le g \le g_3$. The conductivities $k_d^g \bar{X}_g$ and the amount of material in the second region are assumed to be much less than that in the two end regions. Provided the deviation is small so that the linearization of equation (4.10) holds, then in the two end regions

$$\xi_g - \xi_{g-1} - \xi_1 = -\frac{J_g}{k_d^g \bar{X}_g} \cong 0 \tag{4.14}$$

whereas in the second region

$$\xi_g - \xi_{g-1} - \xi_1 = -\frac{J}{k_d^g \bar{X}_g} \tag{4.15}$$

where J is practically independent of g during the pseudo-stationary flow. Equations (4.14) and(4.15) relate the relative monomer perturbation ξ_1 to the relative perturbation ξ_{g^*} of any arbitrary aggregation number g^*. For g^* in the region of proper micelles, summing equation (4.14) from $g = 2$ to $g = g_1$, equation (4.15) from $g = g_1 + 1$ to $g = g_2$ and equation (4.14) from $g = g_2 + 1$ to $g = g^*$ gives

$$\xi_{g^*} = g^* \xi_1 - R_{es} J \tag{4.16}$$

where R_{es} is the resistance to flow in region 2

$$R_{es} = \sum_{g>g_1}^{g_2} \frac{1}{k_d^g \bar{X}_g} \tag{4.17}$$

Using the requirement of material balance

$$\sum_{g=1}^{\infty} g \xi_g \bar{X}_g = 0 \tag{4.18}$$

and the assumption that the amount of material in the second region is negligible, Aniansson and Wall related J to m_3, the amount of excess material in the region of proper micelles.

$$J = \frac{\overline{n_1^2} c_1 + \overline{n_3^2} c_3}{R_{es} \overline{n_1^2} c_1 \overline{n_3} c_3} m_3 \tag{4.19}$$

with

$$m_3 = \sum_{g>g_2} g\xi_g \bar{X}_g$$

$$c_1 = \sum_{g=1}^{g_1} \bar{X}_g \qquad c_3 = \sum_{g>g_2} \bar{X}_g \tag{4.20}$$

$$\overline{n_1^2} = \frac{1}{c_1}\sum_{g=1}^{g_1} g^2 \bar{X}_g \qquad \overline{n_3^2} = \frac{1}{c_3}\sum_{g>g_2} g^2 \bar{X}_g \qquad \overline{n_3} = \frac{1}{c_3}\sum_{g>g_2} g\bar{X}_g$$

To derive a differential equation which describes the slow process, Aniansson and Wall noted that on average each micelle added to region three increased the excess material in that region by $\partial m_3 / \partial \sum_{g>g_2} \xi_g \bar{X}_g$ so that

$$\frac{dm_3}{dt} = \frac{\partial m_3}{\partial \sum_{g>g_2} \xi_g \bar{X}_g} J \tag{4.21}$$

Aniansson and Wall then calculated that

$$\sum_{g>g_2} \xi_g \bar{X}_g = \frac{\sigma^2 c_3 + \overline{n_1^2} c_1}{n_3 n_1^2 c_1} m_3 \tag{4.22}$$

where $\sigma^2 = \overline{n_3^2} - \bar{n}_3^2$, the variance of the micelle size distribution. Using equation (4.19) Aniansson and Wall obtained

$$\frac{dm_3}{dt} == \frac{1}{\tau_2} m_3 \tag{4.23}$$

where

$$\frac{1}{\tau_2} = \frac{1}{Rc_3} \frac{\overline{n_1^2} c_1 + \overline{n_3^2} c_3}{\overline{n_1^2} c_1 + \sigma^2 c_3} \tag{4.24}$$

The solution of equation (4.23) is of the common relaxation form $m_3(t) = m_3(0)e^{-t/\tau_2}$ where τ_2 is the relaxation time. In order to extract the characteristic behaviour of these micellar systems a number of further simplifications reduce equation (4.24) into a more manageable form. Provided that dimers, trimers etc. occur only in negligible quantities so that $\overline{n_1^2} \cong 1$ then

$$\overline{n_1^2} c_1 \cong X_1 \tag{4.25}$$

and

$$\bar{n}_3 c_3 = X_{tot} - \bar{X}_1 = X_{exc} \tag{4.26}$$

where X_{exc} is the total amount of surfactant contained within micelles at the cmc. It follows that,

$$\overline{n_3^2} c_3 = (\overline{n_3}^2 + \sigma^2) c_3 \cong \overline{n_3}^2 c_3 = \overline{n_3} X_{exc} \tag{4.27}$$

Finally, provided the bulk concentration is very much higher than the cmc so that $\overline{n_3} X_{exc} >> \bar{X}_1$ then equation (4.24) can be written in the simpler form

$$\frac{1}{\tau_2} = \frac{N^2}{\bar{X}_1} \frac{1}{R_{es}} \frac{1}{1 + \frac{\sigma^2}{n} a} \tag{4.28}$$

Where the earlier notation for $a = (X_{tot} - \bar{X}_1)/\bar{X}_1$ and N rather than $\overline{n_3}$ has been reintroduced (since a symmetric Gaussian distribution has been assumed). Using equation (4.28) one may begin to explore the factors which are expected to influence the relaxation rate among the abundant micelles.

For concentrations well above the cmc such that $a >> 1$the hyperbolically decreasing factor in equation (4.28) is simplified to yield, after rearrangement, $\tau_2 = \bar{X}_1 R \sigma^2 a / N^3$. Since $\bar{X}_1, \sigma$ and N are expected to vary very little above the cmc the most direct influences of bulk concentration are contained within the factors a and R. Whilst a is proportional to bulk concentration the resistance to flow in the intermediate region R depends inversely on the intermediate concentrations $\bar{X}_g$. The resultant concentration dependence of τ_2 is complicated.

4.2. Micelle size distributions and relaxation

The relaxation times predicted within the Becker-Döring (Aniansson and Wall) model above are heavily dependent upon the shape of the micelle size distribution. Of particular interest is the concentration of aggregates with intermediate sizes which exist between pre-micellar aggregates and micelles proper. The absolute concentration of these species

determines the magnitude of the resistance term, R_{es} in equation (4.28), which ultimately governs the slow relaxation time τ_2.

Determination of the form of the aggregate size distribution for different surfactants and different micelle shapes has also been a subject of extensive debate. Since concentrations in the intermediate aggregate region are orders of magnitude smaller than those close to the peak aggregation number there are no direct experimental methods available for their determination. Some authors [32-35, 37, 41] have attempted to extract information about the size distribution from kinetic data using Aniansson and Wall's solutions to their Becker-Döring model. However, since the derivation of their kinetic model assumes a general form for the size distribution it is preferable to try and model the distribution directly.

Using some basic thermodynamics, it is possible to calculate an equilibrium aggregate size distribution from knowledge of the chemical potential differences between monomers in different sized aggregates. There are two theoretical approaches that provide this information, Molecular Dynamics (MD) computer simulations and Molecular Thermodynamic (MT) modelling.

In MD simulations [127-129] large numbers of model surfactant monomers are surrounded by model solvent molecules in a well-defined volume. To reduce complexity and computational demand surfactant structures are often coarse-grained, that is, groups of atoms are approximated by a single bead. Interaction energies between different beads are defined, commonly with Lennard-Jones potentials. Simulations are run for several million iterations with Brownian surfactant motion and the resulting aggregation of the model surfactant molecules provides information about the free energy of the monomers in different sized aggregates.

Molecular thermodynamic modelling [130-133] considers each of the different contributions that make up the total free energy of aggregation. Several authors have published widely in this field, developing increasingly complex models which hold for more complicated surfactants, polymers and solubilisates. Blankschtein [134] recently showed how a combination of molecular dynamics and molecular thermodynamics can provide a more complete picture of aggregation behaviour for even very complex surfactant structures.

In this work, I have followed Nagarajan and Ruckenstein's predictive molecular thermodynamics model, which gives a priori predictions of aggregation behaviour for a

range of surfactants that form small micelles including the nonionic surfactants of the polyoxyethylene glycol alkyl ether family, C_nE_m. [131]

4.2.1 Molecular Thermodynamics of C_nE_m

A necessary first step in understanding the micelle size distribution is to formulate the equations that govern self-assembly in general statistical thermodynamic terms. A surfactant solution is made up of water molecules, singly dispersed surfactant molecules and surfactant aggregates of all possible shapes and sizes. The standard state for water is defined as the pure liquid whilst the states for all other components (aggregates) are defined in the limit of infinite dilution. The important interactions of the surfactant molecules with water are accounted for in the standard states, whilst inter-aggregate interactions are considered negligible for dilute solutions. Equilibrium thermodynamics requires that in such a system the chemical potential of all identical molecules is the same, regardless of which aggregate they are contained within. We may write the following relation

$$\mu_g^{\circ} + kT \ln Y_g = g[\mu_1^{\circ} + kT \ln Y_1] \tag{4.29}$$

where μ_g° is the standard chemical potential of an aggregate containing g surfactant molecules and Y_g is the mole fraction of those aggregates in solution ($X_g \approx 55.Y_g$). Rearranging equation (4.29) yields the aggregate size distribution equation.

$$Y_g = Y_1^g \exp\left(-\frac{g\Delta\mu_g^{\circ}}{kT}\right) \tag{4.30}$$

where the term $\Delta\mu_g^{\circ}$ is the difference in standard chemical potential between a surfactant molecule present in an aggregate of size g and a singly dispersed molecule in water.

$$\Delta\mu_g^{\circ}(g) = \frac{\mu_g^{\circ}(g)}{g} - \mu_1^{\circ} \tag{4.31}$$

The shape of the aggregate size distribution will be governed by the exact functional form of $\mu_g^{\circ}(g)$. For C_nE_m surfactants Nagarajan and Ruckenstein identify six contributions to the $\Delta\mu_g^{\circ}$ term in equation(4.30).

4.2.1.1. Free energy of tail transfer

Upon aggregation the surfactant tail goes from an environment where it is contact with water to the hydrophobic core, which is assumed similar to a liquid hydrocarbon. Using solubility data for hydrocarbon gases along with vapour pressures, Nagarajan and Ruckenstein evaluated the free energy change upon taking an alkane chain from an aqueous phase to a liquid hydrocarbon phase. For a methylene (CH_2) group the transfer free energy is given by

$$\frac{(\Delta\mu_g^{\circ})_{tr}^{CH_2}}{kT} = 5.85\ln T + \frac{896}{T} - 36.15 - 0.0056T \tag{4.32}$$

where T is the temperature in Kelvin. The corresponding expression for a a methyl (CH_3) group is

$$\frac{(\Delta\mu_g^{\circ})_{tr}^{CH_3}}{kT} = 3.38\ln T + \frac{4064}{T} - 44.13 + 0.02595T. \tag{4.33}$$

This large, negative contribution is the major driving force for the formation of aggregates. Note that the free energy of tail transfer is independent of aggregate size. For a surfactant tail containing n_c carbon atoms the total free energy of tail transfer is given by

$$\frac{(\Delta\mu_g^{\circ})_{tr}}{kT} = (n_c - 1)\frac{(\Delta\mu_g^{\circ})_{tr}^{CH_2}}{kT} + \frac{(\Delta\mu_g^{\circ})_{tr}^{CH_3}}{kT} \tag{4.34}$$

4.2.1.2. Free energy of surfactant tail deformation

Although similar, the micelle core is not identical to a liquid hydrocarbon because one end of the surfactant tail is constrained to remain at the core/shell interface, whilst the entire tail has to assume a conformation consistent with a uniform density equal to that of the liquid hydrocarbon. This conformational constraint is associated with a positive free energy contribution. Nagarajan and Ruckenstein used a lattice model for the micelle core to evaluate the free energy associated with the nonuniform deformation.

For a spherical, ellipsoidal and rodlike micelle the deformation free energy terms are

$$\frac{(\Delta\mu_g^*)_{def}}{kT} = \begin{cases} \frac{3\pi^2}{80}\frac{R_c^2}{PL^2}, & \text{(sphere)} \\ \frac{5\pi^2}{80}\frac{R_c^2}{PL^2}, & \text{(ellipsoid)} \\ \frac{10\pi^2}{80}\frac{R_c^2}{PL^2}, & \text{(rod)} \end{cases} \tag{4.35}$$

where R_c is the radius of the micelle core, L is the dimension of the lattice site and P is the number of lattice sites required to accommodate one surfactant chain. The use of a lattice requires the specification of the size of the molecular segment which can be placed on the lattice without any orientational constraints. Nagarajan and Ruckenstein used a segment containing 3.6 methylene groups and a linear lattice dimension L of 4.6 Å. Since a methyl group is roughly twice the volume of a methylene group, the total number of segments P in a surfactant tail is given by $(n_c+1)/3.6$.

4.2.1.3 Modelling head group interactions

Nagarajan and Ruckenstein developed two limiting models for the micelle shell region both based on a lattice representation of the shell. Both models developed treat the micellar shell region as a polymer solution containing poly(oxyethylene) chains and water. The differences in free energy per molecule of a poly(oxyethylene) chain contained in the micellar shell and one present as an isolated coil in water provide additional contributions to the free energy of micellisation. These contributions are computed by considering the free energy of mixing of polymer segments with water as well as the free energy of polymer chain deformation.

In Model A the shell region has a uniform concentration of polymer segments and therefore a non-uniform radial deformation profile. In Model B the polymer chains have a uniform deformation and non-uniform radial concentration profile. For the surfactants of interest in this work, Model A gives the most accurate predictions of cmc and aggregation number and is briefly reviewed below.

4.2.1.4. Changes in polymer –solvent mixing free energy

A mean field approach is used to calculate the change in the free energy of mixing of the poly(oxyethylene) head group and water when an isolated free polymer coil is transferred to the micellar shell. In this uniform concentration model the segment density of polymer

chains $\phi(r)$ is a constant, independent of the radial coordinate, represented by ϕ_{Eg} and is given by

$$\phi(r) = \phi_{Eg} = g(ML^3 / V_{sh}) \tag{4.36}$$

where M is the number of lattice sites required to accommodate a single headgroup and V_{sh} is the volume of the shell region. Because of the interactions between the segments of a single molecule with the segments of all other molecules, each molecule experiences a potential $U(r)$ that is proportional to the segment density in the shell. The mean potential per molecule $U(r)$ can be written as

$$U(r) = kT\phi(r)(\tfrac{1}{2} - \chi_{wE}) \tag{4.37}$$

where χ_{wE} is the Flory-Huggins type interaction parameter for the water-polyethylene system. The total change in the mixing free energy for an isolated polymer coil transferred to a micellar shell region is given by;

$$\frac{(\Delta\mu_g^{\oplus})_{mix,E}}{kT} = \frac{1}{g}\frac{1}{L^3}\int_{R_c}^{R_c+D}\phi(r)\frac{U(r)}{kT}2\pi r\,dr = M\phi_{Eg}(\tfrac{1}{2} - \chi_{wE}) \tag{4.38}$$

where R_c refers to the location of the core-shell interface and D is the shell thickness (R2 in chapter 3).

4.2.1.5. Headgroup deformation free energy

The approach to calculating the deformation free energy of the headgroup is the same as for the hydrocarbon tail, summing local deformations and minimising the total energy subject to constraints. For a spherical micelle

$$\frac{(\Delta\mu_g^{\oplus})_{def,E}}{kT} = \frac{3}{2}\frac{LR_c}{a_g\phi_{Eg}}\left[\frac{D}{D+R_c}\right], \tag{4.39}$$

where a_g is the area per molecule at the core-shell interface.

4.2.1.6. Headgroup steric interaction free energy

The interactions among poly(oxyethylene) groups has already been accounted for in the previous two contributions. A minor additional contribution arises from the steric repulsions at the sharp micelle core/shell interface. This contribution can be calculated using a van der Waals approach giving

$$\frac{(\Delta\mu_g^{\circ})_{steric}}{kT} = -\ln\left(1-\frac{a_p}{a_g}\right) \tag{4.40}$$

where a_p is the hard core cross sectional area of a polymer segment, taken to equal L^2.

4.2.1.7. Aggregate core-water interfacial free energy

The formation of surfactant aggregates generates an interface between the micelle core and the micelle shell containing polymer segments and water. The free energy associated with this interface is calculated as the product of interfacial area per molecule a_g and interfacial tension of that interface σ_g.

$$\frac{(\Delta\mu_g^{\circ})_{\text{int}}}{kT} = \frac{\sigma_g}{kT}(a_g - a_{sh}) \tag{4.41}$$

where a_{sh} is the area per molecule shielded from contact with water by the headgroup. For polyoxyethylene surfactants a_{sh} is also taken to equal L^2.

For surfactants with compact headgroups we could take σ_g to be the interfacial tension between a hydrocarbon and water. For surfactants with poly(oxyethylene) head groups one must recognise that the interface is that between a liquid hydrocarbon and a polymer/water mixture. Nagarajan and Ruckenstein use the Prigogine theory to calculate the surface tension between polymer solutions and an immiscible liquid.

4.2.1.8. Computational method

Molecular thermodynamic calculations are performed using the Matlab computational package. The difference in chemical potential between a free monomer and a monomer contained within an aggregate is evaluated over a wide range of aggregation space, from

g = 1 up to g = 400. The total chemical potential difference is given by the sum of the contributions described above.

$$\frac{(\Delta\mu_g^{\oplus})_{total}}{kT} = \frac{(\Delta\mu_g^{\oplus})_{tr}}{kT} + \frac{(\Delta\mu_g^{\oplus})_{def}}{kT} + \frac{(\Delta\mu_g^{\oplus})_{mix,E}}{kT} + \frac{(\Delta\mu_g^{\oplus})_{def,E}}{kT} + \frac{(\Delta\mu_g^{\oplus})_{steric}}{kT} + \frac{(\Delta\mu_g^{\oplus})_{\text{int}}}{kT} \quad (4.42)$$

These chemical potential terms are dependent on molecular structure along with aggregate size and shape. In order to find the most feasible aggregate shape at different aggregation numbers the chemical potential variation must be evaluated for a range of shapes and then compared. The shapes I have compared are spheres, rods with spherical end-caps and spheres with a cavity at the centre. In each case a basic knowledge of surfactant monomer dimensions and hydration is required to calculate the core volume and shell volume at each aggregation number.

Chemical potential variation in spherical aggregates

Calculation of chemical potential variation for a spherical structure is the most straightforward application of the equations derived by Nagarajan and Ruckenstein. In order to begin calculating micelle dimensions I used Tanford's equations (3.51) and (3.52) for the maximum volume, V_t, and extended length, L_t, of a carbon chain containing n_c carbon atoms;

For $C_{12}E_8$ the maximum hydrocarbon chain length and tail volume are 16.7Å and 350 Å^3 respectively. Micelle core volume $V_c(g)$ is calculated using $V_c(g) = g.V_t$ and it follows that the micelle core radius is given by $R_c(g) = (3V_c / 4\pi)^{1/3}$. Headgroup volume V_h is evaluated for a hydrated polymer chain using a volume per ethylene oxide unit $V_{EO} = 63$ Å^3 and volume per water molecule $V_{water} = 30.2$ Å^3. The precise number of water molecules per ethylene oxide unit was varied in the range 1 – 6 and found to have a small influence on the chemical potential curve and calculated cmc and peak aggregation number (see below). I found that a value of 3 water molecules per ethylene oxide unit gave the best-fit physical parameters. The volume of the surfactant shell $V_{sh}(g)$ is therefore given by $V_{sh}(g) = g.V_h = g.m(63+90.6)$ Å^3 where m is the number of ethylene oxide units per monomer. The total micelle radius is $R_g(g) = (3(V_c + V_{sh}) / 4\pi)^{1/3}$ and the shell thickness $D(g) = R_g - R_c$. The area per molecule at the core-shell interface is found

using $a_g(g) = 4\pi R_c^2 / g$. Additional parameters required for the use of equations (4.34) - (4.41) are the lattice dimension L = 4.6 Å and the Flory-Huggins interaction parameter $\chi = 0.5$.

Chemical potential variation in spherical aggregates with a spherical cavity.

The spherical micelle model can only be applied up to the point that the core radius exceeds the maximum extended length of the hydrocarbon tail $R_c > L_t$. For larger aggregation numbers alternative structures must be used. One possible structure is a sphere with a cavity at the centre. Mathematically this may be treated by the introduction of an additional term into equation (4.42) to account for the air-oil interface which exists within the micelle. The chemical potential due to the spherical cavity is

$$\frac{(\Delta\mu_g^{\circ})_{cav}}{kT} = \frac{\sigma_{air-oil}}{kT}(a_{cav}) \tag{4.43}$$

where $a_{cav}(g) = 4\pi(R_c - L_t)^2 / g$ and $\sigma_{air-oil}$ is the interfacial tension of the oil corresponding to the surfactant tail structure. It should be noted that in reality a micelle with a cavity at its centre will probably relax to an ellipsoidal structure.

Chemical potential variation in rodlike aggregates with spherical end-caps.

For very large aggregation numbers micelles may begin to elongate, forming rodlike structures. I have considered the case where a micelle, upon reaching the limiting sphere where $R_c = L_t$, begins to elongate with spherical end-caps identical to the hemi-spheres of the limiting sphere and an additional cylindrical region which extends.

Computationally the two different regions of the micelle are treated independently with the total chemical potential variation per surfactant monomer found as a weighted average using

$$\frac{(\Delta\mu_g^{\circ})_{total}}{kT} = \frac{g_{end}}{g}\frac{(\Delta\mu_g^{\circ})_{end}}{kT} + \frac{g_{cyl}}{g}\frac{(\Delta\mu_g^{\circ})_{cyl}}{kT} \tag{4.44}$$

where the subscript *'end'* and *'cyl'* denote the endcaps and cylindrical regions respectively. Both of the terms $(\Delta\mu_g^{\circ})_{end}$ and $(\Delta\mu_g^{\circ})_{cyl}$ contain all of the contributions shown in equation (4.42) and explained above.

For aggregation numbers below the limiting value the $g_{end} = g$ and $g_{cyl} = 0$. Once the limiting sphere is reached the properties of the end-caps remain fixed and all additional monomers are taken up into the cylindrical region. If the core volume and radius of the limiting sphere are $V_{c,\lim}$ and $R_{c,\lim}$ then the core volume of the cylindrical region is given by $V_{c,cyl} = V_c - V_{c,\lim}$ and the length of the cylindrical region by $L_{cyl} = (V_{c,cyl}) / (\pi R_{c,\lim}^2)$ since the radius of the cylinder is fixed at the radius of the limiting sphere. The area per molecule at the core-shell interface in the cylindrical region is calculated using $a_{cyl} = (2\pi R_{c,\lim} L_{cyl}) / g_{cyl}$. The only additional complication is the evaluation of shell thickness which is assumed constant over the whole micelle surface and can be evaluated by solving the corresponding cubic equation for aggregate volume with a boundary condition on total aggregate volume for each aggregation number.

Using these new parameters equations (4.32) - (4.44) yield the chemical potential variation for rodlike micelles with spherical end-caps.

4.2.1.9 A comparison of different structures.

Figure 20 shows the difference in monomer chemical potential relative to an isolated free monomer in water for a range of aggregate sizes and shapes in the case of $C_{12}E_8$. For aggregation numbers less than 55 the spherical core radius is less than the limiting value and all modelling outputs reduce to the perfect sphere case. For larger aggregation numbers it is evident that a rodlike micelle structure is most favourable. The introduction of a spherical cavity at the micelle centre does not provide any improvement relative to the rod structure. Therefore I will focus on a spherical structure which transitions to a rod at large aggregation numbers.

The precise aggregation number at which the spherical chemical potential becomes more positive than the rodlike chemical potential may be denoted by the symbol g_{trans}. The sphere and rod chemical potential curve are matched in region of $g_{trans} \pm 10$ using a fifth order polynomial fitted to the spherical data for aggregation numbers between $g_{trans} - 20 < g < g_{trans} - 10$ and the rod data for $g_{trans} + 10 < g < g_{trans} + 20$. Figure 21 shows this data replotted to highlight the matching curve in the region between spheres with a hole and rods.

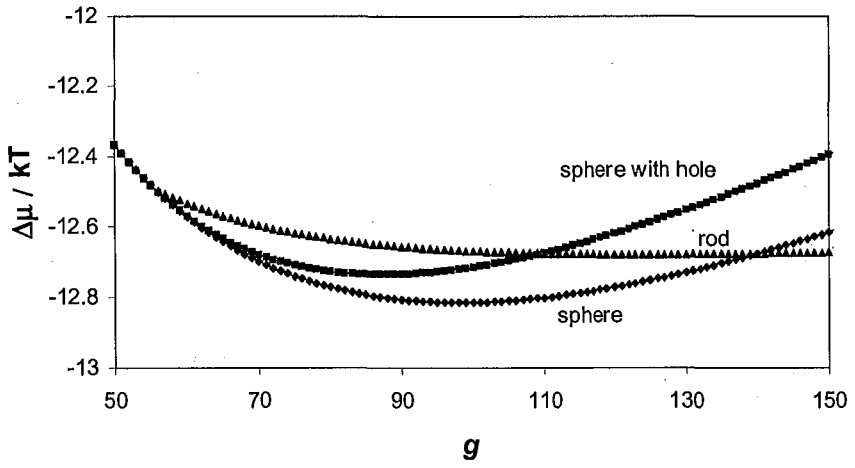

Figure 20: Chemical potential variation for monomers contained within different aggregate sizes using three different model structures. (♦) sphere, (■) sphere with a hole and (▲) rod.

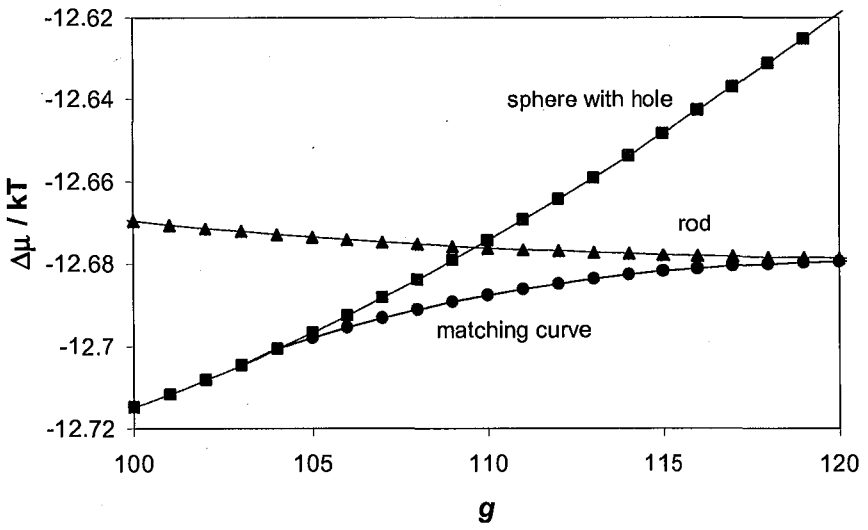

Figure 21: Chemical potential variation for monomers contained within different aggregate sizes plotted to show the matching curve (•) in the crossover region between (■) a sphere with a hole and (▲) rods. using three different model structures.

4.2.1.10. Problems with the model for small aggregation numbers

As can be seen in Figure 20 the chemical potential difference for very low aggregation numbers is positive. Using equation (4.42) to sum the contributions gives a non-zero chemical potential difference between a free monomer and an aggregate containing $g = 1$ monomers, which cannot be the case. It is a failing of the Nagarajan and Ruckenstein model that for aggregates containing less than 5 monomers it is unlikely that a core/shell

aggregate model is an accurate description of the structure assumed in water. As a result of this description the interfacial energy contribution is more positive than the tail transfer free energy is negative for monomers and to a small extent dimers. This error is of the order 5 *kT*. In order to give a physically realistic description of the chemical potential in this region of the curve I use a fifth order polynomial to force a smooth transition between the curve zero and the calculated data at $g = 5$.

In the following section I show that the MT model gives good agreement with experimental values of the cmc and aggregation numbers; it therefore works well in the region of proper micelles. I do not know precisely how small an aggregate needs to be before the MT model begins to contain errors. I will show later that the critical aggregate size for micelle breakdown kinetics contains : 15 – 20 monomers which can plausibly be treated with the MT model. Nevertheless, errors in the model may overestimate the chemical potential in this region.

4.2.2. Chemical Potentials of $C_{12}E_8$

Using the approach described above the chemical potential of a monomer in an aggregate of size *g* relative to the free monomer may be calculated.

Figure 22 shows the difference in standard chemical potential between a surfactant molecule present in an aggregate of size *g* and a singly dispersed molecule in water. For small aggregation numbers the initially rapid decrease in the area per molecule at the core-shell interface results in a rapid stabilisation of aggregates and decrease in the resultant free energy. At higher aggregation numbers the area per molecule changes more slowly with *g* and the increased packing constraints, which affect mixing, deformation and steric repulsion lead an increase in the total free energy and the shallow minimum that is observed.

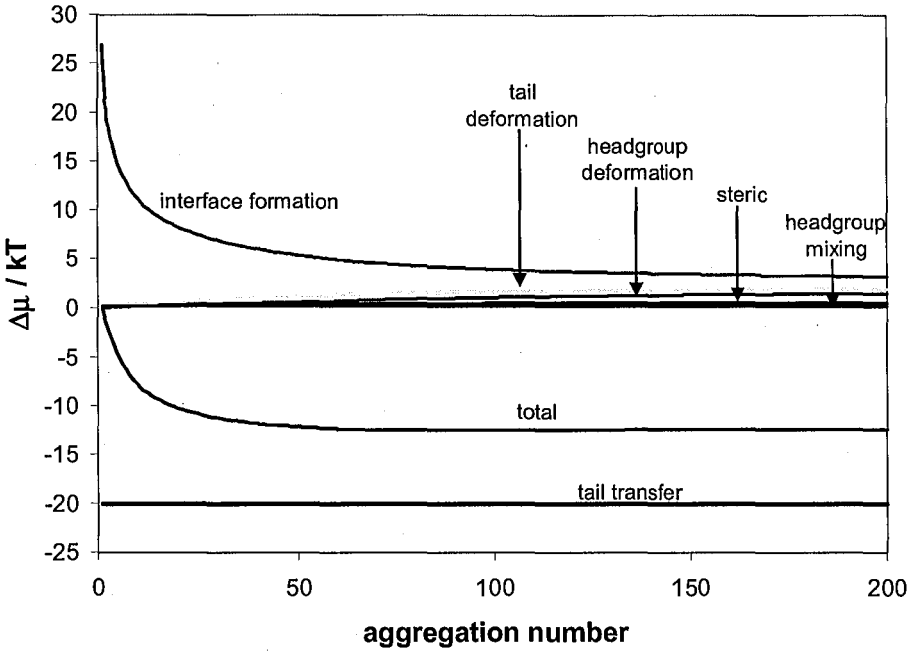

Figure 22: The difference in standard chemical potential between a surfactant molecule present in an aggregate of size *g* and a singly dispersed molecule in water. All calculated contributions are shown.

4.2.2.1. Critical Micelle concentration

The cmc can be determined experimentally as that value of total surfactant concentration at which a sharp change in a physical property is observed, commonly the equilibrium surface tension. In terms of the micelle size distribution we must have a more precise definition. In this work we define the cmc to be that value of monomer concentration X_1 at which the concentration of singly dispersed monomers is equal to the concentration of surfactant in aggregate form, that is

$$X_1 = \sum_{g=2}^{g_{max}} gX_g = X_{cmc} \tag{4.45}$$

The calculated critical micelle concentration for $C_{10}E_8$, $C_{12}E_8$ and $C_{14}E_8$ are in close agreement with experimental values. (Table 15).

	CALCULATED		LITERATURE	
	CMC /MM	N	CMC / MM	N
$C_{10}E_8$	1.7	61	1	60
$C_{12}E_8$	0.13	79	0.071	80
$C_{14}E_8$	0.009	98	0.009	105

Table 15 – Comparison of predicted micelle properties with actual values (aggregation numbers are peak values at bulk concentrations of 4-mM at T=298K with 3 water molecules per EO unit).

4.2.2.2 Size distribution and aggregation number

The total chemical potential variation may be converted into an aggregate size distribution using equation (4.30) with a boundary condition on the total amount of material present in the system,

$$\sum_{1}^{g_{max}} g.X_g = c_b \tag{4.46}$$

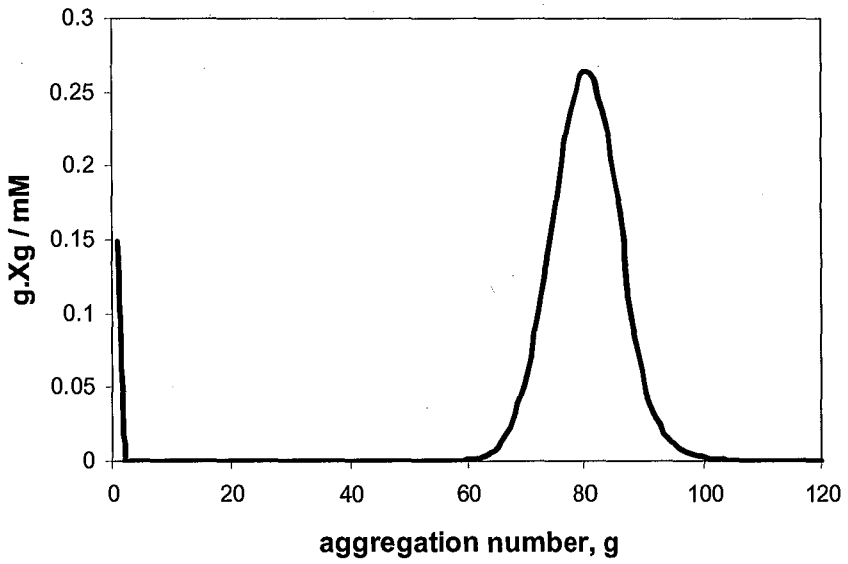

Figure 23: Calculated size distribution for a 4-mM solution of $C_{12}E_8$.

The calculated size distribution for a 4-mM solution of $C_{12}E_8$ is shown Figure 23. The y-axis plots the concentration of aggregates multiplied by the corresponding aggregation number to give the absolute concentration of surfactant in a given aggregation state. There are four clearly defined regions; monomers, intermediate aggregate sizes ($2 \leq g \leq$

60), proper micelles ($61 \leq g \leq 100$) and large aggregates ($g \geq 101$). The first three regions are those required for the application of Aniansson and Walls model. Figure 24 re-plots the data in Figure 23 using a log-scale to show the large variation in the concentrations for aggregates of intermediate size. The concentrations of some intermediate aggregates are 16 orders of magnitude less than the concentration of aggregates at the peak of the micelle size distribution. The peak aggregation numbers for $C_{12}E_8$ along with $C_{10}E_8$ and $C_{14}E_8$ are also in very close agreement with those values determined from SANS and are shown in Table 15.

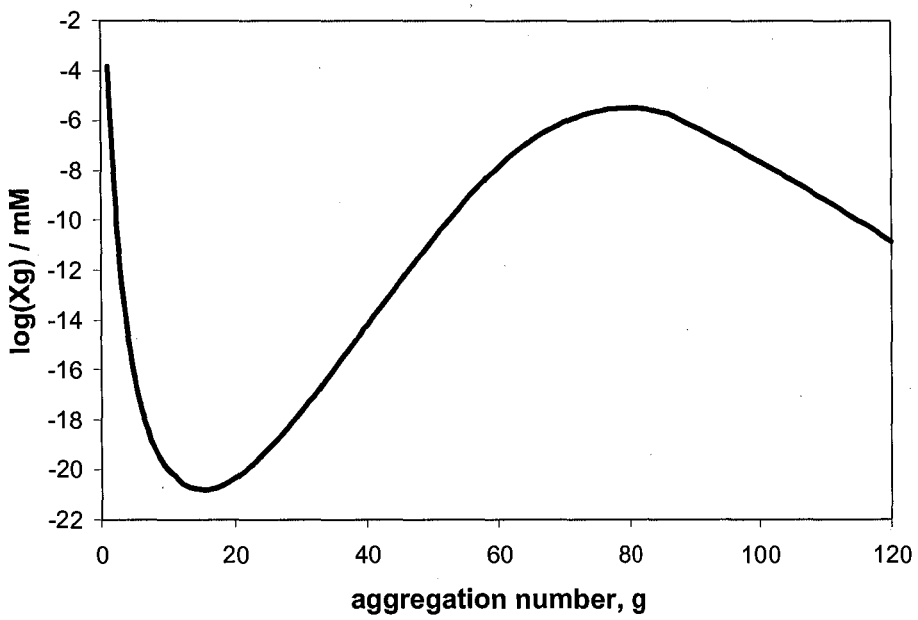

Figure 24: Concentration of $C_{12}E_8$ aggregates plotted on a log-scale

4.2.3. Rate constants for monomer uptake and loss

If we are to proceed with a kinetic analysis based upon this size distribution we must first calculate rate constants for the association and dissociation of monomers. Based on ultrasonic adsorption studies [45, 51] it is expected that the uptake of monomers into micelles will proceed at a close to diffusion controlled rate which is given by

$$k_a^g = 4000 N_A \pi (D_g + D_1)(R_g + R_1); \qquad (4.47)$$

where N_A is Avagadro's number, R_g is the effective radius of an aggregate containing g monomers and D_g is the aggregate diffusion coefficient calculated using Stokes-Einstein

where $D_g = kT/(6\pi\mu R_g)$. Assuming diffusion control provides an upper bound on all calculate rate constants. Dissociation rate constants k_d^g can be calculated from the association rate constants by applying the equilibrium relation

$$K = \frac{k_a^g}{k_d^g} = \frac{[\bar{X}_1][\bar{X}_g]}{[\bar{X}_{g+1}]} \tag{4.48}$$

where the barred values denote equilibrium concentrations. The calculated values of k_a^g and k_d^g for surfactants C_nE_8 (n=10, 12 and 14) are shown in Figure 25 and Figure 26. Note the discontinuity in the slope of k_d^g which is due to the matching of the chemical potential curves for the sphere with a hole and rodlike micelle model. This discontinuity has no effect on the kinetic conclusions drawn later since k_d^g is almost constant in this region.

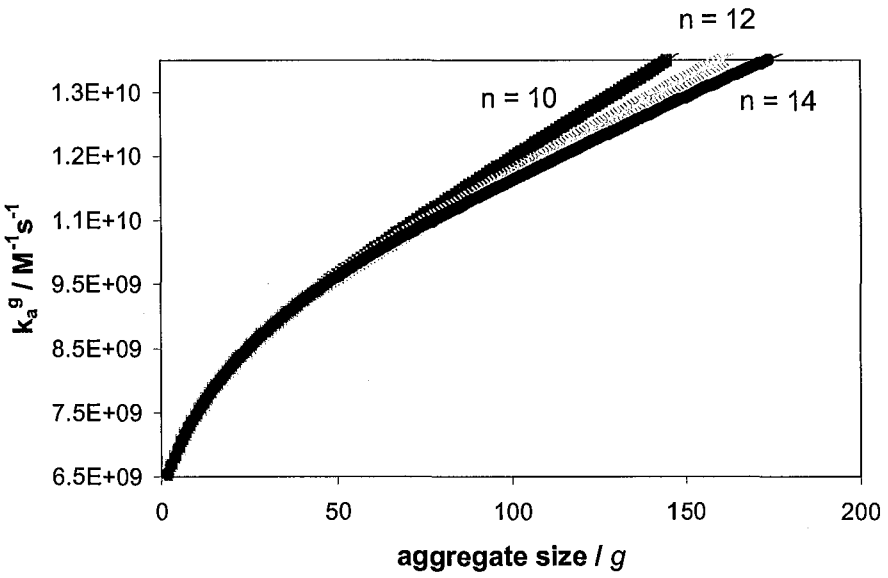

Figure 25: Association rate constants for monomer uptake to micelles of C_nE_8 with n=10, 12 and 14

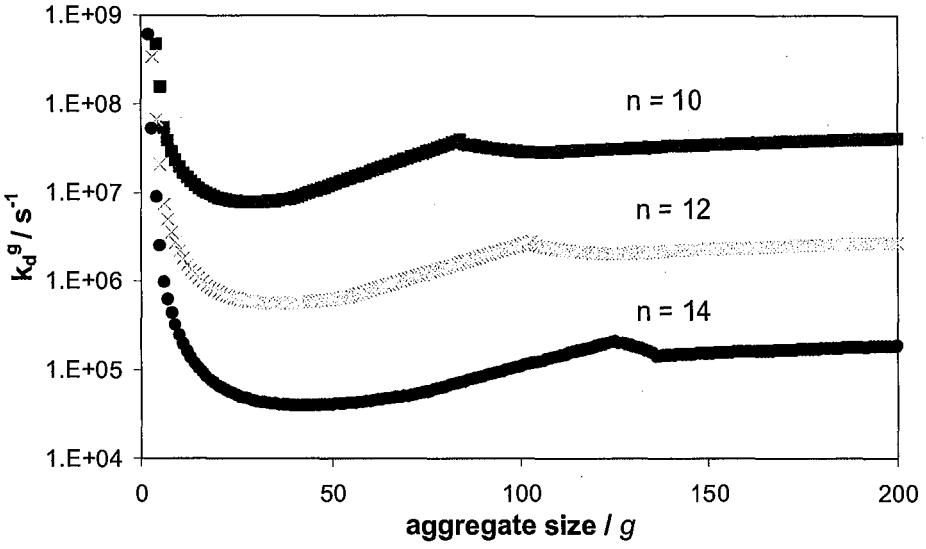

Figure 26: Dissociation constants for monomer loss from micelles of C_nE_8 with n=10, 12 and 14

4.2.4 Calculation of breakdown times using the Becker-Döring model

The size distribution in Figure 23 may be related directly to the micelle relaxation times dervied by Aniansson and Wall with equations (4.13) and (4.28). These relaxation times describe how a micelle system perturbed by a very small amount (< 1%) will relax back to equilibrium. For a 4-mM solution of $C_{12}E_8$ the expected relaxation times are 16 μs and 3.7×10^8 s for τ_1 and τ_2, respectively.

The first relaxation time τ_1 represents the recovery of the monomer concentration through a series of individual monomer releases from all micelles, resulting in a system containing an unchanged number of slightly smaller micelles. We expect the timescale for this process to be similar to the timescale for individual monomer release, which for $C_{12}E_8$ is roughly 1 μs.

The second relaxation time τ_2 represents a reduction in the number of micelles with some micelles breaking down entirely while others consume the monomers released. The experimental results discussed in section 4.1 indicate that this 'slow' process occurs approximately three orders of magnitude slower than the 'fast' process. My calculations reveal a process which occurs on the timescale of 10 years. This value is in line with the work of Nyrkova and Semenov who predicted such long timescales for block copolymer micelles based on their nucleation theory approach. [125]

Based on the size distribution, the concentration in the intermediate aggregate region is up to 16 orders of magnitude less than the concentration in the two end regions. Figure 24 plots the aggregate concentration on a log-axis to emphasise this difference. Resistance to material flow through the region of intermediate aggregates is related to these concentrations; therefore a high resistance to flow between the two end regions is expected. The calculated value of τ_2 reflects the high energy penalty incurred to produce the intermediate aggregates required for breakdown by a Becker-Döring mechanism.

It is significant that these calculated times differ so markedly from experimental values of τ_2. For instance, Patist *et al* give τ_2 values for a range of nonionic surfactants derived from stopped-flow measurements all of which lie in the range 0.1 – 10 seconds. [120] In the next section I present the results of some numerical simulations which provide greater insights into the Becker-Döring model and why it is unlikely that such a model will ever allow micelle breakdown on the second's timescale.

4.2.5. Size distributions from other sources

In the previous section I discussed that values of τ_2 calculated based upon my micelle size distributions and the results of Aniansson and Wall were more than 8 orders of magntiude longer than experimental values reported by other authors. Before proceeding with my analysis I will address the question, how can one be certain that these size distributions are an accurate (or even approximate) description of reality?

My micelle size distribution stems directly from the calculated chemical potential difference between free monomers and aggregates shown in Figure 22. Alternative sources of such data are available from molecular dynamics simulations. Mohan and Kopelvich [129] have investigated the formation and disintegration of spherical non-ionic micelles using molecular dynamic simulations. Their surfactant model is a coarse-grained structure, H_4T_4, with properties similar to the polyoxyethylene alkyl ether surfactant $C_{16}E_8$. A pre-requisite to any kinetic study is an understanding of the micelle size distribution. The relevant chemical potential data are shown in Figure 27. There is a very close similarity in shape between their curve and the total curve shown in Figure 22. If one were to calculate a size distribution for 4-mM $C_{16}E_8$ based upon Mohan and Kopelvich's chemical potential curve one find concentrations in the intermediate aggregate region as low as 10^{-30} mol dm^{-3}.

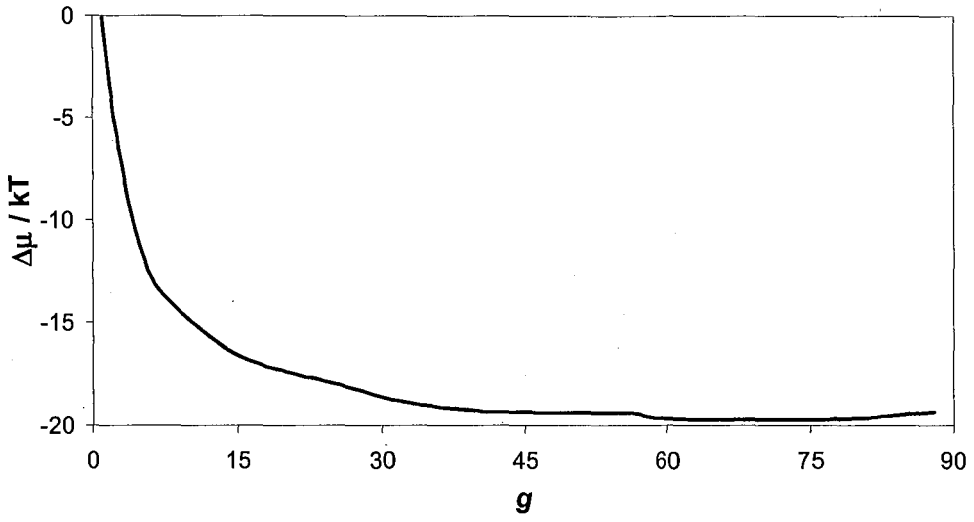

Figure 27: The difference in standard chemical potential between a surfactant molecule present in an aggregate of size *g* and a singly dispersed molecule in water of the model surfactant H4T4 derived using molecular dynamic simulations.

Further support for the calculated chemical potentials is the close agreement between the calculated aggregation numbers and critical micelle concentrations for the C_nE_8 systems of interest in this work and shown in Table 15.

In section 4.2.1.10 I discussed potential problems with the chemical potential curve in the region of small aggregates which lead to an overestimation of aggregate chemical potential. Below, in section 4.3.3 I present a transition state theory treatment which shows that the chemical potential of aggregates containing 15-20 monomers have a large influence on the rate of micelle breakdown. Whilst it is unlikely, it is possible that chemical potential estimates persist into this aggregate size region. Placing a value of : $1kT$ on this overestimate, giving a total difference in chemical potential of a twenty-mer of : $20kT$ would change the rate of micelle breakdown by a factor of: 10^8. This change is highly unlikely. In the next chapter I will show an alternative mechanism for micelle breakdown. The rest of the chapter explores the Becker-Döring route in more detail using numerical simulation techniques.

4.3. Numerical simulations of Becker-Döring breakdown

The analytical solutions solutions derived by Aniansson and Wall for the Becker-Döring breakdown scheme have only limited applicatibility due to the restrictive assumptions made during their derivation. Of particular importance is the assumption that the perturbation from equilibrium is a small one. This restriction is a direct result of linearising the differential equations to allow analytical solution. Semonov and Nyrkova [125] avoided this restriction by focusing on the free energy curves and using nucelation theory. Here, we initially take an alternative approach and use numerical modelling to examine the Becker-Döring model more closely. Through numerical modelling one may also avoid restrictions on perturbation amplitude. Given the magnitude of the slow relaxation time calculated above, I seek to answer the question "how do micellar systems return to equilibrium following a large and rapid dilution"?

4.3.1. A complete Becker-Döring simulation

The experiment that I simulate is the instantaneous dilution of a micellar surfactant solution of bulk concentration c_b by a dilution factor Dil to yield a solution with bulk concentration c_b / Dil. Upon dilution the concentration of all species is reduced. To establish the new equilibrium state there must be a net breakdown of micelles to replenish the depleted monomers. Inputs required are the initial and final state size distributions, which are calculated following the molecular thermodynamics approach described above, along with the rate constants for association and dissociation determined by equations (4.47) and (4.48).

I coded an explicit form of the Becker-Döring system of differential equations (4.5) and (4.6) into Matlab. I used a backward difference scheme to step the aggregate size distribution forward in time, tracking how the concentrations of each species change.

Figure 28 shows the time evolution of the size distribution in the region of proper micelles. The first movement is to smaller aggregation numbers with all micelles releasing a small number of monomers and partially replenishing the monomer concentration. This monomer recovery process is that described by τ_1 and occurs on the timescale predicted by Aniansson and Wall of 20 μs. Figure 29 shows how rapidly the monomer concentration recovers in this case. Once the monomer concentration approaches 90% of the cmc (after roughly 70 μs real time) further monomer release

ceases. After the first 300 μs (in real time) the aggregate size distribution also ceases to change significantly. The simulation does not reach equilibrium on any computable timescale. The simulations therefore confirm the conclusions of the Aniansson and Wall model, that a Becker-Döring model cannot explain micelle relaxation times.

The reason for the failure to establish equilibrium within a Becker-Döring scheme is the high resistance encountered in transferring material from the region of proper micelles to monomers. This barrier reflects the high energy of the intermediate aggregates.

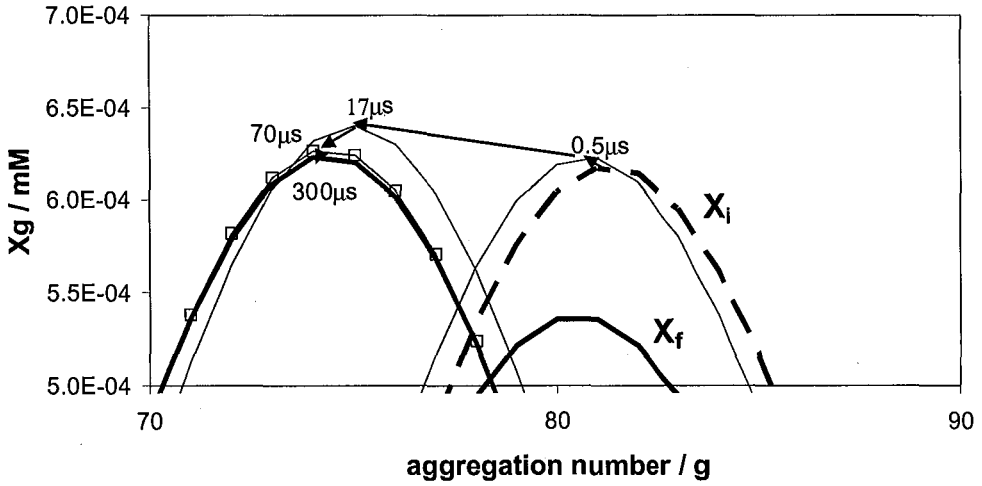

Figure 28: The time evolution of the aggregate size distribution for an 0.8-mM $C_{12}E_8$ solution produced by an instantaneous 5-fold dilution of a 4-mM solution.

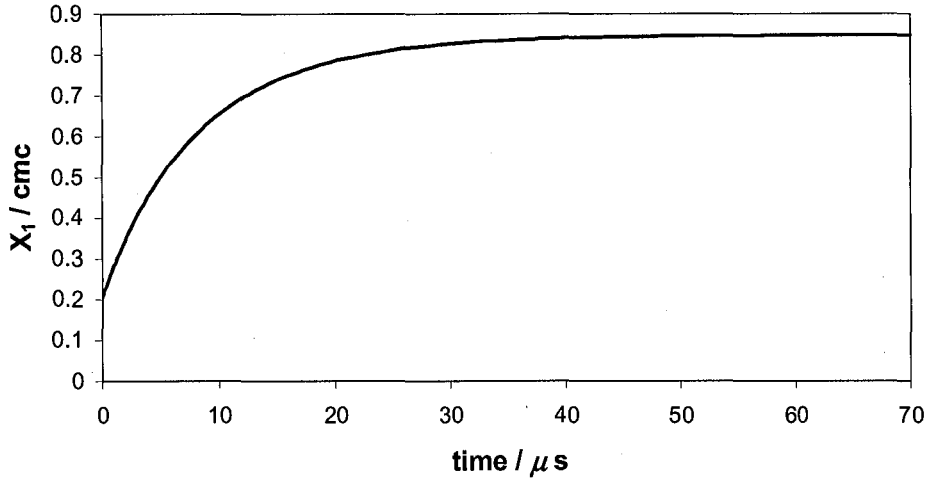

Figure 29: Monomer recovery in a 0.8-mM $C_{12}E_8$ micellar system produced through an instantaneous 5-fold dilution of a 4-mM solution.

4.3.2 Stochastic Simulations

Another way of explaining the barrier to a Becker-Döring mechanism uses stochastic reasoning. In order for a micelle of size g to completely breakdown it must lose g-1 monomers in succession. Rather than attempting to simulate changes in the entire size distribution I will track changes in the aggregation number of a single aggregate. If the probability of monomer uptake and loss were equal then changes in aggregation number would follow a random walk trajectory. A micelle of size N would take $\approx N^2$ steps reach the state $g = 1$. In a real micellar system the probability of monomer uptake and loss is not equal but varies for each aggregate and is dependent on monomer concentration. Numerical simulation techniques are required to follow changes in aggregation number.

I performed a stochastic modelling procedure in Matlab, based on my molecule thermodynamic size distributions, to track changes in the aggregation state of individual aggregates for systems containing different amounts of free monomer. Rate constants for monomer uptake and loss were calculated using equations (4.47) and (4.48). The probability of monomer uptake, P_g^+, by a micelle of size g in time interval Δt is

$$P_g^+ = X_1 k_a^g \Delta t \tag{4.49}$$

and the probability of monomer loss, P_g^-, is

$$P_g^- = k_d^g \Delta t . \tag{4.50}$$

which holds provided the time interval Δt is short enough such that there is a negligible probability of more than one event occurring in time Δt. I chose Δt such that P_g^+ and P_g^- < 0.1. The initial aggregation state was taken to be the peak aggregation number. A random number (rand) between 0 and 1 was generated. For a given monomer concentration X_1 and time interval Δt if rand < P_g^- the aggregate lost a monomer, if rand > $1-P_g^+$ the aggregate gained a monomer and if $P_g^- \leq$ rand $\leq P_g^+$ the aggregation state remained unchanged for that iteration.

These simulations were performed one hundred times at each value of X_1 for which a simulation could be run in a sensible timescale (< 1 hour), and for a range of surfactants.

The number of steps s_{count} required to reach the state g = 1 was recorded for 100 simulations. A typical distribution of the number of steps required is shown in Figure 30. Rather than multiply the mean number of steps $\bar{s}_{count}$ by the time interval Δt to give average micelle lifetime $\bar{t}_{mic}$, which would place a greater weighting on the outlying large values, an alternative calculation is performed using the reciprocals of s_{count}. Average micelle lifetime is given by

$$\bar{t}_{mic} = \Delta t / \frac{\sum \frac{1}{s_{count}}}{100} \tag{4.51}$$

These lifetimes for a range of surfactants are shown in Figure 31 vs. monomer concentration standardised to a percentage of cmc. The rapid increase in micelle lifetimes with monomer concentration leads to prohibitive simulation times and all lifetimes which can be sensibly elucidated are shown in Figure 31.

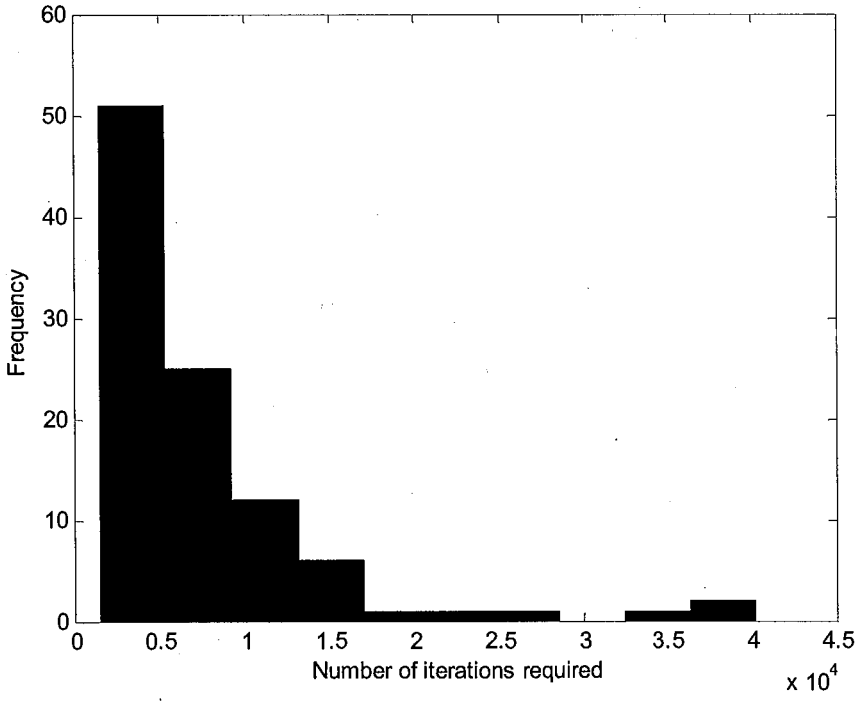

Figure 30: Histogram showing the distribution of the number of iterations required to simulate micelle breakdown in $C_{12}E_8$ systems containing monomer at 50% cmc –repeated 100 times.

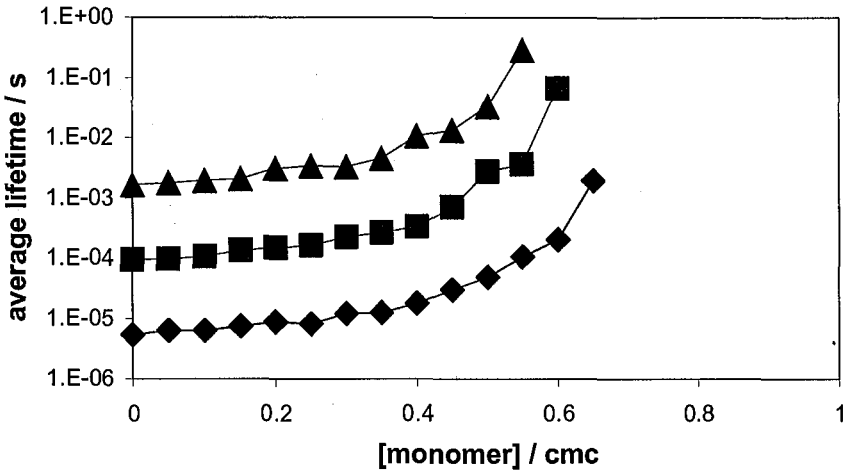

Figure 31: Micelle lifetimes for a range of C_nE_m surfactants as a function of monomer concentration as calculated by a random walk simulation. (♦) $C_{10}E8$, (■) $C_{12}E8$ and (▲) $C_{14}E_8$. Lines are drawn to guide the eye.

Figure 31 demonstrates some very interesting aspects of micelle kinetic behaviour. That micelle lifetime increases by approximately one order of magnitude with an increase in surfactant chain length by 2 carbon units is not unsurprising since k_d^g values are inversely proportional to the cmc and the cmc decreases by approximately a factor of 10 for each addition C_2H_4 unit in the hydrocarbon chain. Figure 31 also shows that micelle lifetime is a strong function of local monomer concentration. In the low monomer concentration limit micelle lifetimes approach the limit of Nk_d^g where changes in aggregation number are always to lower aggregation numbers. As monomer concentration is increased the probability of monomer uptake steps increases and the average micelle lifetime is extended, eventually becoming too long to allow simulations on a sensible timescale. Monomer concentrations in excess of 0.4 – 0.6 cmc (depending on the surfactant) extend micelle lifetimes upwards of the millisecond timescale.

This is an important result for the interpretation of adsorption kinetics measurements. For the case diffusion controlled adsorption the surface must be in local equilibrium with the subsurface. Based upon typical nonionic adsorption isotherms (see Lin *et al* [27, 28]) a surface coverage of up to 80% Γ_{max} corresponds to subsurface concentrations $\leq 50\%$ cmc. These simulations provide strong evidence that close to any expanding surface (where $\Gamma < 0.8\,\Gamma_{max}$) the continuous depletion of monomers may allow rapid, complete micelle breakdown via a Becker-Döring type process, but at a rate inconsistent

with the widely used results of Aniansson and Wall. Nyrkova and Semonov [125] also predicted that the rate of monomer release from micelles would be a strong function of monomer concentration using their nucleation theory approach.

4.3.3 Transition state theory

Both previous approaches, whilst informative, leave an interesting problem in that I still have not been able to elucidate the micelle lifetime for an equilibrium solution, only to confirm that it must be longer than the millisecond timescale if a Becker-Döring model is applied. Neither the full kinetic simulation of the Becker-Döring equations nor the stochastic modelling approach of individual micelles allows the calculation of micelle lifetimes close to equilibrium. There remains a gap between the maximum monomer concentration available from the stochastic simulations ($c_b < 0.6$ cmc) and the results of the Aniansson and Wall equations which apply for $c_b > 0.99$ cmc. Fortunately, as the barrier to micelle breakdown increases there is another approach that yields analytical solutions for micelle lifetimes for 'higher' monomer concentrations.

Consider an individual micelle of size N suspended in a solution with monomer concentration $\bar{X}_1 = Z.X_{cmc}$ where $0 < Z < 1$. The free energy of this micelle at each stage of its breakdown may be evaluated by summing the free energy for an aggregate of size g and $(N-g)$ monomers. Based on equation (4.29) I may write the total free energy G of the system in the form

$$G = [\mu_g^{\ominus} + kT \ln X_g] + (N-g)[\mu_1^{\ominus} + kT \ln X_{cmc} + kT \ln Z] \tag{4.52}$$

Since $\mu_1^{\ominus}$, $\ln X_g$ and $\ln X_{cmc}$ are constants they do not affect the free energy differences of interest so may be removed from equation (4.52) to leave

$$\begin{aligned} G &= \mu_g^{\ddagger} + (N-g)[kT \ln Z] \\ &= g.\Delta\mu_g^{\ddagger} + (N-g)[kT \ln Z] \end{aligned} \tag{4.53}$$

which is easily calculable from the molecular thermodynamics outline in detail above. Equation (4.53) gives the free energy of the aggregate/monomer system at each stage of the aggregate breakdown and with different monomer concentration defined by Z. Some

of these free energies, plotted as potential energy surfaces at different monomer concentrations, are shown in Figure 32.

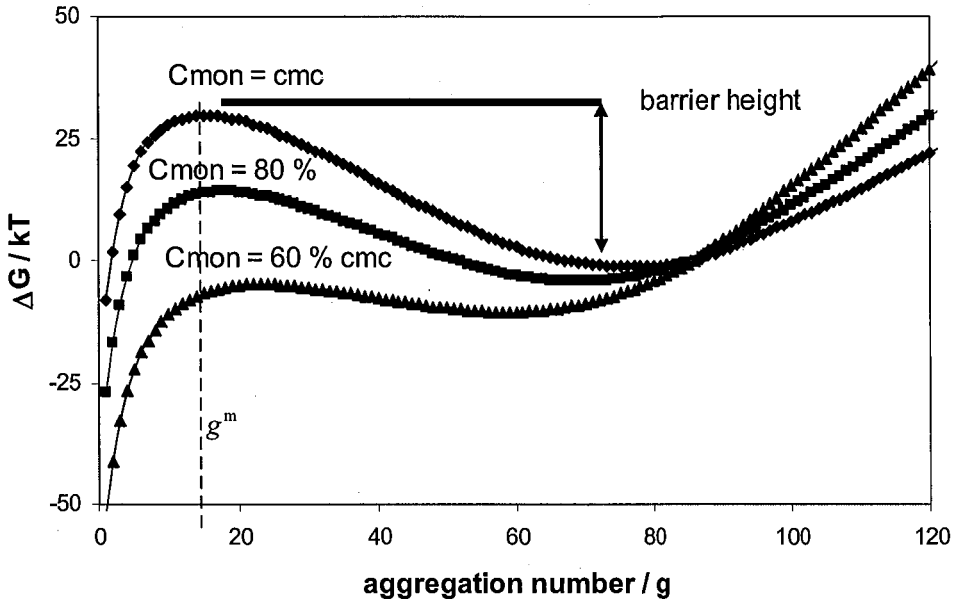

Figure 32: free energy surface as a function of monomer concentration for a $C_{12}E_8$ micelle at varying stages of breakdown Monomer concentrations are (♦) cmc, (■) 0.8 cmc and (▲) 0.6 cmc.

The minima in the free energy curves shown in Figure 32 corresponds to the most favourable size of aggregate at a particular monomer concentration. Notice how these minima shift to lower aggregation numbers as the monomer concentration is reduced. The free energy curves in Figure 32 can be use to calculate the quasi-equilibrium size distribution of aggregates formed at the point where the full Becker-Döring simulation ceases to change.

The barrier height, which is the free energy difference between maxima and minima of these free energy curves, decreases as the monomer concentration is reduced in agreement with other simulation techniques discussed above. The potential energy surface in Figure 32 lends itself to a transition state theory type treatment.

Provided that breakdown rate is slow compared to individual monomer loss, there will be a quasi-equilibrium of aggregates with sizes greater than $g^‡$, where $g^‡$ is the aggregation number at the maxima of the free energy surface. I can therefore use thermodynamic

transition state theory to write the rate constant for passage through the transition state k_{life}

$$k_{life} = \nu e^{-\Delta G^m/kT} \tag{4.54}$$

and

$$\nu = \frac{k_d^{g^m}}{l^2} \tag{4.55}$$

The exponential term in equation (4.54) gives the 'concentration' of aggregates which exist at the transition state $g^{\ddagger}$ and the term ν represents the rate at which aggregates pass through this transition state. Since the free energy surface close to $g^{\ddagger}$ is quite flat it is likely that aggregates close to $g^{\ddagger}$ undergo a diffusion-type process, perhaps passing through the transition state several times before breaking down. This diffusional process will extend micelle lifetimes and reduce the crossing rate ν. I have taken the rate of passage through the state $g^{\ddagger}$ to be the corresponding rate constant for monomer loss divided by the factor l^2 which is a measure of the 'flatness' of the transition state and accounts for the diffusion process which occurs close to the transition state. The value of l is determined by the number of aggregates with free energy with 1 kT of the free energy of the state $g^{\ddagger}$. Typical values of l for $C_{12}E_8$ are 10 – 15 depending on the precise value of monomer concentration Z.

The condition that that breakdown rate is slow compared to individual monomer loss holds provided the barrier height is ≥ 5 kT and leads to estimates for the micelle lifetime at higher monomer concentrations. These data are shown alongside the stochastic simulation data in Figure 33. The agreement between the data for the two approaches is remarkably good, for the C_nE_m family of surfactants.

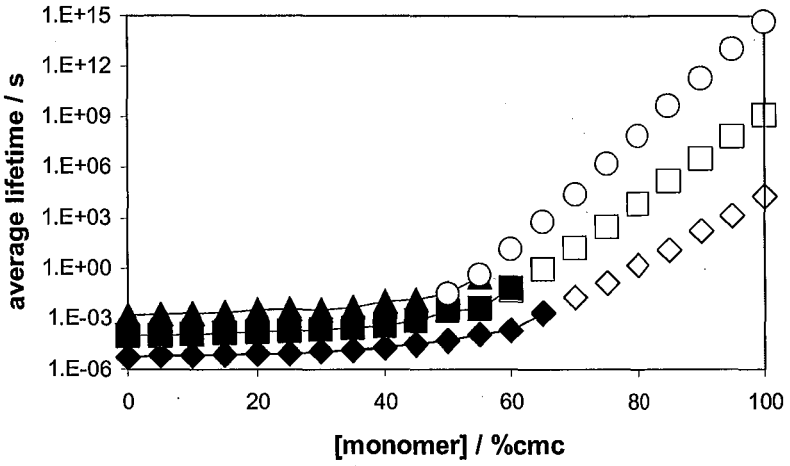

Figure 33: Comparison of micelle lifetimes derived from stochastic simulations and transition state theory calculations. Stochastic results for (♦) $C_{10}E_8$, (■) $C_{12}E_8$ and (▲) $C_{14}E_8$. Transition state theory results for (◊) $C_{10}E_8$, (□) $C_{12}E_8$ and (○) $C_{14}E_8$.

4.4. Summary

In this chapter I have explored the feasibility of a Becker-Döring only relaxation mechanism for micellar systems returning to equilibrium following a perturbation. Analytical solutions for this process were first derived more than thirty years ago by Aniansson and Wall. Their treatment is elegant and provides a very simple pair of equations for two well-separated relaxation times, consistent with experimental observation. These solutions have since been used extensively for the interpretation of micelle relaxation experiments and as a component of models which describe adsorption from micellar systems.

Using a range of numerical modelling approaches I have undertaken a thorough investigation of a Becker-Döring equations and found that the application of the Aniansson and Wall solutions has been subject to two misunderstandings.

First, I have used molecular thermodynamic modelling techniques to generate micelle size distributions which have been confirmed by molecular dynamics simulations. The physical parameters for micelles derived in this way may be fed into the Aniansson and Wall equations to yield two relaxation times. The 'fast' relaxation time is related to individual monomer loss immediately following a perturbation, consistent with the interpretation of most other authors. The 'slow' relaxation time is related to a walk in aggregation space between the region of proper micelles and monomers. For realistic

micelle size distributions, the probability of a complete micelle breakdown in this way tends towards zero as the monomer concentration recovers towards the cmc. Aniansson and Wall's solution reflect this fact, yielding values for τ_2 in excess of several years. Unfortunately, earlier research has started from relaxation data in order to yield information about kinetics and the size distribution. Aniansson and Wall predict well-defined decay curves and indeed these have been observed, leading most researchers to conclude that they were in fact observing complete micelle breakdown by consecutive monomer loss. I propose that micelle relaxation is occurring via a completely different mechanism that will be explored in the following chapter. There is nothing wrong with the equations of Aniansson and Wall, only that the mechanism they describe will lead to micelle breakdown at least several orders of magnitude slower than relaxation experiments measure.

Second, the second fact which has been overlooked by almost all researchers is that micelle lifetime is highly dependent upon local monomer concentration. This conclusion is the logical outcome of any breakdown mechanism which is defined by simultaneous monomer uptake and loss. That micelle lifetime is dependent upon experimental conditions has only been pointed out by a limited number of authors. Most researchers have treated micelle lifetime as a constant for a particular surfactant. This misunderstanding causes the greatest problem during the interpretation of adsorption kinetics from micellar solutions when the monomer concentration is significantly depleted close to a non-equilibrium surface.

Chapter 5

A new pathway for micelle breakdown

In Chapter 4 I explored the micelle breakdown process in a system where changes in aggregation number may only occur in unitary steps. Such a system is the basis for the popular Aniansson and Wall model of micelle breakdown and is mathematically described by the Becker-Döring equations. Using a range of numerical modeling approaches I demonstrated that complete micelle breakdown is highly unlikely to occur on physically realistic timescales via a Becker-Döring mechanism. It is the high free energy of the aggregates that exist between the region of monomers and the region of proper micelles that prohibits the flow of material between the two regions. Complete micelle breakdown by individual monomer loss can still occur provided that the monomer concentration is reduced below the cmc by a sufficient amount to reduce the height of the free energy barrier. Significant monomer depletion of this kind will be evident close to a rapidly expanding interface. This concept will prove very important in Chapter 7 for the interpretation of adsorption kinetics data.

However, it remains unclear how a system subject to a one-off perturbation may return to equilibrium at all, since once the monomer concentration has partially recovered all other changes came to a halt. In this chapter I seek to answer this question by proposing a new pathway for complete micelle breakdown which does not involve aggregates in the low concentration, high free energy region of aggregation space.

5.1. Micelle fusion and fission

In 1981 Kahlweit and co-workers [123] proposed an alternative route for the formation of micelles involving the merging of sub-micellar aggregates. They reasoned that, for ionic surfactants, as the bulk surfactant concentration increases the counter-ions suppress the electrical double layer around each particle raising the probability of reversible coagulation reactions of the form

$$X_i + X_j \underset{k_d^{ij}}{\overset{k_a^{ij}}{\rightleftharpoons}} X_{i+j} \tag{5.1}$$

For nonionic surfactants these coagulation reactions can occur at any bulk concentration. Kahlweit *et al* described the reaction pathway for the breakdown of micelles as a system of two parallel resistors; one that determines the rate of Becker-Döring breakdown and a second that defines the rate of aggregate fusion and fission. Both resistivities are a function of bulk surfactant concentration and are inversely related to each other. Their hypothesis was not outlined in a rigorous mathematical framework but was a guideline for future consideration.

Since I am interested nonionic systems, reactions of the form depicted in (5.1) must be considered in the region of small sub-micellar aggregates for all bulk concentrations. It is necessary to establish whether aggregate fission into other smaller aggregates eases the passage of material through the high energy region of the micelle size distribution. Such a process would be akin to 'tunnelling' through the high energy barrier avoiding the transition state completely.

In order to test this hypothesis I have incorporated the possibility of aggregate fission into the stochastic simulation model described in section 4.3.2 of the previous chapter. The association rate for two aggregates, containing i and j monomers respectively, to form a larger aggregate containing $i+j$ monomers is

$$k_a^{ij} = 4000 B_{ij} N_A \pi (D_i + D_j)(R_i + R_j); \tag{5.2}$$

where N_A is Avagadro's number, R_g is the effective radius of an aggregate containing g monomers and D_g is the aggregate diffusion coefficient calculated using Stokes-Einstein where $D_g = kT/(6\pi\mu R_g)$. The factor B_{ij} has been introduced to allow for the possibility of an activation barrier to micelle merging. For this stochastic simulation B_{ij} is set equal to 1, i.e. diffusion controlled association. These association rate constants, combined with the equilibrium relation, yield dissociation rate constants k_d^{ij} with

$$K_{ij} = \frac{k_a^{ij}}{k_d^{ij}} = \frac{[\bar{X}_{i+j}]}{[\bar{X}_i][\bar{X}_j]} \tag{5.3}$$

where the barred values denote equilibrium concentrations. Although one expects that the association of aggregates will have some degree of activation barrier ($B_{ij} < 1$), as evidenced by the work of Winnik[135], the inclusion of such a barrier would only reduce

the association, and therefore dissociation, rate constants, reducing the probability of this breakdown pathway. By assuming diffusion control I am considering an upper limit for the probability of these additional processes influencing breakdown rate.

In order to perform stochastic simulations for the Becker-Döring model in Chapter 4, the relative probabilities that an aggregate gained a monomer, lost a monomer or had no change of aggregation state in a short time interval were compared with a randomly generated number. To include these entire additional fission steps one may simply include all of the extra possibilities on the relative scale of probability.

The probability that an aggregate of size '$i + j$' fissions into two smaller aggregates of size i and j respectively during a time interval Δt is

$$P_{i+j}^{-} = k_d^{ij} \Delta t \tag{5.4}$$

whilst the probability that an aggregate of size i gains a monomer is

$$P_{i+1}^{+} = X_1 k_a^{i1} \Delta t \tag{5.5}$$

For computational simplicity I am only considering this one possibility for an increase in aggregation number i.e. I do not account for all possible fusion steps. This simplification can only accelerate micelle breakdown since a range of possible processes which oppose micelle breakdown have been neglected.

Conditions for these simulations are the same as those in section 4.3.2. I chose Δt such that P_{i+1}^{+} and $P_{i+1}^{-} < 0.1$. All other dissociation probabilities are smaller still, i.e. $P_{i+1}^{-} > P_{i+2}^{-} > P_{i+3}^{-} > \mathrm{L}$. The probability that micelle aggregation number remains unchanged in this time interval is $P^0 = 1 - P_{i+1}^{+} - \sum_j P_{i+j}^{-}$.

The initial aggregation state was taken to be the peak aggregation number. A random number (rand) between 0 and 1 was generated for each iteration. For a given monomer concentration X_1 and time interval Δt if rand > $1 - P_{i+1}^{+}$ the aggregation number increased by one in that iteration. If $1 - P^0 - P_{i+1}^{+} <$ rand $< 1 - P_{i+1}^{+}$ the aggregation state remained unchanged for that iteration. If $1 - P^0 - P_{i+1}^{+} - P_{i+1}^{-} <$ rand $< 1 - P^0 - P_{i+1}^{+}$ the aggregate lost one monomer. An aggregate loses two monomers if $1 - P^0 - P_{i+1}^{+} - P_{i+1}^{-} - P_{i+2}^{-} <$ rand $<$

$1-P^0-P_{i+1}^+-P_{i+1}^-$ etc. Simulations were run 100 times for each monomer concentration. The total number of steps required for the aggregate to reach $g = 1$ was recorded for each repeat and the micelle lifetime evaluated using equation 4.53.

The results from these simulations are indistinguishable from the Becker-Döring simulations in Chapter 4. No acceleration of micelle breakdown is observed upon inclusion of the additional micelle fission reactions. This result can be easily understood when one considers the probability of micelle fission steps relative to individual monomer loss and gain. For a 4-mM $C_{12}E_8$ solution at equilibrium (X_1 = cmc) the highest energy 'transition state' occurs at aggregation number $g = 15$. If tunneling were to occur it would most likely happen around this aggregation number where the energy barrier is thinnest. For a $C_{12}E_8$ aggregate containing 20 monomers the probabilities of different changes in aggregation state for a time interval 10^{-8}s are given in Table 16. One can immediately see that the likelihood of aggregate fission into other oligomers rapidly is vanishingly small compared to the probability of individual monomer uptake and loss.

Incorporating Kahlweit's concept of oligomer fusion and fission certainly does not enable micelle breakdown to occur via the high energy region of the size distribution.

Δg	+1	0	-1	-2	-3		-10
PROBABILITY	0.012	0.981	0.008	1.2×10^{-7}	3.3×10^{-11}		1×10^{-18}

Table 16: Probabilities for a range of aggregation state changes in a time interval of 10^{-8} s for a 4mM $C_{12}E_8$ solution with X_1 = cmc

5.2. An alternative pathway for micelle breakdown

In this section I propose an alternative mechanism for micelle breakdown that does not proceed through the high energy region of intermediate aggregate sizes. I will outline the fundamental chemistry behind the model and describe some proof of concept numerical modeling that I have carried out in order to test the feasibility of this new pathway. In collaboration with the Oxford Centre for Collaborative and Applied Mathematics (OCCAM) an alternative, a rigorous mathematical description has also been derived by treating micelle size distribution as a continuous variable. The results of that work

essentially agree with the predictions of the proof of concept modelling I will outline below.

5.2.1. A combined fusion-Becker-Döring mechanism

In a real micellar solution reactions of the form of equation (5.1) are not limited to sub-micellar aggregates but are likely to occur across the entire size distribution. That micelles can collide and merge to form transient larger aggregates has been established through work on the exchange kinetics of fluorescent molecules contained within micelles. Winnik *et al* [135, 136] have used a pyrene labelled triglyceride molecule to demonstrate that micelles of Triton X-100 undergo regular collisions producing larger aggregates which persist for at least the time interval necessary for exchange of the solubilised tracer molecule. Winnik concluded that the formation of these larger aggregates occurs at approximately 5000 times less than the diffusion controlled rate, which is still remarkably fast when one considers the reorganisation required for aggregate merging.

Throughout the following description I will use the term 'proper-micelle' to denote a micelle with aggregation number close to the peak of the micelle size distribution and the term super-micelle to describe a larger aggregate formed by the merging of two 'proper-micelles'. Whilst all previous work I am aware of has paid no attention to the super-micelle region, it is this region that provides an alternative mechanism by which proper micelles may break down without forming any aggregates in the high energy region. I begin by considering the potential energy surfaces from the previous chapter, one of which is reproduced in Figure 34 for convenience.

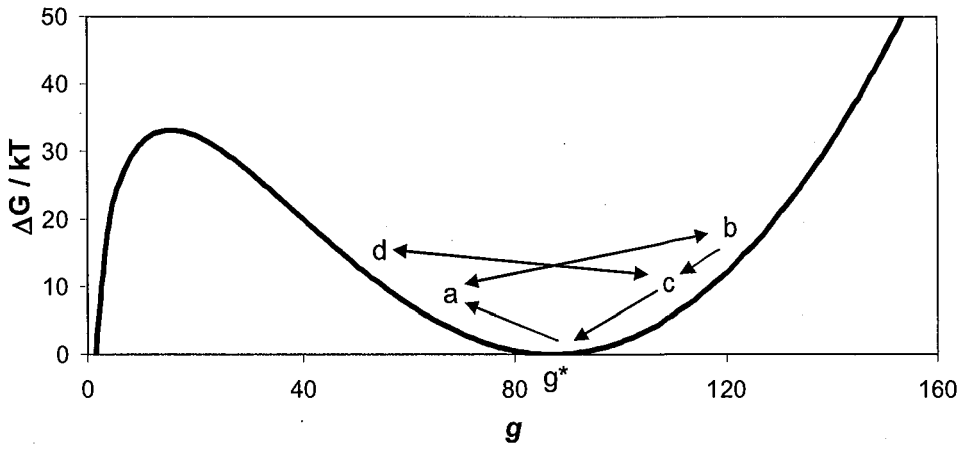

Figure 34: Relative free energies for a $C_{12}E_8$ aggregate of size (g*-N) and N monomers represented as a free energy surface, with monomer concentration X_1 = cmc

From the stochastic reasoning outlined in the previous chapter, immediately following a perturbation that reduces the monomer concentration below the cmc, there will be a rapid loss of monomers which shifts the peak of the micelle size distribution to lower aggregation numbers whilst the monomer concentration recovers towards the cmc. Figure 34 represents this process as a shift from g* to *a*. For the Becker-Döring case the increase in monomer concentration led to a highly stable quasi-equilibrium at the state *a* with only very slow re-equilibration which had to proceed over the high energy barrier. However, the addition of micelle fusion and fission allows the distribution to evolve via an alternative pathway.

I will use Figure 34 to explore the characteristics of proper micelles merging to form super-micelles by considering the energy penalty for doing so. For illustrative purposes I will refer to the merging of identical micelles although all possible aggregate combinations can occur to varying degrees. I begin from the assumption that the merging of micelles does occur within several orders of magnitude of the diffusion controlled rate based upon the work of Winnik *et* al. [135]

For aggregates of size g* the micelle fusion process, $X_{g^*} + X_{g^*} \rightleftarrows X_{2g^*}$, incurs an energy penalty of approximately 50 kT, which is the difference in free energy between the initial and final states. It follows that the equilibrium will lie heavily to the left hand

side. The corresponding small value of the equilibrium constant, K_{gg} ,combined with association rate constants k_a^{gg} within at least several orders of magnitude of diffusion control lead to a large dissociation rate constant k_d^{gg}. Therefore, super-micelles X_{2g^*} that are formed will have only negligible lifetimes.

However, for aggregates of size 'a' the energy penalty for fusion is not nearly as severe. The equilibrium between the two states $X_a + X_a \rightleftarrows X_b$ (where $b = 2a$) will still lie to the left but, with a penalty of the order of only 7 kT, the state 'b' will have a short but non-negligible lifetime. One still expects the primary mechanism for breakdown of the state 'b' to be fission back to the state 'a' but there exists a small but significant probability that 'b' can lose monomers during this lifetime. In fact, if 'b' were able to shed enough monomers to reach the state 'c' then fission into state 'd' is no longer as favourable as monomer loss and monomer loss will prevail, returning the aggregate to the state g*.

I propose that complete micelle breakdown can occur through the merging of aggregates to the left of the equilibrium aggregation number followed by successive monomer loss. This mechanism will be accelerated by monomer depletion and the corresponding shift to smaller aggregation numbers following a perturbation but, unlike the Becker-Döring mechanism, this mechanism remains possible for equilibrium systems as will be demonstrated below. The overall mechanism is a combined fusion-Becker-Döring process.

5.2.2. Proof of concept numerical modelling

I used Matlab to model the fusion-Becker-Döring process in order to test the feasibility of the proposed mechanism. I began by assuming that proper-micelles merge to form super-micelles at a 1/5000th of the diffusion controlled rate based on the work of Winnik *et al* [135, 136]. The implications of this assumption are discussed below.

I needed to calculate the rate of monomer release by the fusion-Becker-Döring process for a micellar system that had been subjected to an instantaneous dilution by a factor *Dil*. Initial and final state size distributions were evaluated following the molecular thermodynamic treatment outlined in Chapter 4. For the initial size distribution, a matrix of all possible association rate constants k_a^{ij} was evaluated using equation (5.2) with

$B_{ij} = 1/5000$ for all processes except those involving monomer gain where $B_{ij} = 1$ as before. There is no physical reason why the introduction of additional micelle merging processes should affect the rate of monomer uptake for any aggregate size. The corresponding matrix of dissociation rate constants k_d^{ij} was determined from the equilibrium condition (5.3). Given these rate constants, the total rate of flow into aggregation state i is given by

$$r_a^i = k_a^{i-1,1} X_{i-1} X_1 + k_d^{i,1} X_{i+1} + \sum_{j=2}^{i_{max}-1} k_a^{i-j,j} X_{i-j} X_j + \sum_{j=2}^{i_{max}-1} k_d^{i,j} X_{i+j} \tag{5.6}$$

where the processes involving monomer uptake and loss have been expressed as separate terms to emphasise the conventional Becker-Döring processes alongside the additional merging steps described by the summation terms. The total rate of flow out of the state i is given by

$$r_d^i = k_a^{i,1} X_i X_1 + k_d^{i-1,1} X_i + \sum_{j=2}^{i_{max}-1} k_a^{i,j} X_i X_j + \sum_{j=2}^{i-1} k_d^{i-j,j} X_i \tag{5.7}$$

with the total rate of change in concentration given by

$$\frac{dX_i}{dt} = r_a^i - r_d^i \tag{5.8}$$

The integer i_{max} in equations (5.6) and (5.7) refers to the limit of considered aggregation space for this kinetic process. In order to evaluate the properties of aggregates containing $i+j$ monomers, it is necessary to perform molecular thermodynamic calculations to twice this value.

Using Matlab I evaluated the rate of flow into each aggregation state, r_a^i , for the region of super-micelles. Based upon the shape of the corresponding micelle size distribution, I have defined a $C_{12}E_8$ super-micelle to be any aggregate containing more than 100 monomers. I then found it necessary to calculate the proportion of these super-micelles that, once formed, are able to return to a proper-micelle state through consecutive monomer loss. I have calculated this value by comparing rate constants for monomer loss, monomer association and the total rate constant for all fission processes that a super-micelle can undergo. The net rate of monomer loss from a super-micelle depends on the

relative rates of monomer uptake and loss. If there are no monomers present then the rate of monomer loss is equal to $k_d^{i-1,1}$ for a super-micelle containing i monomers. When the monomer concentration is non-zero then micelles may also increase in size. My simulations reveal that in the super-micelle region the probability of monomer loss is always greater than monomer gain i.e. $k_d^{i-1,1} > k_a^{i-1,1} X_1$ for $X_1 \leq$ cmc. I calculated the net rate of monomer loss using

$$k_{d,MON}^{i} = k_d^{i-1,1} - k_a^{i,1} X_1 \tag{5.9}$$

The total rate constant for all possible fission processes that a micelle can undergo is given by

$$k_{d,FIS}^{i} = \sum_{j=1}^{i-1} k_d^{i-j,j} X_i \tag{5.10}$$

I compared the rate constants for monomer loss $k_{d,MON}^{i}$ to the rate constants for all possible super-micelle fission processes $k_{d,FIS}^{i}$, to give the probability that any given aggregate loses a monomer during its lifetime. That is, the probability that a super-micelle loses a monomer before undergoing an alternative fission process will be given by $k_{d,MON}^{i} / k_{d,FIS}^{i}$. Figure 35 shows these two rate constants for an 0.5-mM solution of $C_{12}E_8$ with monomer concentration at the cmc, plotted for part of the region of super-micelles.

As can be seen in Figure 35, the net rate constant for monomer loss accounts for most of the outflow from super-micelles with aggregation numbers less than 130. This behaviour can be understood in terms of the potential energy surface in Figure 34. Any aggregate in the range 100 – 130 monomers that fissions into two smaller aggregates (except where one aggregate is a monomer, dimer, trimer etc.) will result in a significant increase in the total free energy of the system. It follows that these processes are highly unlikely to occur, and the corresponding rate constants are much smaller than the rate constant for monomer loss. However, for larger super-micelles that have a higher free energy prior to fission, the rate constants for fission become much larger. This favourability is shown by the steep climb in the value of k_d^{FIS} for aggregates larger than 130. The slight discontinuity in the slope of the $k_{d,MON}^{i}$ curve is a result of a discontinuity in the chemical potential curve where the curves for the sphere with a hole and rodlike micelle model

were matched, as originally explained in section 4.2.3. This discontinuity has no effect on the conclusions which follow, since it only exists on the very limit of the considered aggregation space for this kinetic process.

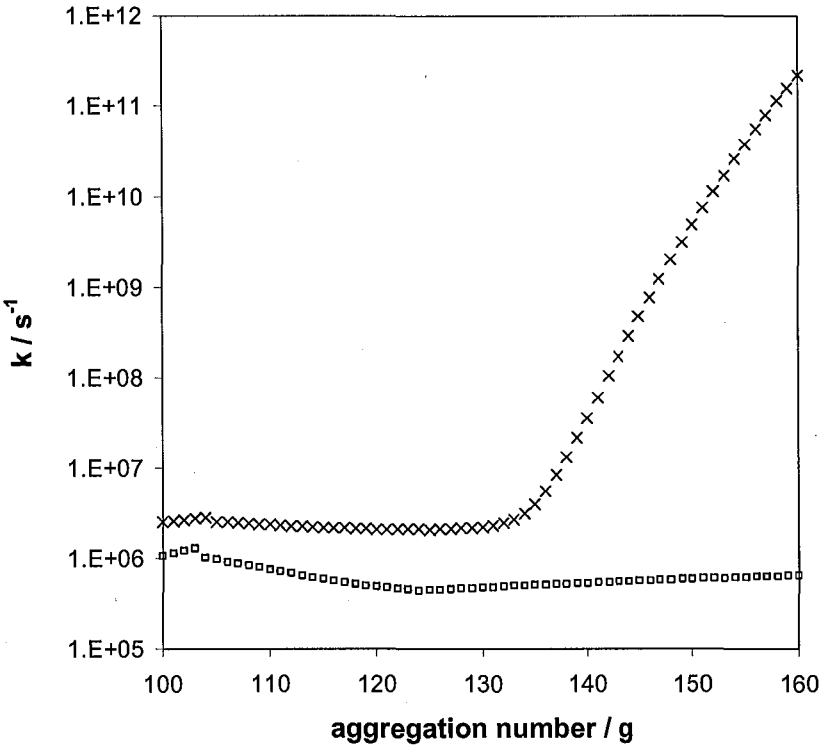

Figure 35: Summed rate constant for all possible outflow processes (×) and rate constants for monomer loss only (□) for an 0.5-mM solution of $C_{12}E_8$ with X1 = cmc.

As can be seen in Figure 35, the rate constant for monomer loss accounts for a large proportion of all outflow processes from super-micelles with aggregation numbers less than 130. This behaviour can be understood in terms of the potential energy surface in Figure 34. Any aggregate in the range 100 – 130 monomers that fissions into two smaller aggregates (except where one aggregate is a monomer, dimer, trimer etc.) will result in a significant increase in the total free energy of the system. It follows that these processes are highly unlikely to occur, and the corresponding rate constants are much smaller than the rate constant for monomer loss. However, for larger super-micelles that have a higher free energy prior to fission, the rate constants for fission become much larger. This favourability is shown by the steep climb in the value of k_d^{FIS} for aggregates larger than 130. The slight discontinuity in the slope of the $k_{d,MON}^{I}$ curve is a result of a discontinuity in the chemical potential curve where the curves for the sphere with a hole and rodlike

micelle model were matched, as originally explained in section 4.2.3. This discontinuity has no effect on the conclusions which follow, since it only exists on the very limit of the considered aggregation space for this kinetic process.

In order to completely break down, a super-micelle of size i must undergo $i-N_{\lim}$ consecutive monomer loss steps where $N_{\lim}$ is the aggregation number which denotes the upper limit of the region of proper-micelles ($N_{\lim}=100$ for $C_{12}E_8$). The probability of a super micelle undergoing $i-N_{\lim}$ consecutive monomer loss steps $P^i_{N\lim}$ is

$$P^i_{N\lim} = P^{i-1}_{N\lim} \times \frac{k^i_{d,MON}}{k^i_{d,FIS}} \tag{5.11}$$

with boundary condition $P^{N\lim}_{N\lim}=1$. These probability values are plotted as a function of aggregation number in Figure 36.

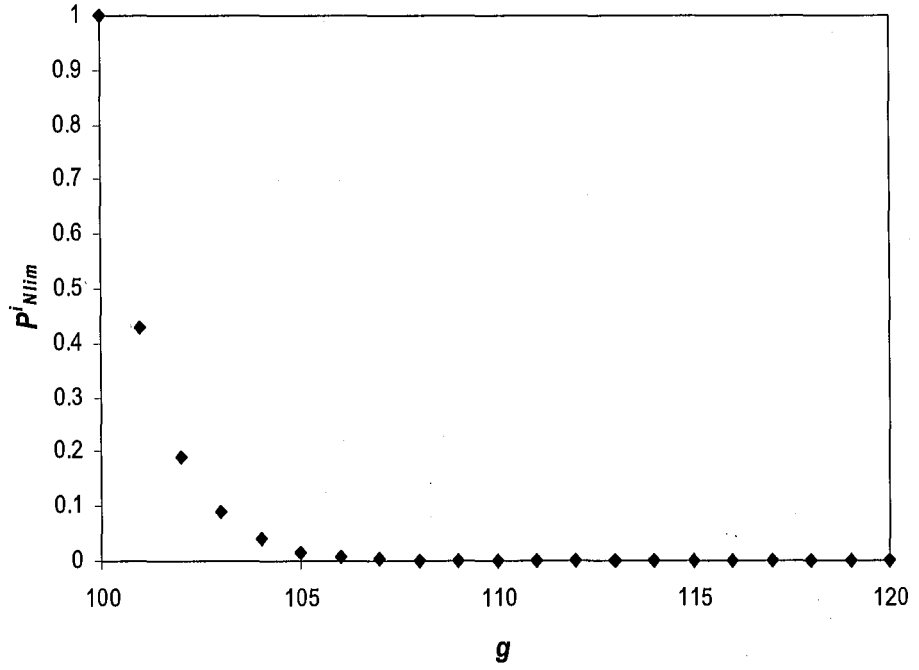

Figure 36: The probability that a super-micelle undergoes enough successive monomer loss steps to reach the region of proper micelles as a function of aggregation number for a 2-fold dilution of an 0.5-mM solution of $C_{12}E_8$ with X1 = cmc.

For a given super-micelle the rate of monomer release is

$$r^i_{mon} = r^i_a \times P^i_{N\lim} \times (i-N) \tag{5.12}$$

which, when summed across all super-micelles provides an estimate of the total rate of monomer release through a combined fusion-Becker-Döring process. This rate may then be multiplied by a suitably small time interval to yield the change in monomer concentration during that interval

$$\Delta X_1 = \Delta t. \sum_{i=N\lim}^{i_{\max}} r_{mon}^{i} \tag{5.13}$$

The monomer concentration in the initial size distribution is adjusted according to equation (5.13), i.e. $X_1(t+\Delta t) = X_1(t) + \Delta X_1$. This new value of X_1 is then used as an input for the subsequent iteration. I chose to evaluate the rate of monomer release, rather than the rate of micelle breakdown to simplify the numerical analysis, since each super-micelle may release a different number of free monomers. It was straightforward to include this variation in equation (5.12). Since each subsequent iteration begins with a re-equilibration between monomers and micelles, as explained below, the results are insensitive to whether monomer release or micelle breakdown is considered.

Having evaluated the change in monomer concentration, the first step in all subsequent iterations is to re-evaluate the number of micelles remaining in the system to satisfy material balance. This calculation is equivalent to re-equilibration between the monomers and micelles present in the system. This re-equilibration is justifiable provided that the time step remains longer than the timescale for rapid monomer release τ_1. In all of my simulations I used a time-step $\Delta t \geq \tau_1$ seconds, which for $C_{12}E_8$ is 20 μs.

I recorded the concentration of both monomers and aggregates as a function of real time and the results for a range of simulations are shown in Figure 37 and Figure 38.

5.2.3. Model predictions

In Figure 37 I have plotted the aggregate concentration vs. time following a 2-fold dilution of a $C_{12}E_8$ solution initially at concentrations of 4, 6, 8 and 10 × cmc multiples (0.508, 0.752, 1.016 and 1.27-mM respectively). The simulations stop when the monomer concentration reaches the cmc. The timescale for each decay curve clearly shows that one should expect higher bulk concentrations to relax more rapidly to equilibrium. This result is consistent with a mechanism that relies on collisions of proper-micelles in order to proceed. It is important to note that in the pure Becker-Döring

(Aniansson and Wall) model the dependence of τ_2 on bulk concentration was less clear due to the presence of concentration terms in both the numerator and denominator of equation (4.28).

Figure 38 shows the response of a $C_{12}E_8$ micellar system initially at 10 × cmc (1.27-mM) subjected to dilutions by a factor of 2, 4, 6 and 8 respectively. It can be seen that larger dilution factors lead to much slower relaxation, due primarily to the reduction in the number of aggregates available for fusion.

This general behaviour will be compared to experimental data in the following chapter and is analysed in terms of the physical processes that I am modelling in the following section.

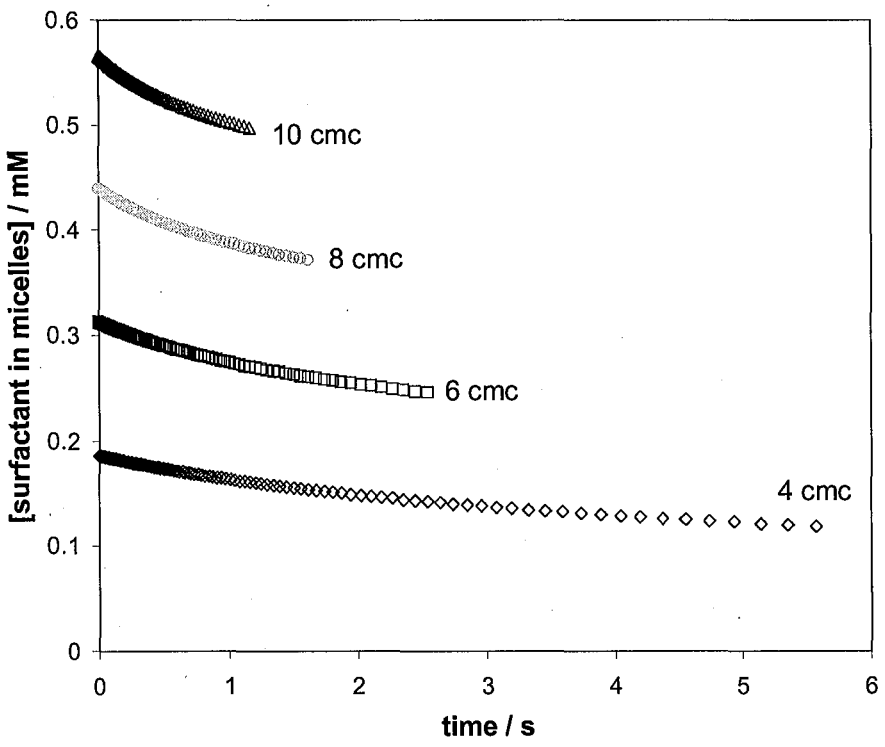

Figure 37: Predictions of the combined fusion-Becker-Döring monomer release model showing the aggregate concentration vs. time for 2-fold dilutions of $C_{12}E_8$ with a range of starting concentrations expressed as cmc multiples and given in graph.

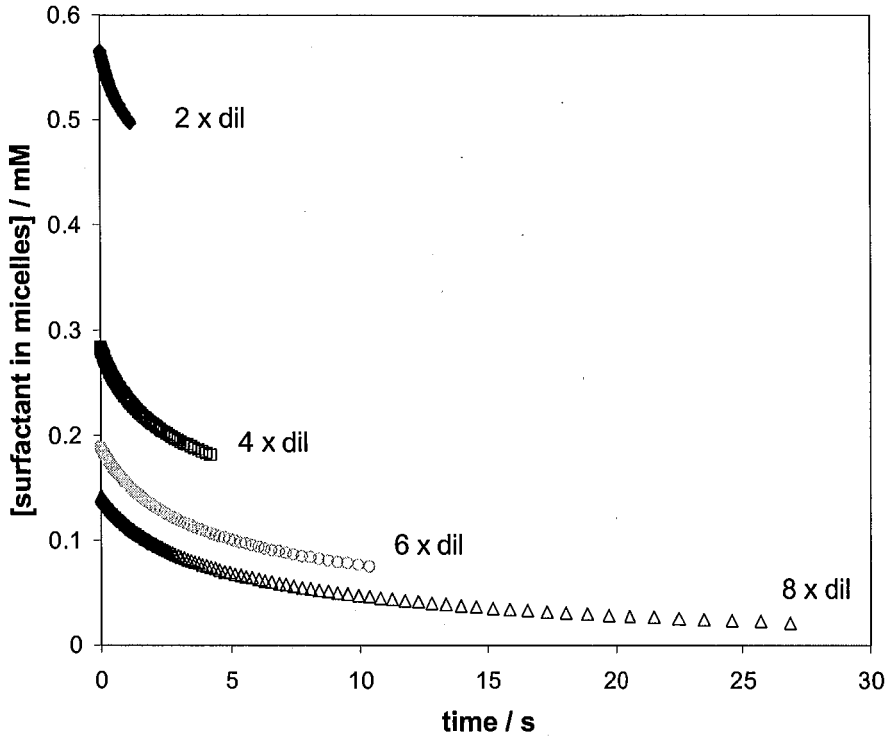

Figure 38: Predictions of the combined fusion-Becker-Döring monomer release mode showing the aggregate concentration vs. time for 1.27 mM (10 x cmc) $C_{12}E_8$ with a range of dilution factors given in the legend.

5.2.4. Interpretation and limitations of this numerical approach

Within the combined fusion-Becker-Döring model one should expect the rate of micelle breakdown to be governed by two system parameters: (1) the number of proper-micelle available for collisions. These collisions will govern the rate of formation of super-micelles. (2) The monomer concentration in the system which will affect the probability of monomer loss from each super-micelle and therefore the proportion of super-micelles that break down.

As micelle systems approach equilibrium following a dilution, the number of proper-micelles decreases and the concentration of monomers increases. Both of these changes should oppose the relaxation rate of remaining proper-micelles. Therefore, I would expect to see micelle relaxation curves characterised by a continuously changing relaxation rate. One can examine the decay rate the decays in Figure 37 and Figure 38 by re-plotting the concentration of surfactant contained within micelles on a log scale. If the decay was characterised by a single decay coefficient then such a plot would give a

straight line. Data for a 2-fold dilution of $C_{12}E_8$ initially at 4 times the cmc is re-plotted in Figure 39. The line is clearly non-linear indicating a continuosly changing decay rate.

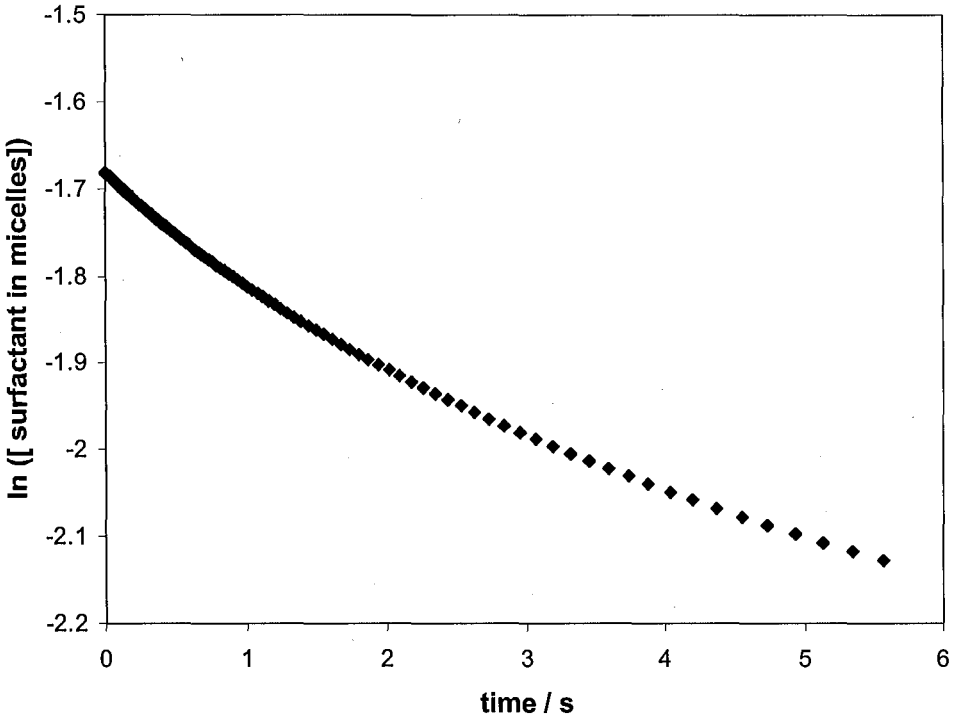

Figure 39: Prediction of the combined fusion-Becker-Döring monomer release model showing the aggregate concentration vs. time for a 2-fold dilution of $C_{12}E_8$ initially at 4 times the cmc.

In the simulations above I calculated the probability that a given super-micelle undergoes enough consecutive monomer loss steps to reach the proper-micelle region by comparing rate constants. I calculated the rate constants for all possible fission processes using equation (5.9). This equation does not capture the full complexity of the monomer loss process, since a super-micelle may gain or lose several monomers during its lifetime before undergoing fission. In the simulations above the monomer loss process was described as having only two outcomes for each aggregation number.

To explore whether the lifetime of super-micelles in more detail I performed a series of stochastic simulations for the region of super-micelles. Rate constants for all possible association and dissociation reactions were calculated using the same procedure outline in section 5.2.2., with B_{ij} = 1/5000 for all processes except monomer uptake and loss

where B_{ij} = 1. The probability of monomer loss, $P^{-}_{i,MON}$, by a super-micelle of size i in time interval Δt is

$$P^{-}_{i,MON} = k_d^{i-1,1}\Delta t \tag{5.14}$$

and the probability of monomer uptake, P_g^{-}, is

$$P^{+}_{i,MON} = k_a^{i,1} X_1 \Delta t\,. \tag{5.15}$$

where X_1 is the concentration of monomers. The probability of all other possible fission processes is

$$P_{i,FIS} = \sum_{j=2}^{i-1} k_d^{i-j,j}\Delta t \tag{5.16}$$

Equations (5.14) - (5.16) hold provided the time interval Δt is short enough such that there is a negligible probability of more than one event occurring in time Δt. The possibility that super-micelle fuse with proper-micelles has been neglected in these simulations for two reasons: (1) the concentration of super-micelles is relatively low and (2) the increase in free energy is severe and the aggregates formed will have very short lifetimes so are unlikely to significantly contribute to the total rate of micelle breakdown.

To simulate an aggregate that may lose a monomer, gain a monomer, fission or do nothing a random number (rand) between 0 and 1 was generated. For a given monomer concentration X_1, aggregation number i and time interval Δt, if rand < $P^{-}_{i,MON}$ the aggregate lost a monomer and the code recorded a monomer loss result. If rand > $1-P_{i,FIS}$ the aggregate underwent fission and the code recorded a fission result. If $P^{-}_{i,MON} \leq$ rand $\leq$ $1-P^{+}_{i,MON}-P_{i,FIS}$ the aggregate gained a monomer and the simulation looped with an increased aggregation number. If none of these conditions are met the aggregation state remained unchanged and the simulation looped. This loop was continued, generating a new random number each time until either the aggregation state reached one less than the initial aggregation state or a fission process occurred. This simulation was repeated 1000 times for each super-micelle in order to evaluate the proportion of monomer loss results relative to fission results.

This process was then repeated with different monomer concentrations. From the relative number of monomer loss/fission results the probability that each super-micelle reached the proper-micelle region was evaluated with

$$P^{i}_{N\lim} = P^{i-1}_{N\lim} \times \frac{N^{-}_{mon}}{N_{fiss} + N^{-}_{mon}} \tag{5.17}$$

Where N^{-}_{mon} is the number of monomer loss results and N_{fiss} is the number of fission results. As before a boundary condition $P^{N\lim}_{N\lim}$ =1 was used. The results of these simulations for several monomer concentrations are plotted in Figure 40.

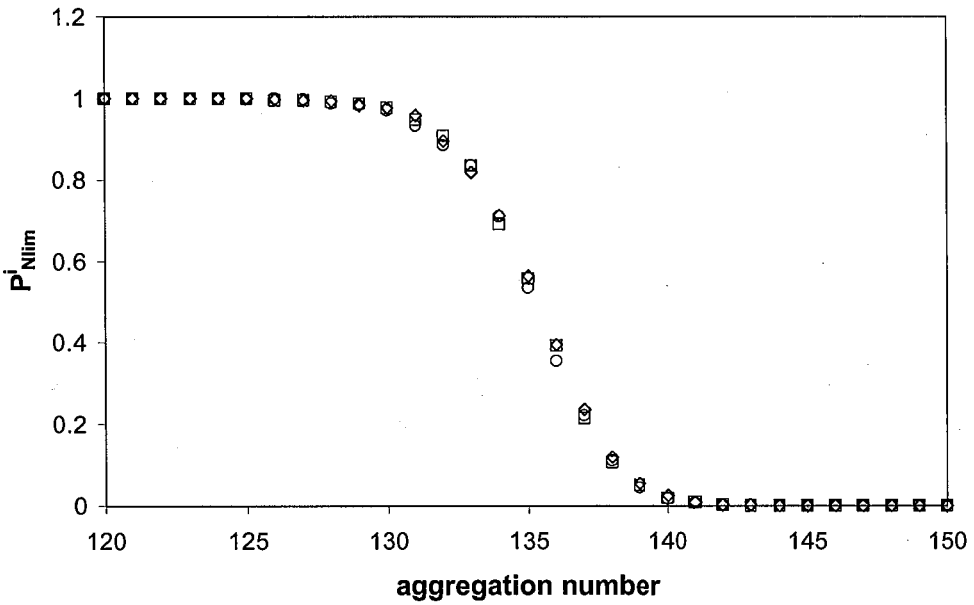

Figure 40: Probability that super-micelles undergo sufficient consecutive monomer loss steps to reach the region of proper-micelles from stochastic simulations with monomer concentrations (□) 0.1 cmc, (◊) 0.5 cmc and (○) cmc.

It is clear from Figure 40 that the monomer concentration has little influence on the probability of monomer release from super-micelles, unlike the proper-micelle case. This effect can be understood if one compares the actual values of $k_d^{i-1,1}$ and $k_a^{i,1}X_1$ across the region of super-micelles. Unlike in the proper-micelle case where these two values are similar at the cmc, and the probability of monomer loss become dominant as monomer

concentration decreases, in the region of super-micelles the value of $k_a^{i-1,1}$ is always greater than $k_a^{i,1}X_1$ regardless of the value of X_1.

It is also evident that the probability that a super-micelle is able to lose a sufficient number of monomers to reach the region of proper-micelles is increased relative to the simple two-outcome analysis included in the modelling described in section 5.2.2 and plotted in Figure 36. This change would accelerate micelle breakdown by increasing the number of super-micelles that are able to make a significant contribution to the rate of monomer release. Future modelling should try and incorporate this additional complexity of the monomer loss versus fission process.

An important omission from my model is the reverse reaction that leads to micelle formation. The principle of microscopic reversibility insists that it is possible to form micelles by the addition of monomers to proper-micelles followed by fission of the super-micelle that is created. It is physically realistic to expect that as monomer concentration increases this reverse process will occur more frequently, slowing the rate of micelle relaxation further. Since I have not included these steps in my simulations I have not been able to capture the entire change of relaxation rate. In chapter 6 I will show how direct measurements of micelle concentration with time do show a continuously changing relaxation rate consistent with the combined fusion-Becker-Döring process.

Another important omission is that the conventional Becker-Döring and the combined fusion-Becker-Döring processes may occur simultaneously. It is reasonable to expect both processes to compete at very short times when the monomer concentration is sufficiently depleted. Allowing both processes to occur simultaneously would have two effects. First, provided that monomer depletion was sufficiently large there would be additional removal of micelles on very short timescales by the conventional Becker-Döring route. In chapter 4 I showed, in detail, how removal of monomers can lower the energy barrier for the passage of material through the region of intermediate sized aggregates. For $C_{12}E_8$, micelle break down may proceed through this region if $X_1 < 0.4$ cmc (Figure 31).

Second, I also explained in chapter 4 how rapid monomer loss in the conventional Becker-Döring route shifts the peak of the micelle size distribution to smaller aggregation numbers on the microseconds timescale (Figure 28). In order to understand why this will

affect the combined fusion-Becker-Döring process, one must consider which parts of the micelle size distribution make the greatest contribution to micelle breakdown. Equation (5.12) gives the rate of monomer release from a given super-micelle. The $P^i_{N\lim}$ terms gives the probability that each super-micelle can undergo enough successive monomer loss steps to reach the region of proper-micelle. Figure 36 (and Figure 39) plots $P^i_{N\lim}$ as a function of aggregation number throughout the region of super-micelles ($g > 100$). It is evident that this probability drops off very rapidly and that only aggregates with sizes in the range 101 – 120 will make a large contribution to the net breakdown rate of micelles. Examination of the association rates into these states reveals that aggregates in the size range 50 – 70 make the largest contribution to the formation of these states (r^i_a in equation (5.12)). Therefore, any shift to smaller aggregation numbers will accelerate the rate of micelle breakdown. However, due to the assumption of a monomer-micelle equilibrium in my combined fusion-Becker-Döring modelling the peak of the aggregate size distribution is constrained to remain at the equilibrium aggregation number.

Another aspect of the fusion-Becker-Döring that has not been explored in detail is the rate of micelle fusion relative to diffusion control. The data shown in Figure 37 and Figure 38 were derived with the assumption that micelle fusion occurs at a fraction of the diffusion controlled rate based on the work of Winnik et al [135, 136]. One might ask how the value of B_{ij} in equation (5.2) affects the outputs of the modelling. A reduction in the association rate of aggregates should have little or no effect on the overall rate of micelle breakdown due to the reversibility of the fusion-fission process. Any reduction in the rate of micelle fusion leads to a corresponding reduction in the rate of micelle fission and an extension in the lifetime of the super-micelles.

Whilst the rate of flow into each super-micelle state r^i_a in equation (5.12) is reduced the probability that the micelle persists long enough to shed N monomers $P_i^{N\lim}$ is increased. Provided that the barrier to micelle fusion is not so large that it prevents the process occurring entirely, the absolute magnitude of such a barrier has little effect on the monomer release process. It is a limitation of the simplified numerical approach above that prevents detailed exploration of this hypothesis. Since $P_i^{N\lim}$ cannot increase by the same factor that r^i_a decreases by upon introduction of an additional barrier to fusion I am unable to probe the effect of the barrier rigorously.

Nevertheless, the numerical modelling I have carried out does suggest that the combined fusion-Becker-Döring model can explain micelle breakdown on physically realistic timescales, unlike the pure Becker-Döring model.

Chapter 6

Stopped Flow Measurements of Micelle Exchange Kinetics

In this chapter I describe my measurements of relaxation kinetics in micellar solutions of nonionic surfactants subjected to large perturbations from equilibrium.

6.1. Introduction

Kinetics of monomer-micelle exchange and micelle breakdown can be studied with techniques that perturb an equilibrium system and monitor the subsequent relaxation back to the new equilibrium state. Techniques which have been applied include stopped flow dilutions [44-46], temperature or pressure jump methods [46-50] and the propagation of ultrasound [45, 51]. Experiments reveal that relaxation processes in micelle solutions are characterised by two distinct relaxation times. The first, more rapid relaxation time is related to changes in monomer concentration due to the individual monomer loss (or gain) from all micelles present in the system. The second, slower relaxation time is related to changes in the number of micelles by complete micelle dissolution (or formation). These two relaxation times differ by at least three orders of magnitude with monomer loss occuring on the μs – ms timescale and complete micelle breakdown on the ms – minutes timescale.

In Chapters 4 I discussed the widely adopted theory of micelle kinetics proposed in the 1970s by Aniansson and Wall. The key assumptions in the Aniansson and Wall model are that changes in aggregation number can only occur in unitary steps and that the aggregate size distribution contains three distinct regions; pre-micellar aggregates and proper micelles of appreciable concentration and a region of intermediate aggregates which exist in only small amounts. Their theoretical framework was the first to explain the existence of two distinct relaxation times and the separation of timescales for the two processes. Rapid monomer loss is a consequence of unbalancing all of the monomer-aggregate equilibria, therefore this process must occur on a similar timescale to individual monomer exchange. Complete breakdown

of micelles by unitary steps is a much slower process, due in part to the larger number of steps required, but also because an aggregate must pass through the region of low concentration to break down which is unfavourable. Aniansson and Wall derived a pair of simple equations that related both relaxation times to the shape of the aggregate size distribution. However, using a combination of molecular thermodynamics and numerical modelling I showed that the high free energies of aggregates with intermediate size prohibits complete micelle breakdown on physically realistic timescales within the Aniansson and Wall model.

In Chapter 5 I proposed an alternative pathway for complete micellar breakdown which does not proceed through the low concentration region of intermediate aggregates. By allowing micelles to merge, forming 'super-micelles' that return to the region of 'proper-micelles' through monomer loss, it is possible for micelles to be removed from the system without the formation of the high energy intermediate aggregates. I showed that this pathway provides a feasible breakdown route with breakdown times of the order of seconds for $C_{12}E_8$.

In this chapter I will describe direct measurements of micelle breakdown times using a combination of stopped-flow dilution and high speed fluorescence detection. In the simplest form of the stopped-flow technique, two reactant solutions are rapidly mixed by being forced into a mixing chamber and then into an observation cell. At some point in time the flow is suddenly stopped and the reaction monitored using a suitable spectroscopic probe such as absorbance, fluorescence or circular dichroism. The change in spectroscopic response as a function of time is recorded. In order to study micelle kinetics the 'reactants' may be a micellar solution and water, or a combination of micellar solutions at different concentrations. The advantage of the stopped-flow technique over other perturbation experiments, such as temperature or pressure jump, is the ability to induce larger perturbations from equilibrium. I have used stopped-flow to mix micellar surfactant solutions with pure water and monitored the system response using the fluorescence spectra of pyrene solubilised within micelles. The use of a fluorescence probe to study a kinetic process in a micellar solution was first attempted in 1964 by Förster and Sellinger, involving excimer formation in micelles containing pyrene. [137] Pyrene is a polycyclic aromatic hydrocarbon consisting of four fused benzene rings resulting in a large flat aromatic system. The

solubility of pyrene in water is 7×10^{-7}M. [138] When pyrene is present in a micellar solution the pyrene molecules are primarily solubilised in micelles. Pyrene is a popular fluorescence probe for the study of micelles due to the rich information which the spectra provide. [139-144] The fluorescence spectrum of pyrene is made up of two components. Monomeric pyrene fluorescence is characterised by five distinct vibronic bands between 375 - 395 nm (Figure 43). The ratio of the intensities of the first I_1(375 nm) and third I_3(385 nm) vibronic bands is related to the polarity of the local pyrene environment. Pyrene in water is characterised by a ratio $I_1 / I_3 = 1.6$. This ratio is lowered for pyrene solubilised in micelles with typical values in the range 0.9 – 1.3 depending on the polarity of the surfactant structure (see Appendix 2). Changes in this ratio provide an additional method for the determination of the cmc using plots of I_1 / I_3 vs. bulk concentration since the formation of micelles results in a change in the environment of pyrene. Additional information from pyrene fluorescence spectra can be obtained from the formation of excited encounter pairs. Excited pyrene monomers may associate with a ground state pyrene monomer to form an excimer which gives a broad structureless emission band centred at 450 nm (Figure 43). The ratio of monomer and excimer emission provides useful information about the average number of pyrene monomers within a micelle. Fluorescence information has been used by many experimentalists to deduce micelle aggregation numbers. [139, 142, 143] Even when micelles contain large numbers of pyrene monomers, the probability that pyrene monomer fluoresces is nonzero, therefore the ratio of monomer to excimer fluorescence does not go to zero.

I have used changes in the fluorescence spectra of pyrene with bulk concentration, which is related to the number of micelles present in the system, to track changes in the number of micelles with time following a stopped-flow dilution experiment. I have used a range of nonionic surfactants with and without the presence of small amounts of cationic surfactants to investigate the mechanism of micelle breakdown. The addition of the cationic surfactant hexadecyl trimethylammonium bromide (CTAB) is expected to introduce a barrier to the merging of proper-micelles, allowing me to test the hypothesis put forward in Chapter 5 regarding the pathway of micelle breakdown.

6.2. Experimental

6.2.1. Stopped-flow instrumentation

Micellar surfactant solutions were rapidly diluted with pure water using an SX20 Stopped-Flow Reaction Analyser (Applied Photophysics, Figure 41). For 1:1 ratio mixing, samples were contained within 2.5 ml drive syringes, driven at 4 bar through a T-mixer into the 20 μl quartz optical cell. Total drive volume was 120 μl to ensure complete flushing of optical cell contents. The flow diagram for the SX20 sample handling unit is shown in Figure 42. Dead time for the instrument in this configuration is 1.1 ms. The drive syringes, optical cell and flow system were thermostatted with a water bath accurate to ± 0.1°C. Experiments were carried out at two temperatures, 5 °C and 20 °C. Particular care was taken when loading surfactant solutions into the drive syringes to avoid the formation of air bubbles which affect the fluorescence spectra by scattering excitation light into the collection optical fibre.

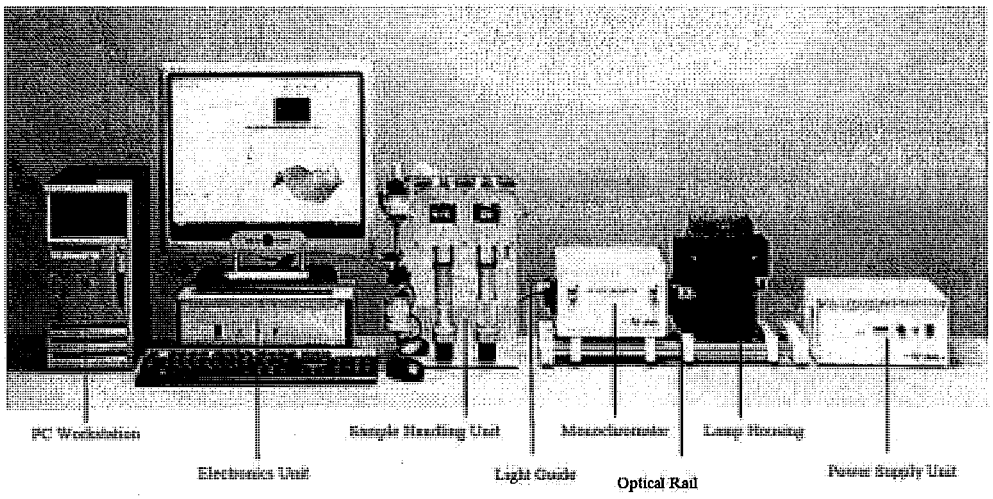

Figure 41: Image of the SX20 Stopped-flow Reaction Analyser (Applied Photophysics)

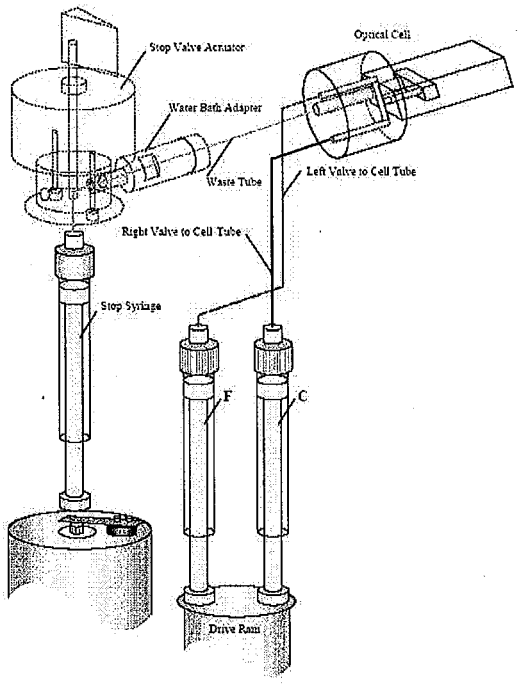

Figure 42: Flow diagram for the SX20 sample handling unit showing the two drive syringes, stop syringe and optical cell.

6.2.2. Equilibrium pyrene fluorescence measurements

Concentrated surfactant solutions containing pyrene were prepared in the following way. Pyrene (sublimed, 99%, Sigma) was dissolved in HPLC grade ethanol to prepare a stock solution of known concentration. A small amount of stock pyrene solution was added to a clean volumetric flask and the ethanol evaporated off under a stream of nitrogen to leave a thin layer of pyrene deposited in the flask. Surfactant was added to the flask and Millipore water used to make up the solution to volume. A stirrer bar was added and the solution left to stir vigorously for at least 24 hours. To minimise any photo-bleaching the flask was covered during the stirring period. No solid pyrene was visible following the stirring period. Surfactant-pyrene solutions used in the stopped-flow dilution experiments reported below were prepared by dilution of the concentrated stock solution approximately one hour before use. Total pyrene concentration was 1% of the bulk non-ionic surfactant concentration. This choice of pyrene concentration is discussed further in section 6.3.1.1 below.

Pyrene fluorescence spectra were acquired with a QE65000 Scientific-grade Spectrometer (Ocean Optics) selected for high sensitivity and relatively fast integration times (≥ 7 ms). The QE65000 contains a Hamamatsu S7031-1006 FFT-CCD area detector that is TE-cooled to minimise dark signal and enables detection of low light levels. The S7031 is a 2D array (1024 × 64 pixels), allowing pixels to be binned in a vertical column that acquires light from the entire height of the spectrometer slit. A 10-μm entrance slit and H3 grating (groove density 600) tuned to detect light in the range 350 – 700 nm provides 3 pixels/nm resolution. Light is delivered to the QE65000 using an 0.5 m length, 1000-μm diameter UV-VIS optical fibre coupled with a precision SMA 905 connector to align the slit and fibre terminus. The acquisition end of the fibre is held against the viewing window of the 20-μl optical cell which is used for both equilibrium and kinetic measurements. Samples are illuminated perpendicular to collection with 337 nm light from a Xe-Ar lamp monochromated with 2-mm slit width equivalent to a 9 nm bandpass. Excitation wavelength was chosen to maximise fluorescence intensity.

Equilibrium spectra were acquired for each surfactant-pyrene system (see section 6.2.3) at a range of bulk concentrations to provide calibration curves that relate fluorescence ratios to the number of micelles in each system. For equilibrium measurements, identical solutions were loaded into each drive syringe and pumped into the optical cell. Data were acquired for each system at two temperatures, 5 °C and 20 °C, with samples allowed to equilibrate within the drive syringes before pumping. Data were also acquired with and without the presence of 10% mole fraction ($\chi = 0.1$) of the cationic surfactant CTAB.

Data acquisition was controlled through the SpectraSuite software package. An integration time of 1000 ms was suitable for equilibrium measurements providing high count rates and detailed spectra. Equilibrium spectra were analysed using the Matlab computational package. The monomer fluorescence ratio I_1 / I_3 for each equilibrium spectra was determined using a peak picking script which identified maximum peak intensities for each vibronic band. Although peak maxima are more subject to noise than a fitting procedure, with a 1000 ms integration time the count rates were sufficiently high to make ensure that any noise effects on the I_1 / I_3 ratio was negligible. For each surfactant an I_1 / I_3 vs. bulk concentration plot was produced

(Appendix 2) . The ratio of monomer to excimer fluorescence I_{mon}/I_{exc} was determined using a least-square fitting procedure to determine the relative amounts of monomer and excimer components by comparison to idealised component spectra. These components are plotted in Figure 44.

The existence of a small amount of excimer emission below the cmc is primarily due to the existence of small aggregates clustering around pyrene molecules. The proportion of excimer emission below the cmc is typically very small, indicating that a very low proportion of the pyrene molecules present are solubilised in this way.

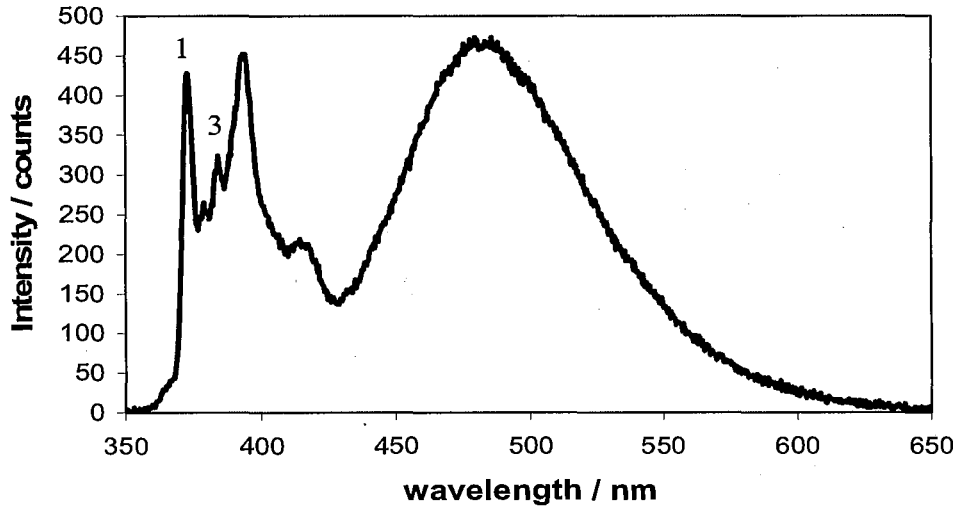

Figure 43: Pyrene fluorescence spectra for 1% pyrene in 0.3 mM TX100 solution excited at 337 nm.

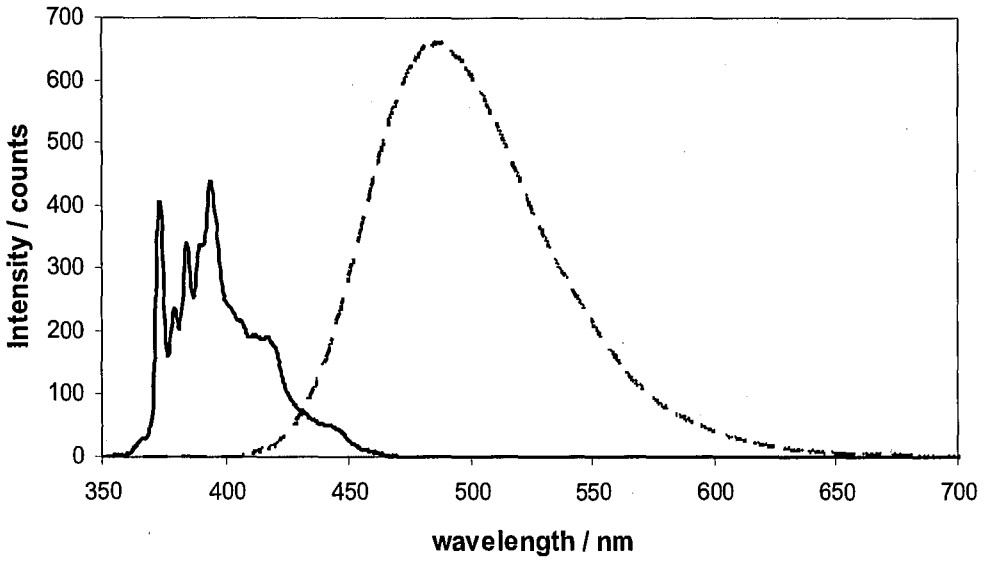

Figure 44: Idealised spectral components for monomeric fluorescence (solid line) and excimer fluorescence (dashed line)

6.2.3. Stopped-flow kinetic measurements of micelle breakdown

Breakdown kinetics were measured at two different temperatures, 5 °C and 20 °C, in the presence and absence of 10% mole fraction of CTAB. However, kinetic data acquired at 20 °C proved difficult to analyse since a significant proportion of micelles had broken down on timescales more rapid than my experiment could determine. Kinetic analysis will be restricted to 5 °C in order to extract trends and make comparison with model predictions.

I have measured the kinetics of micelle breakdown using stopped-flow-fluorescence for five surfactants: Triton X-100, C_{14}DAPS, α-C_{12}malt, β-C_{12}malt and $C_{12}E_8$. The range of surfactants that can be investigated by this method was limited by my chosen probe, the ratio I_{mon} / I_{exc} of pyrene. In order to generate a measurable change in this signal upon dilution there must be a sufficient change in the average number of pyrene monomers per micelle. For my experimental set-up, a sufficient change is induced provided that a micellar surfactant solution is diluted to within at least a factor of 10 of its cmc. For some surfactants used in this project, such as $C_{14}E_8$, the cmc is so low so that at the bulk concentrations required to induce this change the

total fluorescence signal is too low to permit the rapid integration times necessary for kinetic investigation.

Micelle breakdown kinetics were measured in a series of 2-fold dilution experiments, mixing surfactant solution and pure water in a 1:1 ratio. A 2-fold dilution was chosen to match the optimum operating parameters of the SX20 stopped-flow mixing system. Five different starting concentrations were used, defined relative to the surfactant cmc (2, 4, 6, 8 and 10 × cmc). These cmc's were determined from my equilibrium fluorescence measurements and are given in Table 17. The acquisition procedure is explained in the following section and the equilibrium fluorescence ratios are provided in Appendix 2.

For each 2-fold dilution experiment, data were acquired at three different integration times; 10 ms, 100 ms and 1000 ms. In each case 100 spectra were recorded corresponding to total measurement times of 1, 10 and 100 seconds respectively. Each integration time was repeated three times. Data acquisition was triggered on the motion of the stop-syringe using the SpectraSuite external trigger option.

Data were analysed using Matlab. The results of each integration time were treated independently. First I averaged the three sets of data acquired at each integration time, then, using the least-squares fitting procedure described in section 6.2.2, I extracted the relative contribution of monomer and excimer fluorescence to determine I_{mon} / I_{exc} as a function of time. The time dependent I_{mon} / I_{exc} data were converted into micelle concentration by using the equilibrium I_{mon} / I_{exc} data as calibration curves.

6.3. Results and Discussion

6.3.1. Equilibrium Fluorescence Spectra

It is important to study the equilibrium fluorescence spectra to explore the effect that the presence of pyrene has on the micelles. In this first part of my results I will review the information provided by the equilibrium fluorescence spectra.

6.3.1.1 The effect of pyrene on micellisation

Pyrene monomer fluorescence ratios (I_1 / I_3) are related to the local environment of pyrene and provide a measure of the cmc. Figure 45 shows the I_1 / I_3 ratio for solutions of Triton X-100 containing pyrene at 0.5, 1 and 2% pyrene (relative to the bulk surfactant concentration). These experiments were performed to establish whether the presence of pyrene in micelles at low concentrations altered the cmc. The cmc is usually taken to be the point of steepest gradient on the I_1 / I_3 curve, which gives 0.35 mM for each of the curves in Figure 45, in agreement with literature values for Triton X-100 (Table 1). There is no evidence that the presence of pyrene in these low concentrations affects the onset of micellisation for Triton X-100.

Figure 46 shows the I_{mon} / I_{exc} ratio for the same set of Triton X-100 data. As the pyrene concentration is increased the proportion of excimer emission also increases, due to the increased probability that an excited pyrene monomer encounters a ground state pyrene. The minimum monomer to excimer ratio is expected at the cmc, where the average number of pyrene monomers per micelle is maximised. The average pyrene occupancy per micelle N_{PY} is given by

$$N_{PY} = \frac{[Py]N}{(c_b - \text{cmc})} \tag{6.1}$$

As bulk concentration c_b increases above the cmc the average number of pyrene molecules per micelle falls and the I_{mon} / I_{exc} ratio increases. Pyrene molecules are generally considered to be distributed amongst micelles following a Poisson distribution. [145] Therefore the probability that there are k pyrene molecules in a given micelle can be calculated using

$$P(k, N_{PY}) = \frac{N_{PY}^k \exp(-N_{PY})}{k!} \tag{6.2}$$

If one assumes that any micelle containing 2 or more pyrenes will only contribute towards excimer fluorescence and all monomer fluorescence originates from singly occupied micelles then for each bulk concentration one can use equations (6.1) and

(6.2) to calculate the relative probabilities P_{mon} / P_{exc} of monomer and excimer fluorescence

$$\frac{P_{mon}}{P_{exc}} = \frac{P(1, N_{PY})}{\sum_{k=2} P(k, N_{PY})} \tag{6.3}$$

These relative probabilities produce a curve shape very close to the experimental I_{mon} / I_{exc} data. These relative probabilities may be multiplied by a pre-factor, E, to give curve fits very close to the experimental I_{mon} / I_{exc}

$$\frac{I_{mon}}{I_{exc}} = \mathrm{E}\frac{P_{mon}}{P_{exc}} = \mathrm{E}\frac{P(1, N_{PY})}{\sum_{k=2} P(k, N_{PY})} \tag{6.4}$$

where the concentration dependence is contained within the N_{PY} term. Figure 46 contains these curve fits for the Triton X-100 data with pre-factors 4.5, 6.3 and 12 for pyrene concentrations of 0.5, 1 and 2% respectively. The pre-factors may be related to the quantum efficiency and lifetimes of monomer and excimer emission. Deviations from the experimental data are probably due to the failure of the assumption that micelles containing two or more pyrene monomers cannot contribute toward monomer emission and the contribution from free pyrene when the concentration of micelles is very small.

As with the I_1 / I_3 data there is no evidence that the presence of pyrene affects the onset of micellisation in this low concentration regime. The I_{mon} / I_{exc} ratio shows greatest sensitivity to the concentration of micelles at 0.5 % since the average pyrene occupancy is lowest. However, the fluorescence spectra are more noisy due to lower light levels. A pyrene concentration of 1% was used for all subsequent kinetic measurements.

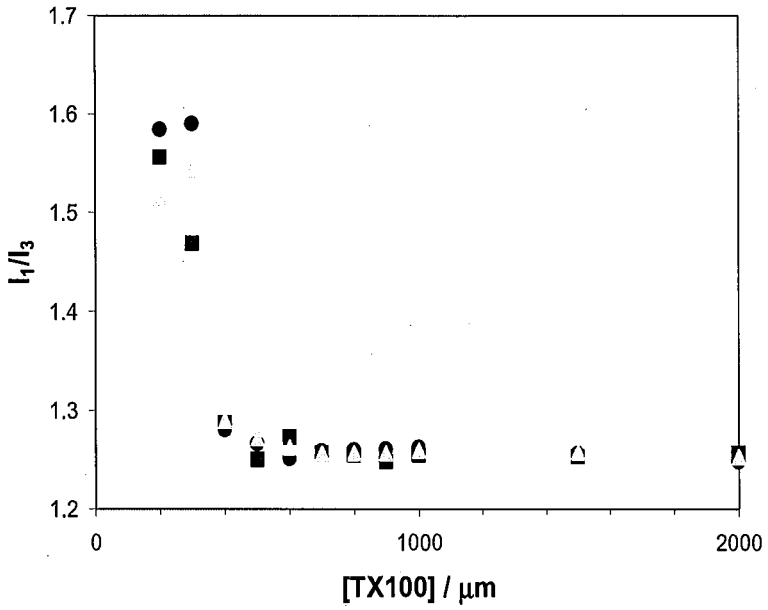

Figure 45: I_1 / I_3 **ratio for pyrene solubilised in Triton X-100 solution at (•) 0.5%, (■) 1 % and ( ) 2% relative concentration respectively. The cmc is usually taken to be the point of maximum gradient on the** I_1 / I_3 **vs. concentration curve = 0.35 mM in this case.**

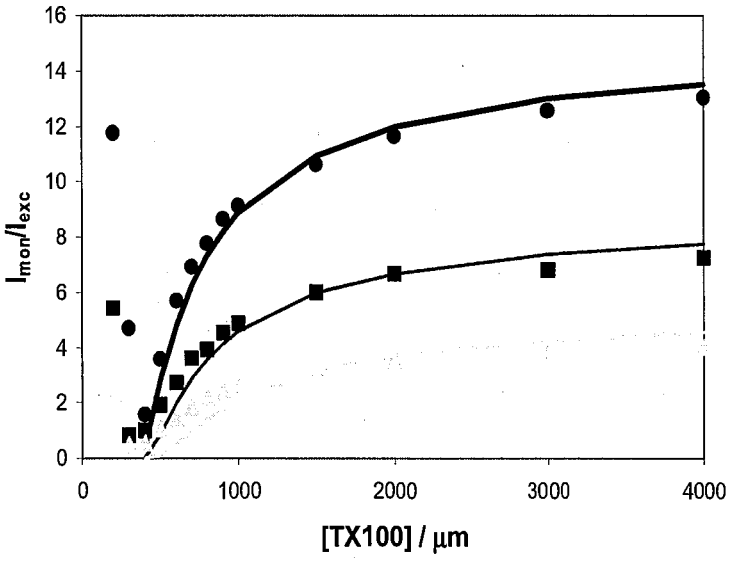

Figure 46: I_{mon} / I_{exc} **ratio for pyrene solubilised in Triton X-100 solution at (•) 0.5%, (■) 1 % and ( ) 2% relative concentration respectively. Lines are drawn following a Poisson distribution and assuming that all monomer emission originates from singly occupied micelles above the cmc.**

6.3.1.2. The effect of temperature on micellisation

Plots of I_1 / I_3 and I_{mon} / I_{exc} for each of the systems studied are shown in Appendix 2 with the corresponding value of the critical micelle concentration obtained from these fluorescence ratios shown in Table 17. In almost all cases the maximum gradient in the I_1 / I_3 curve coincides with the minimum in I_{mon} / I_{exc}, providing strong evidence for the onset of micellisation. The only exception is the data for α-C_{12}malt in the absence of CTAB. The cmc in Table 17 corresponds to the I_1 / I_3 data, with the position of the minimum in I_{mon} / I_{exc} in parenthesis. One possible cause for this discrepancy is a change in micelle aggregation number very close to the cmc. If micelle size for this surfactant does change slightly very close to the cmc, the onset of micellisation could still be accurately identified by I_1 / I_3 data, but I_{mon} / I_{exc} would behave differently very close to the cmc.

The reason that I_{mon} / I_{exc} decreases with increasing temperature may be related to increased mobility of the pyrene monomers within the micelle, favouring association and therefore increased excimer fluorescence.

For both TX-100 and $C_{12}E_8$ which contain a polyoxyethylene chain, an increase in temperature results in a decrease in cmc by 0.05 mM in the absence of CTAB and 0.025 mM in the presence of CTAB. This cmc reduction may be related to the reduction in the number of water molecules hydrating the polar headgroup. As temperature increases the polyoxyethylene chain is dehydrated. The effect of this dehydration may be quantified by equations 4.38, 4.39 and 4.41 of the molecular thermodynamic theory which are all dependent upon ϕ_{Eg}, the volume fraction of polymer in the shell region. Equation 4.38 quantifies the polymer-solvent mixing free energy and becomes more positive as ϕ_{Eg} increases with temperature. However, both the headgroup deformation free energy (4.39) and aggregate-core interfacial free energy (4.41) become more negative as ϕ_{Eg} increases, favouring micellisation. Simulations with different water content in the shell region for $C_{12}E_8$ show the cmc to be highly dependent upon *W*, the number of water molecules per ethylene oxide unit.

Conversely, for the dodecyl maltosides an increase in temperature results in a 0.025 mM increase in cmc. Whilst the polar headgroup for these surfactants contain an ether

linkage and several hyroxyl groups that will bind water molecules, I expect that the cyclic configuration of the headgroup will make the headgroup deformation free energy less dependent upon water content.. This subtle change may allow the tail transfer free energy, which become more positive as temperature is increased, to overcome free energy changes related to the headgroup and the cmc increases accordingly. Unfortunately I have no simple thermodynamic model for maltoside surfactant micellisation to test this hypothesis

No change in cmc is observed for zwitterionic C_{14}DAPS.

cmc / mM	No CTAB		10 % CTAB	
	5°C	20°C	5°C	20°C
TX100	0.35	0.3	0.3	0.275
C_{14}DAPS	0.3	0.3	0.275	0.275
β-C_{12}m	0.175	0.2	0.15	0.175
α-C_{12}m	0.2 (0.3)*	0.225 (0.275)*	0.175	0.2
$C_{12}E_8$	0.175	0.125	0.15	0.125

Table 17: Critical micelle concentrations derived from fluorescence ratios for surfactants studied using stopped-flow fluorescence technique. * indicates where I_1 / I_3 and I_{mon} / I_{exc} give slightly different values. Discussion in text.

6.3.1.3. The effect of CTAB on micellisation

Carnero-Ruiz [64] found an interaction parameter, $\beta \approx -3$, for mixed micelles of $C_{12}E_8$ with the cationic surfactant C_{14}TAB. This interaction parameter corresponds to approximately 95% of added C_{14}TAB partitioned into the nonionic micelles. In my fluorescence experiments, the chain length of all surfactants is similar, so a similar value of β is expected. My equilibrium fluorescence measurements show no significant change in cmc, in terms of total surfactant concentration, upon addition of CTAB.

6.3.2. Micelle relaxation kinetics

Kinetic data have been analysed and conclusions drawn regarding the nature of micelle breakdown in nonionic systems. Before I present my data analysis, I will first

discuss a number of limitations which one should bear in mind when considering the analysis below.

6.3.2.1. Limitations of my analysis

Analysis of data has been limited by a range of factors, both instrumental and theoretical. Consider the sample data plotted in Figure 47 which shows the micelle concentration as a function of time for 10 seconds following a 2-fold dilution of a 1.75 mM $C_{12}E_8$ solution at 5 °C. The data for the entire measured decay are plotted in Figure 48 on a log-log scale. These curves been extracted from the I_{mon} / I_{exc} ratio of the kinetic pyrene fluorescence spectra, using the corresponding equilibrium fluorescence data as a calibration curve and assuming a single aggregation number deduced from small angle neutron scattering. Notice how the data acquired at different integration times do not coincide at very short times, particular the 1000 ms data points which exceed the 10 and 100 ms data. This error is due to an instrumental limitation of the QE65000 spectrometer and is related to the acquisition time used to acquire spectra. When spectra are acquired as a function time using the 'High Speed Acquisition' (HSA) software, all other spectrometer processes are paused. When the HSA is triggered, if the required kinetic integration time differs from the current spectrometer integration time there follows a time delay in the range of one to two integration times before the kinetic acquisition is recorded. For example, if the spectrometer is acquiring data at 100 ms integration time when the HSA is triggered, with a target kinetic integration of 1000 ms, there follows a 1000 - 2000 ms delay before kinetic data are recorded. This limitation has only become apparent upon data analysis. For instance, it became clear that I_{mon} / I_{exc} at the first measured data point always had a lower value than the subsequent second data point, suggesting that this data point corresponded to the system before the stopped-flow mixing i.e. the first kinetic spectra contained information relating to the pre-mixed system. Often the second data point had a lower value than the third data point.

In order to analyse the kinetic decays I modified the timestamps by subtracting a constant time interval from each recorded timestamp (i.e. 15, 150 or 1500 ms depending on the experiment) and discarded the first two data points, e.g. for a 1000 ms acquisition, the third measured data point at 2000 ms became the first reported data point at 500 ms. I chose to subtract 1 ½ time intervals from the recorded time

stamps for two reasons: (1) The acquisition delay was in the range 1 – 2 time intervals and (2) the resulting modified time intervals now confirm that the fluorescence information corresponds to an average over the time interval and is not an instantaneous snapshot of the system. This timestamp modification has no impact on the conclusions drawn later on due to the use of ln[concentration] versus time curves during analysis which render the fitted parameters insensitive to this offset.

A large number of my kinetic measurements appear to reach equilibrium within the 100 seconds measurement time i.e. the kinetic value of I_{mon}/I_{exc} reaches a limiting value and ceases to change on the measured timescale. For a small number of these experiments this limiting value of I_{mon}/I_{exc} was different from the value expected from my equilibrium measurements. Where this discrepancy occurred, I used the kinetic limiting value for I_{mon}/I_{exc} after 100 seconds in my data analysis. These discrepancies may be due to mixing errors or contamination of the pure water with surfactant solution.

Quantitative analysis of these decay curves is limited by the complexity of the micelle relaxation process. In Chapter 5 I proposed a new pathway for micelle breakdown that permits micelle breakdown on physically realistic timescales. Although my numerical simulations were unable to capture all of the pathways in the micelle relaxation process, particularly the reversibility of micelle breakdown as equilibrium is approached, I reasoned that micelle relaxation will be characterised by a continuously changing decay rate as both the monomer concentration and numbers of remaining micelles approach their new equilibrium values. Figure 49 shows the data in Figure 47 re-plotted with micelle concentration on a log scale. Since a single exponential decay would take the form

$$[\text{micelles}]-[\text{micelles}]_{t=\infty} = C\exp[-t/\tau] \qquad (6.5)$$

where τ is the relaxation time, then a plot of $\log([[\text{micelles}]-[\text{micelles}]_{t=\infty})$ against time would be linear if this functional form described the decay. However, the curves in Figure 49 are not linear, indicating that relaxation times are variable. This behaviour is characteristic of all of my measured decay curves and stands in contradiction of the theory of Aniansson and Wall which predicts a single relaxation

time, usually referred to as τ_2. This kind of variable relaxation rate was observed in the outputs of my numerical modelling in Chapter 5 based upon my combine fusion-Becker-Döring model. In order to draw some semi-quantitative conclusions, it is possible to fit the decay curves over a small time interval to extract a local decay rate that can be extrapolated back to $t = 0$ and compared between different micellar systems.

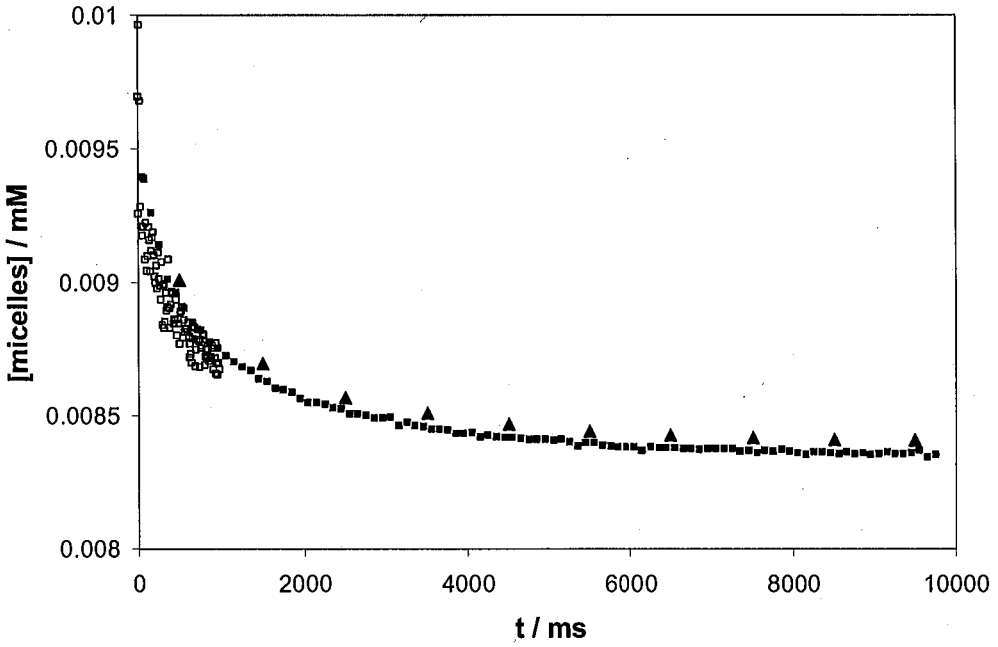

Figure 47: Relaxation of micelle concentration with time for $C_{12}E_8$ at 5 times cmc, created by 2-fold dilution of a 10 times cmc solution at 5 °C. Data are shown for first ten seconds only. (□) 10 ms, (■) 100 ms and (▲) 1000 ms integration time.

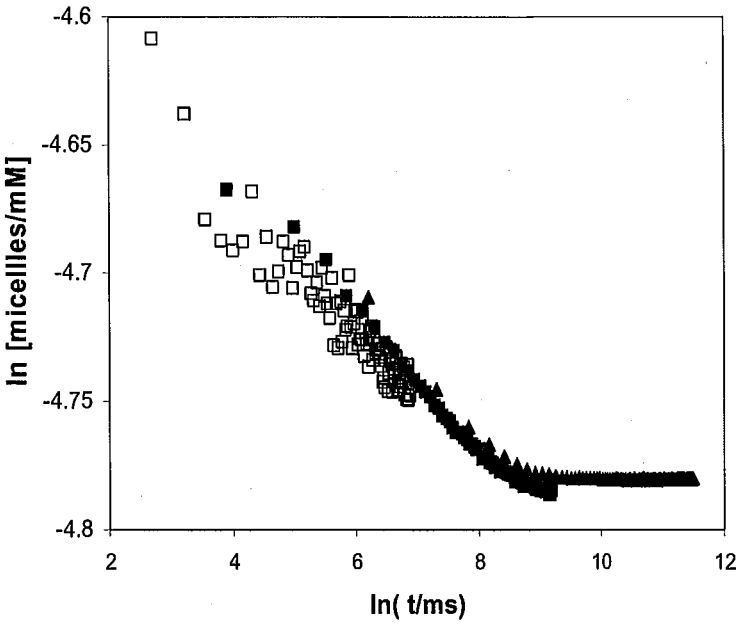

Figure 48: Relaxation of micelle concentration with time for $C_{12}E_8$ at 5 times cmc, created by 2-fold dilution of a 10 times cmc solution at 5 °C. Data are plotted on a log-log scale to show the entire measured decay. (□) 10 ms, (■) 100 ms and (▲) 1000 ms integration time.

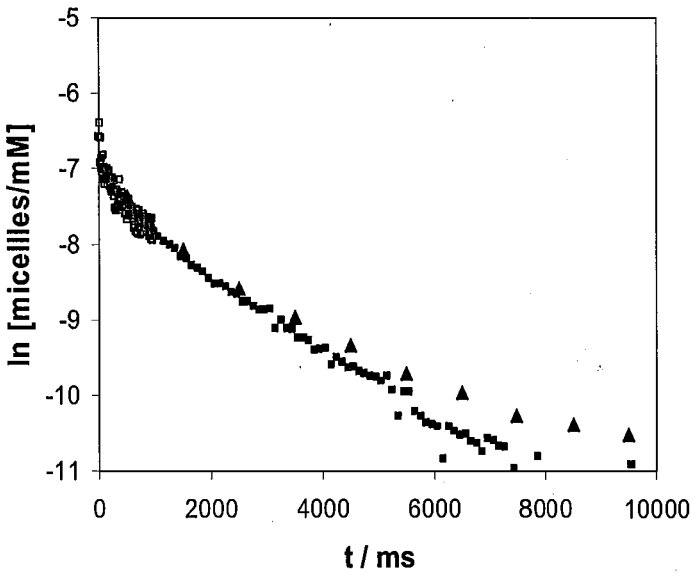

Figure 49: Relaxation of micelle concentration with time for $C_{12}E_8$ at 5 times cmc, created by 2-fold dilution of a 10 times cmc solution at 5 °C. Data are shown for first ten seconds only. (□) 10 ms, (■) 100 ms and (▲) 1000 ms integration time.

6.3.2.2. $C_{12}E_8$ micelle relaxation

Micelle relaxation data for $C_{12}E_8$ provides the best case study because, as the surfactant with lowest cmc of those studied by stopped flow, the micelles are more stable. For some of the higher cmc surfactants, such as TX-100, most micelles have broken down before data collection can begin, even at 5 °C. In order to compare different perturbation amplitudes in a quantitative way I have found it useful to define a reaction progress variable

$$\Delta(t) = \frac{c_{mic}(t) - c_{mic}^{f}}{c_{mic}^{i} - c_{mic}^{f}} .100 \tag{6.6}$$

where $\Delta(t)$ is the 'reaction' progress, $c_{mic}(t)$ is the measured micelle concentration and c_{mic}^{i} and c_{mic}^{f} are the initial and final concentration of micelles calculated from the bulk concentration. Although I will refer to 'reaction progress', $\Delta(t)$ is really the inverse reaction progress since '100' corresponds to no progress and '0' to completion.

Complete micelle relaxation curves for $C_{12}E_8$ dilutions performed at 5 °C and converted into $\Delta(t)$ have been plotted in Figure 50 and Figure 51 for 10 ms and 100 ms integration times, respectively.

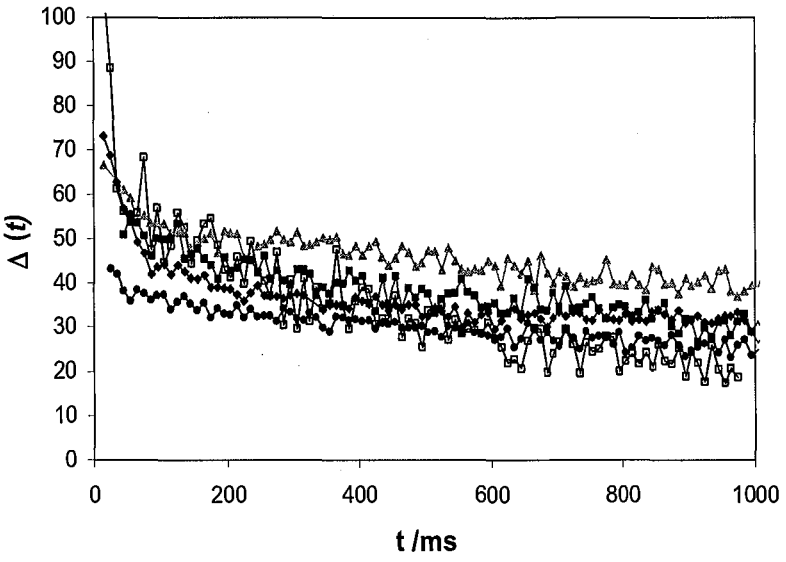

Figure 50: Micelle relaxation curves for $C_{12}E_8$ solutions subjected to 2-fold dilutions at 5 °C plotted as 'reaction progress' . Initial concentrations are (♦) 2 cmc, (■) 4 cmc, (▲) 6 cmc, (●) 8 cmc and (□) 10 cmc. For clarity only 10 ms integration time data have been plotted. Lines have been added to guide the eye.

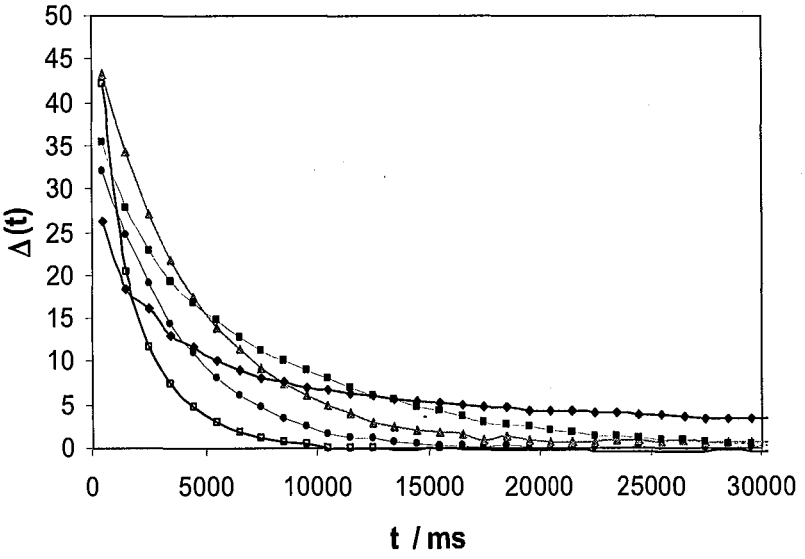

Figure 51: Micelle relaxation curves for $C_{12}E_8$ solutions subjected to 2-fold dilutions at 5 °C plotted as 'reaction progress' . Initial concentrations are (♦) 2 cmc, (■) 4 cmc, (▲) 6 cmc, (●) 8 cmc and (□) 10 cmc. For clarity only 1000 ms integration time data have been plotted. Lines have been added to guide the eye.

There are two important parameters which may be extracted from the relaxation curves in Figure 51: (1) the number of micelles that break down before data acquisition begins; (2) the rate of micelle breakdown in the early stages of the decay curves.

Both of these parameters can be evaluated semi-quantitatively by fitting the decay curves with a simple exponential over a small time interval. In order to ensure that the decay coefficients were insensitive to any remaining timestamp errors, I elected to take the log of my $\Delta(t)$ values and fit each curve using

$$\ln[\Delta(t)] = -At + B \tag{6.7}$$

with A and B allowed to vary. Fits were performed for each dilution factor and integration time over time intervals corresponding to 10 – 100 ms, 100 – 1000 ms and 1000 – 10000 ms for integration times of 10, 100 and 1000 ms respectively.

I will first consider the number of micelles which break down more rapidly than my experiment can determine, i.e. micelle lifetime < 10 ms. This information can be obtained from $\exp(B)$ where B is taken from the fit to my 10 – 100 ms data. These values are given in Table 18 for $C_{12}E_8$.

$c_b(t=0)$	$\Delta(t=0)$
2 - cmc	78
4 - cmc	71
6 - cmc	55
8 - cmc	43
10 - cmc	82

Table 18: $\Delta(t=0)$ $C_{12}E_8$ determined from data fitting to 10 ms decay curves for different initial bulk concentrations at 5 °C.

It appears from the values in Table 18 that the degree to which micelles can break down on very short timescales varies with bulk concentration. Concentrations close to the cmc and very far above the cmc lose fewer micelles than intermediate concentrations. The same pattern is observed for each of the surfactant systems I have investigated using stopped-flow dilution.

Provided that there is sufficient monomer depletion in the system, both the conventional Becker-Döring and the combined fusion-Becker-Döring process permit

rapid micelle breakdown on ms timescales. In the case of the conventional Becker-Döring model, monomer depletion reduces the free energy barrier that exists between the region of monomers and the region of proper micelles. A large enough reduction in the free energy barrier permits micelle breakdown by the conventional Becker-Döring process originally proposed by Aniansson and Wall. This rapid micelle breakdown will cease when the monomer concentration recovers and the free energy barrier becomes prohibitive once more. In the combined fusion-Becker-Döring model I have proposed the net rate of micelle breakdown is also increased by monomer depletion which favours monomer loss from super-micelles. Monomer depletion also prevents the reverse fusion-Becker-Döring reaction which would lead to micelle formation and would slow the net breakdown rate of micelles.

The trends shown in Table 18 allow one to investigate whether it is the conventional Becker-Döring or the combined fusion-Becker-Döring that dominates rapid micelle breakdown in these systems. In the case of the conventional Becker-Döring, rapid micelle breakdown will cease once monomer concentration recovers close to the cmc. The proportion of micelles that are required to breakdown to establish this quasi-equilibrium will increase as bulk concentration is lowered. Therefore, if rapid micelle breakdown in this system occurred through the conventional Becker-Döring I would expect the values in Table 18 to simply increase as bulk concentration increased. Furthermore, stochastic simulations in Chapter 4 predicted that $X_1 < 0.5\,\mathrm{cmc}$ is required to lower micelle lifetimes below 10 ms in the conventional Becker-Döring model (see Figure 31). This situation will only exist for a very short time following dilution.

For the combined fusion-Becker-Döring model, rapid micelle breakdown will also cease once monomer concentration has recovered, but there is an additional requirement that there are enough proper-micelles present in the system to fuse with each other. For bulk concentrations close to the cmc, rapid micelle breakdown will be hindered by the relatively low concentration of proper-micelles. At higher concentrations very few micelles need to break down to establish quasi-equilibrium. It follows that the proportion of micelles lost in rapid micelle breakdown will be greatest for intermediate concentrations if the fusion-Becker-Döring mechanism

governs the rate of micelle breakdown at short times. This is the trend that is observed for each of the systems I have measured using this stopped-flow system.

I will now compare the micelle breakdown rate in the early stages of each decay, following the rapid monomer loss explained above. Table 19 gives the decay coefficient for the linear fits to each decay curve at each integration time.

$c_b(t=0)$	A (10ms)	A (100ms)	A (1000ms)
2 - cmc	6.2	0.5	0.2
4 - cmc	4.5	0.4	0.1
6 - cmc	2.3	0.3	0.2
8 - cmc	1.9	0.3	0.3
10 - cmc	5.3	1.0	0.5

Table 19: Exponential decay coefficient, b, for $C_{12}E_8$ determined from data fitting to decay curves for different initial bulk concentrations and integration times at 5 °C.

A similar pattern emerges when comparing the decay coefficients for micelle breakdown in the early stages of each decay. The decay coefficient is larger at concentrations close to the cmc and far above the cmc than it is at intermediate concentrations.

First one must ask whether this behaviour can be reconciled with the predictions of the conventional Becker-Döring model. Aniansson and Wall predicted that this quasi-equilibrium relaxation process would be characterised by a single relaxation time, τ_2 (equation 4.28). I have already demonstrated in Figure 49 that the measured relaxation of micelles in this work do not behave as though characterised by a single relaxation time. The concentration dependence of the Aniansson and Wall relaxation time is complicated due to the influence of two opposing effects. As the bulk concentration increases the amount of material in the intermediate region of the micelle size distribution, between the regions of monomers and proper micelles, also increases. This increase in material results in a decrease in the resistance to flow through this region, which should accelerate micelle breakdown. However, an increase in bulk concentration also reduces the driving force for re-equilibration since the relative perturbation of aggregates is reduced. The resultant concentration dependence of micelle breakdown rate is complicated. Experimental evidence published by Aniansson and Wall in 1976 [55] indicate that the slow relaxation time, τ_2,

was fairly constant with an increase in bulk concentration for a system of sodium dodecyl sulfate micelles. In order to explain the micelle breakdown behaviour in Table 19 within the Aniansson and Wall model it would be necessary for the resistance to flow through the region of intermediate aggregate sizes to rapidly decrease very close to the cmc, contrary to the expected trend.

Second, one can question whether or not the observed micelle breakdown behaviour can be reconciled with my combined fusion-Becker-Döring hypothesis. There are two factors that influence the rate of micelle breakdown within my proposed pathway: (1) the rate of collisions of proper micelles and (2) the probability that super-micelles are able to shed monomers within their short lifetimes. Numerical simulations in Chapter 4 revealed that the monomer concentration at which quasi-equilibrium is reached increases with bulk concentration. Therefore, for systems closest to the cmc the net probability of monomer loss from super-micelles would remain relatively high since the monomer concentration in the quasi-equilibrium state would be lower than in systems initially at greater bulk concentration.

For systems that are far above the cmc, whilst the monomer concentration will recover almost fully back to the cmc, significantly more micelles remain to undergo collisions to form super-micelles. This increased rate of super-micelle formation may accelerate micelle breakdown.

The values in Table 19 can therefore be reconciled with the proposed fusion-Becker-Döring pathway. Relaxation of the remaining micelles is favoured for systems very close to the cmc since the monomer concentration is unable to recover to the same degree as higher concentration systems, thus favouring monomer release from super-micelles. For systems at much higher concentration micelle breakdown is favoured due to the increased number of collisions of proper-micelles.

6.3.2.3. Effect of CTAB addition on micelle relaxation

Stopped-flow dilution experiments with $C_{12}E_8$ were repeated with 10% mole fraction of CTAB added to each solution. Figure 52 shows the decay in micelle concentration following a 2-fold dilution for each of the $C_{12}E_8$/CTAB mixtures at 5 °C. These curve shapes may be compared with those in Figure 51 for the pure $C_{12}E_8$ case. It is immediately apparent upon visual comparison that addition of small amounts of

positive charge slows micellar relaxation, with increased proportions of micelles remaining at the end of the measured decays.

Within the conventional Becker-Döring model there is no apparent reason why the addition of positive charge should significantly affect the rate of micelle breakdown. However, within the combined fusion-Becker-Döring model the addition of positive charge will introduce a barrier to the merging of proper-micelles and slow the total rate of micelle breakdown. The comparison between Figure 51 and Figure 52 provides additional support for my combined fusion-Becker-Döring model explaining the process of micelle breakdown.

Data fitting to the $C_{12}E_8$/CTAB supports these conclusions. Table 20 shows the proportion of micelles remaining when my measurements begin. For each bulk concentration, the proportion of remaining micelles is greater than that for the corresponding pure $C_{12}E_8$ system. This behaviour is consistent with rapid micelle breakdown via the combined fusion-Becker-Döring route as explained in section 6.3.2.2.

$c_b(t=0)$	$\Delta(t=0)$
2 - cmc	94
4 - cmc	72
6 - cmc	75
8 - cmc	88
10 - cmc	121*

Table 20: $\Delta(t=0)$ $C_{12}E_8$/CTAB determined from data fitting to 10 ms decay curves for different initial bulk concentrations at 5 °C. (* the fitted parameter > 100 is physically unrealistic)

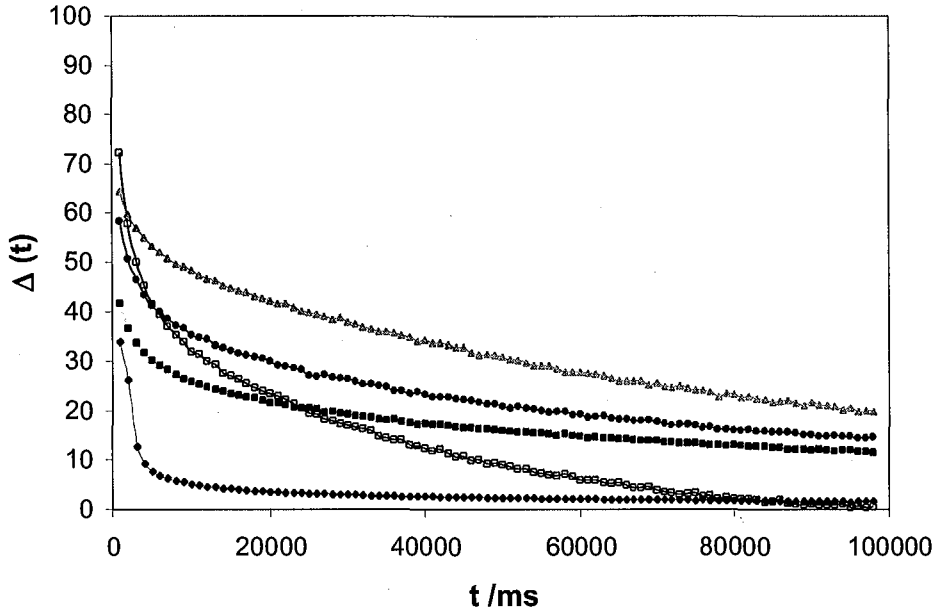

Figure 52: Micelle relaxation curves for solutions of $C_{12}E_8$ + 10 % mole fraction CTAB subjected to 2-fold dilutions at 5 °C plotted as 'reaction progress' . Initial concentrations are (♦) 2 cmc, (■) 4 cmc, (▲) 6 cmc, (●) 8 cmc and (□) 10 cmc. For clarity only 1000 ms integration time data have been plotted.

Furthermore, most of the fitted decay coefficients are smaller than the corresponding values for the pure $C_{12}E_8$ system. These values are given in Table 21. For ease of comparison, I have also plotted the decay coefficients for the 100 – 1000 ms time interval taken from the 100 ms integration time data for both systems in Figure 53.

$c_b(t=0)$	A (10ms)	A (100ms)	A (1000ms)
2 - cmc	4.4	0.2	0.15
4 - cmc	4.2	0.2	0.04
6 - cmc	1.6	0.1	0.02
8 - cmc	4.6	0.2	0.04
10 - cmc	7.7	0.3	0.06

Table 21: Exponential decay coefficient, b, for $C_{12}E_8$ determined from data fitting to decay curves for different initial bulk concentrations and integration times at 5 °C.

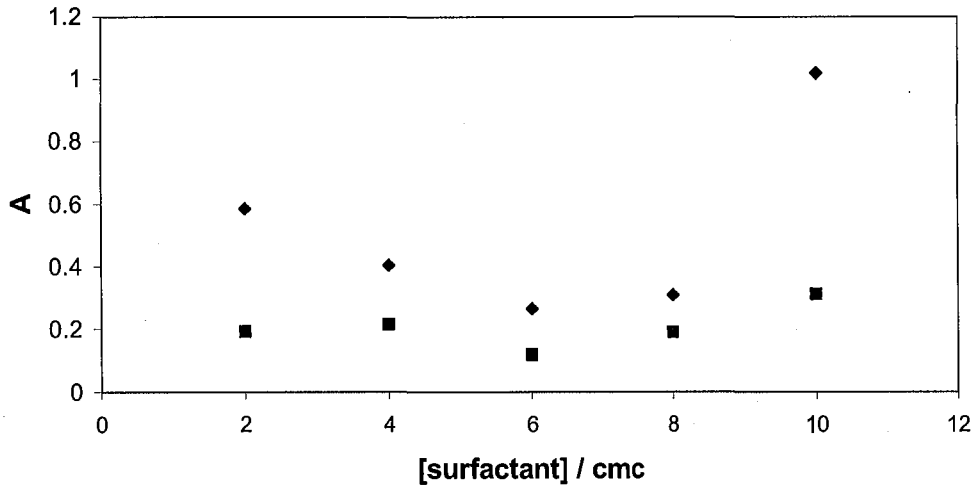

Figure 53: Comparison of decay coefficients for micelle concentration vs. time between 100 – 1000 ms for (♦) $C_{12}E_8$ and (■) $C_{12}E_8$/CTAB at 5 C.

6.4. Summary

A series of experiments have been carried out to measure the breakdown rate of micelles subjected to large perturbations from equilibrium. A number of very important results have been derived regarding the number of micelles that break down on very short timescales and the rate of breakdown for the micelles which do remain. These findings are consistent with the concepts that underlie my combined fusion-Becker-Döring hypothesis and are inconsistent with the Becker-Döring only model used by Aniansson and Wall.

Chapter 7

Adsorption Kinetics Measurements

The ultimate aim of my research is to develop a better understanding of structure-kinetics relationships in micellar solutions. In Chapter 3 I explored some fundamental micellar properties explored using SANS and PFGSE NMR. I have also undertaken a detailed theoretical and experimental investigation of micelle exchange kinetics in bulk solutions which was described in Chapters 4 – 6. In this Chapter my focus switches to another important kinetic process, the rate of adsorption from micellar surfactant solutions. I have carried out extensive measurements of adsorption kinetics from micellar solutions of nonionic surfactants using a gravity-driven laminar water jet that generates a surface with an age in the range 1 – 40 ms. My results show that nonionic micellar surfactant solutions can adsorb significantly on the millisecond timescale. In order to interpret my results and build up a comprehensive picture of the adsorption process from micellar solutions I will draw on knowledge acquired throughout Chapters 3 – 6 regarding bulk micellar properties.

The chapter begins with a description of the experimental set-up followed by a brief review of system hydrodynamics before focusing on adsorption kinetics measurements.

7.1. Experimental Set-up

7.1.1. The liquid jet and pumping system

The liquid jet system I use was designed by Battal and Bain [78] with two major requirements in mind.

1) isolation from sources of vibration to retard jet breakup and to avoid interference with optical systems,

2) an axisymmetric fully developed laminar flow profile

The basic set-up of the pumping system is depicted in Figure 54.

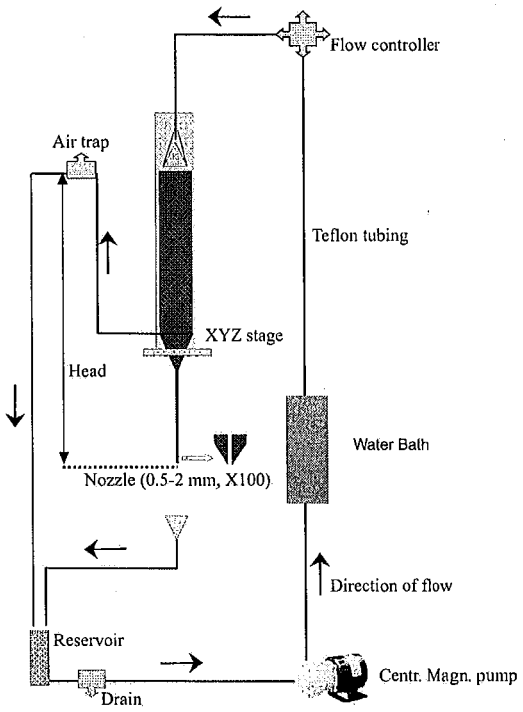

Figure 54: Schematic diagram of the liquid jet and pumping system.

A magnetic drive pump is used, with shaft seals to minimise surfactant contamination and facilitate cleaning. These pumps produce low levels of vibration. To thermostat the system the solution is passed through a coil immersed in a thermostatted water bath accurate to ±0.5°C. The temperature within the jet itself is checked using a calibrated thermocouple.

To prevent any pump vibrations reaching the nozzle there is no direct connection between the pump and reservoir. The solution from the pump is fed over an inverted funnel and allowed to fall freely onto the walls of the reservoir. This delivery method provides a smooth flow of liquid into the reservoir and suppresses foaming. Any flow instabilities are prevented from reaching the nozzle entrance by three Teflon resistance plates (4 mm thickness) and one steel plate (40 mm thickness) with 4 mm holes drilled through, contained within the reservoir. The whole reservoir is mounted on a coarse vertical (z) translation stage with a range of 400 mm and resolution of 0.1 mm, and a fine horizontal (x/y) translation stage with a sensitivity 0.1μm. These stages allow precision mapping of the jet flow in the radial direction.

The nozzle is attached to the bottom of the reservoir. The flow rate through the nozzle is determined by the hydrodynamic pressure difference across the nozzle, which is directly related to the head height of fluid in the reservoir and controlled with an adjustable air trap valve as an overflow. To determine the mean flow rate, $\overline{u}_0$, the solution is collected in a 100-ml measuring cylinder for a measured time. I find the reproducibility to be ≤ 0.005 ms^{-1} for successive measurements, equivalent to approximately 0.5 % of the experimental flow rates.

Nozzles used are sufficiently long (100 times the internal diameter) to ensure a fully developed laminar flow profile within a Reynolds number range $1000 \leq \mathrm{Re} \leq 2000$. The Reynolds number is a dimensionless group defined by

$$\mathrm{Re} = \frac{2R_0 u_0 \rho}{\mu} \tag{7.1}$$

where R_0 is the internal radius of the nozzle, ρ is the fluid density and μ the kinematic viscosity. For $\mathrm{Re} \leq 2000$ one may assume the flow is laminar. [78] Fluid leaving the nozzle is collected in a sump and recirculated.

The nozzle I have used is a high precision stainless-steel tube nozzle (Coopers Needleworks) with an internal diameter, $2R_0 = 1.58$ mm, connected to the reservoir by a 1/8-in BSP coupling. In order to minimise wetting, the nozzle tip is tapered to a wall thickness of 70 μm.

The whole system is mounted on a 12-in thick optical table, to isolate the system from vibrations in the environment, and enclosed with blackout curtains to exclude draughts.

All surfaces that come into contact with surfactant solutions are cleaned by soaking in an alkaline detergent (Decon-90) and rinsed with copious amounts of ultra high quality (UHQ) water.

7.1.2. Flow velocity using laser Doppler velocimetry

The Doppler shift, named after the Austrian physicist Christian Doppler who noticed the effect in 1842, is due to the relative motion of source and receiver. It is a common effect in any form of wave propagation and leads to a change in the observed

frequency. The use of the Doppler shift of laser light to determine flow velocities was first demonstrated in 1964 by Yeh and Cummins [146]. A number of variations of this technique have since been developed but can be generalised as laser Doppler velocimetry (LDV), sometimes called laser Doppler anemometry (LDA) due to the use of the technique to measure flow in gases. Drain [147] gives a good overview of LDV based techniques.

The method employed on the liquid jet is the differential Doppler method. Two beams are focused and crossed at the point of interest. Light scattered from the crossing volume consists of two components corresponding to the two beams of light, each with a corresponding Doppler shift. Since the light from each beam is scattered simultaneously the output from the detector is modulated at a frequency equivalent to the difference in Doppler shift for the two angles of scattering. This differential method has a considerably better signal to noise ratio than other methods, which is especially important when the concentration of scattering particles is low.

The calculation of velocity from differential Doppler frequency may be done most simply using an interference treatment. Consider a pattern of interference fringes created in the crossing volume, as shown in Figure 55.

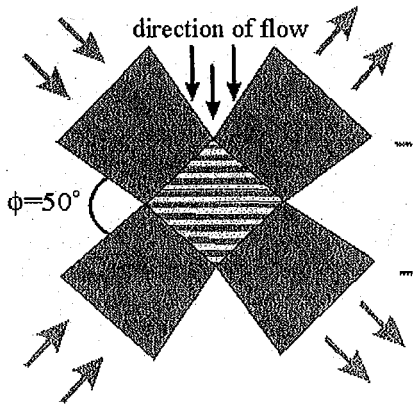

Figure 55: Interference fringes created at the crossing point of two focused laser beams.

The dimensions of the crossing volume and the fringe spacing may be calculated using elementary geometry and Gaussian beam optics. The beam waist at the focus point for a Gaussian beam, w_m, is give by

$$2w_m = \frac{4\lambda f}{2\pi w_0} \tag{7.2}$$

where w_0 is the Gaussian radius of the incident beam at the focusing lens, f is the focal length of the lens and λ is the wavelength of the light. (The Gaussian radius is defined as the radius where the intensity of light has fallen to 1/e of the maximum value).

Given that ϕ is the angle of intersection between the two beams, the dimensions of the crossing volume are given by

$$d_m = \frac{2w_m}{\cos(\phi/2)}$$
$$l_m = \frac{2w_m}{\sin(\phi/2)} \tag{7.3}$$

where d_m and l_m define the dimensions of the crossing volume perpendicular to and parallel to the flow respectively. The fringe spacing, d, is given by

$$d = \frac{\lambda}{2\sin(\phi/2)} \tag{7.4}$$

and the number of fringes by

$$N_{fr} = \frac{d_m}{d} = \frac{4w_m \tan(\phi/2)}{\lambda}. \tag{7.5}$$

To generate a sufficient flux of scattered light, I seed the liquid jet with 2 μm TiO_2 particles at a concentration of roughly 5 mg dm^{-3}. When a particle moves through the probe volume perpendicular to the fringes it scatters light in all directions. The intensity of this light is modulated at the difference frequency which is treated as the frequency of crossing the interference maxima. Given the fringe spacing, d and a difference frequency F_D the velocity, u is given by

$$u = F_D d = \frac{\lambda F_D}{2\sin(\phi/2)} \tag{7.6}$$

Figure 56 shows the optical arrangement for both laser Doppler velocimetry and ellipsometry on the liquid jet. In this section I will focus on the LDV optics and describe ellipsometry below. A He-Ne laser (Laser-2) is expanded to a diameter of 10 mm with a pair of best form lenses (L-3, L-4) with focal lengths f = -25 mm and f = +240 mm. The beam is then split into two equal components by a nonpolarising beam splitter (BS). The two components are deflected along paths of equal lengths by

interferometric quality dielectric mirrors (M-3, M-4, M-5) and finally deflected to the crossing point by a pair of mirrors (M-6, M-7) on kinematic mounts controlled by high resolution differential micrometers (0.07 μm sensitivity). The final focusing lenses (L-5, L-6) are Gradium™, to reduce spherical aberrations, with focal length f = 80 mm. Beam alignment is performed through a 10 μm pinhole using a digital power meter to maximise throughput. At an angle of intersection ϕ = 50° throughput is roughly 50%, although the uncertainty in the foil thickness around the pinhole prevents any direct calculation of the corresponding beam waist. Equations (7.2) - (7.5) give the beam parameters at the focus point, shown in Table 22. It is important to note that the wavelength of light and effective focal length of the lenses is dependent on the refractive index of the media n ($\lambda_{water} = \lambda_{air} / n_{water}$ and $f_{water} = n_{water} f_{air}$ where $n_{water} = 1.333$). These adjustments do not affect the calculation of the beam waist at the focus since the effects cancel out exactly. However, calculations should be performed using an angle of intersection adjusted for refraction at the jet surface using Snell's Law.

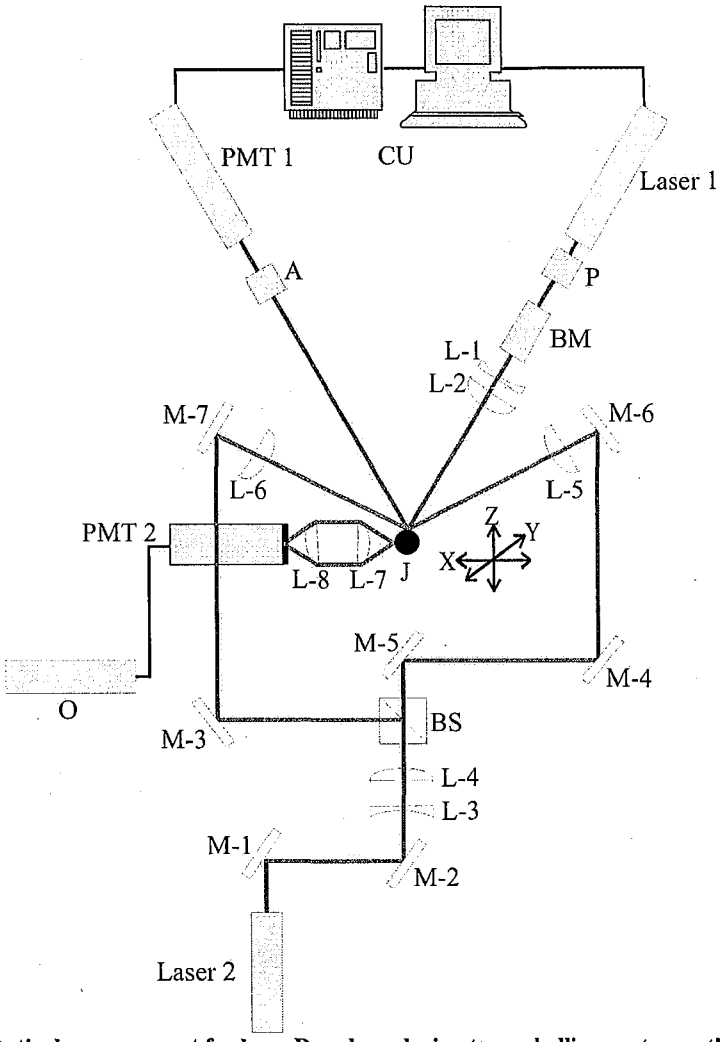

Figure 56: Optical arrangement for laser Doppler velocimetry and ellipsometry on the jet (J).

Incoming beam	Adjusted for water		Interference fringes
$2\omega_0 = 0.01$ m	$2\omega_0 = 0.01$ m		$2\omega_m = 6.4$ μm
$\lambda = 633 \times 10^{-9}$ m	$\lambda = 474 \times 10^{-9}$ m		$d_m = 6.7$ μm
$f = 0.08$ m	$f = 0.106$ m		$l_m = 20.7$ μm
$\phi/2 = 25°$	$\phi/2 = 18°$		$d = 0.77$ μm , N_{fr}=9

Table 22: Beam parameters for laser Doppler velocimeter

A 5 mg dm^{-3} concentration of 2 μm TiO_2 particles is high enough to allow measurements at the jet surface (where only part of the probe is inside the jet), but

low enough to ensure that no more than 1 particle generally passes through the probe at one time. The sideways scattered light is collimated and focused by two identical Gradium^{TM} lenses (L-6, L-7) into a photomultiplier tube (PMT-2). Both of these final lenses (L-6, L-7) and PMT-2 are mounted on a translational stage to allow fine focusing of scattered light from the crossing point to the PMT. A slit (3 mm × 0.75 mm) covers the PMT to minimise stray light and a 633 nm narrow bandpass filter sits between the slit and the PMT to cut out of band light to less than 0.01 %.

Figure 57 shows the output of the PMT modulated at the difference frequency, and the Fourier transformed average over 100 particles passing through the probe volume. This frequency is directly converted to velocity using equation (7.6). Figure 57a shows the voltage modulation of a particle passing through the probe volume. This plot is in fact a trace for a previous optical system which gave a larger beam waist at the focus point. The current traces using the system parameters in Table 22 contain only 9 oscillations, corresponding to fringes, within 1/e of the maxima of the Gaussian envelope. This fringe count is the same as the theoretical predication, verifying that the two beams are focused as tightly as possible.

Three important characteristics of flow may be measured with this set-up.

1) **Jet profiles** – measuring flow velocity, u, as a function of radial position r from the jet centre. Due to refraction which occurs at the jet surface the crossing point extends further beneath the surface than the micrometer indicates. This effect is easily accounted for using Snell's law.

2) **Jet dimensions** – the radius of the jet, R, may be recorded as a function of displacement downstream of the nozzle exit by noting the micrometer readings corresponding to the 'front and back' surfaces as found by LDV.

3) **Surface Velocities (u_s)**– The surface position is defined as the displacement when the rate at which particles trigger the oscilloscope falls to approximately 10 triggers per minute, at which point most of the probe volume lies outside of the jet. Velocity measurement taken at this displacement are taken to be the surface velocity.

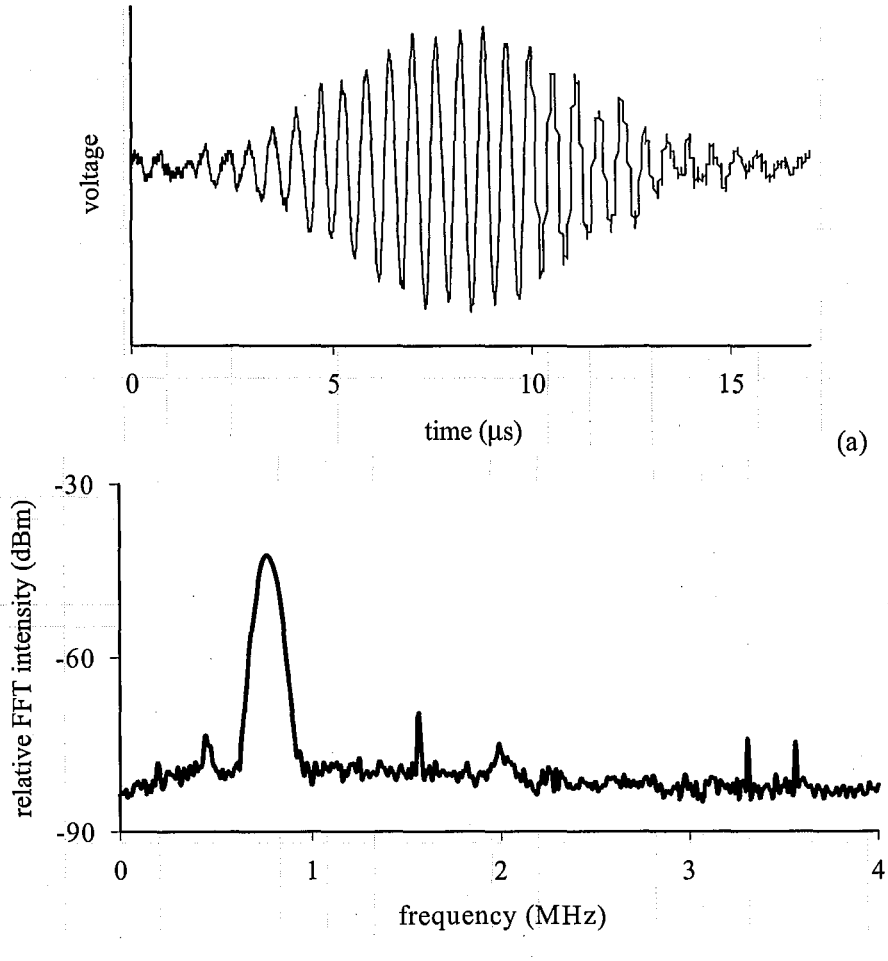

Figure 57: (a) voltage modulation of scattered light, (b) modulation frequency averaged over 100 scans.

7.1.3. Phase modulated ellipsometry

Ellipsometry measures changes in the polarisation of light upon reflection from or transmission through a sample. The polarisation of light is characterised by its components parallel and perpendicular to the place of incidence, referred to as p-light and s-light respectively. The polarisation can be defined by the amplitudes and phases of the p- and s-light which are expressed in a Jones vector [148];

$$\underset{E}{\mathrm{r}} = \begin{pmatrix} |E_p| e^{i\delta_p} \\ |E_s| e^{i\delta_s} \end{pmatrix} = \begin{pmatrix} E_p \\ E_s \end{pmatrix} \tag{7.7}$$

where $|E_p|$ and $|E_s|$ are the amplitudes and δ_p and δ_s are the phases.

The behaviour of p- and s-light in reflection depends upon the angle of incidence and the refractive indices of the media. The Fresnel equations [149] predict this behaviour for perfect dielectric media:

$$r_p = \frac{n_j \cos\theta_i - n_i \cos\theta_j}{n_j \cos\theta_i + n_i \cos\theta_j} \tag{7.8}$$

$$r_s = \frac{n_i \cos\theta_i - n_j \cos\theta_j}{n_i \cos\theta_i + n_j \cos\theta_j} \tag{7.9}$$

where n is the refractive index, θ is the angle and the subscripts i and j refer to incident or transmitted beams as shown in Figure 58. The terms r_p and r_s are known as the amplitude reflection coefficients for p- and s-light respectively.

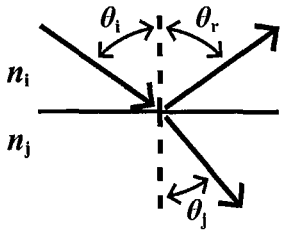

Figure 58: reflection of light at an ideal interface.

For systems where $n_i < n_j$ it follows from Snell's law that $\theta_i < \theta_j$, hence r_s is negative for all angles of incidence. However, r_p begins positive at $\theta_i = 0$ (normal incidence) and becomes negative as θ_i is increased. The angle at which r_p = 0 is known as the Brewster angle, θ_B and occurs when $\theta_i + \theta_j = 90°$, hence $\tan\theta_B = n_j / n_i$.

Ellipsometry measures the ratio $r = r_p / r_s$ [150]. The refractive indices of the incident and transmitting media are related to their dielectric constants. Perfect dielectrics (non-adsorbing media) have real dielectric constants and the reflection coefficients are real. Media that attenuate light have complex dielectric constants so r_p, r_s and their ratio becomes complex causing linearly polarised light to become elliptically polarised upon reflection. Ellipsometry can measure both the real and imaginary parts of the complex ratio;

$$r = \frac{r_p}{r_s} = \Re(r) + i\Im(r) = \tan\Psi e^{i\Delta} \tag{7.10}$$

where $\tan\Psi$ and $\Delta(=\delta_p - \delta_s)$ are the parameters measured by traditional nulling ellipsometry. The parameters measured in phase modulation ellipsometry are much more closely related to $\Re(r)$ and $\Im(r)$ and are defined below.

Other causes of ellipticity include a variation in the refractive index of a surface as a function of distance from the surface (due for instance to surfactant adsorption). At the Brewster angle $\Re(r) = 0$ and the ratio r is purely imaginary. For a perfect interface $\Im(r)$ also goes to zero at the Brewster angle, but for an imperfect (real) interface $\Im(r)$ gives a measure of the surface imperfection, which for my purpose may be related to surface excess of surfactant. When working at the Brewster angle, the imaginary term $\Im(r)$ is known as the coefficient of ellipticity, $\bar{\rho}$.

Drude derived corrections to the Fresnel equations to account for the transition region of two media where the dielectric constant varies with depth, $\varepsilon = \varepsilon(z)$, between the two bulk values, ε_1 and ε_2. Drude gives expressions for r which involve an integral function of the dielectric constants in the transition region:

$$\eta = \int \frac{(\varepsilon - \varepsilon_1)(\varepsilon - \varepsilon_2)}{\varepsilon} dz \tag{7.11}$$

The coefficient of ellipticity is given by

$$\bar{\rho} = \frac{\pi}{\lambda} \frac{\sqrt{\varepsilon_1 + \varepsilon_2}}{\varepsilon_1 - \varepsilon_2} \eta \tag{7.12}$$

Phase modulation ellipsometry was originally devised by Jasperson and co-workers [151] and is a more rapid method for determining ellipticity than the traditional nulling method. The frame of reference for alignment of optical components is the s-direction, perpendicular to the plane of incidence. Laser light is passed through a polariser orientated at 45° to provide incident light with equal s- and p- amplitudes to the birefringence modulator (BM). The BM is an isotropic glass slab set into longitudinal oscillation at its resonant frequency, ω. This mechanical oscillation is

driven electronically by the piezoelectric effect using a quartz crystal attached to the glass slab. The periodic, uniaxial strain induced in the centre of the glass slab results in a periodic change in the refractive index for light polarised parallel to the oscillation direction. This effect is known as the photoelastic effect. The BM may be orientated along either the s- or p- direction and induces a phase shift between the two components of light given by $\delta(\omega) = \delta_0 \sin(\omega t)$. The analyser is orientated at ±45°. The intensity of light arriving at the photomultiplier tube (PMT) is given by;

$$I = I_0 \rho_s^2 \cos^2 A \cos^2 P(1 + \rho'^2 + 2\rho' \cos(\Delta + \delta)) \tag{7.13}$$

with $\rho' = \tan A \tan P \rho$ and $\rho^2 = \Re(r)^2 + \Im(r)^2$. The terms A and P refer to the angles of the polariser and analyser respectively, δ is the strain induced birefringence and $\Delta = \delta_p - \delta_s$ as defined above. Substituting the phase modulation expression for $\delta(\omega)$ and expanding the $\cos(\Delta + \delta)$ term gives three components to the detector signal. A non-modulated (dc) signal and two signals modulated at ω and 2ω respectively. To compensate for fluctuations in light intensity the two modulated signals are normalised with respect to the dc signal. Assuming that A = P = 45° the resulting signals are

$$Y = \frac{S_\omega}{S_{dc}} = -g_y \frac{4J_1(\delta_0)\Im(r)}{1 + \rho^2 + 2J_0(\delta_0)\Re(r)} \tag{7.14}$$

$$X = \frac{S_{2\omega}}{S_{dc}} = -g_x \frac{4J_2(\delta_0)\Re(r)}{1 + \rho^2 + 2J_0(\delta_0)\Re(r)} \tag{7.15}$$

where J_n refers to the n^{th} order Bessel function and g_x and g_y are the gain factors of the system for the ω and 2ω channels respectively. The BM is calibrated such that δ_0 =2.405 radians at which point J_0 = 0 and J_1 and J_2 remain constant. Hence

$$Y = G_y \Im(r) \frac{1}{1 + \rho^2} \tag{7.16}$$

$$X = G_x \Re(r) \frac{1}{1 + \rho^2} \tag{7.17}$$

and since $\rho^2 = \Re(r)^2 + \Im(r)^2$ one may write

$$x = \frac{X}{G_x} = \Re(r)\frac{2}{1+\Re(r)^2+\Im(r)^2} \tag{7.18}$$

$$y = \frac{Y}{G_y} = \Im(r)\frac{2}{1+\Re(r)^2+\Im(r)^2} \tag{7.19}$$

where G_x and G_y are the instrument gain factors set during calibration. The parameters x and y are useful because they behave in a similar fashion to $\Re(r)$ and $\Im(r)$. Both $\Re(r)$ and x go to zero at the Brewster angle. When both $\Re(r)$ and $\Im(r)$ are small one may approximate $\Re(r) \approx x/2$ and $\Im(r) \approx y/2$.

Ellipsometric measurements on the jet are performed using a Picometer Ellipsometer from Beaglehole Instruments, New Zealand. Figure 56 shows the orientation of the components relative to the jet. Light from a He-Ne laser (Laser-1), passed through a polariser (P) is modulated photoelastically at 50 kHz by the birefringence modulator (BM). The beam is expanded and refocused using two best form lenses (L-1, L-2) to a spot size of approximately 0.2 mm at the jet surface. The analyser (A) and photomultipler tube (PMT-1) are mounted on a horizontal translation stage at the Brewster angle (θ_B) relative to the incoming beam and jet surface. The translation stage allows the position of the analyser and PMT to be changed at fixed angle. The signals at 50 and 100 kHz (ω and 2ω) are extracted by lock-in amplifiers (CPU) and the coefficient of ellipticity, $\bar{\rho}$, calculated by the Igor Pro data analysis software.

The Picometer ellipsometer is most commonly used on flat samples and the optical components are usually mounted on automated arms to allow easy identification of the Brewster angle. In my experiment the components are bolted to an optical bench which introduces some experimental difficulties. I have devised a reasonably quick and reliable procedure for efficient location of Brewster angle light reflected from the tightly curved jet surface (Appendix 4).

Once the alignment has been optimised, the optical components remain in fixed positions and the only variable is jet position. Using the z-translation I am able to measure the coefficient of ellipticity to a lower limit of 1 mm from the nozzle exit (limited by inherent jet curvature near the nozzle) and an upper limit of 80 mm from the nozzle exit (due to inherent surface instability), although measurement to 50 mm

is usually sufficient. The conversion of ellipticity to surface excess is described in detail below.

7.2. Hydrodynamic measurements of jet flow

Whilst most of this chapter will be concerned with ellipticity measurements and the determination of surface excess as function of distance from the nozzle exit I will briefly review some of the corresponding hydrodynamics measurements. It is necessary to demonstrate that a fully developed parabolic flow profile is achieved at the nozzle exit. [62] This flow profile was originally demonstrated in the work of Battal and Bain and has since been verified numerous times by myself. Figure 59 shows some experimental velocity profiles, $u(r)$, for a pure water jet as a function of axial distance, z, from the nozzle exit. The velocity profile is almost parabolic close to the nozzle and relaxes towards plug flow as z increases.

It is also essential to demonstrate the ability to map the jet dimensions and most importantly the surface velocity accurately. The jet must contract as the velocity becomes uniform as a consequence of momentum conservation. Figure 60 plots the surface velocity, u_s and jet diameter, $2R$ as function of $z^{1/3}$. There are two important points to note about these measurements. Firstly, the surface velocity data extrapolate to zero velocity at $z = 0$. Secondly the surface strain rate, $\theta = du_s / dz$ is very high just after the nozzle exit. The accuracy of surface velocity measurements is crucial for the determination of these strain rates.

One can estimate the error in the surface velocity measurements by considering the dimensions of the probe volume. When measuring the surface velocity I assume that the focus is placed at the surface. Given the radial probe dimension, l_m = 21 μm, the average depth from which the signal arises is roughly 5 μm. The maximum radial velocity gradient is given by $(du/dr)_{max} = 4\bar{u}_0 / R_0$ [80] giving 4 × 10^3 s^{-1} for the conditions in Figure 60. Therefore 5 μm beneath the surface u is 2 cm s^{-1} higher than u_s. This estimate is a worse case since the radial velocity gradient decreases down the jet.

Given the high precision with which it is possible to determine the surface velocity it has been possible to measure even very small changes in surface velocity due to

surfactant adsorption. Changes in surface velocity due to surface tension gradients, known as Marangoni effects, have now been reported for both cationic surfactants [78] and nonionic surfactants [81] with surface velocity reductions up to 30% observed. Data for the surface velocity of a series of C_nE_8 surfactants which are studied in this work were featured in my 2005 paper [81] and are reproduced here in Figure 61.

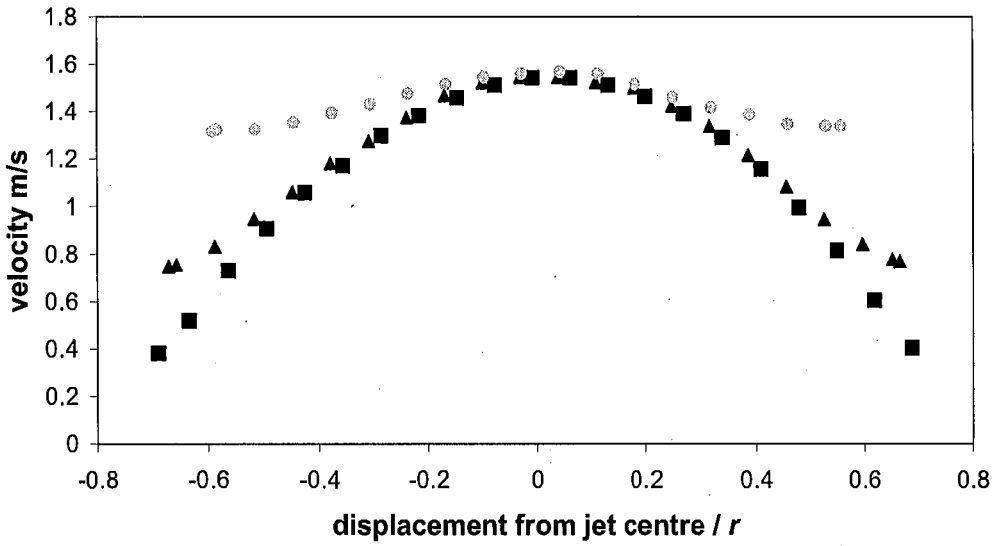

Figure 59: Radial velocity profiles for a pure water jet. (■) z = 1 mm, (▲) z = 10 mm, (•) z = 50 mm. $\bar{u}_0$ = 0.8 ms^{-1}, T = 293 K, Re = 1280

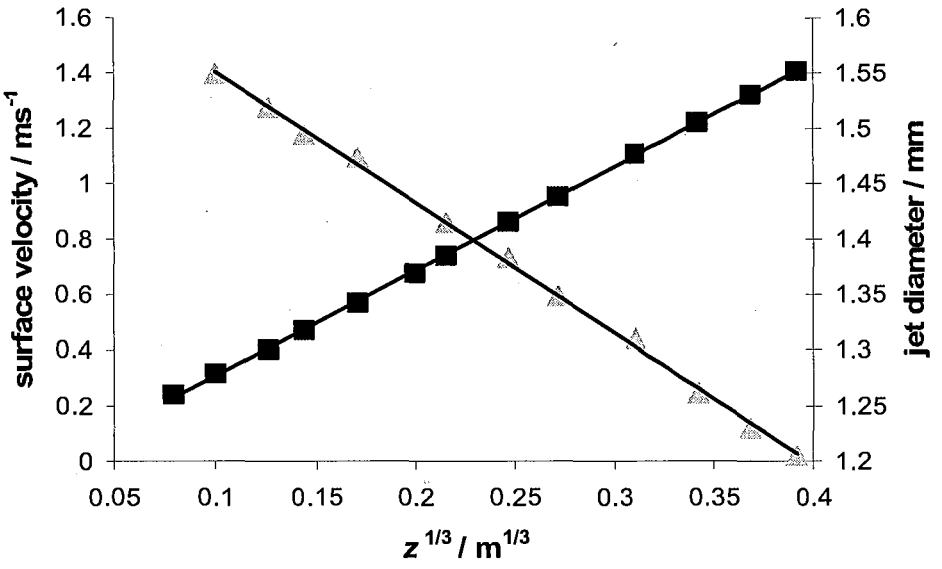

Figure 60: Surface velocity (■) and jet diameter (△) as a function of axial distance down the jet. $\bar{u}_0$ = 0.8 ms^{-1}, T = 293 K, Re = 1280.

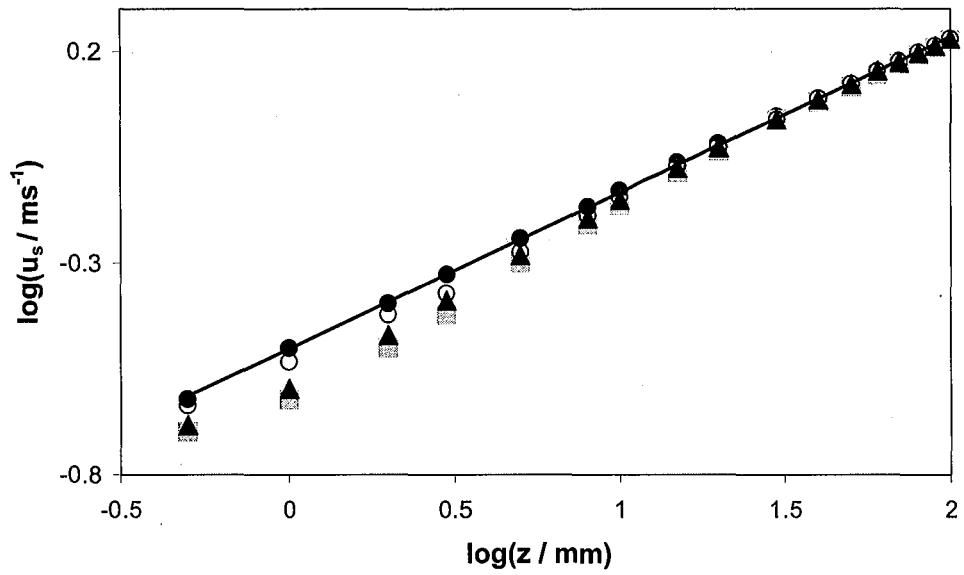

Figure 61: Surface velocity for pure water (●) compared to 1-mM solutions of $C_{12}E_8$ (▩) , $C_{14}E_8$ (▲) and $C_{16}E_8$ (○). $\bar{u}_0$ = 0.8 ms^{-1}, T = 293 K, Re = 1280.

7.3. Adsorption kinetics measurements

7.3.1. Determination of surface excess from ellipticity

The surface excess is deduced from the results of ellipsometry measurements made on the jet surface. Previous measurements in the Bain Group have calibrated the ellipsometric response against direct measurements of surface excess by neutron reflection: for the non-ionic surfactant $C_8E_4OCH_3$, the relationship is accurately linear [76]. A linear relationship has also been found for a fluorocarbon surfactant and for three cationic hydrocarbon surfactants. There is no reason why such a linear relationship should not hold for all the surfactant systems studied here. In the thin film regime the change in the imaginary part of the ellipsometric response is directly proportional to the ellipsometric thickness

$$\eta = \int \frac{(\varepsilon_1 - \varepsilon_0)(\varepsilon_1 - \varepsilon_2)}{\varepsilon_1} dz \tag{7.20}$$

where z is a coordinate normal to the interface, ε_0 is the dielectric constant in the incident medium, ε_1 the dielectric constant in the thin layer and ε_2 the dielectric constant of the substrate. Equation (7.20), also known as the Drude equation, [152] demonstrates that the ellipsometric response is dependent upon the optical contrast of the media and the thickness of the film. One can model a surfactant film with an effective medium approximation (EMA) such as the Lorentz-Lorenz

$$\frac{\varepsilon - 1}{\varepsilon + 2} = \phi_a \frac{(\varepsilon_a - \varepsilon)}{(\varepsilon_a + 2\varepsilon)} + \phi_b \frac{(\varepsilon_b - \varepsilon)}{(\varepsilon_b + 2\varepsilon)} \tag{7.21}$$

where ϕ_a and ϕ_a are the volume fractions and ε_a and ε_b are the dielectric constants of the surface components, in this case surfactant and water. One finds that as ϕ_{water} is varied between 0 and 100 %, the corresponding variation in η is less than 10%. [153] The ellipsometric thickness can therefore be approximated as linear in the surface excess.

A linear relationship requires only two data points to define all intermediate behaviour. Zero surface coverage provides one such data point with

$\Gamma = 0, \bar{\rho} = 0.4\times10^{-3}$. It follows that knowledge of the surface excess at a single concentration determined by neutron reflection or tensiometry and the corresponding equilibrium ellipticity is all that is required to convert dynamic ellipsometric values to surface excesses. Literature values of the limiting (c > cmc) surface excess along with the corresponding equilibrium ellipticity measurements are given in Table 23. These equilibrium ellipticity values were determined using a conventional phase modulated ellipsometer and 1 mM surfactant solutions contained within petri dishes and allowed to equilibrate for up to 15 minutes.

Literature values for Γ_{max} were used, except in the case of $C_{16}E_8$ and α-C_{12}malt where I could find no value. For $C_{16}E_8$ I calculated the value of 3.3×10^{-6} mol m^{-2} by extrapolation from equilibrium ellipticity values of other C_nE_8 surfactants. The measured equilibrium ellipticities can be examined with respect to the literature surface excess values using a slab model, which splits the equilibrium ellipticity into three components

$$\bar{\rho}_{eq} = \bar{\rho}_r + \bar{\rho}_h + \bar{\rho}_c \tag{7.22}$$

Where $\bar{\rho}_r$ is a surface roughness term, and $\bar{\rho}_h$ and $\bar{\rho}_c$ are contributions from the head group and hydrocarbon chain respectively. $\bar{\rho}_r$ scales inversely with surface tension, so for a surfactant at its cmc $\bar{\rho}_r = \bar{\rho}_{r(H_2O)}\sqrt{\gamma_{H_2O}/\gamma_{cmc}}$ where $\bar{\rho}_{r(H_2O)} = 0.38\times10^{-3}$. [154]. This estimate gives a roughness contribution for C_nE_8 surfacants of $\bar{\rho}_{r(C_nE_8)} = 0.55\times10^{-3}$.

The headgroup contribution to ellipticity was studied in detail by Goates, Schofield and Bain [155] and was found to scale linearly with surface excess. For an E_8 headgroup with $\Gamma = 2.7\times10^{-6}$ mol m^{-2} the headgroup contribution $\bar{\rho}_{h(E_8)} = -1.36\times10^{-3}$.

The hydrocarbon chain contribution can be calculated by treating it as an oil film with the same density (750 kg m^{-3}) and refractive index (1.422) as dodecane. From equation (7.20)

$$\eta_c = \frac{(\varepsilon-1)(\varepsilon-\varepsilon_{H_2O})}{\varepsilon} L_c \tag{7.23}$$

Where the layer thickness, $L_c = V_c \Gamma N_A$, molecular volume V_c is 376 Å^3 and N_A is Avogadro's number. For a C_{12} chain with $\Gamma = 2.7\times10^{-6}$ mol m^{-2} the hydrocarbon contribution $\bar{\rho}_{c(C_{12})} = 0.8\times10^{-3}$. Within this oil film model $\bar{\rho}_c$ scales linearly with surface excess and approximately with the hydrocarbon chain length n.

Combining all three contributions with relevant scaling parameters and inserting them into equation (7.22) gives an expression for the equilibrium ellipticity of C_nE_8

$$\bar{\rho}_{eq(C_nE_8)}/10^{-3} = 0.55 - \frac{\Gamma_{max}}{2.7\times10^{-6}}\left[1.36 + \left(0.8\times\frac{n}{12}\right)\right] \qquad (7.24)$$

For n = 10, 12 and 14 the literature values of Γ_{max} in Table 23 give calculated equilibrium ellipticities $\bar{\rho}_{eq}$ of −1.49, −1.85 and −2.19 respectively. These values are in good agreement with my measured values. Therefore I have used equation (7.24) to calculate the surface excess for n = 16 and this value is given in Table 23.

For α-C_{12}malt I assume that the value is the same as that for β-C_{12}malt since the equilibrium ellipticity is almost identical and the structures are very similar.

Surfactant	Γ_{max} / 10^{-6} mol m^{-2}	$\bar{\rho}_{eq}$ / 10^{-3}
$C_{10}E_8$	2.7 [156]	-1.70
$C_{12}E_8$	3.0 [6]	-1.80
$C_{14}E_8$	3.2 [110]	-2.13
$C_{16}E_8$	3.3 *	-2.41
$C_{12}E_6$	3.2 [6]	-2.13
$C_{14}E_6$	3.3 [157]	-2.33
α-C_{12}malt	-	-2.93
β-C_{12}malt	3.3 [111]	-2.95
β-C_{14}malt +	3.7* [100]	-3.36
C_{14}DAPS	3.2 [112]	-1.83
Triton X-100	2.8 [113]	-2.64

Table 23 – Equilibrium surface properties of surfactants in the current work (* calculated as explained in text, + measured at 40 °C)

7.3.2 Adsorption rates of nonionic surfactants

Experimental conditions for all the adsorption measurements reported in this study are jet diameter $2R_0 = 1.58$ mm, bulk flow rate $\bar{u}_0 = 0.87$ ms^{-1} and, unless other stated,

temperature $T = 293K$. Measurements of a pure water surface reveal that in the absence of surface tension gradients, the surface velocity, $u_s(z)$, of a free jet in boundary-layer flow takes the form $u_s(z) = a\, z^{1/3}$, where z is the axial displacement in meters (Figure 60). For the experimental conditions in this work the constant a = 3.7 $m^{2/3}$ s^{-1}. Marangoni effects for surfactant solutions vary $u_s(z)$ by less than 30%.[81] Neglecting jet contraction, the mean surface age, $\bar{t}(z)$, is given by $\bar{t}(z) = z / u_s(z) = a^{-1} z^{2/3}$.[82] For z = 1–50 mm, $\bar{t}(z)$ is in the range of 2–40 ms.

Typical experimental concentrations of 0.5 – 4-mM ensure significant adsorption without immediate surface saturation on these timescales. The surface excess as a function of distance from the nozzle exit for each surfactant at 1-mM is shown in Figure 62. The data are plotted in the dimensionless units of percentage monolayer so that comparisons may be most easily drawn, where % monolayer = $100.(\Gamma_{meas}(z) / \Gamma_{max})$.

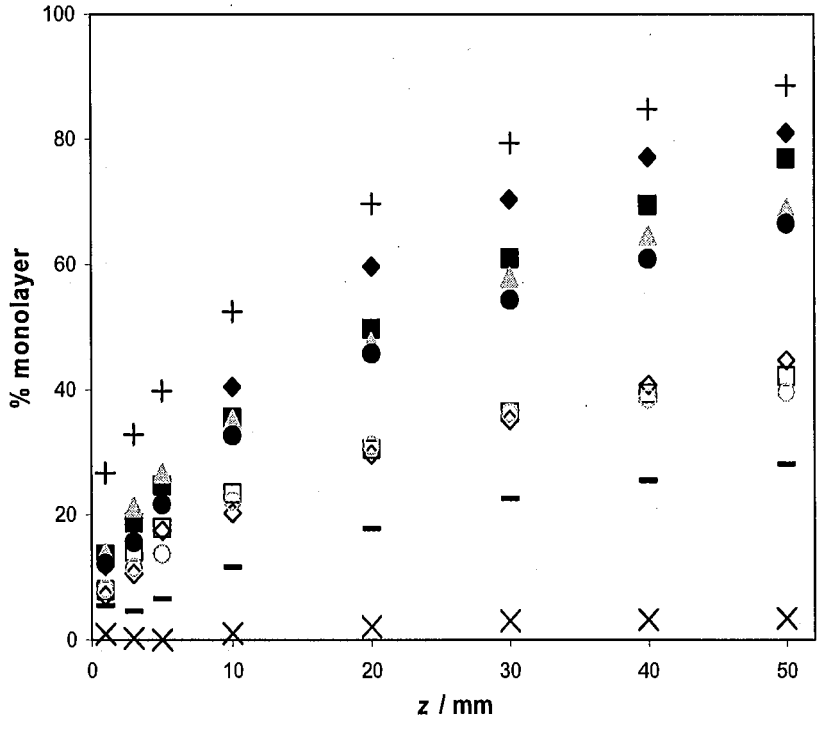

Figure 62: Adsorption curves for 1-mM surfactant solutions in the liquid jet. u_0 = 0.87 ms^{-1}, T = 20 °C, (+) TX-100, (♦) C_{14}DAPS, (■) α-C_{12}m, (▲) $C_{12}E_8$, (•) β-C_{12}m, (□) $C_{14}E_8$, (◊) $C_{12}E_6$, (○) $C_{16}E_8$, (—) β-C_{14}m and (×) $C_{14}E_6$. [data for β-C_{14}m acquired at 40 °C due to Krafft temperature T_k = 31.5 C]

The change in the adsorbed amount for different surfactants is large. Broadly speaking surfactants appear to fall into three classes. Five surfactants (TX100, C_{14}DAPS, $C_{12}E_8$, α-C_{12}m and β-C_{12}m) adsorb up to 70-90% of a surfactant monolayer within 50 mm of the nozzle exit. Four surfactants ($C_{12}E_6$, $C_{14}E_8$, $C_{16}E_8$ and bC_{14}m) adsorb in the range 20-45% of a monolayer within 50 mm of the nozzle exit, whilst $C_{14}E_6$ adsorbs very little on these timescales.

I now consider, in turn, the varying proportion of micelles and monomers in each solution, changes in micelle mass transport and the effect of micelle breakdown kinetics.

7.3.3. Free monomer contribution to surface excess

As the cmc changes the amount of free monomer available for adsorption to the nascent surface at the nozzle exit changes. Since monomers are smaller than micelles they have larger diffusion coefficients and adsorb more rapidly. To assess the different contributions to adsorption from free monomer one may begin by assuming the micelles are frozen on this experimental timescale and treat the mass transport of micelles and monomers independently. Once the free monomer adsorption has been accounted for any further adsorption must be due to surfactant originally contained within micelles. For surfactants with a sufficiently large cmc to give appreciable adsorption, the best way to assess free monomer contribution is to measure the adsorption curve with $c_0 = \text{cmc}$. In the current study Triton X100 has the highest cmc (0.35mM). As can be seen in Figure 63, adsorption from initially free Triton X100 monomer accounts for approximately 40% of the total adsorption in a 1-mM micellar solution. Therefore 60% of the adsorbed surfactant must initially be contained within micelles. For all other surfactants in this work which have smaller cmc's the percentage of the adsorbed surfactant that must be released from micelles increases. Measurements reveal that adsorption is negligible for concentrations < 0.1 mM indicating that for surfactants with cmc's smaller than this value the independent monomer contribution is minimal.

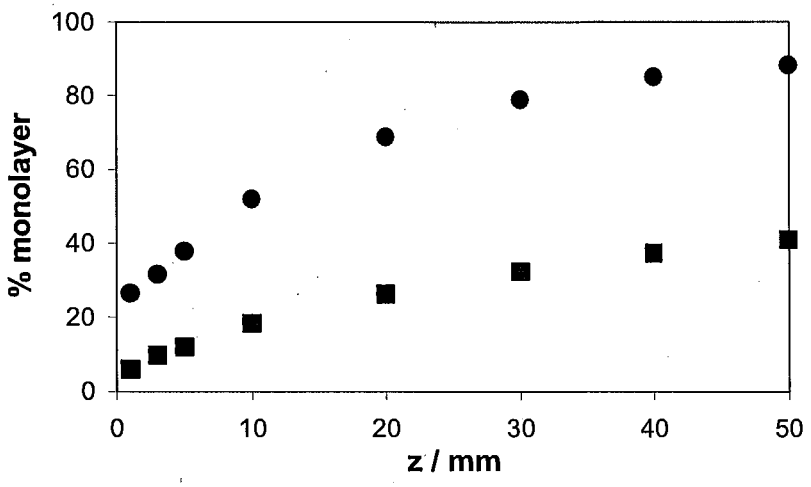

Figure 63: Comparison of surface excess vs. distance from the nozzle exit for (■) 0.35-mM TX100 and (●) 1-mM TX100.

7.3.4 Micelle mass transport effects on measured surface excess

A second factor influencing adsorption rate differences are changes in the mass transport of micelles towards the interface. In order to assess the effect of micelle mass transport on adsorption rate I have compared micelle diffusion coefficients from a range of sources. Not only are these values important for the interpretation of the adsorption curves, but comparison of diffusion coefficients taken from different sources provides a valuable insight into the adsorption mechanism from micellar solutions.

Micelle diffusion coefficients for each of the systems of interest have been measured directly using pulsed field gradient spin echo NMR measurements. These measurements were performed by Nicolas Peron, a postdoctoral research assistant working in the Bain group. Monomer and micelle diffusion coefficients measured in this way, D_{mon}^{NMR} and D_{mic}^{NMR}, for 1-mM surfactant solutions are listed in Table 24. These measurements were taken in D_2O and the values in Table 24 have been adjusted to account for the viscosity difference between H_2O and D_2O using the Stokes-Einstein equation.

I have also calculated a second set of values for micelle diffusion coefficients from the best fit micelle dimensions to my SANS data. I discussed these dimensions in

detail in Chapter 3. For spherical micelles I use $D = kT / f$ where k is the Bolzmann constant, T is the temperature in Kelvin and the friction coefficient is given by the Stokes-Einstein expression $f = 6\pi\mu r_{mic}$. [158]When the diffusing species are anisometric, more complicated expressions are required. For ellipsoids of revolution with $r_a = r_b$, Perrin used the the axial ratio, $p = r_a / r_c$ and the concept of an equivalent sphere of radius $r_{eq} = (r_a^2 r_c)^{1/3}$, to derive the following expressions for diffusion coefficient

$$D = \frac{D_{eq} p^{2/3}}{(1-p^2)^{1/2}} \ln\left[\frac{1+(1-p^2)^{1/2}}{p}\right] \qquad (p<1) \qquad (7.25)$$

$$D = \frac{D_{eq} p^{2/3}}{(1-p^2)^{1/2}} \arctan(p^2-1)^{1/2} \qquad (p>1) \qquad (7.26)$$

where $D_{eq} = kT / 6\pi\mu r_{eq}$. The cases p < 1 and p > 1 correspond to prolate and oblate ellipsoids of revolution respectively. Finally, in the limiting case of a rod of length L and radius R, I use the alternative expression $D = (kT / 3\pi\mu L)\ln(L / 2R)$. [159]These expressions give the average diffusion coefficient of an ellipsoid or rod taking random orientations. In experiments where shear alignment of rods may occur, simpler expressions that only account for certain degrees of freedom could be used. [160] Shear alignment is unlikely for the systems I have studied, with the possible exception of $C_{14}E_6$ which will be discussed below. Micelle diffusion coefficients calculated in this way, D_{mic}^{CALC}, are also listed in Table 24.

A third set of micelle diffusion coefficients may be extracted from the adsorption curves themselves. An analytical model of the jet flow and adsorption under diffusion controlled conditions has been developed in a collaborative project with Weiss and Darton. [80] Using a boundary-layer treatment and assuming diffusion controlled adsorption of the surfactant species leads to an expression for the surface excess variation with axial distance from the nozzle exit

$$\Gamma = 0.244\left(\frac{D}{\bar{u}_0}\right)\left(\frac{2R_0\bar{u}_0\rho}{\mu}\right)^{2/3}\left(\frac{\mu}{\rho D}\right)^{1/2} c_b \left(\frac{1}{R_0}\right)^{1/3} z^{1/3} \qquad (7.27)$$

where D is the diffusion coefficient of the adsorbing species, c_b is the bulk concentration, R_0 is the nozzle radius, ρ is the density and μ is the kinematic viscosity of the solution. As all of the flow parameters are known, equation (7.27) reduces to $\Gamma = Hc_b D^{1/2} z^{1/3}$ where all of the flow parameters are contained within the constant H. The adsorption curves in Figure 62 have been fitted to extract micelle diffusion coefficients D_{mic}^{FIT} using

$$\Gamma = H[\text{cmc}.D_{mon}^{1/2} + (c_b - \text{cmc})D_{mic}^{1/2}]z^{1/3} \qquad (7.28)$$

Equation (7.28) implies that micelles do not gain or release monomers on my experimental timescale, which is unlikely to be true when the monomer concentration is depleted below the cmc. This assumption will be discussed further below. Monomer diffusion coefficients are not expected to vary significantly for different surfactant systems. For simplicity, the value for D_{mon} has been taken to be 3×10^{-10} m^2s^{-1} in each case. This value is similar to the of monomer diffusion coefficients measured by Nicolas Peron using by PFGSE NMR (Table 24). I have also fitted adsorption curves for TX-100 and C_{14}DAPS for solutions with $c_b = \text{cmc}$. The fitted values for D_{mon} are 3.6×10^{-10} m^2s^{-1} and 4.2×10^{-10} m^2s^{-1} respectively. A typical data fit is shown in Figure 64.

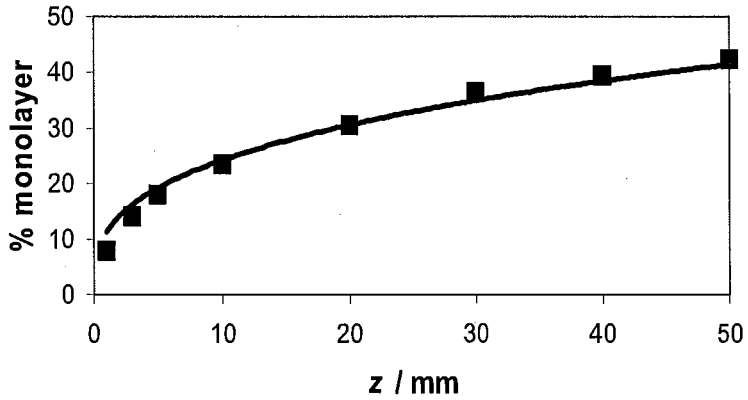

Figure 64: Adsorption curve data for $C_{14}E_8$ fitted using equation (7.28), u_0 = 0.87 ms^{-1}, T = 20 °C. (■) 1 mM $C_{14}E_8$ and (solid line) data fit.

It should be noted that equation (7.27) was derived assuming a pure water flow profile whereas in real surfactant solutions surface age is increased due to Marangoni effects.

It is therefore unsurprising that experimental surface excesses are slightly above the theoretical prediction for $z > 30$ mm where the real surface age is greater than the theoretical prediction assumes. This reasoning also explains why fitted diffusion coefficient values taken from liquid jet adsorption data tend to be slightly larger than values from other sources. Very close to the nozzle exit the measured values for surface excess are slightly less than the theoretical prediction. The origin of this discrepancy is unclear, although it may be due to a breakdown in the assumption of a linear relationship between ellipticity and surface excess at very low surface coverages.

Surfactant	D_{mic}^{FIT} / 10^{-10} m^2 s^{-1}	D_{mic}^{CALC} /10^{-10} m^{2}s^{-1}	D_{mon}^{NMR} / 10^{-10} m^{2}s^{-1}	D_{mic}^{NMR} /10^{-10} m^{2}s^{-1}
TX-100	**4.42**	**0.50**	**2.46±0.02**	**0.45 ± 0.03**
C_{14}DAPS	**3.31**	**0.61**	**3.39±0.03**	**0.61 ± 0.01**
α-C_{12}m	**2.75**	**0.62**	**2.69±0.02**	**0.61 ± 0.03**
$C_{12}E_8$	**1.97**	**0.54**	**2.59±0.03**	**0.51 ± 0.03**
β-C_{12}m	**2.0**	**0.54**	**2.62±0.03**	**0.49 ± 0.01**
$C_{14}E_8$	**0.91**	**0.49**	**2.55**	**0.44 ± 0.02**
$C_{16}E_8$	**0.90**	**0.40**	**2.47**	**0.42 ± 0.01**
$C_{12}E_6$	**0.77**	**Prolate = 0.56**	**2.91±0.04**	**0.47 ± 0.03**
β-C_{14}malt*	**0.37**	**Rod = 0.36** **Prolate = 0.72** **Rod = 0.43**	**4.46**	**0.49 ± 0.06**
$C_{14}E_6$	**0.004**	**0.05**	**2.82**	**0.14 ± 0.03**

Table 24: Diffusion coefficients for surfactant micelles determined from adsorption data, micelle dimensions from SANS and PFGSE NMR measurements. (* data for β-C_{14}m acquired at 40 °C)

It is satisfying to note that micelle diffusion coefficients calculated based upon micelle dimensions generally agree very well with those values determined directly

using PFGSE NMR techniques, i.e. $D_{mic}^{CALC} \approx D_{mic}^{NMR}$. This is particularly true for the small micellar systems which showed no evidence of elongation with an increase in bulk concentration. For $C_{12}E_6$, β-C_{14}malt and $C_{14}E_6$ which do show evidence of elongation, the agreement is less good, but still satisfactory at 1 mM bulk concentration.

Agreement between fitted diffusion coefficients D_{mic}^{FIT} and calculated values D_{mic}^{CALC} is less good. Surfactant systems which adsorb most rapidly at 1 mM do tend to have higher diffusion coefficients, but in many cases the fitted diffusion coefficient is more than twice calculated value. This comparison leads to a very important result; despite the fact that the majority of surfactant monomers are contained within micelles at the nozzle exit ($t = 0$), adsorption occurs at a diffusion controlled rate and in many cases several times faster to reach near saturation coverage by $z = 50$ mm ($t \approx 40$ ms). This result will be considered in more detail below.

7.3.5. The effect of micelle breakdown on adsorption kinetics

A third factor affecting the kinetics of surfactant adsorption is the rate of micelle breakdown beneath the surface. Figure 65 shows the ratio $D_{mic}^{FIT} / D_{mic}^{CALC}$ plotted as function of surfactant cmc for each system at 1 mM bulk concentration. For $C_{12}E_6$ and β-C_{14}malt D_{calc}^{mic} has been taken from the rod model fits. Surfactants with cmc > 0.1 mM appear to diffuse (and adsorb) much more rapidly than the calculated diffusion coefficient predicts, whilst systems with cmc < 0.1 mM appear to diffuse at a rate similar to the calculated value.

The most likely cause of this behaviour is the failure of the assumption in equation (7.28) that micelles do not gain or release monomers during the adsorption process. In Chapters 4 – 6 I explored the relationship between micelle-monomer exchange kinetics and local monomer concentration. My results showed that when monomer concentration is reduced below the cmc, which is the case close to an expanding interface, micelle breakdown is accelerated significantly. This acceleration increases the proportion of monomers relative to the frozen micelle case and therefore increases the effective diffusion coefficient. This acceleration will be greatest for systems with higher cmc's since the rate of individual monomer release is greater and the reduction

in monomer concentration required to facilitate rapid breakdown is lessened. Figure 31 shows the effect of monomer depletion on micelle lifetime for a series of C_nE_8 surfactants.

The trends in Figure 65 may be explained by rapid micelle breakdown due to monomer depletion that occurs at a rate governed by the system cmc. Surfactants with a cmc < 0.1 mM remain intact on the timescale of the liquid jet experiment despite the corresponding monomer depletion. Adsorption kinetics are governed by direct micelle adsorption as evidence by the observation that D_{mic}^{FIT} remains comparable with D_{mic}^{CALC}. For surfactants with cmc > 0.1 mM direct micelle adsorption can still occur but adsorption kinetics are governed by rapid micelle breakdown as a result of local monomer depletion.

It remains unclear, however, why such a large acceleration is observed for some systems such as TX-100 since the monomer concentration can never exceed the cmc. If the adsorption data in Figure 63 for TX-100 with c_b = cmc is fitted for a monomer diffusion coefficient, the fitted value $D_{mon}^{FIT} = 3.6\times10^{-10}$ is only marginally larger than the value measured by PFGSE-NMR.

These deductions are based upon theoretical models and calculations. In the following section I will present more adsorption measurements acquired in the presence of charge doping which support the conclusions above.

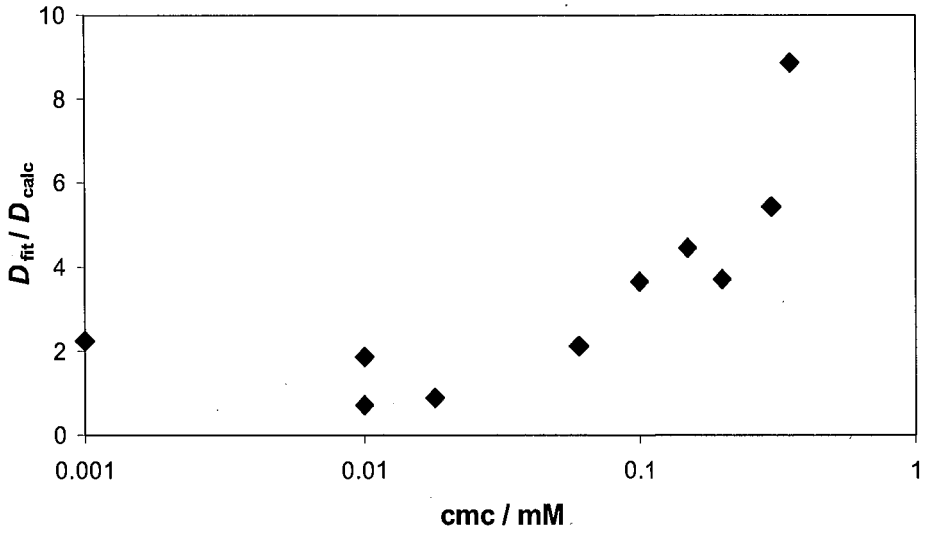

Figure 65: Ratio of D_{mic}^{FIT} to D_{mic}^{CALC} for nonionic surfactant micelle solutions at 1-mM plotted as a function of cmc.

7.4. Charge Doping

Doping the non-ionic micelles with an ionic surfactant provides a simple way of distinguishing between direct micelle adsorption and rapid micelle breakdown. In both chapter 3 and chapter 6 I introduced small amounts of the cationic surfactant CTAB into my micellar solutions. In chapter 3 I reported that my SANS measurements showed no evidence of a change in micellar size or shape upon this addition. In chapter 6 I further showed that this introduction did not change the system cmc significantly, although it did provide evidence in support of the combined fusion-Becker-Döring breakdown pathway over the conventional Becker-Döring model since the rate of micelle breakdown was decelerated upon CTAB addition.

Charge doping can also be used very effectively within the liquid jet adsorption experiment. I have performed an experiment which has two possible outcomes depending on whether rapid breakdown or direct micelle adsorption is the dominant adsorption mechanism. The presence of this charge within the micelle will increase the mutual diffusion coefficient, D_m, of the micelles due to the presence of migration fields generated by the smaller, more mobile counterions. D_m is given by

$D_m = (1+q)/(1/D_{mic} + q/D_{Br^-})$ where q is the charge (in electrons) on the micelle and D_{Br^-} is the self-diffusion coefficient of the counterion. Since D_{Br^-} is at least an order of magnitude larger than D_{mic} the diffusion rate of the micelles increases linearly with q. [161] Tominaga has validated this equation for mixtures of several nonionic and zwitterionic surfactants with long-chain ionic surfactants. [65, 162-166] Addition of 10% mole fraction of C_{18}TACl to solutions of C_{14}DAPS, $C_{12}E_8$ and $C_{12}E_6$ increases the mutual diffusion coefficient of the micelle by 4, 5 and 7 times respectively. Therefore, if the micelles are able to breakdown on the millisecond timescale the addition of charge will increase the adsorbed amount since mass transport towards the interface will be accelerated.

Conversely, if micelles adsorb directly to the interface without first breaking down there will be an electrostatic barrier to that adsorption and the adsorbed amount will decrease.

Figure 66 shows the percentage change in the surface excess measured at 50 mm from the nozzle exit upon addition of 0.1mM CTAB to a 1-mM surfactant solution plotted as function of cmc. There is a dramatic variation in the affect of charge addition across the different surfactants. For surfactants with higher cmc's the addition of charge increases the adsorbed amount consistent with a rapid micelle breakdown model whilst the adsorption of lower cmc surfactants is reduced consistent with direct micelle adsorption. $C_{10}E_8$ is added a control since 1-mM $C_{10}E_8$ is entirely monomeric and no effect is observed indicating that the mechanism for adsorption change operates via micelles only.

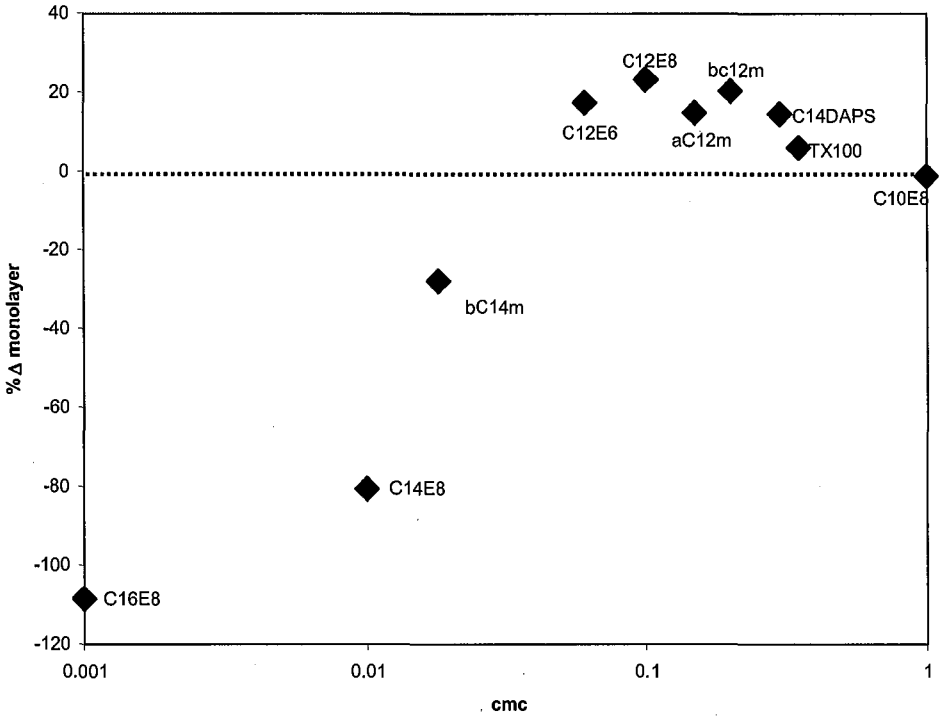

Figure 66 – Changes in the % monolayer coverage on addition of 0.1 mM CTAB to 1-mM surfactant solutions measured at z = 50mm plotted as a function of cmc

These measurements indicate a shift in the controlling adsorption mechanism with cmc, consistent with the diffusion coefficient comparisons considered in the section 7.3.4. I conclude that for systems with cmc's > 0.1 mM, monomer depletion close to the interface is sufficient to accelerate micelle breakdown and increase the monomer contribution to adsorption and consequently increase the effective diffusion coefficient. Direct micelle flux to the interface remains possible but rapid micelle breakdown and monomer adsorption dominates. For systems with cmc's < 0.1 mM micelle lifetimes are extended such that micelles persist within the liquid jet experiment. Under these conditions direct micelle flux to the interface remains the dominant adsorption mechanism. Systems with a cmc very close to this limit, such as $C_{12}E_6$, show traits of both adsorption mechanisms with an increase in adsorbed amount in Figure 66 but a fitted diffusion coefficient very close to the calculated value (Figure 65).

It should be noted that Tominaga measured an increase by more than a factor of 5 in the mutual diffusion coefficients of $C_{12}E_8$ when C_{18}TACl was added. [65, 162-166] With such large increases in the micellar diffusion coefficient expected based upon Tominaga's work, it is remains unclear the adsorbed amount only increases by ~ 20% for each surfactant system in my 'high cmc' category. One possible explanation is that rapid micelle breakdown prevents micelles from dominating mass transport and that the net mass transport rate is not directly proportional to D_m.

7.5. Higher concentrations

Experiments with surfactants at 1 mM are highly informative since it is possible to measure significant adsorption without immediate surface saturation. I have also carried out adsorption kinetics measurements with solutions of each surfactant studied at bulk concentrations of 2 and 4 mM. Figure 67 shows the adsorption kinetics of each surfactant from a 4 mM solution.

Under diffusion controlled adsorption, if one neglects Marangoni effects, one would expect the rate of surfactant adsorption to be proportional to bulk concentration. The degree of surfactant adsorption that occurs within 2 ms ($z < 1$ mm) is increased for all surfactant systems as indicated by the surface excess for the first measured data point, consistent with the increase in bulk concentration.

For the rest of the measured adsorption curve, near saturation coverage is observed for most surfactants which are dominated by rapid micelle breakdown (TX100, C_{14}DAPS, aC_{12}m, $C_{12}E_8$ and bC_{12}m). However, for surfactants that are dominated by direct micelle adsorption the increases in surface excess from 1 to 4 mM are not as large as expected using diffusion controlled considerations. It appears that the rate of surfactant adsorption slows as surface coverage increases.

This adsorption slowdown is seen most clearly in Figure 68 which shows the adsorption of both $C_{14}E_8$ and $C_{16}E_8$ at bulk concentrations of 2- and 4-mM. Once these surfactants reach ~ 40 % surface coverage the rate of adsorption falls dramatically. This slowdown can be ascribed to an adsorption barrier to direct micelle adsorption. These adsorption barriers may be related to the availability of adsorption sites on a surface, since adsorption of an entire micelle would spread a lot of

monomer onto a surface. One must also consider the structure of a micelle in solution. Although a micelle is commonly depicted as a relatively simple structure containing well separated hydrophilic and hydrophobic domains, this picture is physically unrealistic. A micelle in solution is a highly dynamic structure, continually exchanging monomers with the bulk solution and exposing parts of the hydrophobic core to solution. Mohan and Kopelvich discuss these fluctuations when considering the likelihood of monomers entering micelles. Micelle adsorption at an interface will be more probable if one of these short-lived hydrophobic patches encounters an unoccupied surface site, rather than the hydrophilic tail of an adsorbed surfactant monomer. The probability of these events will be inversely related to surface coverage.

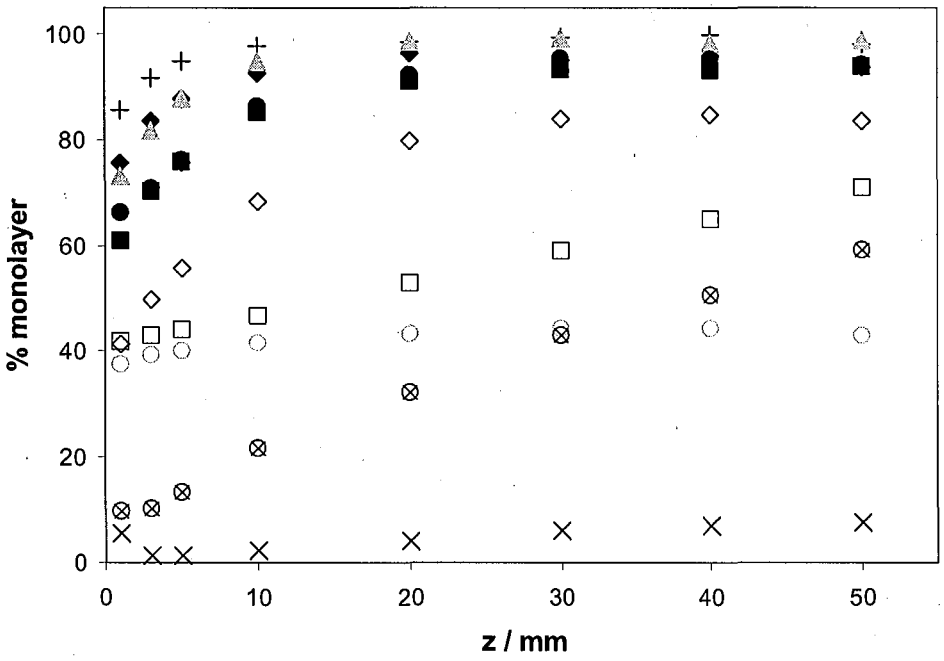

Figure 67- Adsorption curves for 4-mM surfactant solutions in the liquid jet. $u_0 = 0.87$ ms^{-1}, T = 20 °C, (+) TX-100, (♦) C_{14}DAPS, (■) α-C_{12}malt, (▲) $C_{12}E_8$, (●) β-C_{12}malt, (□) $C_{14}E_8$, (◊) C12E6, (○) $C_{16}E_8$, (⊗) β-C14m and (×) C14E6. [data for β-C14m acquired at 40 °C]

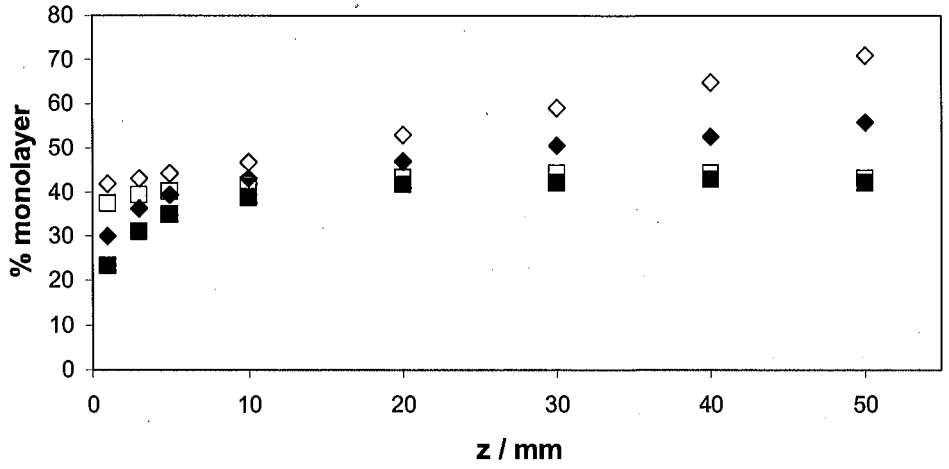

Figure 68 – Adsorption curves for 2 and 4-mM surfactant solutions in the liquid jet. $u_0 = 0.87$ ms^{-1}, T = 20 °C, (♦) 2 mM $C_{14}E_8$, (◊) 4 mM $C_{14}E_8$, (■) 2 mM $C_{16}E_8$ and (□) 4 mM $C_{16}E_8$

7.6. Summary

For a wide range of micellar nonionic surfactant solutions significant adsorption is possible on the millisecond timescale despite the majority of surfactant monomer being contained within micelles. There are two possible explanations for these observations both of which run contrary to other established literature. For some surfactant systems, monomer depletion close to an expanding interface is sufficient to allow rapid micelle breakdown and monomer release which dominates surfactant adsorption kinetics, with fitted diffusion coefficients approaching the monomer diffusion limit. For other surfactant systems a direct flux of non-ionic micelles to an air-water interface remains the dominant adsorption mechanism. The switch between these two adsorption limits is a fairly gradual one that, for the conditions in the liquid jet, occurs when the cmc is close to 0.1 mM.. Whilst this general behaviour is likely to apply to many systems, it will be the precise hydrodynamics of the system which determine where this switchover occurs.

Chapter 8

Conclusion

The aim of this work was to develop a deeper understanding of structure-kinetics relationships in micellar solutions of nonionic surfactants. I have identified two key areas in which existing kinetic theory requires further development and these have formed the core of this work.

Firstly, the conventional treatment of micelle breakdown in bulk solution has very limited applicability. The Aniansson and Wall model for micelle breakdown has been the cornerstone for the analysis of micelle relaxation measurements for more than three decades. However, examination of the original derivation of their theory quickly reveals that it should only be applied to systems at, or very close to, equilibrium and should not have been applied to most of the experiments to which it has been. The starting point for my kinetic analysis was to test this generally accepted theory of micelle breakdown using a numerical modelling approach.

It is the micelle size distribution which ultimately determines micelle breakdown rate within the Aniansson and Wall model. Starting from the fundamental thermodynamics which underlie surfactant aggregation, I calculated a series of realistic micelle size distributions for the nonionic surfactants C_nE_m. When these realistic size distributions are used as inputs, the equations of Aniansson and Wall predict micelle lifetimes which seem unphysically large, many orders of magnitude longer than the experiments which claim to support the model suggest. This discrepancy seems odd, since so many authors have used the equations of Aniansson and Wall to fit their data. However, since the primary approach to using the Aniansson and Wall theory has been to assume that the theory is true and extract information on the micelle size distribution from kinetic data, the failure to notice this discrepancy is unsurprising.

In order to verify that the Aniansson and Wall model does not provide a mechanism by which micelles breakdown on the milliseconds to second's timescale, I performed a range of numerical simulations to test how micelle systems would respond to a perturbation such as a dilution. Full kinetic simulations, which track the concentration

of all aggregates in the system following a dilution, reveal that the relaxation of monomer concentration initially proceeds very much as Aniansson and Wall predicted. Each micelle in the system loses a small number of monomers on a timescale determined by the rate of individual monomer exchange. Once the monomer concentration has relaxed, however, the system enters a quasi-equilibrium state where no further change in aggregate concentrations is observed.

In order to gain further insight into this quasi-equilibrium I also performed a series of stochastic simulations whereby I considered changes in aggregation number for an individual micelle. These simulations led to a very important result; that micelle lifetime is a very strong function of local monomer concentration. When monomer concentration is reduced below the cmc the probability of micelle breakdown in unitary steps increases rapidly and micelle lifetimes tends towards the limit of N/k^- where k^- is the average rate constant for individual monomer loss. Finally, in order to calculate micelle lifetimes when the monomer concentration is not depleted, i.e. in the quasi-equilibrium state, I used a transition state theory approach by converting the chemical potential variation of each aggregate into a free energy surface. This approach revealed that micelle lifetimes at equilibrium within the Becker-Döring model are of the order 10^5 s, 10^9 s and 10^{14} s for $C_{10}E_8$, $C_{12}E_8$ and $C_{14}E_8$, respectively. These lifetimes are in close agreement with the predictions of the Aniansson and Wall model.

These simulations strongly suggest that micelle breakdown, as measured in relaxation experiments for more than fifty years, does not in fact proceed by the Aniansson and Wall model for many surfactants. I do not imply that the Aniansson and Wall model is incorrect and does not occur, only that if one uses realistic, exogenously determined micelle size distributions then the calculated micelle lifetimes are significantly longer than experiments suggest. There must be an alternative route that allows micelles to break down. My hypothesis is that micelles break down by a combined fusion-Becker-Döring route whereby micelles collide and merge to form super-micelles which then shed monomers. The net effect of this process is that two micelles can be transformed into single micelle and some monomers without incurring the high energy penalty corresponding to the formation of intermediate sized aggregates. I have tested this hypothesis using numerical methods and have shown that this

pathway provides a feasible micelle breakdown route. Experimental measurements of micelle breakdown rates using stopped-flow fluorescence are also consistent with this breakdown pathway.

Secondly, I questioned the assumption that micelles may not adsorb directly to an expanding air-water interface. My own early work measuring the adsorption kinetics of a single nonionic micellar system suggested that this assumption that was not generally valid. [42] Based upon my own measurements I hypothesised that nonionic surfactant micelles could indeed adsorb directly to a nascent air-water interface at a diffusion controlled rate. There is no physical reason why an uncharged micelle should not approach and adsorb to a clean air-water interface. However, since the no-flux assumption is a key component of every theory developed to explain adsorption kinetic data from micellar solutions it was essential to test my hypothesis more rigorously as part of this study.

Using the well-tested liquid jet platform I measured the adsorption kinetics for nine nonionic surfactants and one zwitterionic surfactant at a range of bulk concentrations. Comparison of fitted diffusion coefficients with values from direct measurements using PFGSE NMR and with values calculated based upon micelle dimensions suggest two types of adsorption mechanism. Surfactants with cmc < 0.1 mM behave in a manner consistent with the direct, diffusion controlled adsorption of micelles, whilst systems with cmc > 0.1 mM behave as though micelles break down before reaching the surface. This rapid micelle breakdown, several order of magnitude faster than literature values for micelle lifetimes, is the result of local monomer depletion and is entirely consistent with my theory of micelle breakdown kinetics. This switchover in adsorption mechanism is further supported by the results of my charge doping experiments. Neither of these adsorption mechanisms is incorporated into existing theories of micelle adsorption, which assume a single micelle breakdown time and do not allow a direct flux of micelles to the interface.

The results of my work have wide-reaching implications for the analysis of both micelle breakdown and adsorption kinetics measurements. In the case of micelle breakdown measurements, unless the perturbation from equilibrium is very small (<1%) and it can be shown that the free energy of intermediate-sized aggregates is not so high as to prohibit breakdown by a Becker-Döring mechanism, the Aniansson and

Wall results should not be applied. Instead, models need to recognise that (i) micelle breakdown time is dependent upon local monomer concentration and is not a colligative system property and (ii) micelle breakdown rate is governed by the collision rate of existing micelles and the rate of monomer loss from super-micelles. In the case of adsorption kinetics it will be necessary to develop a quantitative model of adsorption behaviour that incorporates a direct flux of micelles to a nascent air-water interface and considers the variation in monomer concentration with depth beneath the surface. These new insights into adsorption mechanisms may not change the interpretation of dynamic surface tension and adsorption data for experiments on the timescale of seconds or longer. However, for instruments that measure adsorption kinetics on millisecond timescales, such as the maximum bubble pressure apparatus, overflowing cylinder and liquid jet, these considerations are important.

The key priorities for future work are in two areas of modelling. First, a more rigorous mathematical model that describes the combined fusion-Becker-Döring process for micelle breakdown, which incorporates the possibility of micelle formation via supermicelles and which captures the change in micelle breakdown rate close to equilibrium needs to be developed. Work is currently in progress at the Oxford Centre for Collaborative and Applied Mathematics (OCCAM), to achieve this outcome by treating the micelle size distribution as a continuous rather than discrete variable. This model will permit quantitative analysis of my stopped flow experiments. Second, the mathematical description of micelle breakdown needs to be incorporated into a numerical model for adsorption to the surface of the liquid jet. To provide quantitative predictions of experimental data, this model will need also to incorporate Marangoni effects and the coverage-dependence of direct micelle adsorption when it occurs.

References

1. Rosen, M. J., *Surfactants and Interfacial Phenomena, 3rd Edition*, 2004.
2. Chang, C.-H., Franses, E. T., *Colloids and Surfaces A*, 1995, **100**, 1-45.
3. Bradley, J. E., Lee, E. M., Thomas, R. K., Willatt, A. J., Ward, R. C., Gregory, D. P., Waschkowski, W., Penfold, J., *Langmuir*, 1988, **4**, 821-826.
4. Penfold, J., Thomas, R. K., *J. Phys.: Condens. Matter*, 1990, **2**, 1369-1412.
5. Lu, J. R., Simister, E. A., Lee, E. M., Thomas, R. K., Rennie, A. R., Penfold, J., *Langmuir*, 1992, **8**, 1837-1844.
6. Lu, J. R., Thomas, R. K., Penfold, J., *Advances in Colloid and Interface Science*, 2000, **84**, 143-304.
7. Duhkin, S. S., Kretzschmar, G., Miller, R., *Dynamics of Adsorption at Liquid Interfaces*, Elsevier, Amsterdam, 1995.
8. Fainerman, V. B., Mobius, D., Miller, R., *Surfactants: Chemistry, Interfacial Properties, Applications*, Elsevier, Amsterdam, 2001.
9. Eastoe, J., Dalton, J. S., *Advances in Colloid and Interface Science*, 2000, **85**, 103-144.
10. Hansen, R. S., Wallace, T. C., *J. Phys Chem*, 1959, **63**, 1085-1091.
11. Posner, A. M., Anderson, J. R., Alexander, A. E., *Journal of Colloid and Interface Science*, 1952, **7**, 623-644.
12. Ward, A. F. H., Tordai, L., *Journal of Chemical Physics*, 1946, **14**, 453-461.
13. Johannsen, E. C., Chung, J. B., Chang, C. H., Franses, E. I., *Colloids and Surfaces A*, 1991, **53**, 117-134.
14. Sutherland, K. L., *Aust. J. Sci. Res, Ser. A*, 1952, **5**, 683-696.
15. Hansen, R. S., *J. Phys Chem*, 1960, **64**, 637-341.
16. Van den Bogaert, R., Joos, P., *J. Phys Chem*, 1979, **83**, 2244-2248.
17. Fainerman, V. B., Makievski, A. V.,Miller, R., *Colloids and Surfaces A*, 1994, **87**, 61-75.
18. Baret, J. F., *J. Phys Chem*, 1968, **72**, 2755-2758.
19. Borwankar, R. P., Wasan, D. T., *Chemical Engineering Science*, 1983, **38**, 1637-1649.
20. Hsu, C.-T., Chang, C-H., Lin, S-Y., *Langmuir*, 1999, **15**, 1952-1959.
21. Liggieri, L., Ravera, F., Passerone, A., *Colloids and Surfaces A*, 1996, **114**, 351-359.
22. Liggieri, L., M. Ferrari, A. Massa and F. Ravera, *Colloids and Surfaces, A: Physicochemical and Engineering Aspects*, 1999, **156**, 455-463.
23. Lin, S.-Y., McKeigue, K., Maldarelli, C., *Langmuir*, 1991, **7**, 1055-1066.
24. Lin, S.-Y., McKeigue, K., Maldarelli, C., *Langmuir*, 1994, **10**, 3442-3448.
25. Lin, S.-Y., Lu, T-L., Hwang, W-B., *Langmuir*, 1995, **11**, 555-562.
26. Lin, S.-Y., Chang, H-C., Chen, E-M., *J. Chem. Eng. Jap.*, 1996, **29**, 634-641.
27. Lin, S.-Y., Tsay, R-Y., Lin, L-W., Chen, S-I., *Langmuir*, 1996, **12**, 6530-6536.
28. Lin, S.-Y., Tsay, R-Y., Lin, L-W., Chen, S-I., *Langmuir*, 1997, **13**, 3191-3197.
29. Lee, Y.-C., Stebe, K. J., Liu H.-S., Lin, S.-Y., *Colloids and Surfaces, A: Physicochemical and Engineering Aspects*, 2003, **220**, 139-150.
30. Danov, K. D., Kralchevsky, P. A., Ananthapadmanabhan, K. P., Lips, A., *Colloids and Surfaces A*, 2006, **282-283**, 143-161.
31. Danov, K. D., Vlahovska, P. M., Horozov, T., Dushkin, C. D., Kralchevsky, P. A., Mehreteab A., Broze, G., *Journal of Colloid and Interface Science*, 1996, **183**, 223-235.
32. Fainerman, V. B., *Colloids and Surfaces*, 1992, **62**, 333-347.

33. Fainerman, V. B., Makievski, A. V., *Colloids and Surfaces*, 1993, **69**, 249-263.
34. Fainerman, V. B., Mys, V. D., Makievski, A. V., Petrov, J. T., Miller, R., *Journal of Colloid and Interface Science*, 2006, **302**, 40-46.
35. Frese, C., Ruppert, S., Sugar, M., Schmidt-Lewerkuhne, H., Wittern, K. P, Fainerman, V. B., Miller, R., *Journal of Colloid and Interface Science*, 2003, **267**, 475-482.
36. Frese, C., Ruppert, S., Schmidt-Lewerkuhne, H., Wittern, K. P., Eggers, R., Fainerman V. B., Miller, R.,*Colloids and Surfaces, A: Physicochemical and Engineering Aspects*, 2004, **239**, 33-40.
37. Liao, Y.-C., Basarn, O. A. E., Franses, I., *AIChE*, 2003, **49**, 3229-3240.
38. Miller, R., *Colloid and Polymer Science*, 1981, **259**, 1124-1128.
39. Mitrancheva, J. V., Dushkin C. D., Joos, P., *Colloid and Polymer Science*, 1996, **274**, 356-367.
40. Noskov, B. A., *Advances in Colloid and Interface Science*, 2002, **95**, 237-293.
41. Rillaerts, P., *Journal of Physical Chemistry*, 1982, **86**, 3471-3478.
42. Colegate, D. M., Bain, C. D., *Physical Review Letters*, 2005, **95**, 198302.
43. Song, G., Couzis, A., Somasundaran, P., Maldarelli, C., *Colloids and Surfaces A*, 2006, **282-283**, 162-182.
44. Lang, J., Auborn, J., Eyring, E., *Journal of Colloid and Interface Science*, 1972, **41**, 484-490.
45. Yasunaga, T., Takeda K., Harada, S., *Journal of Colloid and Interface Science*, 1973, **42**, 457-463.
46. Tondre C., Zana, R., *Journal of Colloid and Interface Science*, 1978, **66**, 544-558.
47. Mijnlieff, P. F., Ditmarsch, R., *Nature*, 1965, **5013**, 889-891.
48. Baumgardt, G., Strey, R., *Berichte der Bunsen-Gesellschaft*, 1979, **83**, 1222-1229.
49. Kresheck, G. C., Hamori, E., Davenport, G., Scheraga, H. A., *Journal of the American Chemical Society*, 1966, **88**, 246-253.
50. Lang, C.; Zana, R.; Bauer, R.; Hoffman, H.; Ulbricht, W., *J. Phys Chem*, 1975, **79**, 276-283.
51. Teubner, M., *J. Phys Chem*, 1979, **83**, 2917-2920.
52. Muller, N., *J. Phys Chem*, 1972, **76**, 3017-3020.
53. Aniansson, E. A. G., Wall, S. N., *J. Phys Chem*, 1974, **78**, 1024-1030.
54. Aniansson, E. A. G., Wall, S. N., *J. Phys Chem*, 1975, **79**, 857.
55. Aniansson, E. A. G., Wall, S. N., et al, *J. Phys Chem*, 1976, **80**, 905-921.
56. Wennerstrom, H., Lindman, B., *Physics Reports (Review Section of Physics Letters)*, 1979, **52**, 1-86.
57. Eastoe, J. D., Downer, A., *Langmuir*, 1998, **14**, 1937-1939.
58. Yushmanov, I.; Stilbs, P., *Langmuir*, 2006, **22**, 2002-2004.
59. Lucassen, J., *Faraday Discussions of the Chemical Society*, 1976, **59**, 76-87.
60. Fainerman, V. B., *Kolloidn. Zh.*, 1981, **43**, 94.
61. Dushkin, C., Ivanov I., Kralchevski, P.,*Colloids and Surfaces*, 1991, **60**, 235-261.
62. Bain, C. D., Manning-Benson, S., Darton, R. C., *Journal of Colloid and Interface Science*, 2000, **229**, 247-256.
63. Penfold J., et al, *ACS Symposium Series*, 2003, **861**.
64. Carnero-Ruiz, C., Aguiar, J., *Colloids and Surfaces A*, 2003, **224**, 221-230.
65. Nogami, Y., Iwata, M., Tominaga, T., *J. Mol. Liquids*, 2005, **119**, 83-87.

66. Ueno, *Colloid and Polymer Science*, 1981, **259**, 761-766.
67. Becher, *Nonionic Surfactants*, Marcel Dekker, New York, 1987.
68. Herrmann, K. W., *Journal of Colloid and Interface Science*, 1966, **22**, 352-359.
69. Dupuy, C., Auvray, X., Petipas, C., Rico-Lattes I., Lattes, A., *Langmuir*, 1997, **13**, 3965-3967.
70. Zhang, *Langmuir*, 1996, **12**, 2371-2373.
71. Patil, *Soft Matter*, 2008, **4**, 840-848.
72. Zhmud, *Langmuir*, 2000, **16**, 2557-2565.
73. Frescura, *J. Phys Chem*, 1995, **99**, 11494-11500.
74. Campbell, R. A., Bain, C. D., *Langmuir*, 2004, **20**, 8470-8753.
75. Manning-Benson, S., Bain, C. D., Darton, R. C., *Journal of Colloid and Interface Science*, 1997, **189**, 109-116.
76. Valkovska, D., Wilkinson, K. M., Campbell, R. A., Bain, C. D., Wat R., Eastoe, J., *Langmuir*, 2003, **19**, 5960-5962.
77. Valkovska, D. S., Shearman, G. C., Bain, C. D., Darton, R. C., Eastoe, J., *Langmuir*, 2004, **20**, 4436-4445.
78. Battal, T., Bain, C. D., Weiss, M., Darton, R. C., *Journal of Colloid and Interface Science*, 2003, **263**, 250-260.
79. Marangoni, C., *Ann. Phys.*, 1871, **143**, 337.
80. Weiss, M., Darton, R. C., Battal T., Bain, C. D., *Industrial & Engineering Chemistry Research*, 2004, **43**, 5203-5220.
81. Colegate, D. M., Bain, C. D., *Aus. J. Chem*, 2005, **58**, 678-682.
82. Hansen, R. S., *J. Phys Chem*, 1964, **68**, 2012.
83. Davies, J. T., Makepiece, R. W., *AICheE*, 1978, **24**, 524-530.
84. Jobert, P. P., Leblond, J., *Journal of Colloid and Interface Science*, 1979, **68**, 478-485.
85. Roe, R.-J., *Methods of X-ray and neutron scattering in polymer science*, Oxford University Press, New York, 2000.
86. Robson, R. J., Dennis, E. A., *J. Phys Chem*, 1977, **81**, 1075-1078.
87. Coppola, L., La Mesa, C., Ranieri, G. A., Terenzi, M., *Colloid and Polymer Science*, 1989, **267**, 86-91.
88. Goyal et al, *Physical Review E*, 1995, **51**, 2308-2315.
89. Nilsson, P. G., Wennerstroem H., Lindman, B., *Journal of Physical Chemistry*, 1983, **87**, 1377-1385.
90. Kato, T., Anzai, S., Takano S., Seimiya, T., *Journal of the Chemical Society, Faraday Transactions 1: Physical Chemistry in Condensed Phases*, 1989, **85**, 2499-2506.
91. Corti, M., Degiorgio, V., Hayter, J. B., Zulauf, M., *Chemical Physics Letters*, 1984, **109**, 579-583.
92. Hedin, N., Furo, I., *Langmuir*, 2000, **16**, 7548-7550.
93. Zulauf, K.; Hayter, J. B.; Degiorgio, V.; Corti, M., *Journal of Physical Chemistry*, 1985, **89**, 3411-3417.
94. Cummins, P. G., Staples, E., Penfold J., Heenan, R. K., *Langmuir*, 1989, **5**, 1195-1199.
95. Penfold, J., Staples, E., Tucker I., Cummins, P., *Journal of Colloid and Interface Science*, 1997, **185**, 424-431.
96. Sato, T., Saito Y., Anazawa, I., *Journal of the Chemical Society, Faraday Transactions 1: Physical Chemistry in Condensed Phases*, 1988, **84**, 275-279.

97. Hamada N., Einaga, Y., *Journal of Physical Chemistry B*, 2005, **109**, 6990-6998.
98. Yoshimura, S, Einaga, Y., *Journal of Physical Chemistry B*, 2004, **108**, 15477-15487.
99. Richtering, W. H., Burchard, W., Jahns, E., Finkelmann, H., *J. Phys Chem*, 1988, **92**, 6032-6040.
100. Ericsson, C. A., Soederman, O., Garamus, V. M., Bergstroem M., Ulvenlund, S., *Langmuir*, 2005, **21**, 1507-1515.
101. del Mar Graciani, M., Rodriquez, A., Munoz, M., Moya, M. L., *Langmuir*, 2005, **21**, 7161-7169.
102. Di Profio, P., Germani, O., Savelli, G., Giorgio, C., Chiarani, M., Mancini, G., Bunton, C. A., Gilitt, N., *Langmuir*, 1998, **14**, 2662-2669.
103. Molina-Bolivar, J. A., Aguiar, J., Ruiz, C. C. , *Molecular Physics*, 2001, **99**, 1729-1741.
104. Heenan, R., *FISH reference manual*, 2007.
105. Israelachvili, J., *Intermolecular and Surface Forces*, 2 edn., Academic, London, 1991.
106. Heenan, R., Editon edn., 2007.
107. Eagland, D., Crowther, N. J., Butler, C. J., *Polymer*, 1992, **34**, 2804-2808.
108. www.sigmaaldrich.com.
109. Zhuo, K., Zhang, H., Wang, Y., Liu, Q., Wang, J., *Journal of Chemical and Engineering Data*, 2009, **50**, 1589-1595.
110. Islam, M. N., Kato, T., *Langmuir*, 2003, **19**, 7201-7205.
111. Drummond, C. J., Warr, G. G., Grieser, F., Ninham B. W., Evans, D. F., *Journal of Physical Chemistry*, 1985, **89**, 2103-2109.
112. Sesta, M. B., *Colloid and Polymer Science*, 1989, **267**.
113. Janczuk, B. B., Gonzalez-Martin, M. L., Dorado-Calasanz, C., *Langmuir*, 1995, **11**, 4515-4518.
114. Colen, A., *J. Phys Chem*, 1974, **78**, 1676-1680.
115. Leung R., Shah, D. O., *Journal of Colloid and Interface Science*, 1986, **113**, 484-499.
116. Malliaris, J., Zana, R., *J. Phys Chem*, 1986, **90**, 655-660.
117. Kato, S., Nomura, H., Honda, H., Zielinski, R., Ikeda, S., *J. Phys Chem*, 1988, **92**, 2305-2310.
118. Michels. M., Frindi, B., Zana, R., *Journal of Physical Chemistry*, 1994, **98**, 6607-6611.
119. Chertkov, E. V., Saidov, A. A., Khabibullaev, P. K. , *Colloids and Surfaces A*, 2000, **168**, 185-191.
120. Patist, J. R.; Shukla, P. K.; Shah, D. O., *Journal of Colloid and Interface Science*, 2002, **245**, 1-15.
121. Kahlweit, M., *Pure and Appl. Chem.*, 1981, **53**, 2069-2081.
122. Hall, D. G., *Faraday Transactions. 2*, 1981, **77**, 1973-2006.
123. Lessner, E., Teubner M., Kahlweit, M., *Journal of Physical Chemistry*, 1981, **85**, 3167-3175.
124. Kuni, F. M., Rusanov, A. I., Grinin, A. P., Shcheckin, A. K., *Colloid Journal (Translation of Kolloidnyi Zhurnal)*, 2001, **63**, 792-800.
125. Nyrkova, I. A., Semenov, A. N., *Macromolecular Theory and Simulations*, 2005, **14**, 569-585.
126. Doring. W., Becker, R., *Ann. Phys.*, 1935, **24**, 719-752.
127. Moraes, J. N. B., Figueiredo, W., *Phys. Stat. Sol.*, 2001, **1**, 57-62.

128. Jorge, M., *Langmuir*, 2008, **24**, 5714-5725.
129. Mohan, G., Kopelvich, D. I., *J. Chem. Phys.*, 2008, **128**.
130. Nagarajan, R., Ruckenstein, E., *Journal of Colloid and Interface Science*, 1979, **71**, 580-604.
131. Nagarajan R., Ruckenstein, E., *Langmuir*, 1991, **7**, 2934-2969.
132. Puvvada, S., Blankschtein, D., *J. Chem. Phys.*, 1989, **92**, 3710-3724.
133. Nagarajan R., Ruckenstein, E., *J. Phys Chem*, 1981, **85**, 3010-3014.
134. Stephenson, B. C., Beers, K., Blankschtein, D., *Langmuir*, 2006, **22**, 1500-1513.
135. Rharbi, Y., Li, M., Winnik, M. A., Hahn Jr, K. G., *Journal of the American Chemical Society*, 2000, **122**, 6242-6251.
136. Rharbi, Y., Winnik, M. A., Hahn Jr, K. G., *Langmuir*, 1999, **15**, 4697-4700.
137. Förster, T., Sellinger, B. K. , *Z. Naturforsch*, 1964, **19**, 38.
138. Mohan, S. V., Prasanna, D., Reddy, B. P., Sarma, P. N. , *International Biodeterioration and Biodegradation*, 2008, **62**, 162-169.
139. Nilsson, S., Holmberg, C., Sundelof, L.-O., *Colloid and Polymer Science*, 1995, **273**, 83-95.
140. Geiger, M. W., Turro, N. J., *Photochemistry and Photobiology*, 1975, **22**, 273-276.
141. Turro, N. J., Kuo, P. L., *J. Phys Chem*, 1987, **91**, 3321-3325.
142. Kano, K., Ueno, Y., Hashimoto, S., *J. Phys Chem*, 1985, **89**, 3161-3166.
143. Lianos, P., Zana, R., *J. Phys Chem*, 1980, **84**, 3339-3341.
144. Rodenas, E., Perez-Benito, E., *J. Phys Chem*, 1991, **95**, 4552-4556.
145. Infelta, P. P., Gratzel, M., *J. Chem. Phys.*, 1979, **70**, 179-186.
146. Cummins, H. Z., Yeh, Y., *Appl. Phys. Letters*, 1964, **4**, 176.
147. Drain, L. E., *Laser Focus Foberopt. Comm.*, 1980, **16**, 68.
148. Mobius, D., Miller, R., *Novel Methods to Study Interfacial Layers*, Elsevier, 2001.
149. Hecht, E., *Optics*, 2 edn., Addison-Wesley, 1974.
150. Beaglehole, D., *Physica*, 1980, **100B**, 163.
151. Jasperson, S. N., Burge, D. K., O'Handley, R. C., *Surface Science*, 1973, **37**, 548-558.
152. Drude, P., *The theory of optics (translated from german by C. Riborg Mann and Robert A. Millikan)*, Longmans, Green, and Co., New York, 1902.
153. Curwen, T., PhD Thesis, University of Oxford, 2007.
154. Meunier, J., *Light Scattering by Liquid Surfaces and Complementary Techniques, Chapter 17*, Marcel Dekker, New York, 1992.
155. Goates, S. R., Schofield, D. A., Bain, C. D., *Langmuir*, 1999, **15**, 1400.
156. Campbell, R. A., *Vibrational Spectroscopy*, 2004, **35**, 205-211.
157. Staples, E., Penfold, J., Tucker, I., Thomas, R. K., Woodling, R., Dong, C. C., *Journal of Colloid and Interface Science*, 2003, **262**, 235-242.
158. Lyklema, J., *Fundamentals of Interface and Colloid Science*, 2 edn., Academic Press Ltd, London, 1991.
159. Natishin, Y. A., Liu, H., Shiyanovskii, S. V. , Lavrentovich, O. D. , Kostko, A. F. , Ansimov, M. A. , *Physical Review E*, 2004, **70**, 051706.
160. Cummins, P. G., Hayter, J. B., Penfold J., Staples, E., *Chemical Physics Letters*, 1987, **138**, 436-440.
161. Atkins, P. W., *Physical Chemistry*, 6 edn., OUP, Oxford, 1998.
162. Nogami, Y., Watnabe, H., Ohtaka-Saiki, H., Tominaga, T., *Colloids and Surfaces A*, 2000, **169**, 227-232.

163. Tominaga T., Nakamura, T., *Journal of Molecular Liquids*, 1997, **73,74**, 413-417.
164. Tominaga, T., Nakamura T., Saiki, H., *Chemistry Letters*, 1997, 979-980.
165. Tominaga T., Nishinaka, M., *Journal of the Chemical Society, Faraday Transactions*, 1993, **89**, 3459-3464.
166. Tominaga T., Nishinaka, M., *Journal of Molecular Liquids*, 1995, **65/66**, 333-336.

Appendix 1: Best fit curves to SANS data

$C_{12}E_8$

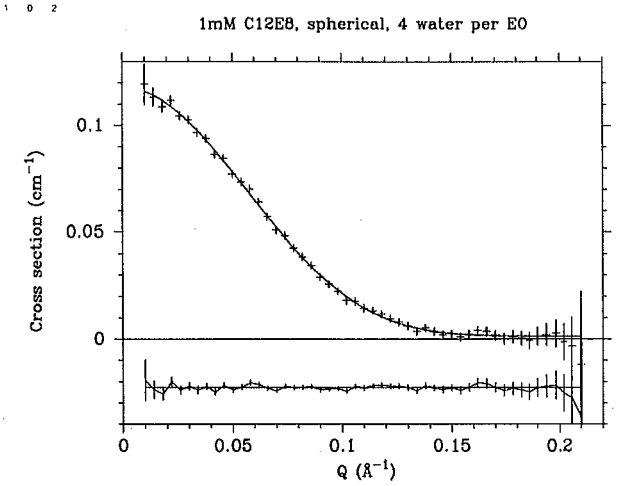

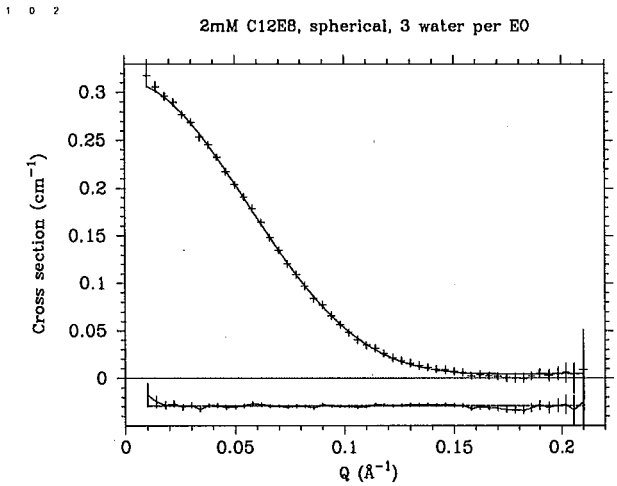

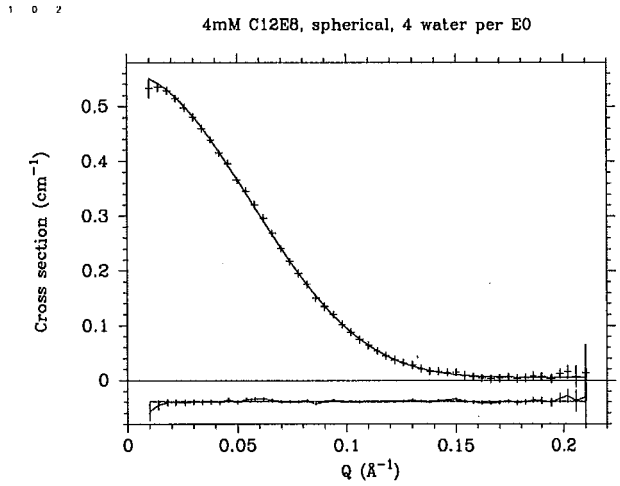

$C_{14}E_8$

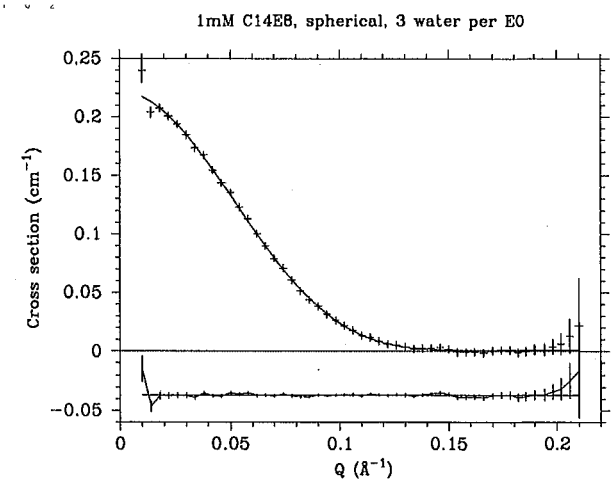
1mM C14E8, spherical, 3 water per EO
Cross section (cm^{-1})
Q (Å^{-1})
0.25
0.2
0.15
0.1
0.05
0
−0.05
0
0.05
0.1
0.15
0.2

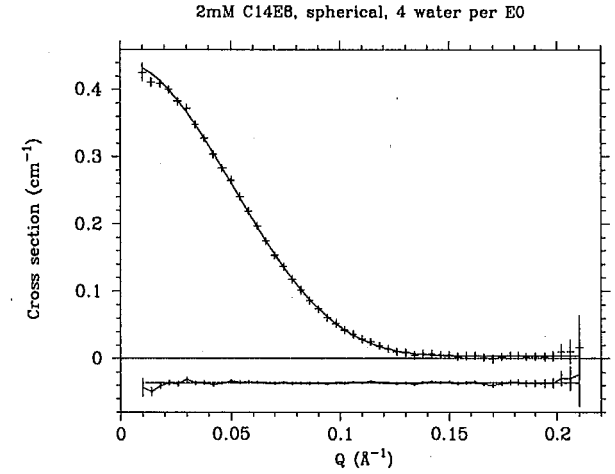
2mM C14E8, spherical, 4 water per EO
Cross section (cm^{-1})
Q (Å^{-1})
0.4
0.3
0.2
0.1
0
0
0.05
0.1
0.15
0.2

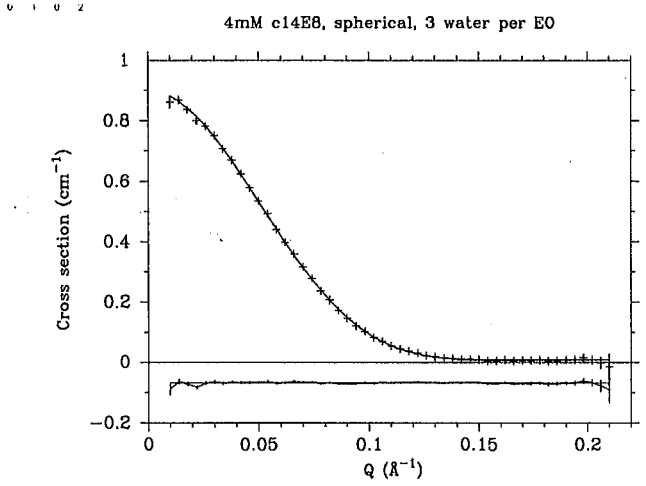
4mM c14E8, spherical, 3 water per EO
Cross section (cm^{-1})
Q (Å^{-1})
1
0.8
0.6
0.4
0.2
0
−0.2
0
0.05
0.1
0.15
0.2

C_{14}DAPS

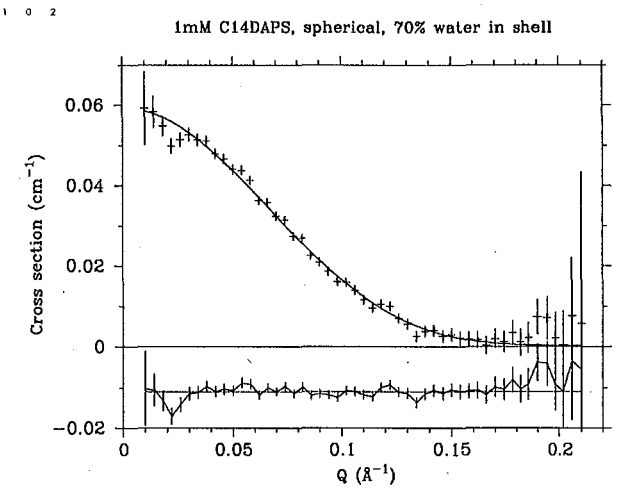
1mM C14DAPS, spherical, 70% water in shell
Cross section (cm^{-1})
0.06
0.04
0.02
0
−0.02
0
0.05
0.1
0.15
0.2
Q (Å^{-1})

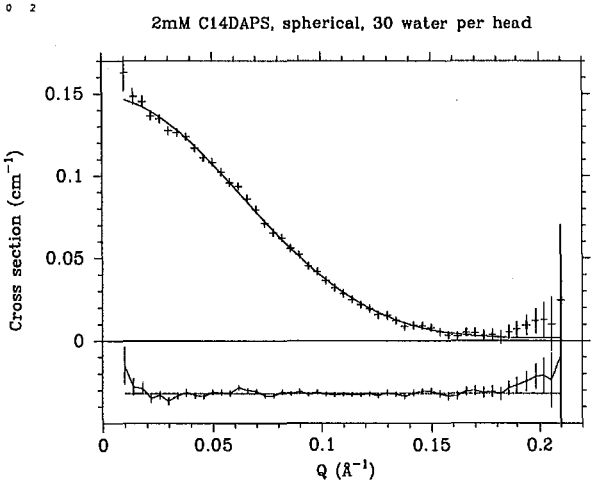
2mM C14DAPS, spherical, 30 water per head
Cross section (cm^{-1})
0.15
0.1
0.05
0
0
0.05
0.1
0.15
0.2
Q (Å^{-1})

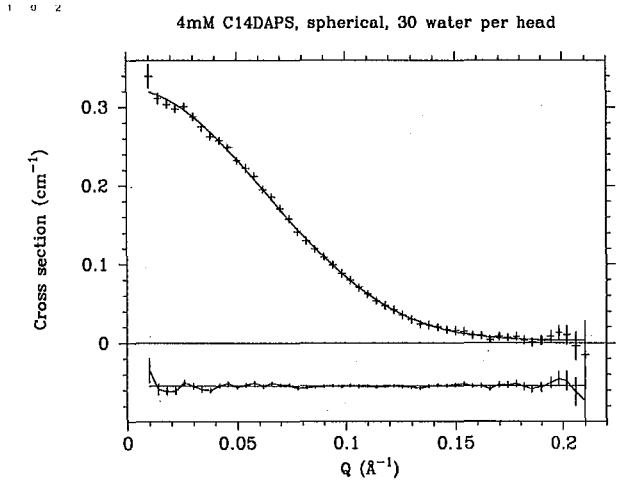
4mM C14DAPS, spherical, 30 water per head
Cross section (cm^{-1})
0.3
0.2
0.1
0
0
0.05
0.1
0.15
0.2
Q (Å^{-1})

α-C_{12}malt

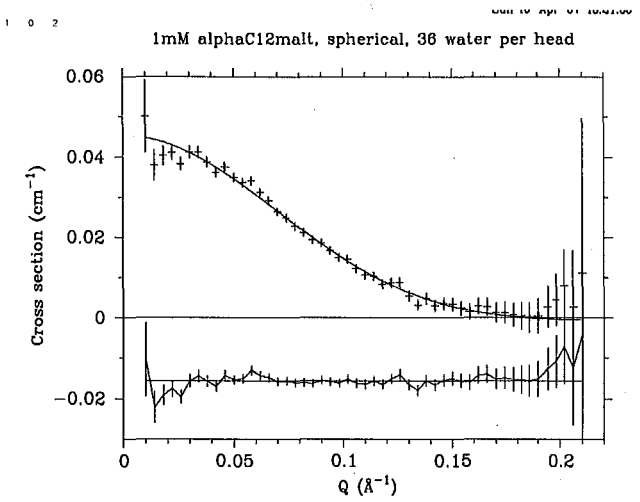
1mM alphaC12malt, spherical, 36 water per head
Cross section (cm^{-1})
0.06
0.04
0.02
0
−0.02
0
0.05
0.1
0.15
0.2
Q (Å^{-1})

β-C_{12}malt

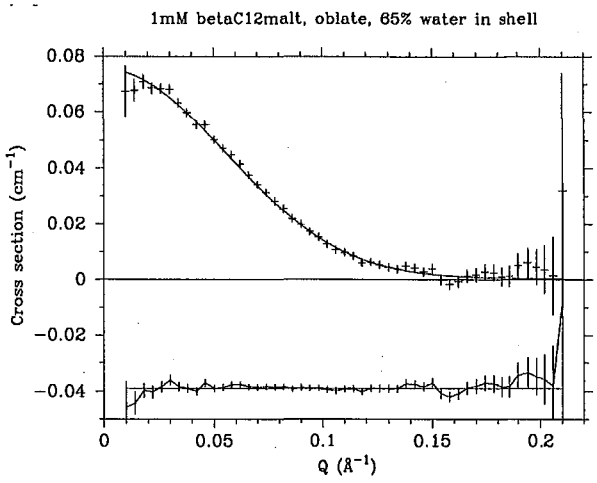
1mM betaC12malt, oblate, 65% water in shell
Cross section (cm^{-1})
Q (Å^{-1})

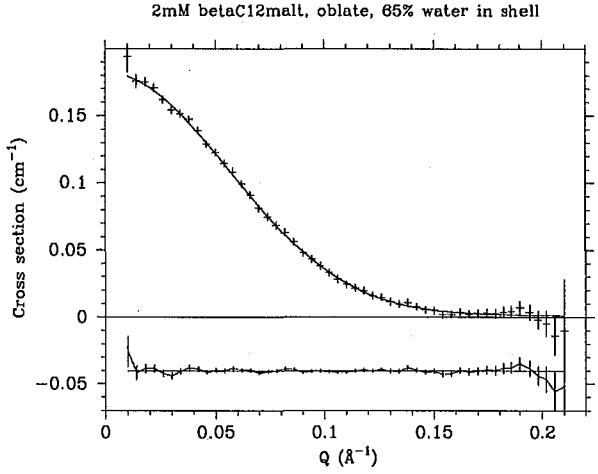
2mM betaC12malt, oblate, 65% water in shell
Cross section (cm^{-1})
Q (Å^{-1})

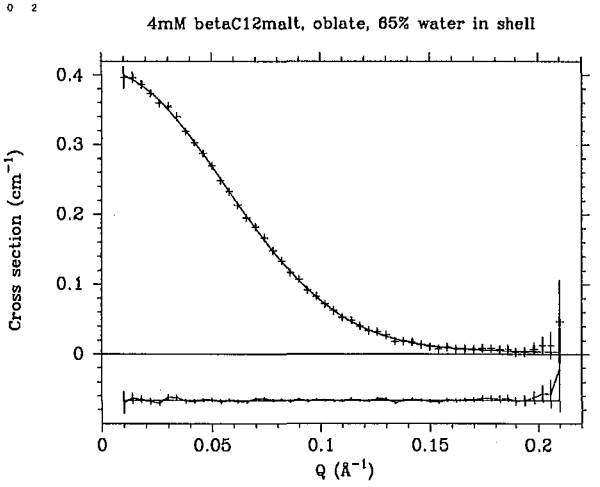
4mM betaC12malt, oblate, 65% water in shell
Cross section (cm^{-1})
Q (Å^{-1})

$C_{16}E_8$

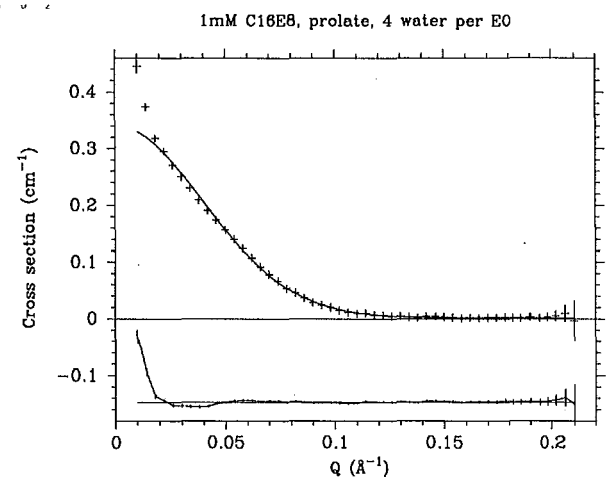
1mM C16E8, prolate, 4 water per EO
Cross section (cm^{-1})
Q (Å^{-1})

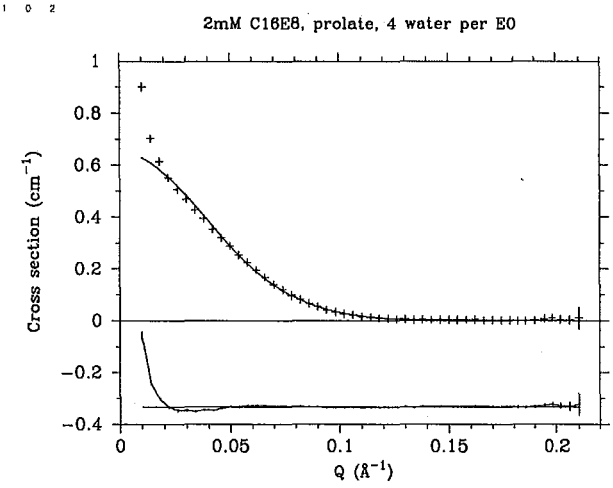
2mM C16E8, prolate, 4 water per EO
Cross section (cm^{-1})
Q (Å^{-1})

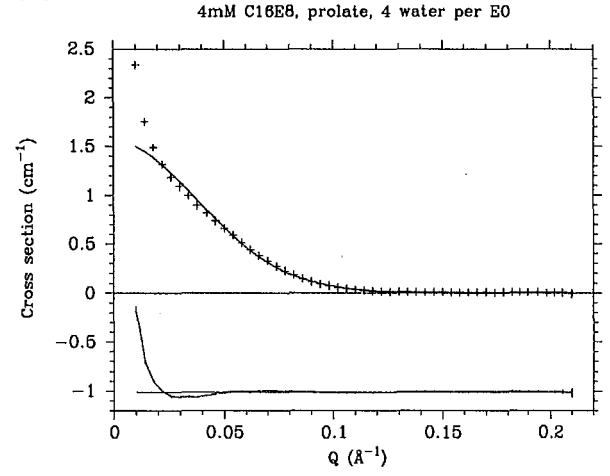
4mM C16E8, prolate, 4 water per EO
Cross section (cm^{-1})
Q (Å^{-1})

TX-100

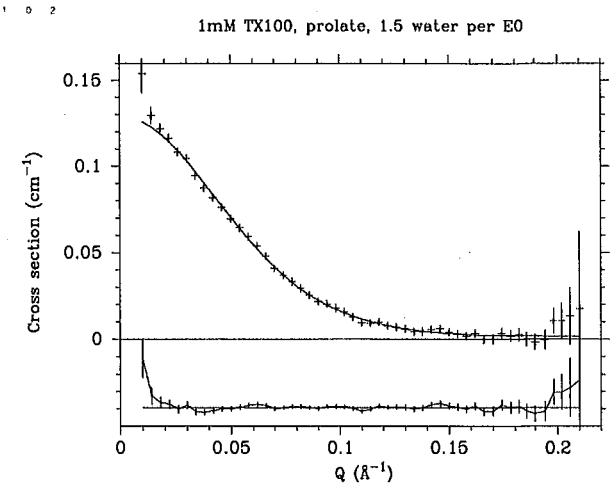
1mM TX100, prolate, 1.5 water per EO
Cross section (cm^{-1})
Q (Å^{-1})
0.15
0.1
0.05
0
0.05
0.1
0.15
0.2

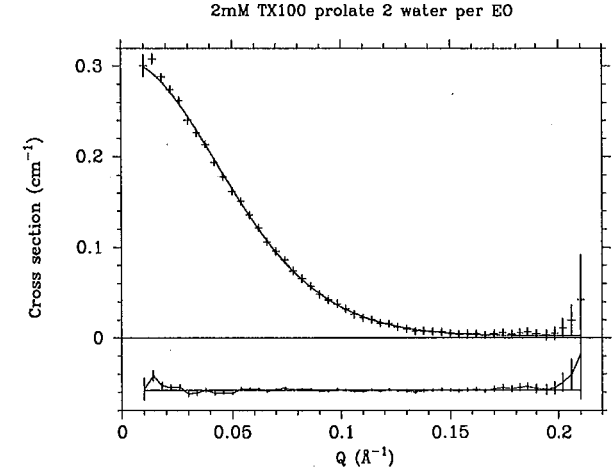
2mM TX100 prolate 2 water per EO
Cross section (cm^{-1})
Q (Å^{-1})
0.3
0.2
0.1
0
0.05
0.1
0.15
0.2

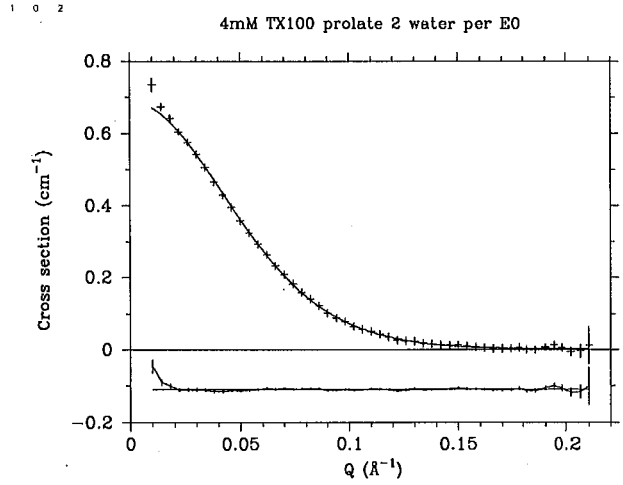
4mM TX100 prolate 2 water per EO
Cross section (cm^{-1})
Q (Å^{-1})
0.8
0.6
0.4
0.2
0
−0.2
0.05
0.1
0.15
0.2

βC_{12}malt

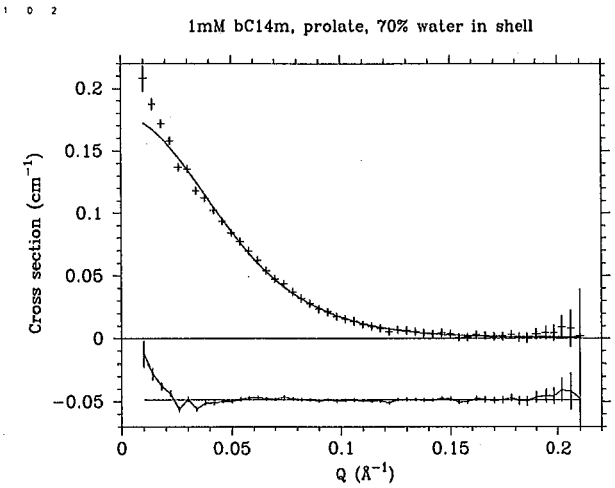

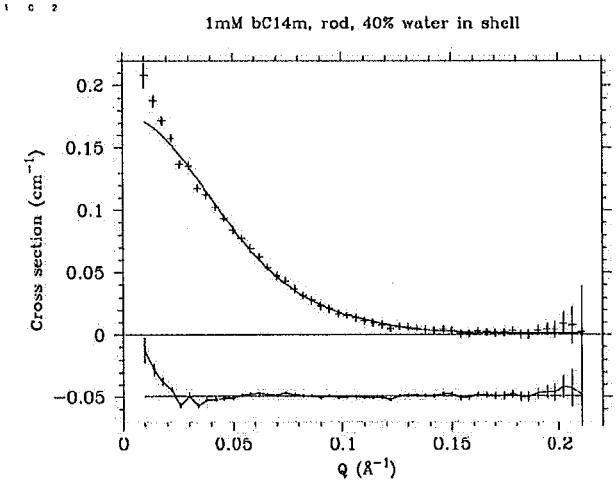

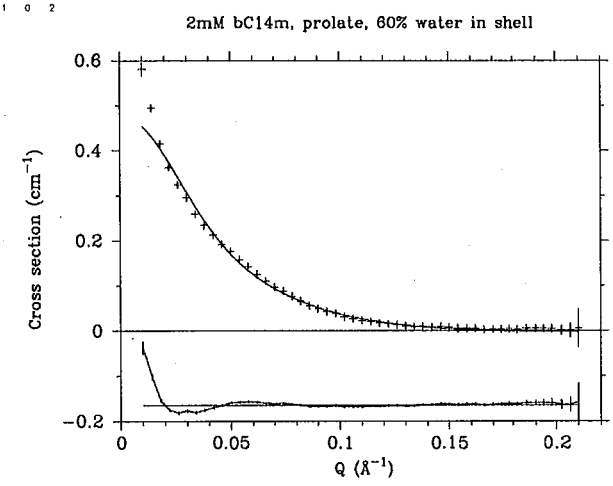

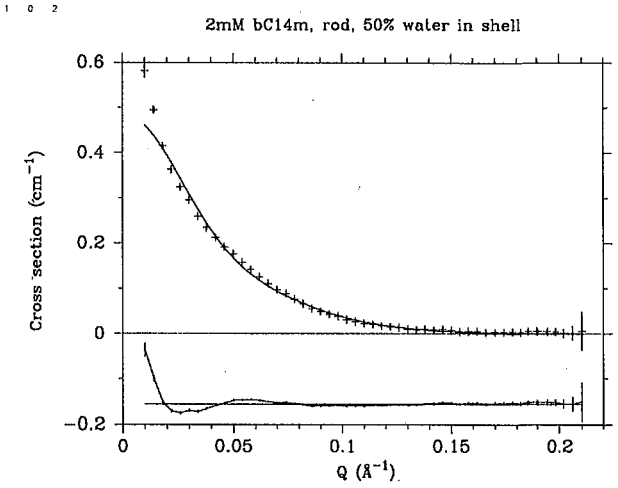
1 0 2
2mM bC14m, rod, 50% water in shell
Cross section (cm^{-1})
0.6
0.4
0.2
0
−0.2
0
0.05
0.1
0.15
0.2
Q (Å^{-1})

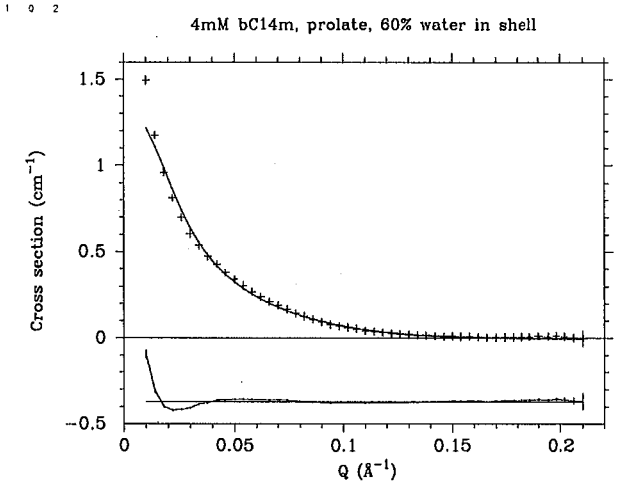
1 0 2
4mM bC14m, prolate, 60% water in shell
Cross section (cm^{-1})
1.5
1
0.5
0
−0.5
0
0.05
0.1
0.15
0.2
Q (Å^{-1})

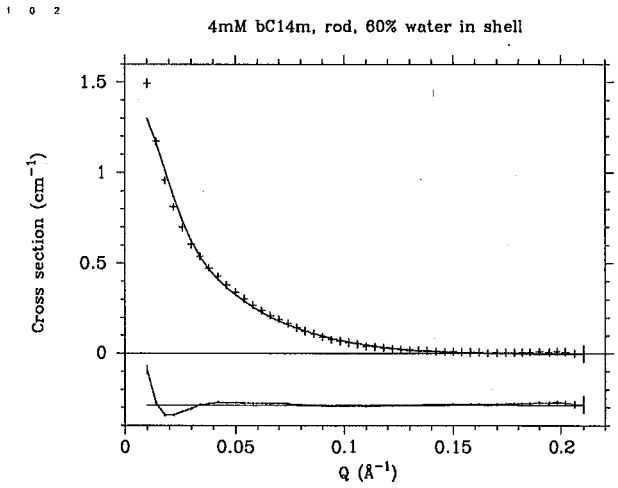
1 0 2
4mM bC14m, rod, 60% water in shell
Cross section (cm^{-1})
1.5
1
0.5
0
0
0.05
0.1
0.15
0.2
Q (Å^{-1})

$C_{12}E_6$

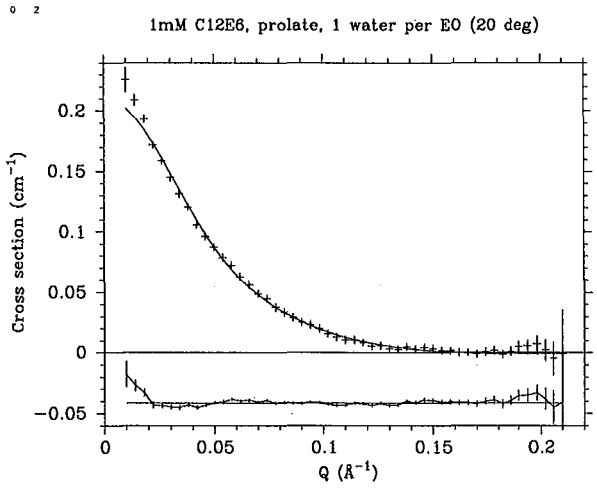
1mM C12E6, prolate, 1 water per EO (20 deg)
Cross section (cm^{-1})
Q (Å^{-1})
0.2
0.15
0.1
0.05
0
−0.05
0.05
0.1
0.15
0.2

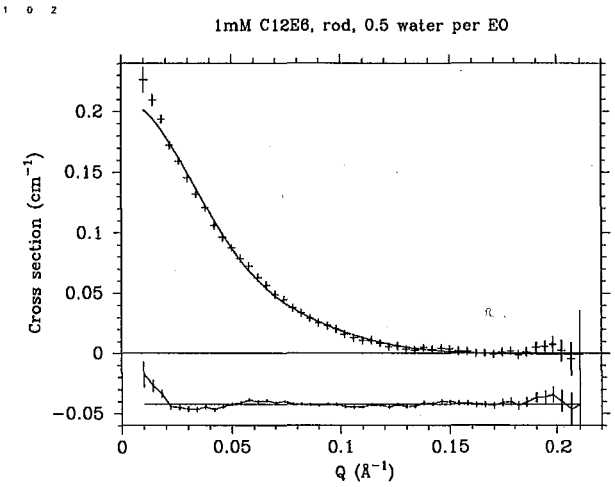
1mM C12E6, rod, 0.5 water per EO
Cross section (cm^{-1})
Q (Å^{-1})
0.2
0.15
0.1
0.05
0
−0.05
0.05
0.1
0.15
0.2

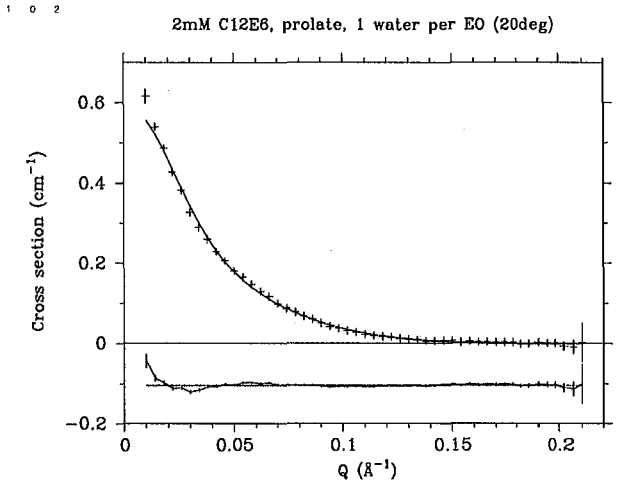
2mM C12E6, prolate, 1 water per EO (20deg)
Cross section (cm^{-1})
Q (Å^{-1})
0.6
0.4
0.2
0
−0.2
0.05
0.1
0.15
0.2

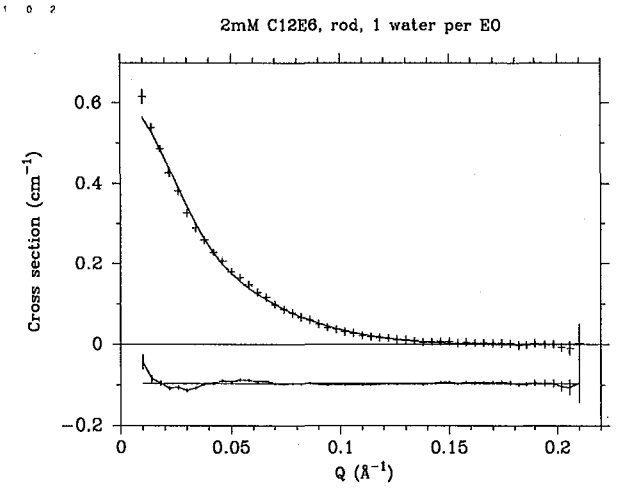
2mM C12E6, rod, 1 water per EO
Cross section (cm^{-1})
0.6
0.4
0.2
0
−0.2
0
0.05
0.1
0.15
0.2
Q (Å^{-1})

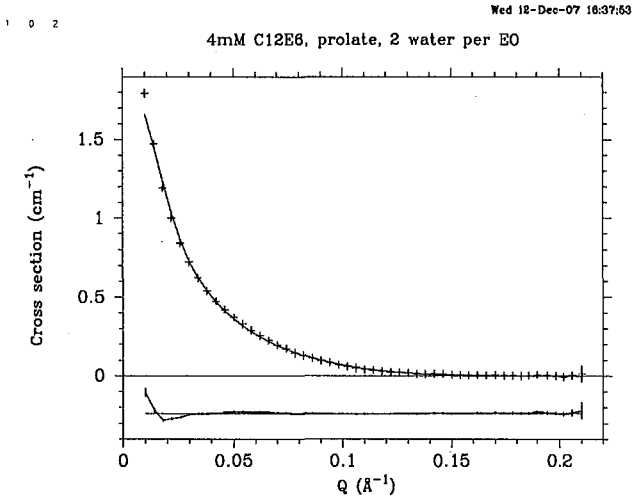
Wed 12-Dec-07 16:37:53
4mM C12E6, prolate, 2 water per EO
Cross section (cm^{-1})
1.5
1
0.5
0
0
0.05
0.1
0.15
0.2
Q (Å^{-1})

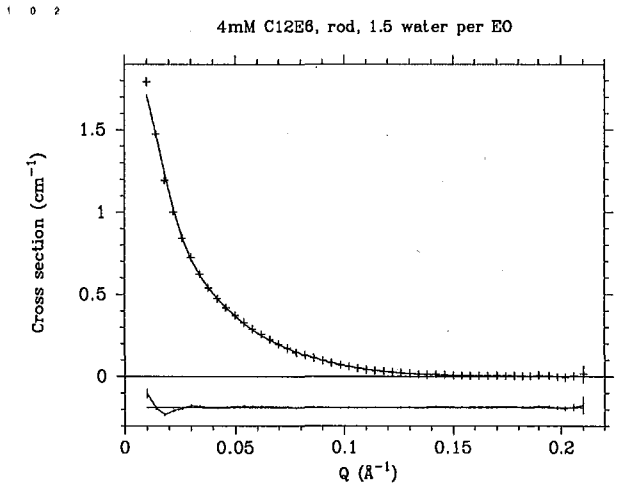
4mM C12E6, rod, 1.5 water per EO
Cross section (cm^{-1})
1.5
1
0.5
0
0
0.05
0.1
0.15
0.2
Q (Å^{-1})

$C_{14}E_6$

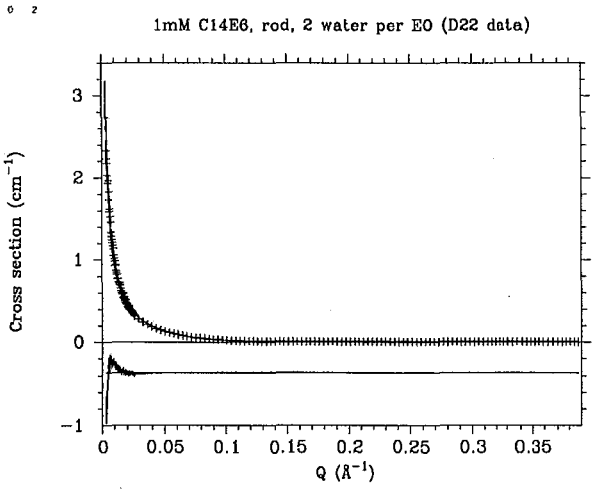
1mM C14E6, rod, 2 water per EO (D22 data)
Cross section (cm^{-1})
3
2
1
0
−1
0
0.05
0.1
0.15
0.2
0.25
0.3
0.35
Q (Å^{-1})

Appendix 2 – Equilibrium Fluorescence Spectra

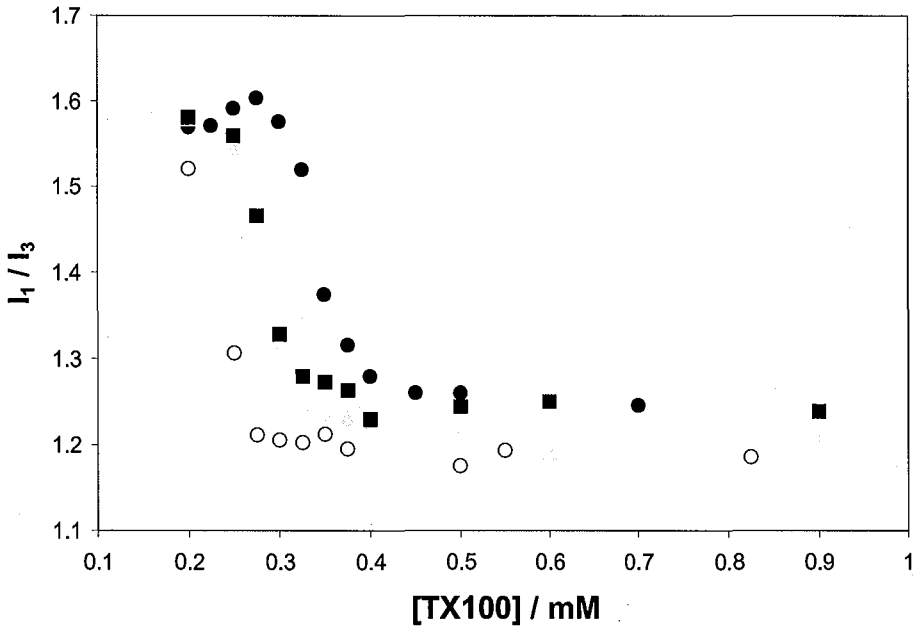

Figure A: I_1 / I_3 **in TX100 solutions containing 1% pyrene at (•) 5 °C, (■) 5 °C + 10 % CTAB, ( ) 20 °C and (○) 20 °C + 10% CTAB**

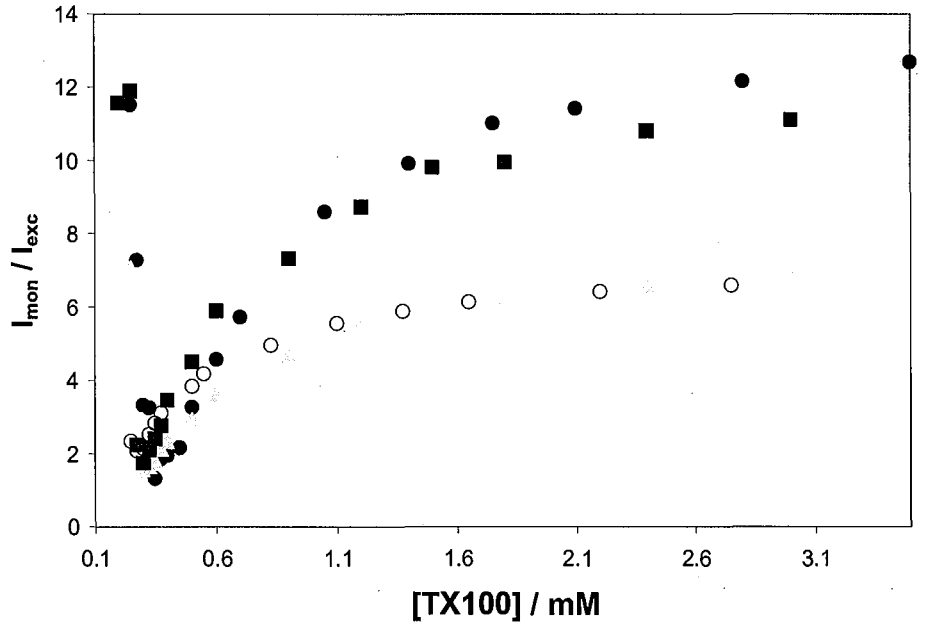

Figure B: I_{mon} / I_{exc} **in TX100 solutions containing 1% pyrene at (•) 5 °C, (■) 5 °C + 10 % CTAB, ( ) 20 °C and (○) 20 °C + 10% CTAB**

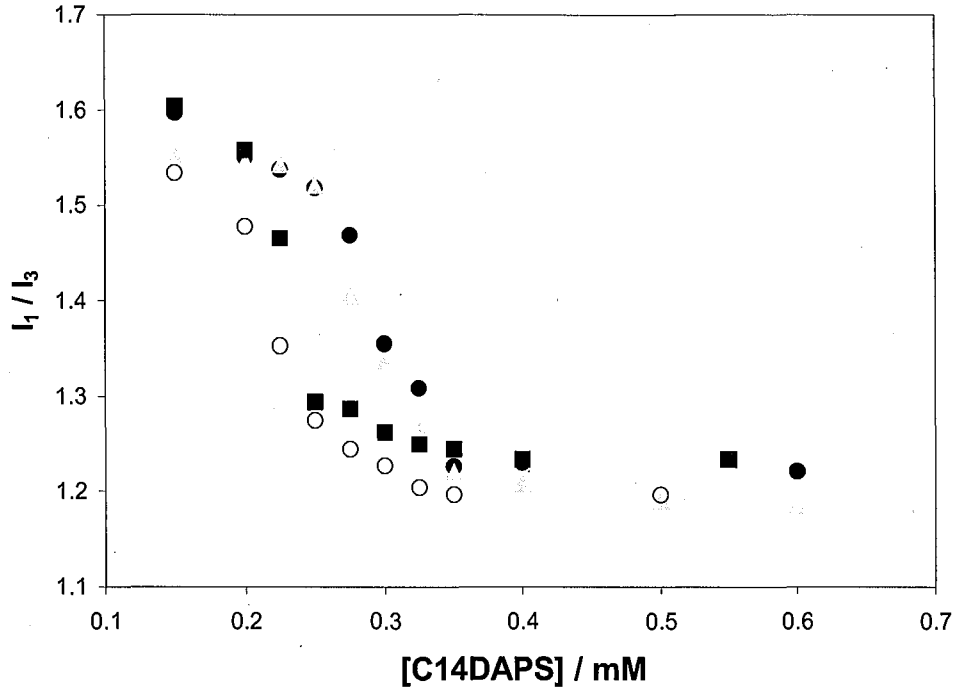

Figure C: I_1 / I_3 **in C14DAPS solutions containing 1% pyrene at (•) 5 °C, (■) 5 °C + 10 % CTAB, ( ) 20 °C and (○) 20 °C + 10% CTAB**

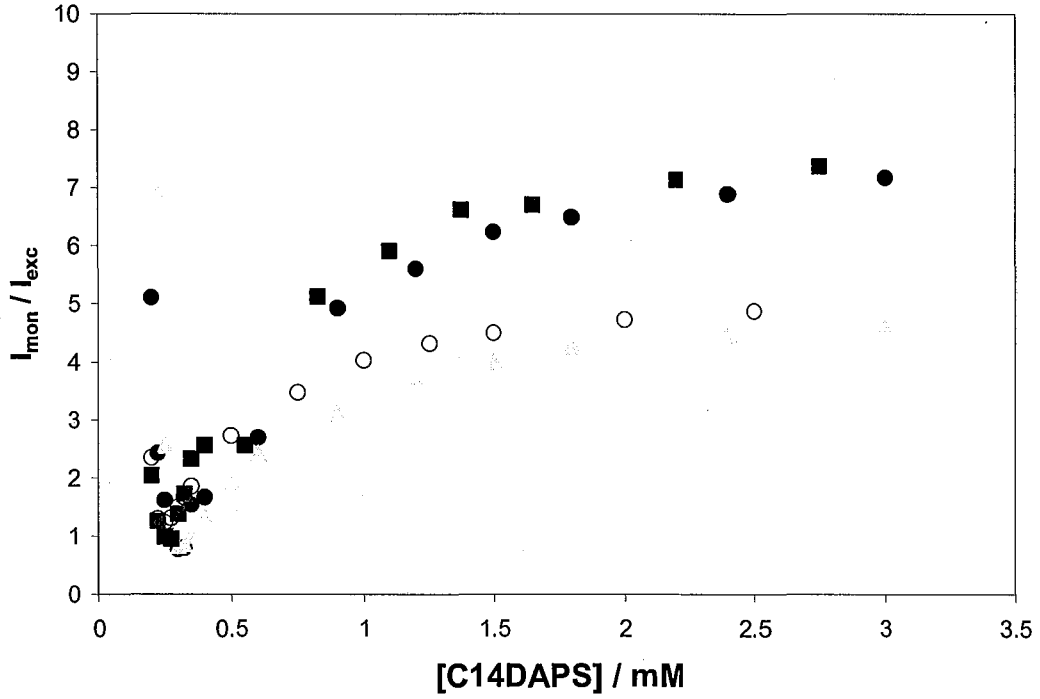

Figure D: I_{mon} / I_{exc} **in C14DAPS solutions containing 1% pyrene at (•) 5 °C, (■) 5 °C + 10 % CTAB, ( ) 20 °C and (○) 20 °C + 10% CTAB**

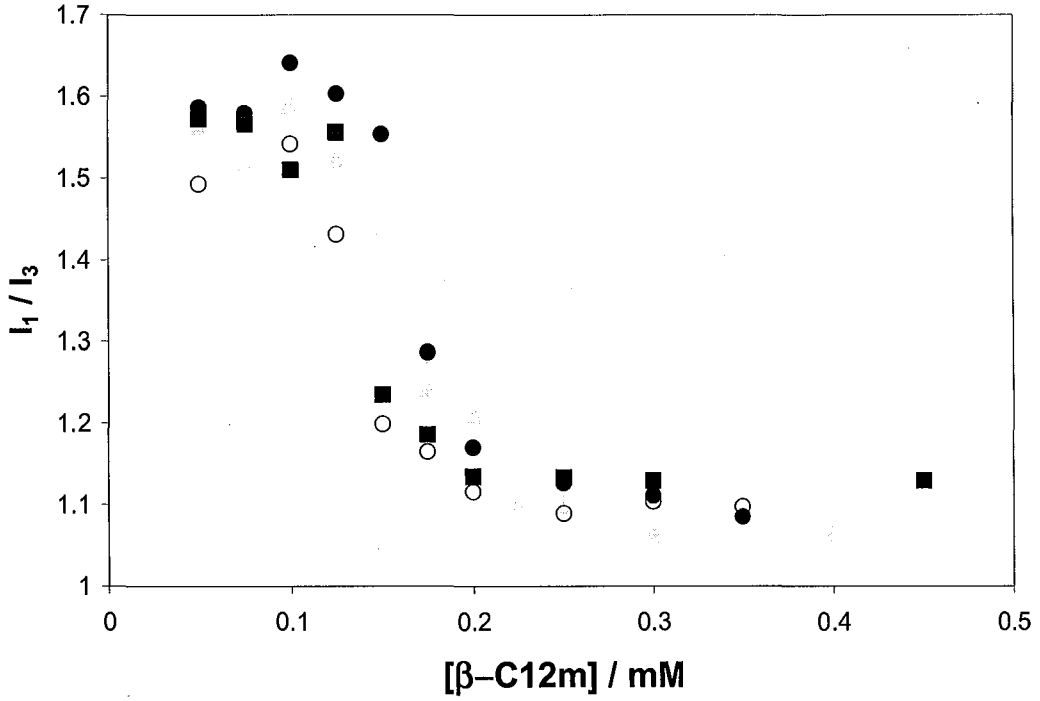

Figure E: I_1 / I_3 **in β-C_{12}m solutions containing 1% pyrene at (•) 5 °C, (■) 5 °C + 10 % CTAB, ( ) 20 °C and (○) 20 °C + 10% CTAB**

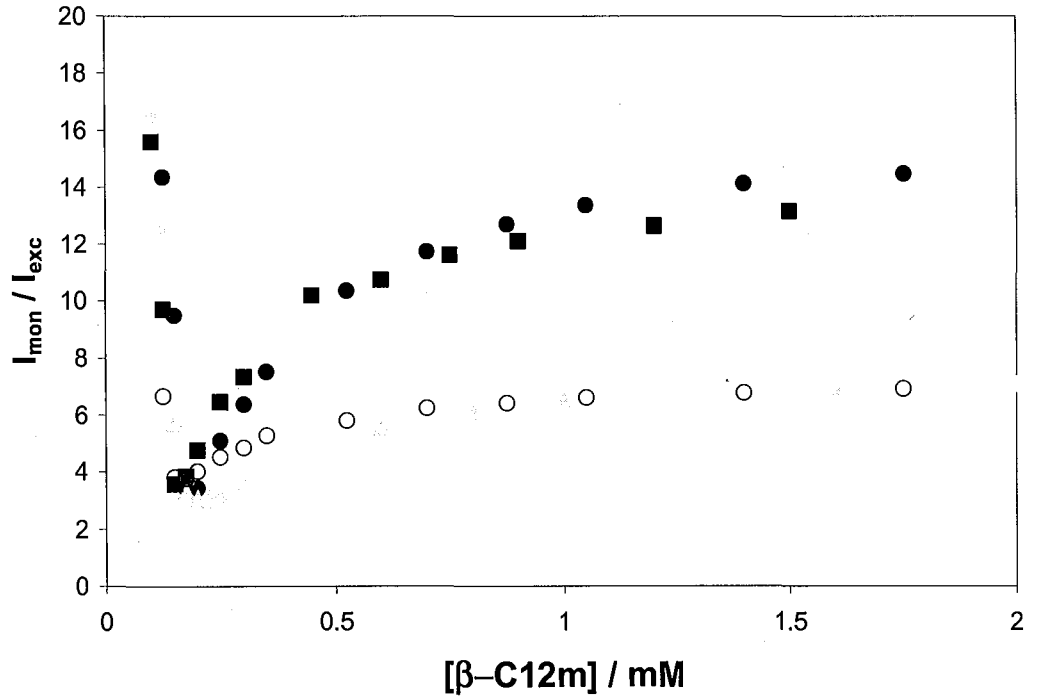

Figure F: I_{mon} / I_{exc} **in β-C_{12}m solutions containing 1% pyrene at (•) 5 °C, (■) 5 °C + 10 % CTAB, ( ) 20 °C and (○) 20 °C + 10% CTAB**

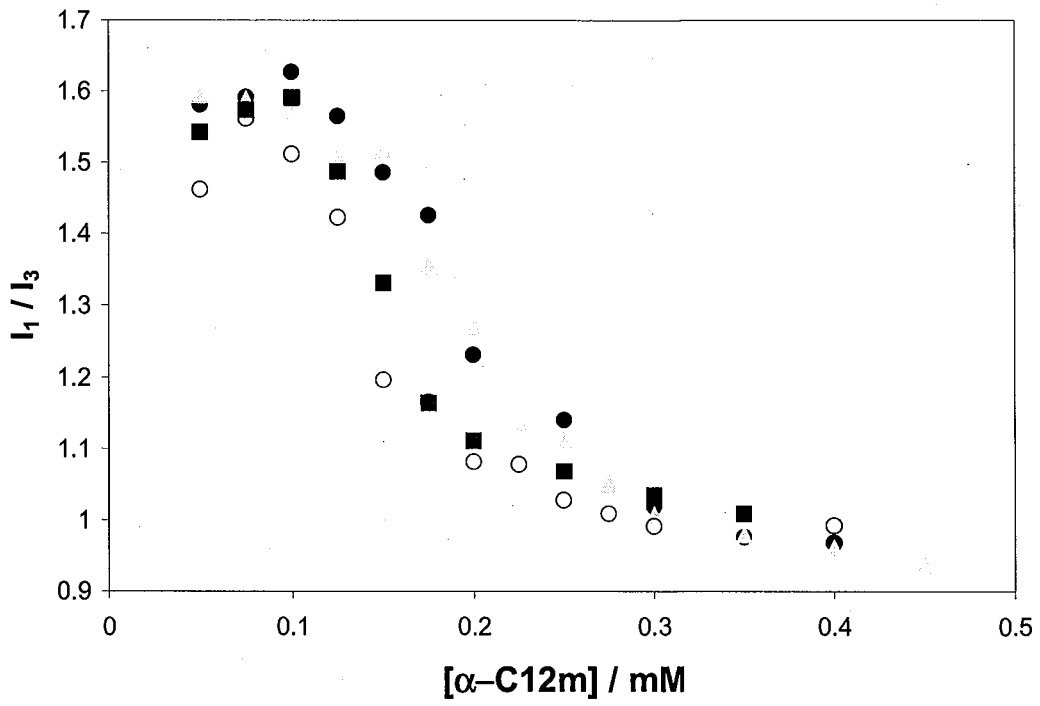

Figure G: I_1 / I_3 **in α-C_{12}m solutions containing 1% pyrene at (•) 5 °C, (■) 5 °C + 10 % CTAB, ( ) 20 °C and (○) 20 °C + 10% CTAB**

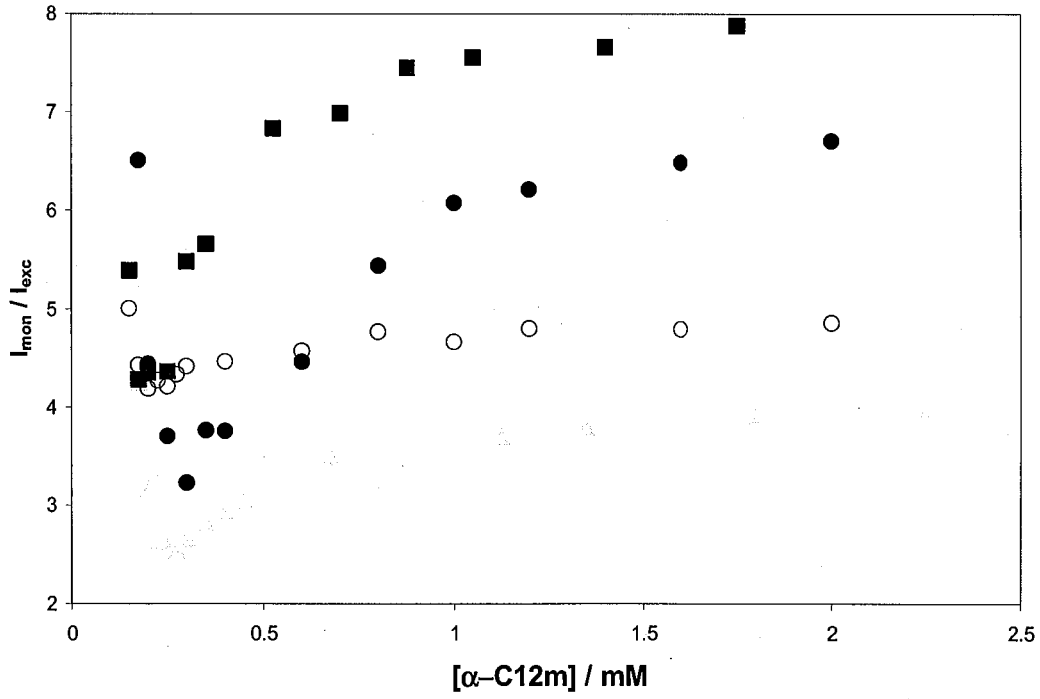

Figure H: I_{mon} / I_{exc} **in α-C_{12}m solutions containing 1% pyrene at (•) 5 °C, (■) 5 °C + 10 % CTAB, ( ) 20 °C and (○) 20 °C + 10% CTAB**

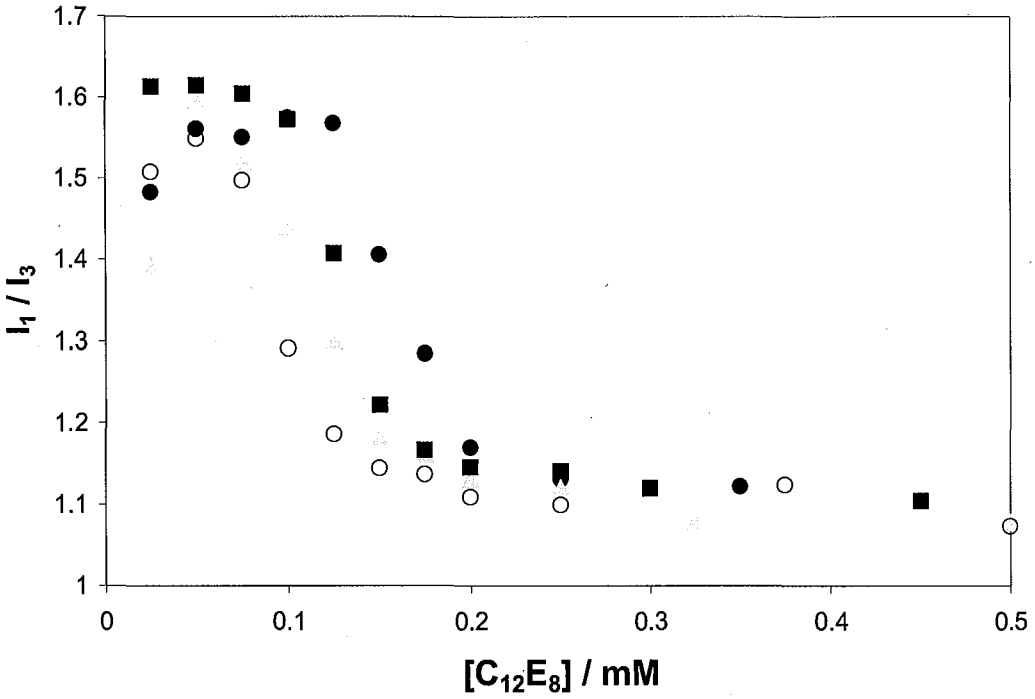

Figure I: I_1 / I_3 **in** $C_{12}E_8$ **solutions containing 1% pyrene at (•) 5 °C, (■) 5 °C + 10 % CTAB, ( ) 20 °C and (○) 20 °C + 10% CTAB**

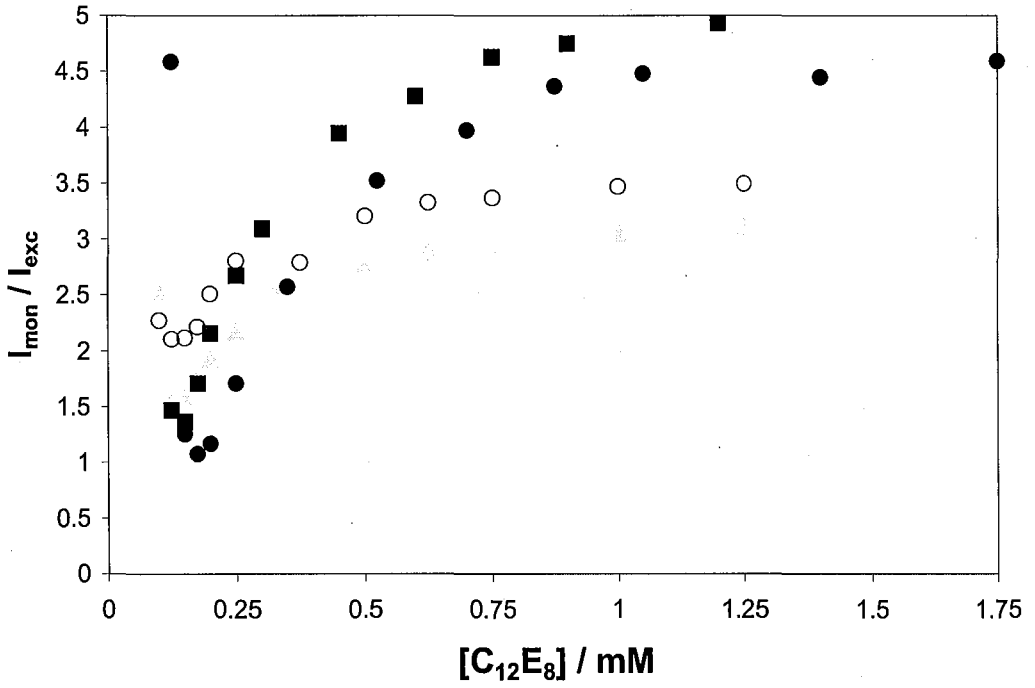

Figure J: I_{mon} / I_{exc} **in** $C_{12}E_8$ **solutions containing 1% pyrene at (•) 5 °C, (■) 5 °C + 10 % CTAB, ( ) 20 °C and (○) 20 °C + 10% CTAB**

Matlab code to evaluate the chemical potential variation in a spherical aggregate

```
%%Dmu: Spherical aggregates with a hole: Uniform Concentration

%Micelle thermodynamics based upon Ruckenstein and Nagarajans molecular
%thermodynamics model. Langmuir 1991, 2934-2969.

%Contributions to the free energy of micellisation may be broken down into
%components that reflect the molecular processes taking place.

%Key to symbols for inputs and calculated parameters
%g = aggregation number      gmax = limit of  considered 'aggregation space'
%T = temperature / K         k = Boltzmann constant
%n = number of carbons       m = number of EO units
%Veo = Volume of EO          W = water molecules per EO
%Vt = volume of tail (A^3)   Vh = volume of headgroup (A^3)
%Vc = Volume of core (A^3)   Vs = Volume of shell (A^3)
%Rc = core radius (A)        a = area/molecule at tail/shell interface (A^2)
%D = shell thickness (A)     Rg = total aggregate radius (A)
%L = Linear dimension of lattice spacing (for deformation modelling)
%N = number of lattice segments which make up surfactant tail
%M = number of lattice segments which make up the head group
%MW = molecular weight of hydrocarbon (g mol-1)
%phiEg = Volume fraction of polymer segments (uniform concentration)
%phiS = concentration of polymer segments in the surface monolayer
%chi = Flory-Huggins interaction parameter
%sw = surface tension of water (mNm-1)
%ss = surface tension of aliphatic hydrocarbon (mNm-1)
%se = surface tension between peo and water (mNm-1)
%ssw = surface tension between water and surfactant tails (mNm-1)
%sse = surface tension between peo and surfactant tails (mNm-1)

%The distribution
%mug + kT ln Xg = g[mu1 + kt ln X1]
%Xg = X1^g * exp [(mug - g*mu1)/kT] = X1^g * exp [(g*Dmu)/kT]
%Dmu = mug/g - mu1 = difference between free molecule and one in micelle
%Xg can be rewritten in terms of any arbitrary value of aggregate size M

%Free energy contributions (all will be scaled by 1/kT i.e Dmu = Dmu/kT)
%Dmu = sum of free energy terms
%Dmutt = Transfer free energy of surfactant tail
%Dmudt = Deformation free energy of surfactant tail
%Dmumh = head group mixing free energy
%Dmudh = head group deformation free energy
%Dmush = head group steric interaction free energy
%Dmuac = Aggregate/core interfacial free energy

global n m phiEg chi M sse ssw k T Vt g gmax Dmu

%Setting up the surfactant
```

```
%User defined variables
%n=input('How many carbons in the surfactant tail? n=');
%m=8;%input('How many EO groups in the surfactant head? m=');
%W=3;%input('How many water molecules per EO unit? W=');
T=20;%input('What is the temperature (in Celsius)? T=');


%Other parameters
gmax=400;
g=(1:1:gmax);
k=1.38e-23;
T=T+273;
Veo=63;
Vt=(27.4+(26.9*n));
Vh=Veo*m;
Vc=g.*Vt;
Vs=(g.*(Vh+(W*30.23)));
Rc=((Vc.*3)./(4*3.142)).^0.33333;
Rg=(((Vc+Vs).*3)./(4*3.142)).^0.33333;
D=Rg-Rc;
a=(4*3.142*Rc.^2)./g;

%core packing parameter
P=(Vt./(a.*Rc));

%Calculating free energy contributions
%1 - Dmutt
Dmutt=((3.38*log(T))+(4064/T)-44.13+(0.02595*T))+(n-
1)*((5.85*log(T))+(896/T)-36.15-(0.0056*T));

%2 - Dmudt
L=4.6;
N=(n+1)/3.6;
Dmudt=((9.*P*3.142^2)./80).*((Rc.^2)./(N*L^2));

%3 - Dmumh
M=(m*Veo)/L^3;
phiEg=(g.*M.*L^3)./Vs;
phiEg=mean(phiEg);
%chi=0.5;
Dmumh=(M*(0.5-chi)).*phiEg;

%4 - Dmudh
Dmudh=1.5.*((L.*Rc)./(a.*phiEg)).*(D./(D+Rc));

%5 - Dmush
Dmush=-1*log(1-(L^2./a));

%6 - Dmuac
%Calculate all the surface tension terms first
MW=(14*(n-1))+15;
sw=72-(0.16*(298-T));
ss=35-(325*(MW^-0.666))-(0.098*(T-298));
ssw=sw+ss-(2*0.55*((ss*sw)^0.5));
se=42.5-(19*(m^-0.66666))-(0.098*(T-298));
```

```
sse=sw+se-(2*((ss*se)^0.5));
a0=L^2;

phiS=fminbnd(@phis2,0,1);  %run a solvers as equation for phiS is implicit

sg=1e20*((k*T)/Vt^0.66666)*(log((1-phiS)/(1-phiEg)))+(((M-1)/M)*(phiS-
phiEg))+(chi*((0.5*phiS*phiS)-(0.75*phiEg*phiEg)))+ssw;

Dmuac=((sg/1000)/(k*T))*(a-a0)*1e-20; % /1e-20 as a has units of A^2


% scale=-Dmutt(1)/(Dmuac(1));
%
% Dmuac=Dmuac.*scale;
%7 once radius exceeds maxiumum hydrocarbon there will be a hole in the
%middle of the micelle which gives an extra surface tension term. The
%surface tension is that of the air-hydrocarbon (ss). Need to calculate
%hole radius, hence surface area per molecule, then surface energy.
Lt=1.5+(1.265*n);
ahole=zeros(1,gmax);

for A=1:gmax
    if Rc(A) > Lt
        ahole(A)=(4*3.142*(Rc(A)-Lt)^2)/A;
    end
end

Dmuhole=((ss/1000)/(k*T))*(ahole)*1e-20; % /1e-20 as a has units of A^2

%8 - Dmu
Dmu=(Dmutt+Dmudt+Dmumh+Dmudh+Dmush+Dmuac+Dmuhole);

%Some of the assumptions seem to break down for low g, therefore to keep
%Dmu(1) = 0 as it must be by construction, and get a smooth transition back
%to the real curve I will need to fudge it slightly. I tried a straight
%line but the slope was discontinuous. Instead I am using a high order
%polynomial

xdata=[1,6,7,8,9,10];
ydata=[0,Dmu(6),Dmu(7),Dmu(8),Dmu(9),Dmu(10)];

%fit an exponential to this data
%[estimates,model]=fitcurve(xdata,ydata);

%Fit a polynomial
p=polyfit(xdata,ydata,3);

%Calculate the remaining Dmu values
Dmu(1:5)=(p(1).*(g(1:5).^3))+(p(2).*(g(1:5).^2))+(p(3).*(g(1:5).^1))+p(4);
```

Matlab code to evaluate a micelle size distribution and the corresponding Aniansson and Wall micelle lifetimes

```
%M-file to determine starting size distribution
uc  %calls the M-file to calculate chemical potential variation

%%%%%%%%%%%%%%%%%%%%%%%%%%%%%%%%%%%%%%%%%%%%%%%%%%%%%%%%%%%%%%%%%%%%%%%%%%%%
% Now get the distribution for a given bulk concentration. To do this will
% need to evaluate the size distribution relative to an arbitrary value of
% g. Choose value corresponding to Dmu(min) which should be close to
% average aggregation number. Label this value j with mole fraction Xj.
[i,j]=min(Dmu);
Dmumg=(Dmu(j)-Dmu);

%Initial conditions
disp ('%
*************************************************************************
***')
disp ('% Evaluate the size distribution for a given bulk concentration
*')
disp ('%
*************************************************************************
***')

Cb=input('Bulk concentration / mM: ');

Cb=Cb/1000;

%Now vary Xj to give correct amount of material for initial and final
%states
%STEP-1 calculate distribution corresponding to Cb
Xji = 1e-10;
while sum((55*(((1^(1/j)).*((Xji^(1/j)).*exp(Dmumg)).^g))))<(Cb);
    Xji = Xji+1e-9;
end

%STEP-2 Evaluate the distribution
Xg=(1./g).*(55).*(((Xji^(1/j)).*exp(Dmumg)).^g);

figure(2)
plot(g,Xg)

%Calculate the A+W tau1 and tau2 values for this distribution
%parameters required
aa=(Cb-Xg(1))/Cb;

ka=1000*6.02e23*4*3.142.*(Ds+Ds(1)).*(1e-10*(Rg+Rg(1)));

kd=zeros(1,gmax);
for A=1:1:gmax;
    if A<=(gmax-1)
        kdd=ka(A)*((Xg(1)*Xg(A))/Xg(A+1));
```

```
    else kdd=kd(A-1);
    end
    kd(A)=kdd;
end

kminus=mean(kd(10:200));

realconc=g.*Xg;
[u,w]=max(realconc(2:gmax));

start=w;

X=w;

while realconc(X)>(u/2)
    X=X-1;
end

bot=X;

X=w;

while realconc(X)>(u/2)
    X=X+1;
end

top=X;

sigma=top-bot;

nn=w;

tau1=1/((kminus/(sigma^2))+((kminus/nn)*aa*2))

recip=1./(kd.*Xg);
R=sum(recip(10:bot-20));

tau2=1/((nn^2/Xg(1))*(1/R)*(1/(1+((sigma^2)/n)*aa)))

[ii,jj]=max(Xg(3:gmax))
```

Matlab code to perform a full Aniansson and Wall kinetic simulation

```
%Aniansson and Wall full kinetic simulation of the micelle system

%Get the initial size distribution
sizedis
close all

%Get the dilution factor
D=input('What is the dilution factor?:')

%What are the initial and final states of the system
Xi=Xg./D;

%For final state run a variation of sizedis with concentration Cb/D
sizedis2
close all

%%%%%%%%%%%%%%%%%%%%%%%%%%%%%%%%%%%%%%%
%Now evaluate the kinetics rate constants for monomer uptake (ka) and loss
%(kd)

%Evaluate ka assuming diffusion controlled collision of spherical
%aggregates. For clarity note that ka(g) relates to the addition of monomer
to
%aggregate of size g to form aggregate g+1.
%kd(g) refers to the breakdown of aggregate g+1 to form aggregate g
%association rate adjusted to 'normal' units by *1000Na

ka=1000*6.02e23*4*3.142.*(Ds+Ds(1)).*(1e-10*(Rg+Rg(1)));

kd=zeros(1,gmax);
for A=1:1:gmax;
    if A<=(gmax-1)
        kdd=ka(A)*((Xf(1)*Xf(A))/Xf(A+1));
    else kdd=kd(A-1);
    end
    kd(A)=kdd;
end

%%%%%%%%%%%%%%%%%%%%%%%%%%%%%%%%%%%%%%%
%It only remains to try and timestep this bad boy forward
%I will try the matrix method

X=Xi;   %initial distribution
AX=zeros(gmax);    %matrix of rates of change
b=zeros(gmax,1);   %vector of rate of change
h0=1e-8;           %initial time step
t=200;           %iterations
H=0;               %cumulative time
h=h0;              %time step at any given time
```

```
for B=1:t

%code the AX matrix
%Five row/column/diagonal rules
for A=2:1:gmax;
AX(A,1)=(ka(A)*X(A))-(ka(A-1)*X(A-1));
end

for A=2:1:gmax;
AX(1,A)=(ka(A)*X(1))-(kd(A-1));
end

for A=2:1:gmax;
AX(A,A)=kd(A-1)+(1/h)+(ka(A)*X(1));
end

for A=2:1:gmax-1;
AX(A,A+1)=-kd(A);
end

for A=2:1:gmax-1;
AX(A+1,A)=-kd(A)*X(1);
end

%Some useful summations
suma=sum(ka(1:gmax-1).*X(1:gmax-1));
sumb=sum(kd(1:gmax-1).*X(2:gmax))-sum(ka(1:gmax-1).*X(1:gmax-1).*X(1));

%Five exceptional entries
AX(1,1)=(1/h)+(ka(1)*X(1))+suma;
AX(1,gmax)=-kd(gmax-1);
AX(2,1)=(ka(2)*X(2))-(2*(ka(1)*X(1)));
AX(gmax,1)=(-ka(gmax-1)*X(gmax-1));
AX(gmax,gmax)=kd(gmax-1);

%Now code the bX vector
for A=2:gmax-1
    b(A)=(ka(A-1)*X(1)*X(A-1))+(kd(A)*X(A+1))-(kd(A-1)*X(A))-
(ka(A)*X(1)*X(A));
end

%Exceptions
b(1)=sumb;
b(gmax)=(ka(gmax-1)*X(1)*X(gmax-1))-(kd(gmax-1)*X(gmax));

%Now solve for the dX vector
x=AX\b;

%Now add it on
X=(B/B).*(X+x');

 X(1)
```

```
H=H+h;
h=(B^1.1)*h0;
 plot(g(70:80),Xi(70:80),g(70:80),Xf(70:80),g(70:80),X(70:80))
 pause(0.01)

 %keep track of X1/X1(f)
 Xc=X(1)/Xf(1);
 X1t(B)=(B/B)*Xc;


 %keep track of number of aggregates
 Nmic=sum(X(10:gmax));
 Nmict(B)=(B/B)*Nmic;

 %Keep track of time
 Ht(B)=(B/B)*H;

 %Get out if monomer concentration stops changing
 if B~=1
     test=1-X1t(B-1);
    if test < 0.000001
        break
    end
 end


end

%Give me the results I want to look at. Monomer change with time
%and aggregate number change with time

Ht=Ht';
X1t=X1t';
Nmict=Nmict';

Result(:,1)=Ht;
Result(:,2)=X1t;
Result(:,3)=Nmict;
```

Procedure to align Picometer Ellipsometer to carry out measurements on the liquid jet

The procedure outlined below has been discovered and refined through significant trial and error and leads to highly reproducible ellipticity measurements for surfactant solutions placed in the liquid jet. The instructions below assume that the reader is familiar with the liquid jet system.

1. Ensure that the laser arm mount (holding the laser, birefringence modulator, analyser and lenses) and the collection arm (holding the analyser and PMT) are at an angle of roughly 107° with the liquid jet at the apex.

2. Set the axial displacement of the jet so that the ellipsometer laser is incident at $z = 10$ mm.

3. Move the liquid jet forward/backward in the laser beam whilst monitoring the cathode voltage on the Picometer Ellipsometer hardware panels. Position the jet to minimise this cathode voltage, maximising the amount of light entering the PMT.

4. Open the IGOR Pro software and set up to perform an ellipsometry scan with 41 data points and time interval 1.2 seconds. Click 'Measure'.

5. Using the translation stage beneath the collection arm, adjust the lateral position of the PMT and monitor the 'x' signal in the IGOR command window. Adjust this position until the 'x' signal fluctuates around zero. This indicates the Brewster angle.

6. Make a note of the 'y' signal. This is the ellipticity. If 'y' $\approx 0.8\times10^{-3}$, congratulations the system is aligned. If not, move the jet forward by 0.1 μm and repeat steps 4 and 5.

7. Iterate between 4, 5 and 6, adjusting the jet position and minimising the 'x' signal until the 'y' signal is correct. At this point ellipsometer is aligned.

8. To carry out ellipsometry measurements, simply adjust the axial jet position. At each axial displacement, adjust the forward/backward position of the jet to get the 'x' signal to zero and record the 'y' signal averaged over a period of time.